Caractérisation acoustique et aérodynamique d'écoulements cisaillés

Thomas Castelain

Université Lyon 1
43 boulevard du 11 Novembre 1918 - 69622 Villeurbanne cédex

Laboratoire de Mécanique des Fluides et d'Acoustique
École Centrale de Lyon, Université Lyon I, Insa de Lyon, Cnrs
36, Avenue Guy de Collongue - 69134 Écully cédex

Synthèse des activités de recherche et d'enseignement
Habilitation à Diriger des Recherches

Caractérisation acoustique et aérodynamique d'écoulements cisaillés

Thomas Castelain

---

soutenue le 04/02/2020 devant le jury composé de :

E.Piot	Maître de Recherches - onera	Rapporteur
R. Camussi	Full professor - Univ. Roma Tre	Rapporteur
L. David	Professeur des Universités - Univ. Poitiers	Rapporteur
C.Bogey	Directeur de recherche - cnrs - lmfa	Examinateur
J.Borée	Professeur des Universités - ensma	Examinateur
M.Lance	Professeur des Universités - Univ. Lyon 1	Examinateur

Table des matières

Nomenclature

Partie 3.1 et 3.3

BBSAN	Bruit de choc large bande (Broad-Band Shock-Associated Noise)
C38	Tuyère convergente de diamètre terminal D=38mm
D	Diamètre terminal de tuyère pour l'étude des jets
M_d	Nombre de Mach de design d'une tuyère convergente/divergente
M_j	Nombre de Mach équivalent pour un écoulement parfaitement détendu
σ_i	Valeur RMS de la composante de la vitesse dans la direction i

Partie 3.2

C_μ	Coefficient de quantité de mouvement des jets pulsés
f_{act}	Fréquence d'actionnement des jets pulsés
$f^u_{1/4}$	Fréquence de résonance en mode 1/4 d'onde du conduit amont à l'électrovanne
$f^d_{1/4}$	Fréquence de résonance en mode 1/4 d'onde du conduit en aval de l'électrovanne
H	Hauteur de la maquette 3D
U_u	Vitesse de soubassement dans la maquette de véhicule terrestre
U_∞	Vitesse de l'écoulement infini amont
$U_{\max}$	Vitesse maximale du jet pulsé au cours d'un cycle, mesurée en sortie de fente
γ_p	Taux de recompression au culot de la maquette 3D
W	Largeur de la maquette 3D
ζ_i	Flux de quantité de mouvement au travers d'une surface de contrôle définie en figure 14

Partie 3.3

C_p	Coefficient de pression à la paroi d'un corps
D	Diamètre terminal de tuyère pour l'étude des jets
M_j	Nombre de Mach équivalent pour un écoulement parfaitement détendu

1 Résumé

Dans ce document sont présentées mes différentes activités de recherche depuis ma prise de poste d'enseignant-chercheur en septembre 2008. Elles concernent une approche expérimentale de l'aéroacoustique des jets compressibles subsoniques et aussi des jets supersoniques sous-détendus, pour une part, et du contrôle d'écoulement pour l'amélioration des performances aérodynamiques des véhicules terrestres industriels d'autre part. Elles sont soutenues par des développements de métrologies qui sont particulièrement adaptées à l'étude des écoulements compressibles, sans toutefois se restreindre à ce champ de recherche.

En co-encadrement avec mes collègues HDR, en particulier D.Juvé et C.Bailly, j'ai encadré quatre thèses de doctorat sur la période 2010-2017 :

- deux thèses (S.Chaligné et M.Szmigiel) portant sur l'utilisation du contrôle d'écoulement sur des maquettes de véhicules de transport de marchandises. Pour ces véhicules, des contraintes d'exploitation figent la forme de la partie arrière, qui correspond à un culot droit où se produit un détachement massif de l'écoulement contournant le véhicule. À partir d'études sur géométries simplifiées, une stratégie de contrôle d'écoulement sur corps tridimensionnel a été mise en œuvre en soufflerie, sur une maquette de poids-lourd à échelle 1/8e . Cette approche originale repose sur la combinaison de jets pulsés/synthétiques et de surfaces solides rapportées au culot de la maquette. Les performances de cette approche, ainsi que les spécificités de l'écoulement autour d'un véhicule poids-lourds, ont été identifiées notamment dans le cadre du programme ANR Activ_ROAD (AAP 2015, 01/2016-09/2020) dont j'assure la coordination. Cette activité a conduit à 3 publications et 22 participations à des congrès et réunions de spécialistes.
- deux thèses (B.André et B.Mercier) ont porté sur l'étude des sources de bruit spécifiques aux jets supersoniques sous-détendus, liées à la présence d'une structure de cellule de chocs avec laquelle interagit la turbulence dans la couche de cisaillement. Selon la nature de cette interaction, un bouclage aéroacoustique peut s'établir (screech) et influencer l'interaction propre de la turbulence avec le réseau de cellules de choc responsable par ailleurs du bruit de choc large bande. Elles ont donné lieu à 16 publications et 20 participations à des congrès et réunions de spécialistes.

Les perspectives proposées sur la base de ces premiers résultats concernent l'identification fine de mécanismes physiques complexes à l'origine des phénomènes observés, d'ordre aérodynamique (comment la vorticité induite dans l'écoulement par le système de contrôle modifie le développement du proche sillage du corps et donc la pression au culot ?) ou aéroacoustique (quel(s) mécanisme(s) spécifiques aux jets supersoniques imparfaitement détendus conduisent à des sources de bruit si efficaces et marquées fréquentiellement ?). Pour cela, l'utilisation et le développement d'outils métrologiques à haute performance sont nécessaires. L'approche expérimentale ayant ses propres limites, il sera aussi indispensable d'identifier les situations où les simulations numériques réalisées par les spécialistes du groupe pourraient apporter un éclairage inaccessible à l'expérience.

Summary

My different research activities since 2008 are summarized in this document. They concern an experimental approach of subsonic and under-expanded jets aeroacoustics in one hand and flow control for aerodynamics of ground vehicles in the other hand. They are supported by the development of measurement systems well suited - but not restricted - to compressible flow analyses.

Together with colleagues authorized to supervize researches (HDR), in particular D.Juvé and C.Bailly, I supervised 4 doctoral theses during the years 2010-2017 :

- 2 doctoral theses (S.Chaligné and M.Szmigiel) focused on flow control over models of heavy-duty vehicles. For these vehicles, operating constraints lead to a square back shape, inducing a massive flow detachment at the vehicle rear. On the basis of studies on simplified geometries, a flow control strategy has been applied to 3D models taking into account the peculiarities of heavy vehicles in terms of momentum balance between the underside flow and the free flow. This original approch relies on the combination between unsteady (pulsed or synthetic) jets and solid surfaces plugged on the model base. The performances of this approach has been partly assessed during the ANR (french research agency) programm I am co-ordinating. This activity led to 3 papers in peer-reviewed journals and 22 conference proceedings or workshops.

- 2 doctoral theses (B.André and B.Mercier) concerned aeroacoustics of underexpanded jets. Different noise sources due to the interaction between turbulence in the jet shear layer and the shock-cell structure which develops in the jet core have been studied. Of particular interest is the screech phenomenon, linked with a feedback process which leads to intense pure tonal noise. The influence of screech on the broad-band shock-associated noise, which comes from the interaction between broad-band turbulence and shocks, was examined. These studies led to 16 papers in peer-reviewed journals and 20 conference proceedings or workshops.

The perspectives of this work concern a finer identification of the physical mechanisms at work either from the aerodynamics viewpoint (how the vorticity induced in the flow by the control system leads to changes in the near-wake beneficial to pressure drag reduction ?) or from the aeroacoustics angle (which mechanism(s) lead(s) to such efficient and frequency-marked noise sources specific to underexpanded jets ?). In that respect, the use and development of high performance measurement systems are needed. The use of data frmo numerical simulations can also usefully complement the experiments.

2 Curriculum Vitae

Thomas Castelain
Né le 12/11/1979
Marié - 2 enfants

Coordonnées professionnelles
✉ thomas.castelain@ec-lyon.fr
✆ 04.72.18.60.15

Fonction actuelle

Maître de Conférences à l'Université Lyon I. **depuis sept.2008**

- Recherche au Laboratoire de Mécanique des Fluides et d'Acoustique, UMR 5509
  - Groupe de recherche 'Acoustique'
  - Thématique 'Dynamique et acoustique des écoulements cisaillés compressibles'
- Enseignement en Mécanique à l'IUT Lyon 1 - Département GMP.

Encadrement, publications et diffusion des résultats

- Encadrant principal de 4 doctorants (soutenances entre 2012 et 2016), 2 thèses en cours,
- Encadrant principal de 3 post-doc, 2 étudiants de master M1,
- 24 publications dans des revues avec comité de lecture,
- 40 conférences avec actes,
- 14 communications au cours de colloques et réunions de spécialistes

Formation

- **Thèse de doctorat.** Spécialité : Acoustique **2003-2006**

sous la direction des professeurs J.-C. Béra & M. Sunyach (Université Lyon I)
Contrôle de jet par microjets impactants. Mesure de bruit rayonné et analyse aérodynamique.

- **DEA d'acoustique** de l'École Centrale de Lyon. **2002-2003**
- **Ingénieur de l'École Centrale de Lyon** **2000-2003**

Parcours professionnel

- Stage **post-doctoral** **2008**

Lehrstuhl für Strömungsmechanik, Friedrich-Alexander-Universität, Erlangen, Allemagne
Bourse accordée par la fondation bavaroise de recherche (*Bayerische Forschungsstiftung*)

- **ATER** à l'UFR de Mécanique - Université de Lyon I **2007 - 2008**
- **ATER** à l'École Centrale de Lyon **2006 - 2007**
- **Allocataire - Moniteur de l'École Centrale de Lyon** **2003 - 2006**

3 Synthèse des activités

3.1 Activités d'enseignement

Mes activités d'enseignement ont essentiellement lieu au département de Génie Mécanique et Productique (GMP) de l'IUT Lyon 1. J'y enseigne la mécanique du solide, la mécanique des fluides, auprès des étudiants de deuxième année (équivalent L2). J'interviens également auprès d'étudiants en Licence Professionnelle (formation par alternance) et, plus ponctuellement, en cycle ingénieur de la formation ITII (Institut des techniques d'ingénieur de l'industrie). Depuis 2016, je participe à l'enseignement d'Acoustique générale en M1 au sein du Master international d'Acoustique de l'Université de Lyon. En complément du tableau de synthèse (Table 1) qui indique les disciplines enseignées et les publics correspondants, je détaillerai ci-après quelques aspects originaux du développement des enseignements de Mécanique du solide et de Mécanique des Fluides à l'IUT.

Discipline	**Année**	**Niveau**	**Établissement**	**Heures (⋆)**
Mécanique	2008→	L2	IUT Lyon 1 - Dpt GMP	140
Mécanique des fluides	2008→	L2	IUT Lyon 1 - Dpt GMP	95
Mécanique	2013→2015 2016-2017	L1	IUT Lyon 1 - Dpt GMP	12
Mécanique	2013 → 2016	LP CIRI (1)	IUT Lyon 1	16
Mécanique des fluides	2018 →	LP M2IAC (2)	IUT Lyon 1	16
Acoustique	2016→	Master	Université de Lyon	36
Suivi projet	2008→	L2	IUT Lyon 1 - Dpt GMP	7.1 étu/an
Suivi stage	2008→	L2	IUT Lyon 1 - Dpt GMP	3.1 étu/an
Service				265

(⋆) *les chiffres indiqués dans cette colonne correspondent à un volume annuel moyen heqTD sur la période concernée, ou, pour les projets et stages, à un nombre moyen d'étudiants suivis*

(1) Chargé d'intégration en robotique industrielle

(2) Maintenance et intégration d'installations agroalimentaires et contraintes

TABLE 1 – Bilan de la répartition des activités d'enseignement (type/volume horaire)

3.1.1 Enseignements en Mécanique du solide

Responsables des enseignements	:	T.Castelain & J.-P. Chaomleffel
Étudiants concernés	:	2A GMP (L2)
Organisation	:	9h CM, 28h TD, 8h TP

Dans ce module d'enseignement, on souhaite d'une part que les étudiants continuent à s'entraîner à la détermination de l'équation du mouvement des solides indéformables à 1 degré de liberté (Principe Fondamental de la Dynamique et théorèmes énergétiques, en accord avec le programme pédagogique national des IUT) et d'autre part qu'ils appliquent ces résultats à l'analyse de mouvements oscillatoires (en particulier à des fins d'isolation vibratoire). Une ouverture sur le mouvement des systèmes paramétriques et les mouvements oscillatoires de grande amplitude est également proposée. Depuis 2010, je suis **responsable de la gestion de l'enseignement** de cette discipline, ce pourquoi je cherche à **proposer des outils pédagogiques adaptés** (développement/mise à jour de bancs de TP, TICE, développement des supports à destination des étudiants). À ce titre, j'ai la charge de la **gestion des examens** (organisation des épreuves, rédaction des sujets) : cette action est décrite ci-après.

Gestion des examens

Les examens communs à l'ensemble de la promotion (250 étudiants) peuvent prendre la forme de tests rédigés ou de QCM. Pour ces derniers, j'ai **développé un outil** qui permet la **rédaction de sujets de QCM scientifiques** (LaTeX) et une **correction automatisée** des documents réponse des étudiants (Matlab). Quatre versions d'un même sujet sont produites ; l'ordre des questions est le même dans les différentes versions du sujet, mais pour chaque question, l'ordre des choix varie d'un sujet à l'autre, ce qui a pour but de limiter la triche (ou au moins son intérêt). Pour la plus récente utilisation de ce procédé, les résultats des 250 étudiants étaient connus 2h après la fin de l'examen. L'automatisation de la correction permet de plus d'évaluer le taux de réussite des étudiants par question ou par thème abordé, et ainsi d'organiser efficacement une correction d'examen ciblée. L'ensemble de cette procédure qui couvre les différentes étapes nécessaires de la rédaction du sujet à la correction est mise à disposition du service ICAP de l'université Lyon 1, dans le but d'une mise en commun auprès de collègues intéressés.

Outils pédagogiques

• Pour chaque application vue en TD, j'ai créé un **modèle numérique simplifié** dans l'environnement Algodoo (simulation des mouvements plans de systèmes mécaniques) pour faciliter le traitement des exercices en aidant à la visualisation du mouvement. La figure 1 illustre ce procédé.

• Avec l'aide de collègues du département de fabrication, il m'a été possible de **développer quelques maquettes** de petite taille pour faciliter leur utilisation par tous, en TD et cours. Les **bancs développés** permettent de **fournir des données quantitatives** sur la position de centre de gravité de solides plans (fig.2a), sur les propriétés des mouvements pendulaires (2b), celles du roulement sans glissement d'une bille sur un support circulaire, sur l'effet du moment d'inertie à masse constante sur le roulement sans glissement (2c), et sur le mouvement

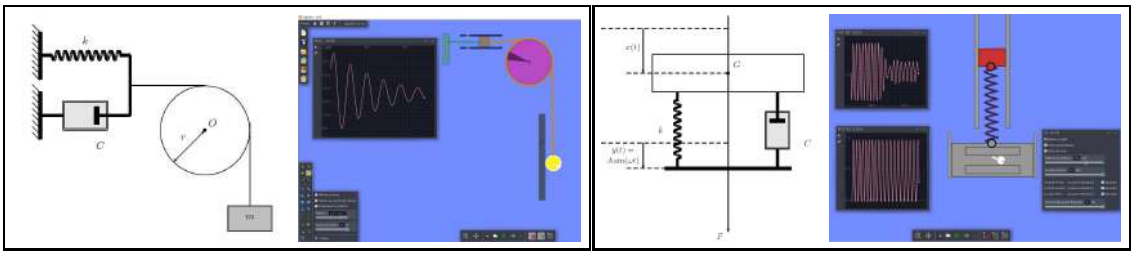

(a) (b)

FIGURE 1 – Exemples de modèles numériques développés pour l'analyse des exercices de TD. (a) mouvement libre de deux corps liés par un cable inextensible, (b) mouvement forcé d'un système à 1DDL (isolation vibratoire)

oscillatoire forcé de grande amplitude (fig.2d).

• J'ai obtenu à deux reprises, en 2010 et en 2015, un **soutien du service ICAP** de l'Université suite à l'appel à projets **'Pratiques Pédagogiques Innovantes'**. Le constat à l'origine de ces projets est que les étudiants passent peu de temps en Travaux Pratiques, cadre dans lequel ils se trouvent souvent plus à l'aise qu'en TD ou en cours. L'objectif de ces projets est de s'appuyer sur les ressources disponibles en TP (démonstrateurs instrumentés) pour réaliser des **films explicatifs** en accès libre pour les étudiants, et utilisés pour une **analyse approfondie en TD ou cours**. Par exemple, l'exploitation de **certaines séquences filmées à haute cadence** d'acquisition sur la base d'un système en rotation autour d'un axe fixe permet d'aborder progressivement les **notions de moment d'inertie**, de **frottements**, de **mouvements libres et forcés** (Figure 3).

• Pour stimuler l'activité - intellectuelle - des étudiants en séance et favoriser l'interaction, j'utilise Plickers (TD) et VoTAR (cours). Ces applications permettent d'utiliser avec beaucoup de souplesse des QCM à destination des étudiants (Figure 4). Les éléments nécessaires à l'utilisation de ces applications sont mis à disposition de mes collègues de l'équipe d'enseignement.

3.1.2 Enseignements en Mécanique des Fluides

Responsables des enseignements	:	F.Colin
Étudiants concernés	:	2A GMP (L2)
Organisation	:	20h CM, 28h TD, 16h TP

Ce module d'enseignement est une introduction aux principes fondamentaux de la Mécanique des Fluides (statique, dynamique des fluides parfaits et pertes de charge en conduite) et de la Thermodynamique (étude de machines thermiques). Je suis **responsable** de la **gestion des bancs de TP** pour la Mécanique des Fluides et Thermodynamique (**130 étudiants concernés au S4**). Outre la rédaction des documents à destination des étudiants (énoncés, notice technique des appareils) ou à destination des encadrants (notices d'utilisation), cette responsabilité me conduit à assurer la maintenance des installations, en lien avec l'équipe de techniciens du département. J'ai proposé le **renouvellement d'installations** (j'ai par exemple participé à la rénovation du banc d'essais présenté à la Figure 5) et **suivi les appels d'offre**

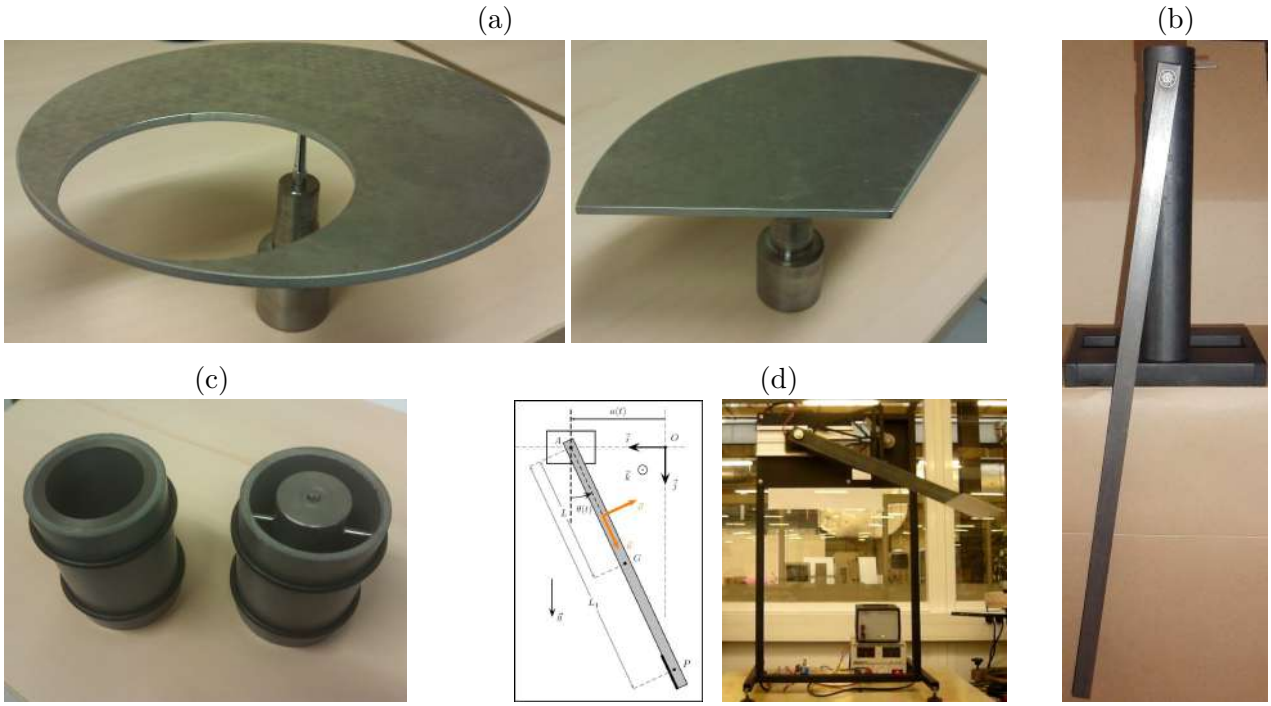

FIGURE 2 – Illustration des maquettes réalisées à l'IUT pour l'illustration des cours et TD.

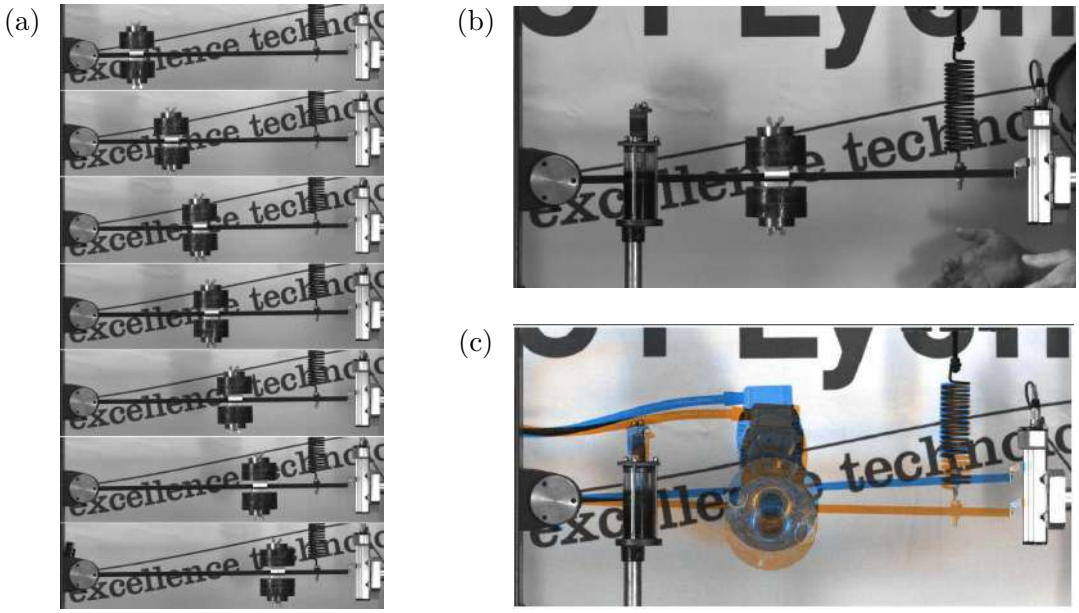

FIGURE 3 – Différentes configurations d'un même système mécanique (solide en rotation autour de l'axe fixe situé à gauche) ; modification du moment d'inertie (a), des frottements par ajout d'un amortisseur visqueux (b), mouvement forcé par un balourd (c)

FIGURE 4 – Utilisation de l'application VoTAR en cours ; l'analyse d'images permet de déterminer la distribution de réponses à une question posée, parmi 4 réponses possibles.

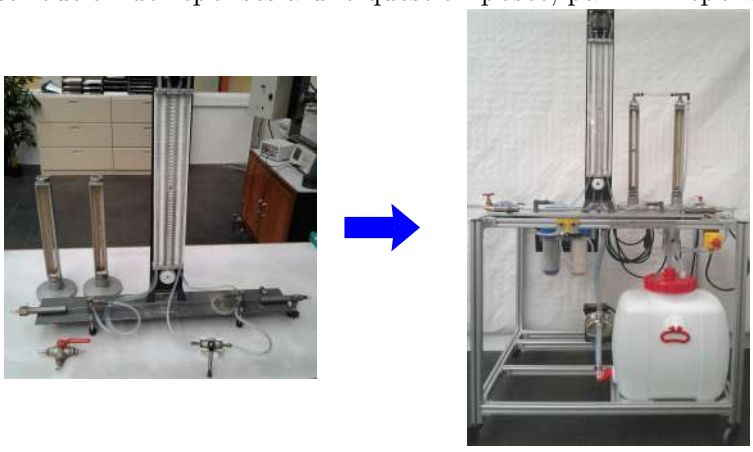

FIGURE 5 – Rénovation d'un banc de TP illustrant l'influence du régime d'écoulement sur les pertes de charge rencontrées dans une conduite cylindrique de grand allongement.

pour les nouveaux bancs suivants :

- Analyse des forces de poussée (2011- budget 3 keuros)
- Principe de fonctionnement d'une pompe à chaleur (2011- budget 15 keuros)
- Mur de pertes de charge linéiques et singulières (2013 - budget 10 keuros)

3.1.3 Enseignements en Acoustique

Responsables des enseignements	:	T.Castelain & J.-C. Béra
Étudiants concernés	:	Master d'Acoustique (M1)
Organisation	:	16h CM, 16h TD, 16h TP

Ce module d'enseignement est une **introduction à l'Acoustique**. Son programme concerne l'évaluation des niveaux sonores, l'établissement de l'équation d'onde en milieu homogène, l'étude du comportement d'ondes planes et sphériques et la notion d'impédance acoustique (milieux avec changement d'indice).

3.2 Encadrement d'étudiants et projets de recherche

3.2.1 Étudiants encadrés

Dès 2009, j'ai eu la chance d'être associé à l'encadrement d'étudiants au Laboratoire. Le tableau 2 liste les étudiants dont j'ai assuré le suivi en tant qu'encadrant principal. Les étudiants co-encadrés actuellement sont indiqués dans le tableau 3. J'ai eu l'opportunité de coencadrements avec différents collègues assurant la direction de la thèse au Laboratoire et aussi en dehors du LMFA.

	Formation	**Co-encadrant** (HDR)	**Période**	**Nb publications**	**Ref.** (⋆)
B. André	Doctorat	C.Bailly	01/10/2009 - 29/11/2012	7	A14-19, CR3
S. Chaligné	Doctorat	D.Juvé	01/10/2010 - 12/12/2013	2	CR1-2
M. Szmigiel	Doctorat	D.Juvé	01/04/2014 - 05/05/2017	3	A8
B. Mercier	Doctorat	C.Bailly	01/10/2014 - 06/12/2017	3	A5-6 ;9
B. André	Post-Doc	C.Bailly	01/12/2012 - 31/08/2013	2	A12-13
B. Mercier	Post-Doc	C.Bailly	01/01/2018 - 01/10/2018	3	A2-4
P. Sujar	Post-Doc	M.Michard	01/05/2018 - 01/05/2019		C1
B. Bacher	Master 1		09/05/2011 - 29/07/2011		
I. Kurek	Master 1		23/04/2019 - 28/06/2019		

TABLE 2 – Encadrements d'étudiants durant la période 2008-2017 ; (⋆) les références concernent la liste des publications fournie au paragraphe 3.4

Y. Haffner	Doctorat	J.Borée	17/10/2016 -		C2, C4-5, C8
R. Da Mota (†)	Doctorat	C.Bogey M.Michard	01/10/2017 -		C3

TABLE 3 – Encadrements d'étudiants en cours

(†) Démission au 30/09/2019

J'ai eu à deux reprises le plaisir de proposer aux étudiants de l'IUT d'effectuer leur stage de fin d'études de deux mois au LMFA :

- Laurent Delolme - Dessin d'une sonde de pression statique adaptées aux écoulements supersoniques (2010)
- Romain Blanc - CAO et intégration d'une méthode de visualisation sur un banc d'essais et contribution au développement d'une nouvelle méthode de visualisation (2017)

3.2.2 Implication dans des projets collaboratifs de recherche

Depuis 2010, mes activités de recherche sont structurées autour de projets de recherche permettant la collaboration avec différents partenaires à l'échelle nationale et internationale. Une synthèse des actions menées dans ces différents projets est proposée ci-après :

Intitulé : **Optimisation de Systèmes de Contrôle Actifs pour la Réduction de bruit de jet**		
Acronyme : OSCAR	Financement : FNRAE	**2006-2010**

Partenaires du projet
ONERA-DAAP, ONERA-DMAE, LMFA, IEMN

Étude expérimentale de la faisabilité du contrôle de bruit de jet subsonique par actionneurs instationnaires. Deux concepts technologiques différents visant à générer des petits jets de contrôle instationnaire à haute fréquence ont été développés par les partenaires (IEMN et ONERA-DMAE) et testés en soufflerie anéchoïque sur un jet à $Re_D \approx 10^6$ et $M_j = 0.9$. Le premier concept, dont l'objectif est la génération de jets pulsés à une fréquence de l'ordre du kHz, correspond à un actionneur dont le principe de fonctionnement s'appuie sur des techniques de micro-électronique pour la réalisation de micro électrovannes. Le deuxième concept correspond à un réseau de cavités équipées d'électrodes entre lesquelles une différence de potentiel est appliquée pour générer un arc électrique. La détente du gaz contenu dans la cavité provoque l'expulsion de gaz chaud au travers de l'ouverture de cavité. Le refroidissement de la cavité provoque l'aspiration d'air extérieur dans la cavité, permettant ainsi le renouvellement du cycle à une fréquence un peu inférieure au kHz.

Intitulé : **Jets supersoniques choqués et couplages Aéroacoustiques**		
Acronyme : JESSICA	Financement : ANR	**2010 à 2013**

Partenaires du projet
LMFA (porteur C.Bailly), Institut PPRIME, LaMSID

L'objectif de ce projet consistait à caractériser le screech, bruit tonal intense obtenu dans le cas de jets imparfaitement détendus, par une approche modale et la localisation de sources de bruit en soufflerie anéchoïque.

Intitulé : **cOoperation with Russia in the field of advanced engIne NOise COntrol based on plasma actuators**		
Acronyme : ORINOCO	Financement : FP7 Collaborative Projects	**2010 à 2014**

Partenaires du projet

ONERA, LMFA (resp. T.Castelain), TsAGI (R), Aviadvigatel (R), CIAM (R), CIRA, General Physics Institute (R), Joint Institute for High Temperatures (R), Institut Pprime, NLR, Institute for Innovation and Fusion Research (R), Universita Roma Tre

---

Ce prolongement des travaux menés dans le programme OSCAR a permis d'évaluer l'effet des jets synthétiques par actionneur plasma (ONERA-DMAE) sur le développement des couches de cisaillement du jet contrôlé, et la corrélation avec leur effet sur le bruit rayonné. Deux campagnes de mesure ont été réalisées en soufflerie anéchoïque sur la caractérisation du jet de référence ($M_j = 0.6$ et $M_j = 0.9$). Ce programme a également permis une collaboration avec les collègues de l'Univ.Roma 3, sur l'application d'une méthode originale d'analyse du bruit de jet à partir de mesures en champ proche et champ lointain [A6, A9-10].

Intitulé : **Technologies Innovantes pour Grands Routiers Economes**		
Acronyme : TIGRE	Financement : ADEME	**2010 à 2014**

Partenaires du projet

Renault Trucks, LMFA (resp. T.Castelain), Plastic Omnium, Michelin, Tenesol, Renault, IFP Énergies Nouvelles, Mines Paris Tech, CETHIL

Il s'agit du premier partenariat avec Renault Trucks sur le contrôle actif d'écoulement pour l'amélioration des performances aérodynamiques. Une première stratégie de contrôle du sillage de la remorque d'une maquette de camion a été miss en œuvre, au travers d'essais réalisés sur maquette à échelle réduite ($1/43^{e}$) au Laboratoire et à plus grande échelle ($1/8^{e}$) en soufflerie d'essais. Le contrôle s'appuie sur des jets synthétiques positionnés sur l'arête supérieure du culot de la remorque, couplés à un volet. Cette première approche a permis de faire la preuve de l'intérêt *a priori* du concept, puisqu'un gain d'environ 5 % sur la traînée a été obtenu par le contrôle. Ces travaux ont été réalisés dans le cadre de la thèse de S.Chaligné et ont donné lieu aux publications CR1 et CR2.

Intitulé : **Flexible & Aerodynamic truck for Low CONsumption**		
Acronyme : FALCON	Financement : FUI	**2017 à 2021**

Partenaires du projet

Renault Trucks, LMFA (resp. T.Castelain), POLYRIM, FRUEHAUF, STYL'MONDE, BENOMAD, WEZZOO, IFSTTAR, TOTAL, FAURECIA, ENOGIA

Ce projet est lié aux modifications aérodynamiques induites par le remplacement de rétroviseurs latéraux de la cabine des futurs poids-lourds par des caméras de petites dimensions. Deux effets antagonistes sont en effet à l'œuvre avec un tel changement :

- les rétroviseurs actuellement utilisés sont de grandes dimensions, leurs sillages sont sources de pertes et de traînée aérodynamique. Une caméra de plus petite dimension intégrée à la cabine conduit donc potentiellement à un gain en traînée aérodynamique
- néanmoins, les rétroviseurs actuels permettent de canaliser l'écoulement au contournement du pied-A (montant faisant la jonction entre le pare-brise et la vitre latérale), et limitent ainsi le décollement dans cette zone ; avec une caméra de petites dimensions, le décollement devient plus massif, et source de traînée aérodynamique additionnelle.

La contribution du LMFA pour ce programme est d'explorer par voie expérimentale des dispositifs de contrôle, passif ou actif, visant à réduire ou à éliminer le décollement sur le pied-A. Dans cet objectif, deux campagnes d'essais sur véhicule réel (piste de La Valbonne) ont permis l'acquisition de données à partir de visualisations par fils de laine et de mesures embarquées de pression pariétale sur le vitrage du véhicule et de vélocimétrie par anémométrie à fil chaud.

Intitulé : **Active Reduction Of Aerodynamic Drag**		
Acronyme : Activ_ROAD	Financement : ANR	**2016 à 2020**

Partenaires du projet

LMFA (porteur T.Castelain), Pprime, Ampère, Renault Trucks, PSA Peugeot Citroen

Ce projet porte sur l'amélioration des performances aérodynamiques de véhicules terrestres dont la forme arrière correspond à un culot droit (que l'on trouve pour une grande classe de véhicules particuliers et pour les poids lourds). Pour ces véhicules, on note un sillage turbulent marqué par une zone de recirculation associée à une zone de faible pression responsable d'une perte énergétique qui s'accroît avec la vitesse du véhicule. L'objectif du projet est l'exploitation de stratégies spécifiques de contrôle d'écoulement pour augmenter la pression au culot et ainsi diminuer la trainée. La méthode de contrôle proposée dans le projet s'appuie sur une composante passive (volets plats ou courbés) et une composante active qui consiste en l'injection à proximité immédiate du culot de la maquette étudiée de perturbations à haute fréquence par utilisation de jets pulsés. On privilégie ici une approche expérimentale pour évaluer, comprendre, modéliser et contrôler de manière robuste le gain en traînée aérodynamique. Pour ces travaux, un post-doc (P.Sujar) et un doctorant (Y.Haffner) sont intervenus au Laboratoire ; l'équipe du LMFA (P.Sujar, M.Michard, E.Jondeau, T.Castelain) a participé à trois campagnes d'essais dans la soufflerie de l'ENSMA, avec l'appui de l'équipe locale, pour la réalisation des essais de contrôle d'écoulement sur la configuration représentative des applications 'poids-lourd'. Le programme de recherche s'appuie sur une forte interaction entre les différents partenaires, ce qui se traduit notamment par la conception d'une maquette commune intégrant un système de jets pulsés pilotés par une électronique de commande dévelopée par AMPÈRE, par des échanges scientifiques et techniques très réguliers (à l'occasion notamment des réunions plénières bi-annuelles) et des participations communes aux conférences spécialisées de l'aérodynamique des véhicules terrestres. Plusieurs comptes-rendus sous forme de synthèses écrite et orale répondant aux exigences de l'ANR ont été structurés à partir des contributions des différents partenaires et fournis en juillet 2017, décembre 2017 et juillet 2018. Le rapport final du programme est prévu pour septembre 2020 (date de fin scientifique du programme).

3.3 Responsabilités administratives

Responsabilités liées aux activités de recherche

- Responsable de la thématique 'Contrôle actif du bruit et des écoulements' (quad.2010-2014)
- Membre du Conseil scientifique du CNRT R2A 'Aérodynamique et aéroacoustique des véhicules terrestres' (depuis fév.2016)
- Coordinateur scientifique du programme ANR Activ_ROAD (jan.2016 - sept.2020)
- Relecture d'articles (25 depuis 2013) pour différents journaux : Journal of Fluid Mechanics, AIAA j., Acta Acustica, Journal of Visualization, Exp. In Fluids, Sensors & Actuators : A. Physical, Applied Physics Letters, Shock Waves, Journal of Heat and Fluid Flow (liste non exhaustive)

Participation à la vie des structures

- Membre élu du bureau du Conseil de Dép. GMP, IUT Lyon 1 (fév.2015 - sep.2018)
- Membre nommé de la Commission Personnel Enseignant du Dép. GMP, IUT Lyon 1 (depuis janv. 2016)
- Gestion d'appels d'offre pour l'acquisition de matériels optiques (caméra rapide, laser rapide ; budget 100 keuros pour chaque action)
- Examinateur de la thèse de G.Bonnavion : "Dynamiques des modes instables de sillages en aérodynamique automobile : des modèles simplifiés aux véhicules réels" (5/10/2018 à ENSTA Paris Tech)
- Examinateur de la thèse de Y.Wang : "Experimental study of wheel-vehicle aerodynamic interactions" (28/03/2019 à ISAE-ENSMA)
- Rapporteur de la thèse de D.J.Tan : "Aeroacoustic Analysis of Broadband Shock-Associated Noise Sources In Screeching Round Jets" (31/03/2019, LTRAC, Australie)
- Membre de la commission de recrutement Poste 2362 (4378) en Lettres Modernes Expression/Communication pour le Dpt GMP - IUT Lyon 1 (oct. & nov. 2016)
- Membre du comité de sélection pour le poste MCF n°0164, en section 60, au Département d'enseignement MFAE/ Laboratoire LMFA - Ecole Centrale Lyon (avr. & mai 2016)
- Membre du comité de sélection pour le poste MCF n°4481, en section 28, pour le Département GMP - IUT Lyon 1 et le Laboratoire ILM (avr. & mai 2018)
- Membre du comité de suivi de thèse de T.Kubwimana (direction L.Soulhac, P.Salizzoni ; ED MEGA) (sep. 2017)
- Président de jurys de Baccalauréat :
  - Baccalauréat général, session 2013, SVT, Lycée B.Pascal, Charbonnières les Bains
  - Baccalauréat technologique, session 2009, STI, Lycée Martinière Diderot, Lyon
- Participation à l'organisation des journées du GDR 2502 'Contrôle des Décollements' à Lyon (nov.2016)

3.4 Liste des publications et communications

• Articles •

A1. Yuta OZAWA, Taku NONOMURA, Bertrand MERCIER, **Thomas CASTELAIN**, Christophe BAILLY, and Keisuke ASAI. Cross-spectral analysis of psp images for estimation of surface pressure spectra corrupted by the shot noise. *Exp Fluids*, 60 :135, 2019.

A2. Bertrand MERCIER, **Thomas CASTELAIN**, and Christophe BAILLY. Experimental study of the coherent vorticity in slightly under-expanded supersonic screeching jets. *International Journal of Aeroacoustics*, 18 :207–230, 2019.

A3. Bertrand MERCIER and **Thomas CASTELAIN**. Dynamic analysis of a rayleigh scattering setup using synthetic light signals from a modulated led. *Rev. Sci. Instrum.*, 90 :063109, 2019.

A4. Bertrand MERCIER, Emmanuel JONDEAU, **Thomas CASTELAIN**, Yuta OZAWA, Christophe BAILLY, and Geneviève COMTE-BELLOT. High frequency temperature fluctuation measurements by rayleigh scattering and constant-voltage cold-wire techniques. *Exp Fluids*, 60 :110, 2019.

A5. Bertrand MERCIER, **Thomas CASTELAIN**, Emmanuel JONDEAU, and Christophe BAILLY. Density fluctuations measurement by rayleigh scattering using a single-photomultiplier. *AIAA j.*, 56-4 :1310–1316, 2018.

A6. Bertrand MERCIER, **Thomas CASTELAIN**, and Christophe BAILLY. Experimental investigation of the turbulent density - farfield sound correlations in compressible jets. *International Journal of Aeroacoustics*, 17(4-5) :521–540, 2018.

A7. Matteo MANCINELLI, Tiziano PAGLIAROLI, Alessandro DI MARCO, Roberto CAMUSSI, and **Thomas CASTELAIN**. On the hydrodynamic and acoustic nature of pressure pod modes in the near field of a compressible jet. *Journal of Fluid Mechanics*, 836 :998–1008, 2018.

A8. **Thomas CASTELAIN**, Marc MICHARD, Mathieu SZMIGIEL, Damien CHACATON, and Daniel JUVÉ. Identification of flow classes in the wake of a simplified truck model depending on the underbody velocity. *Journal of Wind Engineering and Industrial Aerodynamics*, 175 :352–363, 2018.

A9. Bertrand MERCIER, **Thomas CASTELAIN**, and Christophe BAILLY. Experimental characterization of the screech feedback loop in underexpanded round jets. *Journal of Fluid Mechanics*, 824 :202–229, 2017.

A10. Roberto CAMUSSI, Alessandro DI MARCO, and **Thomas CASTELAIN**. Statistical analysis of the hydrodynamic pressure in the near field of compressible jets. *International Journal of Heat and Fluid Flow*, 64 :1–9, 2017.

A11. Matteo MANCINELLI, Tiziano PAGLIAROLI, Alessandro DI MARCO, and **Thomas CASTELAIN**. Wavelet decomposition of hydrodynamic and acoustic pressures in the near field of the jet. *Journal of Fluid Mechanics*, 813 :716–749, 2017.

A12. Benoît ANDRÉ, **Thomas CASTELAIN**, and Christophe BAILLY. Experimental study of flight effects on slightly underexpanded supersonic jets. *AIAA j.*, 55 :57–67, 2017.

A13. Benoît ANDRÉ, **Thomas CASTELAIN**, and Christophe BAILLY. Investigation of the mixing layer of underexpanded supersonic jets by particle image velocimetry. *International Journal of Heat and Fluid Flow*, 50 :188–200, 2014.

A14. Benoît ANDRÉ, **Thomas CASTELAIN**, and Christophe BAILLY. Experimental exploration of underexpanded supersonic jets. *Shock Waves*, 24 :21–32, 2014.

A15. Benoît ANDRÉ, **Thomas CASTELAIN**, and Christophe BAILLY. Broadband shock-associated noise in screeching and non-screeching underexpanded supersonic jets. *AIAA j.*, 51 :665–673, 2013.

A16. Benoît ANDRÉ, **Thomas CASTELAIN**, and Christophe BAILLY. Shock oscillations in a supersonic jet exhibiting antisymmetrical screech. *AIAA j.*, 50 :2017–2020, 2012.

A17. Benoît ANDRÉ, **Thomas CASTELAIN**, and Christophe BAILLY. Broadband shock-associated noise in screeching and non-screeching underexpanded supersonic jets. *ERCOFTAC Bulletin*, 90 :10–14, 2012.

A18. Benoît ANDRÉ, **Thomas CASTELAIN**, and Christophe BAILLY. Experimental study of flight effects on screech in underexpanded jets. *Physics of Fluids*, 23 :1–14, 2011.

A19. Benoît ANDRÉ, **Thomas CASTELAIN**, and Christophe BAILLY. A shock-tracking procedure for studying screech-induced oscillations. *AIAA j.*, 49 :1563–1566, 2011.

A20. **Thomas CASTELAIN**, Michel SUNYACH, Daniel JUVÉ, and Jean-Christophe BÉRA. Jet-noise reduction by impinging microjets : an acoustic investigation testing microjet parameters. *AIAA*, 46 :1081–1087, 2008.

• Comptes-Rendus à l'Académie des Sciences •

CR1. Sébastien CHALIGNÉ, **Thomas CASTELAIN**, Marc MICHARD, Damien CHACATON, and Daniel JUVÉ. Fluidic control of wake-flow behind a two-dimensional square-back bluff body. *C. R. Méc.*, 342 :349–355, 2014.

CR2. Sébastien CHALIGNÉ, **Thomas CASTELAIN**, Marc MICHARD, and Daniel JUVÉ. Active control of the flow behind a two-dimensional bluff body in ground proximity. *C. R. Méc.*, 341 :289–297, 2013.

CR3. Benoît ANDRÉ, **Thomas CASTELAIN**, and Christophe BAILLY. Effect of a tab on the aerodynamical development and noise of an underexpanded supersonic jet. *C. R. Méc.*, 341 :659–666, 2013.

CR4. **Thomas CASTELAIN**, Jean-Christophe BÉRA, and Michel SUNYACH. Noise reduction of a mach 0.7-0.9 jet by impinging microjets. *C. R. Méc.*, 334 :289–297, 2006.

Pour les présentations orales listées ci-après, le nom de l'intervenant est souligné.

• Conférences internationales avec actes publiés •

C1. Patricia SUJAR-GARRIDO, Marc MICHARD, Thomas CASTELAIN, and Yann HAFFNER. Identification of efficient flow control strategies for truck model drag reduction. In *11th International Symposium on Turbulence and Shear Flow Phenomena (TSFP11), Southampton, UK*, 2019.

C2. Yann HAFFNER, Jacques BORÉE, Andreas SPOHN, and Thomas CASTELAIN. Unsteady coanda forcing for drag reduction of a turbulent wake. In *11th International Symposium on Turbulence and Shear Flow Phenomena (TSFP11), Southampton, UK*, 2019.

C3. Rafael DA MOTA, Marc MICHARD, Thomas CASTELAIN, and Christophe BOGEY. Sensibilité à des perturbations de l'écoulement au contournement du pied-a d'une maquette de véhicule industriel en vue du contrôle de décollement. In *24e Congrès Français de Mécanique, Brest*, 2019.

C4. Yann HAFFNER, Andreas SPOHN, Jacques BORÉE, and Thomas CASTELAIN. Transient dynamics of the turbulent wake of a three-dimensional blunt body. In *17TH EUROPEAN TURBULENCE CONFERENCE, TORINO, ITALY*, 2019.

C5. Yann HAFFNER, Jacques BORÉE, Andreas SPOHN, and Thomas CASTELAIN. Manipulation of wake asymmetries of a blunt body - wake equilibrium and drag reduction. In *71st APS DFD Meeting, Atlanta*, 2018.

C6. Bertrand MERCIER, Yuta OZAWA, Emmanuel JONDEAU, Thomas CASTELAIN, and Christophe BAILLY. Estimation spectrale de fluctuations de température par diffusion de rayleigh. In *Congrès Francophone de Techniques Laser, Dourdan, 17 - 21 septembre 2018*, 2018.

C7. Bertrand MERCIER, Thomas CASTELAIN, and Christophe BAILLY. Identification of jet-noise source signature from rayleigh scattering measurements. In *25th International Congress on Sound and Vibration, ICSV 2018 : Hiroshima Calling*, 2018.

C8. Bertrand MERCIER, Thomas CASTELAIN, and Christophe BAILLY. Experimental identification of the single source of screech in supersonic round jets. In *25th International Congress on Sound and Vibration, ICSV 2018 : Hiroshima Calling*, 2018.

C9. Bertrand MERCIER, Emmanuel JONDEAU, Thomas CASTELAIN, and Christophe BAILLY. Rayleigh scattering for aeroacoustics : correlations between density fluctuations and the far-field acoustics. In *53rd 3AF International Conference on Applied Aerodynamics, Salon de Provence*, 2018.

C10. Yann HAFFNER, Jacques BORÉE, Andreas SPOHN, Thomas CASTELAIN, Marc MICHARD, Sylvie SESMAT, and Eric BIDEAUX. Forcing three-dimensional large-scale flow asymmetries in the wake of a blunt body : wake equilibrium and drag reduction. In *Third International Conference in Numerical and Experimental Aerodynamics of Road Vehicles and Trains (Aerovehicles 3), Milano*, 2018.

C11. Bertrand MERCIER, Emmanuel JONDEAU, Thomas CASTELAIN, and Christophe BAILLY. Measurement of density fluctuations in jets by a rayleigh scattering method. In *52nd 3AF International Conference on Applied Aerodynamics, Lyon*, 2017.

C12. Mathieu SZMIGIEL, Thomas CASTELAIN, Marc MICHARD, Damien CHACATON, and Daniel JUVE. Experimental study of the wake of a simplified truck model in ground proximity in view of defining a control strategy for drag reduction. In *52nd 3AF International Conference on Applied Aerodynamics, Lyon*, 2017.

C13. Thomas CASTELAIN, Romain GOJON, Bertrand MERCIER, and Christophe BOGEY. Estimation of convection speed in underexpanded jets from schlieren pictures. In *22nd AIAA/CEAS Aeroacoustics Conference, Lyon, Paper 2984*, 2016.

C14. Didier DRAGNA, Sébastien OLLIVIER, Cyril DESJOUY, Thomas CASTELAIN, and Philippe BLANC-BENON. Reflection of weak shockwaves from a rough surface. In *22nd AIAA/CEAS Aeroacoustics Conference, Lyon, Paper 3013*, 2016.

C15. Matteo MANCINELLI, Tiziano PAGLIAROLI, Alessandro DI MARCO, Roberto CAMUSSI, Thomas CASTELAIN, and Olivier LÉON. Hydrodynamic and acoustic wavelet-based separation of the near-field pressure of a compressible jet. In *22nd AIAA/CEAS Aeroacoustics Conference, Lyon, Paper 2864*, 2016.

C16. Bertrand MERCIER, Thomas CASTELAIN, and Christophe BAILLY. A schlieren and nearfield acoustic based experimental investigation of screech noise sources. In *22nd AIAA/CEAS Aeroacoustics Conference, Lyon, Paper 2799*, 2016.

C17. Bertrand MERCIER, Thomas CASTELAIN, and Christophe BAILLY. Mesure des fluctuations de masse volumique dans les jets par la méthode de diffusion de rayleigh. In *15ème Congrès Francophone de Techniques Laser, Toulouse*, 2016.

C18. Mathieu SZMIGIEL, Thomas CASTELAIN, Marc MICHARD, Damien CHACATON, and Daniel JUVÉ. Impact of the underside velocity on the base pressure of a trailer model using a passive control system. In *Aerovehicles 2, Göteborg, Sweden*, 2016.

C19. Sébastien OLLIVIER, Cyril DESJOUY, Didier DRAGNA, Thomas CASTELAIN, Maria KARZOVA, and Philippe BLANC-BENON. Interaction non linéaire d'ondes de choc acoustiques au voisinage d'une frontière rigide. In *13ème Congrès Français d'Acoustique*, 2016.

C20. Bertrand MERCIER, Thomas CASTELAIN, and Christophe BAILLY. Investigation of underexpanded jet screech associated convective velocity based on high frequency sampled schlieren visualisations. In *22ème Congrès Français de Mécanique, 24 au 28 août, Lyon, Paper 67687, S18*, 2015.

C21. Mathieu SZMIGIEL, Thomas CASTELAIN, Marc MICHARD, Damien CHACATON, and Daniel JUVÉ. Contrôle par jets pulsés du sillage d'un corps bidimensionnel en interaction avec le sol. In *22ème Congrès Français de Mécanique, 24 au 28 août, Lyon, Paper 67286, S08c*, 2015.

C22. Sébastien CHALIGNÉ, Thomas CASTELAIN, Marc MICHARD, and Daniel JUVÉ. Experimental application of active flow control on a 1 :8 scale, simplified truck model.

In *First international conference in numerical and experimental aerodynamics of road vehicles and trains (Aerovehicles 1), 23-25 June 2014, Bordeaux*, 2014.

C23. Sébastien CHALIGNÉ, Thomas CASTELAIN, Marc MICHARD, and Daniel JUVÉ. Vélocimetrie par images de particules dans le sillage d'une maquette simplifiee de véhicule industriel avec contrôle actif d'écoulement. In *14ème Congrès Francophone de Techniques Laser, Marseille*, 2014.

C24. Benoit ANDRÉ, Thomas CASTELAIN, and Christophe BAILLY. Investigation of the mixing layer in a slightly underexpanded supersonic jet by particle image velocimetry. In *TSFP 8 : International Symposium onTurbulence and Shear Flow Phenomena Conferences*, 2013.

C25. Benoit ANDRÉ, Thomas CASTELAIN, and Christophe BAILLY. Experimental study of flight effects on slightly underexpanded supersonic jets. In *19th AIAA/CEAS Aeroacoustics Conference, Berlin, Germany*, 2013.

C26. Sébastien CHALIGNÉ, Thomas CASTELAIN, Marc MICHARD, Emmanuel JONDEAU, and Daniel JUVÉ. Contrôle d'écoulement autour d'un corps non profilé bidimensionnel en interaction avec le sol. In *21ème Congrès Français de Mécanique, Bordeaux*, 2013.

C27. Benoit ANDRÉ, Thomas CASTELAIN, and Christophe BAILLY. Experimental study of flight effects on underexpanded supersonic jet noise. In *Acoustics 2012, 11ème Congrès Français d'Acoustique & 2012 Annual IOA (Institute of Acoustics, UK), 13-17 April, Nantes, 2341-2346*, 2012.

C28. Maria KARZOVA, Edouard SALZE, Sébastien OLLIVIER, Thomas CASTELAIN, Benoît ANDRÉ, Petr YULDASHEV, Vera KHOKHLOVA, Oleg SAPOZHNIKOV, and Philippe BLANC-BENON. Interaction of weak shocks leading to mach stem formation in focused beams and reflections from a rigid surface. In *Acoustics 2012, 11ème Congrès Français d'Acoustique & 2012 Annual IOA (Institute of Acoustics, UK), 13-17 April, Nantes, 1111-1115*, 2012.

C29. Benoit ANDRÉ, Emmanuel JONDEAU, Thomas CASTELAIN, and Christophe BAILLY. Observations par méthodes optiques de la dynamique d'un choc dans un jet supersonique. In *13ème Congrès Francophone de Techniques Laser, 18-21 sept., Rouen*, 2012.

C30. Benoit ANDRÉ, Thomas CASTELAIN, and Christophe BAILLY. Experimental study of flight effects on screech in underexpanded jets. In *17th AIAA/CEAS Aeroacoustics Conference, Portland, Oregon, United States*, 2011.

C31. Benoit ANDRÉ, Thomas CASTELAIN, and Christophe BAILLY. Experimental exploration of an underexpanded supersonic jet. In *28th International Symposium on Shock Waves, Manchester, United Kingdom.*, 2011.

C32. Benoit ANDRÉ, Thomas CASTELAIN, Christophe BAILLY, and Daniel JUVÉ. Experimental investigation of screech by an underexpanded supersonic jet with forward flight effect. In *10ème Congrès Français d'Acoustique, 12-16 avril, Lyon*, 2010.

C33. Benoit ANDRÉ, Thomas CASTELAIN, Christophe BAILLY, and Daniel JUVÉ. Experimental investigation of aerodynamical and acoustical properties of an underexpanded supersonic jet with forward fight effect. In *45th Symposium in Applied Aerodynamics, AAAF, Polytech Marseille, 23-25 mars*, 2010.

C34. Thomas CASTELAIN, Jean-Christophe BÉRA, Nathalie GROSJEAN, and Michel SUNYACH. Contrôle par microjets impactants d'un jet à mach 0.9 : influence du nombre de microjets sur le développement des structures tourbillonnaires générées par le contrôle. In *18ème Congrès français de mécanique, Grenoble*, 2007.

C35. Thomas CASTELAIN, Michel SUNYACH, Daniel JUVE, and Jean-Christophe BÉRA. Jet noise reduction by impinging microjets : an aerodynamic investigation testing microjets parameters. In *13th AIAA/CEAS Aeroacoustics Conference, Rome, Italy*, 2007.

C36. Thomas CASTELAIN, Michel SUNYACH, Daniel JUVE, and Jean-Christophe BÉRA. Effect of microjets on a high-subsonic jet. parametric study of far-field noise reduction. In *12th AIAA/CEAS Aeroacoustics Conference, Cambridge, Massachusetts, United States*, 2006.

C37. Thomas CASTELAIN, Michel SUNYACH, Daniel JUVE, and Jean-Christophe BÉRA. Contrôle de bruit de jets à l'aide de microjets impactants. In *Journée Contrôle des Ecoulements, Lyon*, 2006.

C38. Thomas CASTELAIN, Michel SUNYACH, and Jean-Christophe BÉRA. Noise reduction of a mach 0.7-0.9 jet by impinging microjets. In *Active Control of Aircraft Noise : Concept to Reality, 9th CEAS-ASC Workshop, Stockholm, Suède*, 2005.

C39. Thomas CASTELAIN, Maximilian DIETRICH, Michel SUNYACH, and Jean-Christophe BÉRA. Mesures acoustiques sur un jet subsonique à haut re et mach restreint. effet des jets impactants sur les composantes spectrales du bruit de jet. In *17ème Congrès Français de Mécanique, Troyes*, 2005.

C40. Jean-Christophe BÉRA, Thomas CASTELAIN, Maximilian DIETRICH, and Michel SUNYACH. Contrôle par microjets d'une couche de mélange : exploitation de mesures piv de champs de vitesse par une visualisation des lignes de courant par convolution intégrale linéaire (lic). In *11ème Colloque de Visualisation et Traitement d'Images en Mécanique des Fluides, FLUVISU 11, Ecole Centrale de Lyon*, 2005.

C41. Thomas CASTELAIN, Maximilian DIETRICH, Michel SUNYACH, and Jean-Christophe BÉRA. Contrôle par microjets d'une couche de mélange. exploitation de mesures piv synchronisées. In *40ème Colloque d'Aérodynamique Appliquée, Association Aéronautique & Astronautique de France (AAAF), Toulouse*, 2005.

C42. Thomas CASTELAIN, Maximilian DIETRICH, Michel SUNYACH, and Jean-Christophe BÉRA. Contrôle de jet par action de microjets continus tangents. In *39ème Colloque d'Aérodynamique Appliquée, Association Aéronautique & Astronautique de France (AAAF), Paris*, 2004.

• **Exposés présentés à des colloques et réunions de spécialistes** •

W1. Rafael DA MOTA, Thomas CASTELAIN, Marc MICHARD, Christophe BOGEY, and Damien CHACATON. Mesures aérodynamiques embarquées dans une cabine de poids-lourd à échelle 1, sur circuit. In *Réunion du CNRT-R2A, ONERA Meudon, 6 février*, 2019.

W2. Thomas CASTELAIN, Bertrand MERCIER, Emmanuel JONDEAU, Romain BLANC, and Christophe BAILLY. Mesure par voie optique des fluctuations de densité dans un écoulement compressible. In *Congrès National de la Recherche des IUT, Aix-en-Provence*, 2018.

W3. Marc MICHARD, Sylvie SESMAT, Thomas CASTELAIN, Emmanuel JONDEAU, Eric BIDEAUX, and Antoine BOURGEOIS. Unsteady pulsed jets using pneumatic valves for flow separation control : effect of internal acoustic waves on external flow structure. In *GdR Contrôle des écoulements, Polytech' Orléans, 8-9 novembre*, 2017.

W4. Bertrand MERCIER, Benoît ANDRÉ, Thomas CASTELAIN, Emmanuel JONDEAU, and Christophe BAILLY. Supersonic jets : experimental characterizations. In *Conférence invitée, Aeroacoustics of Propulsion and Ventilation Systems, Valpré conference center, CeLyA Summer school, Ecully, 3-5 Juillet*, 2017.

W5. Mathieu SZMIGIEL, Sébastien CHALIGNÉ, Thomas CASTELAIN, Marc MICHARD, Damien CHACATON, and Daniel JUVÉ. Analyse du sillage d'un modèle réduit de véhicule industriel : effet du flux de sous-bassement. In *Réunion du CNRT-R2A, ONERA Meudon, 1er février*, 2017.

W6. Sébastien CHALIGNÉ, Mathieu SZMIGIEL, Marc MICHARD, Thomas CASTELAIN, Jean-Michel PERRIN, Nathalie GROSJEAN, Pierre ROLAND, and Pascal SOUCHOTTE. Stratégies de réduction de la traînée sur véhicule industriel : application du contrôle actif. In *Réunion du CNRT-R2A, ONERA Meudon, 3 février*, 2016.

W7. Mathieu SZMIGIEL, Thomas CASTELAIN, and Marc MICHARD. Effet de la variation de la vitesse de soubassement sur le développement du proche sillage d'un corps non profilé en interaction avec le sol. In *GdR Contrôle des écoulements, Ecole Centrale de Lyon, 28-29 novembre*, 2016.

W8. Mathieu SZMIGIEL, Marc MICHARD, Thomas CASTELAIN, and Damien CHACATON. Réduction de trainée d'un véhicule industriel : étude préliminaire sur maquette 3d. In *GdR Contrôle des écoulements, Ecole Centrale de Nantes, 18-19 novembre*, 2015.

W9. Sébastien CHALIGNÉ, Mathieu SZMIGIEL, Thomas CASTELAIN, Marc MICHARD, and Daniel JUVÉ. Réduction de traînée aérodynamique par association de jets synthétiques et d'éléments rapportés pour un obstacle non profilé à culot droit. In *GdR Contrôle des écoulements, LIMSI, Orsay, 17-18 novembre*, 2014.

W10. Thomas CASTELAIN, Sébastien CHALIGNÉ, Marc MICHARD, Damien CHACATON, and Daniel JUVÉ. Fluidic control of wake-flow behind a two-dimensional square-back bluff body. In *GdR Contrôle des écoulements, Ecole Centrale de Lille, 6-7 novembre*, 2013.

W11. Thomas CASTELAIN. Caractérisation expérimentale de jets supersoniques - applications aéroacoustiques. In *Conférence invitée, Journées scientifiques IROQUA, Paris, 24-25 octobre*, 2013.

W12. Thomas CASTELAIN, Benoit ANDRÉ, Emmanuel JONDEAU, Christophe BAILLY, and Daniel JUVÉ. Experiments on aeroacoustics of imperfectly-expanded supersonic jets. In *Journée thématique de l'Association Française de Vélocimétrie Laser, Orsay, 23 mai*, 2013.

W13. Sébastien CHALIGNÉ, Thomas CASTELAIN, Marc MICHARD, Damien CHACATON, and Daniel JUVÉ. Contrôle du sillage d'un obstacle à culot droit en interaction avec le sol : association d'un jet synthétique et d'un élément déflecteur. In *GdR Contrôle des écoulements, Université Paris-Sud 11, Orsay , 15-16 novembre*, 2012.

W14. Sébastien CHALIGNÉ, Thomas CASTELAIN, Marc MICHARD, Daniel JUVÉ, Laurent KINT, and Damien CHACATON. Contrôle d'écoulement autour d'une géométrie de type culot droit. In *GdR Contrôle des écoulements, ENS Cachan, 24-25 novembre*, 2011.

• **Chapitre d'ouvrage** •

B1. Christophe BAILLY, Christophe BOGEY, and Thomas CASTELAIN. *Subsonic and supersonic jet mixing noise*, pages 1–62. Lecture Series 2016-04, von Kàrmàn Institute for Fluid Dynamics, isbn-13978-2-87516-110-9 edition, 2016.

B2. Christophe BAILLY, Christophe BOGEY, Olivier MARSDEN, and Thomas CASTELAIN. *Subsonic and supersonic jet mixing noise*, pages 1–57. Lecture Series 2015-01, von Kàrmàn Institute for Fluid Dynamics, isbn-13 978-2-87516-082-9 edition, 2015.

4 Rapport sur les activités de recherche

Un résumé de mes activités de recherche est proposé ci-après. Par souci de concision, les parties 4.1 et 4.2, qui concernent les travaux portant sur la **caractérisation aéroacoustique des jets rapides** et l'application du **contrôle d'écoulement** en boucle ouverte à des **modèles de véhicules terrestres**, font directement référence aux travaux publiés joints en annexe. La troisième partie porte quant à elle sur les **développements métrologiques** effectués au Laboratoire au travers des thèses et stages encadrés depuis 2010 ; certains de ces travaux constituent un savoir-faire maintenant acquis au Laboratoire sans pour autant avoir donné lieu à publication en tant que tels. Pour cette raison, cette dernière partie entre dans plus de détails que les deux premières.

4.1 Études aéroacoustiques des jets

Les jets libres à haut nombre de Mach M_j sont des sources de bruit connues et étudiées expérimentalement et numériquement depuis plusieurs décennies. La structure de ces jets présente certaines caractéristiques invariables, quelle que soit la valeur de pression génératrice P_0 régnant en amont de la sortie de tuyère de diamètre D. En particulier, une zone axisymétrique appelée **couche de cisaillement** se développe à l'interface entre le cœur du jet et l'environnement extérieur, lui-même au repos ou en mouvement (figure 6(a)). La couche de cisaillement est le lieu d'**interactions hydrodynamiques entre structures turbulentes** responsables du **bruit de mélange turbulent**. Pour une valeur suffisamment faible de P_0, la partie interne du jet est dite potentielle, ce qui correspond à un écoulement subsonique et idéalement homogène et stationnaire. Pour une valeur accrue de P_0, et typiquement dans le cas d'un écoulement d'air pour $P_0 \geq 1.89 \times P_\infty$ où P_∞ correspond à la pression ambiante dans l'air entourant le jet en sortie de tuyère tel que représenté sur la figure 6(b), le nombre de Mach M du jet en sortie de tuyère devient constant et égal à 1. La tuyère est dite amorcée, et la pression statique en sortie de tuyère P_e est significativement différente de la pression ambiante ce qui provoque le développement d'ondes de détente depuis les lèvres de la tuyère. **Une structure de cellules de choc** s'établit dans la zone supersonique de l'écoulement ; au travers des chocs constitutifs de cette structure, la pression tout comme les autres paramètres caractéristiques de l'écoulement évoluent significativement. Une manière d'éviter ce phénomène, dont on rappelle ci-dessous les conséquences acoustiques, est de faire en sorte que la pression en sortie de tuyère corresponde à P_∞ ; pour cela, on utilise une **tuyère convergente/divergente** (figure 6(c)) dont le dessin spécifique, caractérisé par une valeur particulière M_d de Mach - dit de design - permet de former un jet parfaitement détendu pour $M_j = M_d$, décrit en figure 6(c). La structure de cet écoulement est tout à fait comparable à celle du jet subsonique de la figure 6(a).

Sur un plan acoustique, le **bruit de mélange turbulent** est un **bruit large bande** dont les propriétés ont été largement étudiées [10, 73, 75]. Un spectre universel pour chaque direction

d'observation permet de reproduire les propriétés principales de ce bruit [74]. La présence d'une structure de **cellules de choc** dans un **jet sous-détendu** peut induire des **sources de bruit supplémentaires** ; l'interaction de la turbulence dans la couche de cisaillement avec les pointes de ces cellules est associée à un **bruit de choc large bande** (BBSAN pour *Broad-Band Shock-Associated Noise*), et un phénomène de rétroaction aéroacoustique appelé ***screech*** peut conduire à la génération d'un **bruit tonal** éventuellement intense, dont la directivité est très marquée. Pour illustrer les différentes signatures de ces sources acoustiques, on reporte les spectres de bruit mesuré en champ lointain en figure 7 et 8. En premier lieu, on considère un jet sous-détendu à M_j=1.35 issu d'une tuyère convergente (figure 6(b)), dont le spectre de bruit rayonné est reporté en figure 7 pour différents angles d'écoute de θ=30° (direction paraxiale) à θ=130° (direction amont). Le screech y figure sous la forme de composantes tonales dont la fréquence fondamentale, ici 3.5 kHz, est indépendante de θ. Le contenu large bande du bruit rayonné dépend quant à lui fortement de l'angle d'écoute : d'une part le bruit de mélange turbulent est marqué dans la direction paraxiale, avec une amplitude maximale autour de 1 kHz, d'autre part le BBSAN, traduit par une bosse restreinte dans le spectre entre 6 et 10 kHz selon les angles, devient prépondérant dans la direction amont ($\theta \geq 90°$). On retrouve sur cette figure 7 un résultat classique : la fréquence centrale du BBSAN dépend de l'angle d'observation.

Pour synthétiser les motivations de mes travaux de recherche sur le bruit de jet (supersonique en particulier), la figure 8 est d'une aide précieuse. Elle est construite à partir de mesures réalisées dans la thèse de **B.André** [1], et offre une synthèse de 3 résultats obtenus dans différentes configurations, avec M_j=1.35 et une température totale de 30°C. Les spectres de bruit présentés sur cette figure concernent d'une part un jet issu de tuyère convergente, donc avec la structure de cellule de chocs induisant *a priori* screech et BBSAN, et d'autre part un jet issu d'une tuyère convergente/divergente de M_d=1.35 pour laquelle ces deux sources de bruit sont absentes puisque $M_d = M_j$. Il se trouve que pour ce point de fonctionnement et cette tuyère convergente, le screech était naturellement intermittent, ce qui a rendu possible l'évaluation du spectre de bruit lorsque le screech est présent et également lorsqu'il est absent. On peut faire plusieurs constats à partir de la figure 8 :

- Le bruit de mélange en basse fréquence (typiquement $f < 10^4$ Hz pour θ=50°, $f < 5\times10^3$ Hz pour θ=90°) dans le cas de la tuyère adaptée est identique à celui relevé pour la configuration tuyère convergente sans screech ; le bruit de choc large bande peut donc être identifié à la bosse spectrale centrée ici sur 20 kHz ($\theta = 50°$) ou 8 kHz ($\theta = 90°$). On note une **augmentation du niveau de bruit large bande à haute fréquence** dans le cas de la tuyère convergente par rapport à la configuration avec tuyère adaptée ; ce phénomène est donc clairement lié à l'existence d'une structure de cellules de choc dans le jet issu de la tuyère convergente.
- La présence de **screech** a plusieurs effets. Il induit une **augmentation du niveau de bruit large bande** en basse fréquence, ce qui peut correspondre au résultat de l'excitation tonale du jet par le screech comme ce qui a pu être observé pour des jets excités dans le cas d'un contrôle instationnaire à haute fréquence selon un mode d'ordre faible [66]. D'autre part, on constate que le screech implique un **décalage fréquentiel du maximum de la bosse spectrale du bruit de choc large bande**. Il y a donc

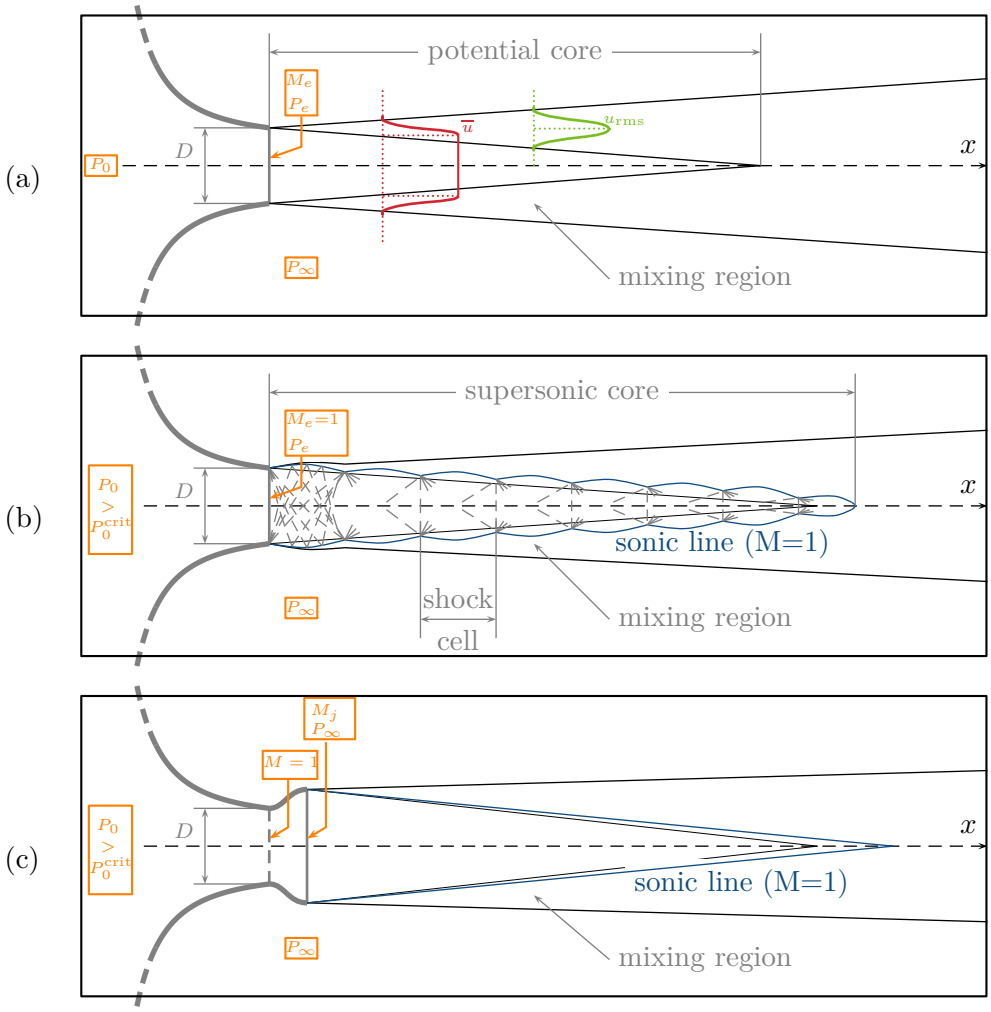

FIGURE 6 – Structure schématique moyenne des jets en condition subsonique (a), supersonique sous-détendu (b), supersonique parfaitement détendu (c).

un **couplage** entre screech et BBSAN, peu étudié jusqu'ici.

Dans cette partie, on présente donc l'approche mise en oeuvre pour préciser les liens existant entre screech et BBSAN ; pour cela, on a caractérisé la structure des jets modéremment sous-détendus (paragraphe 4.1.2), puis les mécanismes hydrodynamiques et acoustiques liés au screech. L'effet de ce dernier sur la structure de cellule de chocs du jet est ensuite précisé (paragraphe 4.1.3) pour enfin aborder les aspects acoustiques de ce problème (paragraphe 4.1.4). Dans un premier temps, on présente les travaux effectués à propos du bruit de mélange turbulent (paragraphe 4.1.1), en lien notamment avec le programme ORINOCO.

4.1.1 Analyse du bruit de mélange turbulent

Pour l'étude du bruit de mélange turbulent, on a cherché à isoler dans le champ hydrodynamique la signature des sources acoustiques, notamment en développant des outils de mesure et d'analyse adaptés. En premier lieu, au travers de la thèse de **B.Mercier** [46], le bruit de mélange turbulent a été étudié sur un jet subsonique ($M_j = 0.9$) et sur un jet supersonique

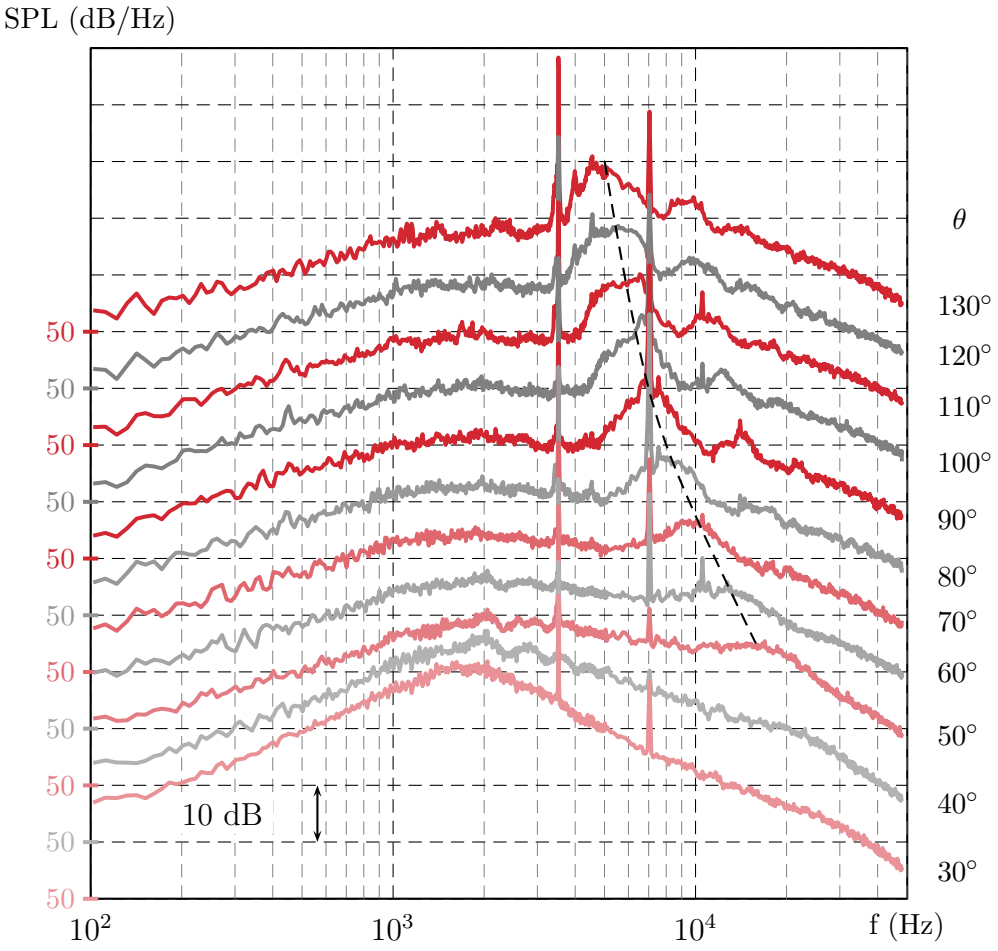

FIGURE 7 – Bruit de jet supersonique sous-détendu issu de la tuyère C38, $M_j = 1.35$, pour différentes directions d'observation θ mesurées par rapport à l'axe aval. La ligne discontinue indique la dépendance de la fréquence centrale du BBSAN avec l'angle d'écoute θ

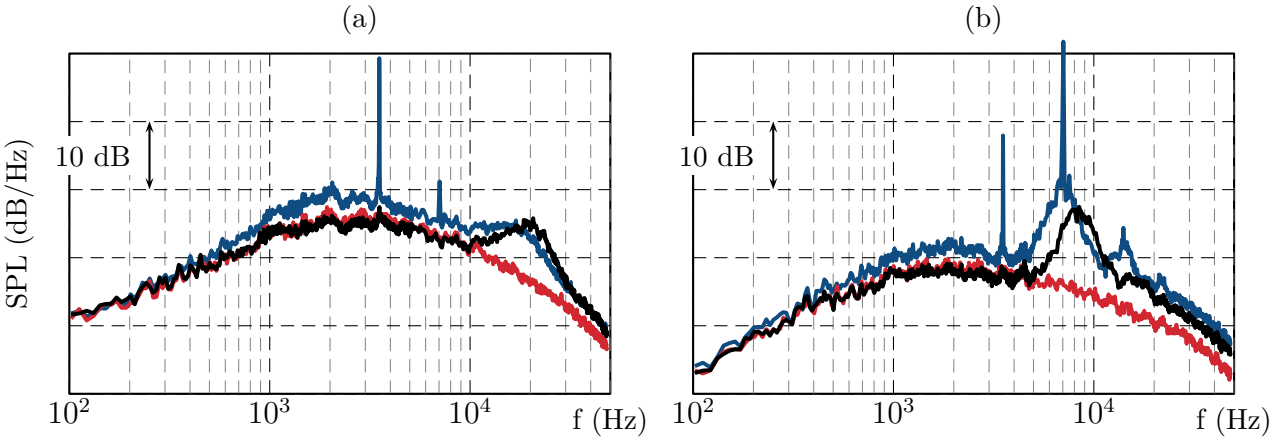

FIGURE 8 – Spectres de bruit mesurés dans la direction θ= 50° (a) et 90° (b), pour un jet à M_j=1.35 issu de la tuyère C38 avec screech (—), sans screech (—), et issu de la tuyère CD (—)

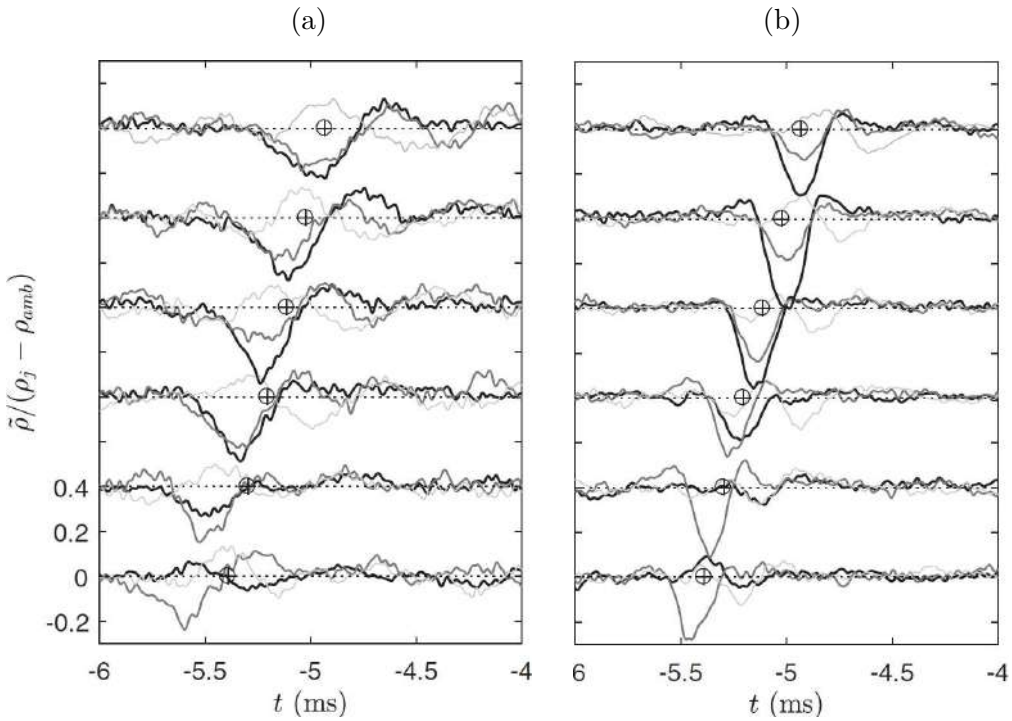

FIGURE 9 – Moyenne de l'évolution temporelle de la densité conditionnée par les pics positifs de pression relevés sur le signal acoustique mesuré à θ=30°. M_j=0.9 (a) et M_j=1.32 (b). Le symbole $\bigoplus$ représente le décalage temporel attendu lié à la propagation acoustique entre la position du microphone et le point dans l'écoulement où est effectuée la mesure. Les relevés sont effectués à la position radiale y/D=0 (━), y/D=¼ (━), et y/D=½ (━).

parfaitement détendu ($M_j = 1.32$). Une mesure non intrusive de l'évolution temporelle de densité, conditionnée à l'apparition d'événements dans le signal de pression acoustique mesuré en champ lointain dont on sait l'importance pour le bruit de mélange turbulent [35, 37], a été réalisée. Elle révèle la **signature d'un événement turbulent** ayant un caractère convectif, dont l'amplitude sur le signal de densité est maximale autour de x/D=8 [49], comme l'indique la figure 9.

Une étude complémentaire à laquelle les collègues de l'université Roma Tre m'ont associé dans le cadre du programme européen ORINOCO concerne l'analyse des **fluctuations de pression en champ proche**, enregistrées sur une antenne linéaire de microphones de manière synchronisée à l'enregistrement du champ lointain acoustique grâce à une deuxième antenne de microphones. Différentes valeurs de M_j sont considérées pour les jets subsoniques étudiés : $M_j = 0.6$ et 0.9. L'application de transformées en ondelettes a permis la **séparation des composantes acoustique et hydrodynamique** et la détermination de leur propriétés statistiques intrinsèques [43]. Elle a également apporté une caractérisation fine des **phénomènes intermittents** en champ proche acoustique [15]. La technique de décomposition POD appliquée aux fluctuations de pression en champ proche a permis également de distinguer les **modes acoustiques**, **hydrodynamiques** ne contribuant pas au rayonnement acoustique, **et hybrides** appelés hydro-acoustiques [42]. Cette distinction s'appuie sur l'analyse spectrale en fréquence-nombre d'onde des différents modes de POD. Elle conduit à identifier la contribution de certains

modes (acoustique et hydro-acoustiques) au bruit rayonné en champ lointain. Ma contribution à ces études portées par Univ.Roma Tre est très modeste ; si les échanges avec les autres auteurs à l'occasion de la rédaction de ces articles sont indéniablement intéressants, ils ne suffisent pas à faire de moi un spécialiste des traitements de signal par ondelette ou POD.

4.1.2 Structure de jets modérement sous-détendus

La structure de cellules de choc détaillée en figure 6(b) est une des signatures typiques d'un **jet imparfaitement détendu**. Si sa visualisation par strioscopie est aisée, celle-ci ne fournit cependant pas une **évaluation quantitative du champ de pression ou de vitesse**. Une telle caractérisation a été réalisée en utilisant une sonde de pression statique (dont le principe de fonctionnement est détaillé au paragraphe 4.3.1.2) et par LDV [7], où l'on a montré qu'au travers des zones d'expansion et de compression, les grandeurs caractéristiques de l'écoulement jusqu'à M_j=1.50 et mesurées dans le cone supersonique ont une évolution axiale correspondant essentiellement à une oscillation 'douce'. Pour M_j suffisamment élevé (et typiquement supérieur à 1.45), la présence d'un disque de Mach dans la première cellule de choc a fourni un cas test permettant d'évaluer la performance de la **correction d'inertie des particules** appliquée aux mesures LDV dans l'ensemble de l'écoulement [7]. Cette étude permet de mieux préciser la structure de la partie supersonique du jet.

Les sources de bruit se trouvant dans la couche de cisaillement du jet, c'est cette zone également que l'on a étudiée. Ainsi, les travaux menés au Laboratoire dans le cadre des thèses de **B.André** [1] et **B.Mercier** [46] ont aussi porté sur la caractérisation du **développement de la turbulence** dans la couche de cisaillement de jets sous-détendus, en particulier l'influence de la présence des pointes de choc émergeant dans la partie supersonique de la couche de cisaillement. Les gradients de vitesse moyenne au travers des chocs entre la 3eme et la 8eme cellule de choc de jets sous-détendus (M_j = 1.15 à M_j = 1.50), lieux présumés des sources du bruit de choc large bande, ont été déterminés par PIV avec une résolution spatiale élevée [8]. On a montré que le niveau maximum de turbulence dans la couche de cisaillement de jets faiblement sous-détendus (M_j= 1.10 et 1.15) est constant pour $x/D \geq$1, ce qui d'une part est très semblable aux résultats obtenus pour les jets subsoniques, et d'autre part indique que la présence de la structure de cellules de choc n'a pas d'effet sur le développement de la turbulence dans la couche de cisaillement dans ces conditions. Pour les jets modérement sous-détendus étudiés (M_j= 1.35 et 1.50), on trouve au contraire qu'il existe une **modulation du niveau de turbulence** par la structure de cellules de choc avec un maximum très marqué de fluctuations axiales de vitesse à la fin de chaque cellule et un minimum moins marqué de fluctuations radiales de vitesse. La figure 10 illustre ce résultat.

Les caractéristiques de l'écoulement moyen et de la turbulence dans ces jets ont été évaluées également en présence d'un **effet de vol** [9], avec en particulier la détermination de l'influence de l'effet de vol sur la croissance axiale des échelles de turbulence comme sur la longueur des cellules de choc, ce paramètre intervenant directement dans l'évaluation de la fréquence centrale de bruit de choc large bande (voir paragraphe 4.1.4) comme de celle du screech (voir paragraphe 4.1.3).

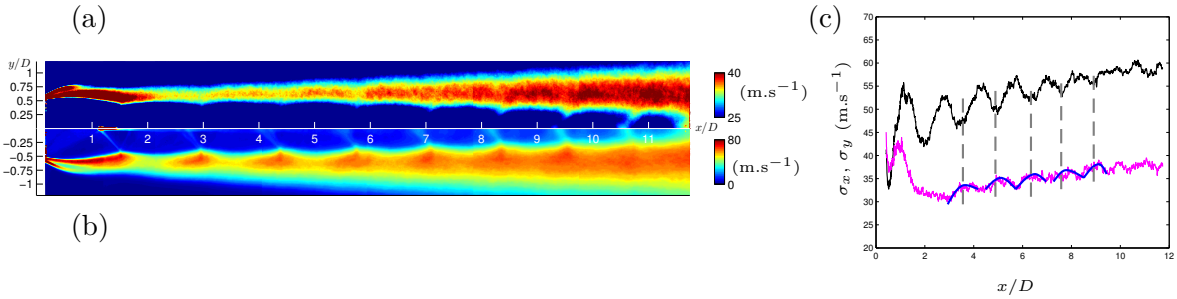

FIGURE 10 – Cartographies de la valeur RMS de la composante radiale de la vitesse, σ_y (a) et de sa composante axiale, σ_x (b) dans un jet sous-détendu pour M_j= 1.50 ; le profil axial de ces mêmes quantités en $r/D = 0.67$ est fourni en (c) : σ_x (—) et σ_y (—), les lignes (—) correspondant à un lissage spatial des résultats obtenus pour σ_y. Les lignes discontinues verticales figurent la position des maxima de σ_x, qui correspond à celle des minima de σ_y.

4.1.3 Étude du screech

L'idée qu'une structure de cellules de choc serait définie de manière figée pour un M_j donné est une représentation sur-simplifiée de la réalité. En effet, les ondes de détente issues des lèvres de la tuyère se réfléchissent sur l'enveloppe sonique dans l'écoulement pour former la structure de cellules de choc. Des phénomènes instationnaires dans la couche de mélange peuvent modifier la position et l'orientation locale de cette enveloppe. Cela se traduit par un **changement d'orientation des cellules de choc** tel qu'illustré par la figure 11. Sous l'effet du screech par exemple, une oscillation des chocs a pu être mesurée par l'utilisation d'une analyse d'images strioscopiques [3], indiquant que la fréquence du mouvement des chocs est égale à celle du screech, et que le mode d'oscillation des chocs [64] est le même que celui du screech (axisymétrique ou sinueux, dans le cas des jets étudiés), l'amplitude du mouvement augmentant avec l'amplitude du screech. On peut concevoir que la **structure modale des ondes d'instabilité associées au screech** impose la **structure modale du mouvement de la structure de cellules de choc**, ce qui a été vérifié expérimentalement par l'utilisation de plusieurs systèmes schlieren synchronisés [4]. Dans le cas du mode *b* présentant une instationnarité de la position du plan d'antisymétrie du mode sinueux, le suivi temporel de l'amplitude du mouvement des chocs et de l'amplitude des fluctuations de pression en champ proche a montré que le plan d'antisymétrie du mouvement de la structure de cellules de choc peut être vu comme le prolongement dans l'écoulement du plan d'antisymétrie du champ acoustique (voir les résultats détaillés au paragraphe 4.3.2.3). L'intérêt de cette caractérisation réside dans le fait que ces mouvements peuvent contribuer aux différences constatées sur les spectres de BBSAN avec et sans screech ; le changement périodique d'orientation relative des chocs par rapport à l'observateur à la fréquence du screech peut être un facteur influençant la directivité du BBSAN, comparativement à un modèle où les sources sont fixes [32].

Les mécanismes physiques liés au screech sont encore mal compris. S'il est clair que ce phénomène est le résultat d'une rétroaction aéroacoustique [63], les caractéristiques exactes des composants de cette boucle de rétroaction ne sont pas identifiées de façon indiscutable. L'existence de modes azimutaux pour les jets ronds est bien établie expérimentalement, mais

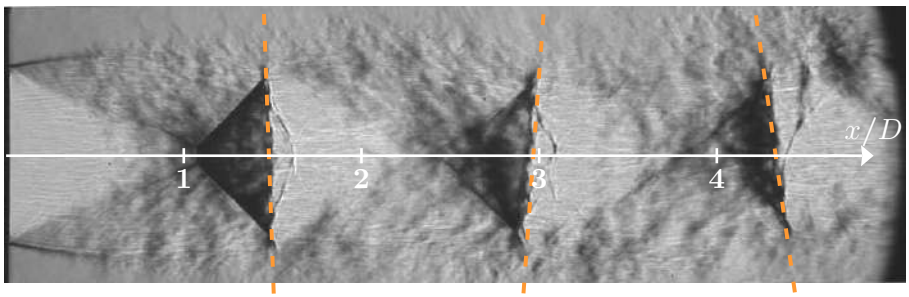

FIGURE 11 – Visualisation strioscopique d'un jet à M_j=1.50 (sans effet de vol) ; les traits discontinus marquent l'inclinaison des cellules de choc par rapport à la normale à l'axe du jet.

les mécanismes physiques de passage d'un mode à l'autre restent à préciser. Pour un jet sous-détendu entouré d'un écoulement secondaire subsonique visant à reproduire l'effet de vol, les caractéristiques principales de la boucle de rétroaction sont modifiées : la vitesse de convection des structures dans la couche de cisaillement change, tout comme la vitesse des ondes acoustiques regagnant la lèvre de la tuyère par l'extérieur du jet supersonique. On a pu caractériser l'effet de vol sur la fréquence du screech mesurée pour un jet de Mach M_j entre 1.10 et 1.50, et sur la structure modale du screech dans ces conditions. On a remarqué que, si la structure de cellule de chocs s'étire progressivement lorsque l'**effet de vol** augmente (*i.e.* lorsque la vitesse de l'écoulement secondaire augmente), **plusieurs sauts fréquentiels** existent sans pour autant que la structure modale du **screech** ne soit modifiée [2]. Ces sauts fréquentiels sont associés à un comportement hystérétique. Avec l'aide de mesures acoustiques en champ proche et de visualisations schlieren à haute fréquence, une étude détaillée portant sur l'identification des différents composants de la boucle de rétroaction associée au screech [48] a montré que pour un jet à M_j<1.50 donné, **une source principale du screech peut être isolée**. La position de cette source principale correspond par exemple à la position de la quatrième pointe de cellule de choc pour le mode A du screech. De plus, le temps total pour fermer la boucle de rétroaction du screech a été évalué pour les différents modes, ce qui a permis notamment d'expliquer la différence entre le mode A2 (temps total pour la rétroaction correspondant à 5 périodes de screech) et le mode A1 (temps total de 4 périodes de screech). La partie hydrodynamique de cette boucle de rétroaction a été étudiée par utilisation de PIV en moyenne de phase pour isoler les **champs de vorticité cohérente** dans la couche de cisaillement pour un jet à Mach M_j=1.10 et 1.15. La structure de cette vorticité cohérente est analysée en lien avec le phénomène de *shock-leakage* [71, 12] et un modèle simplifié permettant d'identifier la zone de l'écoulement où ce *shock-leakage* est susceptible d'intervenir est proposé, confirmant le role de la quatrième pointe de cellule de choc pour le mode A du screech [50].

4.1.4 Influence du screech sur le bruit de choc large bande

On a montré en figure 8 qu'il existe des valeurs de M_j pour lesquelles, sur notre installation, le screech présente une intermittence marquée. On a déjà indiqué les modifications de caractéristiques du BBSAN induites par le screech ; sachant que, entre ces deux sources de bruit, seul le BBSAN est retrouvé dans les applications aéronautiques, il est indispensable à l'échelle du Laboratoire de caractériser aussi cette source en l'absence de screech. Pour cela, l'effet d'une **protubérance mécanique** (appelée *tab*) placée en sortie de tuyère sur le **bruit de choc large bande** a été évalué, comparativement à celui d'une tuyère dite crénelée, dont la lèvre est pourvue d'indentations régulières de l'ordre du millimètre de profondeur et de largeur [6]. On a montré qu'il est **impossible** d'utiliser une *tab* pour étudier le BBSAN, compte-tenu du fait que l'efficacité de ce dispositif pour supprimer le screech provient d'une forte asymétrisation de la structure de cellule de choc et une réduction de la longueur moyenne de cellule de choc. Mais surtout, on a pu montrer qu'en utilisant une *tab*, la fréquence centrale et l'amplitude du BBSAN mesurées sur le spectre large bande dépendent de la position de la *tab* par rapport au microphone. A l'inverse, une **tuyère crénelée** permet de supprimer sinon fortement limiter le niveau de screech sans modification des caractéristiques moyennes de la structure de cellules de choc. C'est donc ce dispositif qui a été utilisé pour étudier l'influence du screech sur le BBSAN. Comme déjà suggéré plut haut par l'analyse de la figure 8, on a pu montrer qu'un **accordement en fréquence** a lieu entre le screech et le BBSAN pour l'ensemble des valeurs de M_j testées (donc l'ensemble des modes de screech rencontrés) [5]. Ce résultat est reporté en figure 12. On peut y remarquer que l'évolution de la fréquence centrale du BBSAN sans screech est pratiquement monotone, alors que cette même grandeur en présence de screech suit une évolution très semblable à celle de la fréquence du screech lui-même. En particulier, pour M_j <1.06 où le screech est quasiment inexistant, la fréquence centrale du BBSAN est identique pour le jet issu de la tuyère C38 et pour celui issu de la tuyère crénelée. Pour $M_j \in$[1.16 ;1.28] et $M_j \approx$1.40 dans la configuration avec screech où plusieurs modes ont des amplitudes comparables, on constate que la fréquence centrale du BBSAN peut prendre une valeur intermédiaire entre celles des différents modes de screech. Pour les autres valeurs de M_j, pour lesquelles un mode de screech domine, la fréquence centrale du BBSAN correspond à la fréquence du screech.

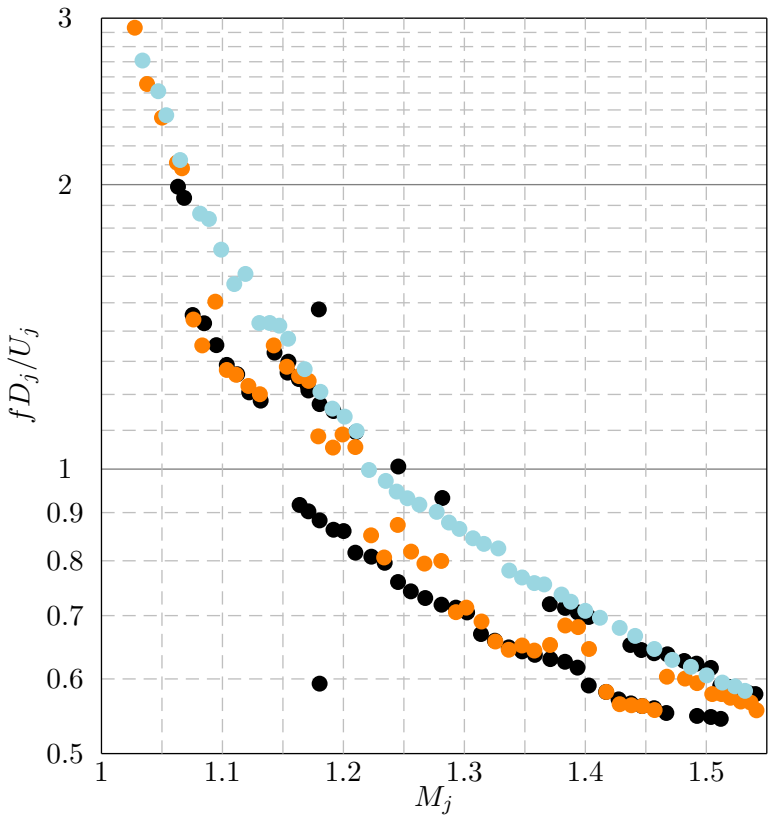

FIGURE 12 – Évolution avec M_j de $2f_s$ (avec f_s fréquence fondamentale du screech) (•) et de la fréquence centrale du BBSAN f_p pour θ=90° adimensionnée par les caractéristiques de l'écoulement U_j et D_j, avec tuyère C38 (•) et tuyère crénelée supprimant le screech (•).

4.2 Contrôle d'écoulement pour la performance aérodynamique de véhicules terrestres

Les activités de contrôle de l'aérodynamique des véhicules terrestres ont débuté à la suite d'une sollicitation de Renault Trucks, au travers de la thèse de S.Chaligné [18] adossée au programme TIGRE (voir paragraphe 3.2.2). La question générale alors posée est la suivante : est-il possible et énergétiquement rentable d'appliquer une méthode de contrôle d'écoulement permettant de réduire le coefficient de traînée C_x d'un véhicule poids-lourd de gamme 'grand routier' sans modification de sa forme extérieure ? La contrainte de forme est imposée par la réglementation actuelle (limitation de la longueur totale de l'ensemble tracteur-remorque) et par le caractère opérationnel de la remorque (un grand parallélépipède destiné à recevoir un chargement constitué de parallélépipèdes). Notre travail a porté sur le **contrôle du sillage de la remorque**, qui est un contributeur majeur à la traînée totale du véhicule (env. 30% de la traînée selon l'évaluation faite par Renault Trucks). Il faut reconnaître que les actions menées sur ce thème depuis 2010 n'ont répondu qu'à une partie de la question de départ, tout en soulevant d'autres interrogations qui ont certainement permis d'élargir la vision initiale du problème. L'objectif de cette partie est de présenter la démarche suivie pour s'assurer de la représentativité des modélisations successives effectuées à échelle réduite dans le cadre des deux thèses successives sur ce thème [18, 72], d'expliquer les choix effectués pour les systèmes de contrôle employés et d'indiquer quelques résultats significatifs issus de ces travaux.

4.2.1 Représentativité des modélisations effectuées

L'objet de notre étude expérimentale porte *in fine* sur la modification du sillage d'un corps tridimensionnel de grand allongement, à culot droit, soumis à un écoulement de vitesse U_∞ inférieure ou égale à 25 m.s^{-1} et placé à proximité d'un sol défilant par rapport au véhicule à une vitesse proche de U_∞. Au cours des études menées au Laboratoire, on a cherché à prendre progressivement en compte ces différentes caractéristiques en utilisant des configurations expérimentales de plus en plus élaborées. Réaliser des essais sur véhicule à échelle 1 est inenvisageable en soufflerie pour des questions de coût ; des essais sur piste, à la manière de [27, 26] ou de ce qui est fait actuellement dans le programme FALCON (voir paragraphe 3.2.2) sur une autre thématique, demeurent peu accessibles et fournissent des résultats dont l'analyse est complexe ; du reste, la mise en œuvre de techniques de mesures avancées y est fastidieuse voire impossible. Les programmes de recherche des deux thèses sur ce sujet ont été ainsi structurés autour de géométries à échelle réduite, d'abord bidimensionnelle puis tridimensionnelle, étudiées au Laboratoire ou dans une soufflerie industrielle (ACE, Magny-Cours).

En anticipant les contraintes géométriques liées aux travaux prévus dans la thèse de **S.Chaligné** [18] sur maquette tridimensionnelle à une échelle suffisamment réduite pour être compatible avec les souffleries du Laboratoire, une première étude a porté sur un modèle bidimensionnel à culot droit. Ce modèle, dont une illustration est donnée en figure 13(a), a une forme avant profilée dont l'unique fonction est d'éviter tout décollement de l'écoulement au nez de la maquette.

L'étude porte sur le développement du sillage de cette maquette placée suffisamment près du sol pour **limiter l'écoulement de soubassement**, si bien que le rapport U_u/U_∞ est proche de 1/2. Grandemange et al. [29] et McArthur et al. [44] ont utilisé la même approche, sur géométrie tridimensionnelle, pour illustrer l'influence du paramètre U_u/U_∞ sur la pression moyenne au culot et sur la structure du sillage. Dans ces deux études, la modification des caractéristiques du sillage proche de la maquette résulte des effets combinés de deux mécanismes physiques (influence de la proximité du sol sur le développement du sillage, influence de la quantité de mouvement du flux de soubassement) induits par la seule modification de la garde au sol. Une configuration expérimentale permettant d'isoler le seul effet de la vitesse de soubassement a donc été étudiée d'abord sur la maquette bidimensionnelle [18], puis sur une maquette simplifiée à échelle 1/43e (93 mm de hauteur totale, dont 74 mm de hauteur de culot) illustrée par la figure 13(b). L'étude sur cette dernière maquette a permis d'isoler l'effet de l'écoulement de soubassement sur la **structure du sillage**. Sur toute la gamme de variation possible pour la vitesse de soubassement, quatre structures différentes pour ce sillage ont été identifiées au travers de critères quantitatifs liés à la quantité de mouvement de l'écoulement de soubassement (voir la figure 14(a)) et à la courbure de cet écoulement [17]. Ces 4 classes d'écoulement se traduisent également par des valeurs très différentes de la pression moyenne au culot de la maquette et du gradient vertical de la pression. Les résultats obtenus à petite échelle ont pu être comparés à ceux issus de simulations numériques effectuées par D.Chacaton de Renault Trucks (configuration en sol fixe) et de mesures effectuées sur des maquettes à plus grande échelle ($\approx 1/8^{\text{e}}$), dans le cadre des thèses de **S.Chaligné** [18] et de **M.Szmigiel** [72] ainsi que du stage post-doctoral de **P.Sujar** dans le cadre du programme ACTIV_ROAD [70]. Cette comparaison est illustrée en figure 14(b) et (c). Les valeurs obtenues pour le flux de quantité de mouvement au travers des différentes surfaces de contrôle sont très similaires dans tous ces cas, ce qui constitue un résultat fort sur la **représentativité des essais effectués** à échelle réduite et sur la **pertinence de l'identification des différentes classes d'écoulement**. On peut notamment remarquer que les résultats obtenus pour une maquette intégrant des volets sur l'arête supérieure et sur les arêtes latérales obéissent à la même tendance que les résultats obtenus pour une maquette à culot droit (sans volet). On peut expliquer ce résultat par le fait que dans les deux configurations comparées (avec et sans volets), il n'y a pas de volet sur l'arête inférieure du culot, ce qui préserve l'orientation locale de l'écoulement issu du soubassement et par conséquent la répartition des flux entre $\zeta_2^\star$ et $\zeta_3^\star$. On voit que seul le résultat obtenu en figure 14(c) pour le modèle réduit de camion RT ne présente pas un très bon accord avec toutes les autres configurations étudiées. On peut interpréter cette différence par le fait qu'un diffuseur est présent sur le modèle réduit, donnant une orientation moyenne de l'écoulement de soubassement différente des autres configurations où la face inférieure de la remorque est parallèle au sol.

La prise en compte du vent latéral, importante pour l'application visée plus que pour les applications liées aux véhicules particuliers compte-tenu des vitesses maximales autorisées, a été rendue possible lors de la thèse de **M.Szmigiel** [72] et lors du programme ACTIV_ROAD par l'utilisation d'un plateau tournant intégrant une balance pour l'évaluation des efforts aérodynamiques. La prise en compte du défilement du sol n'a pas été possible expérimentalement

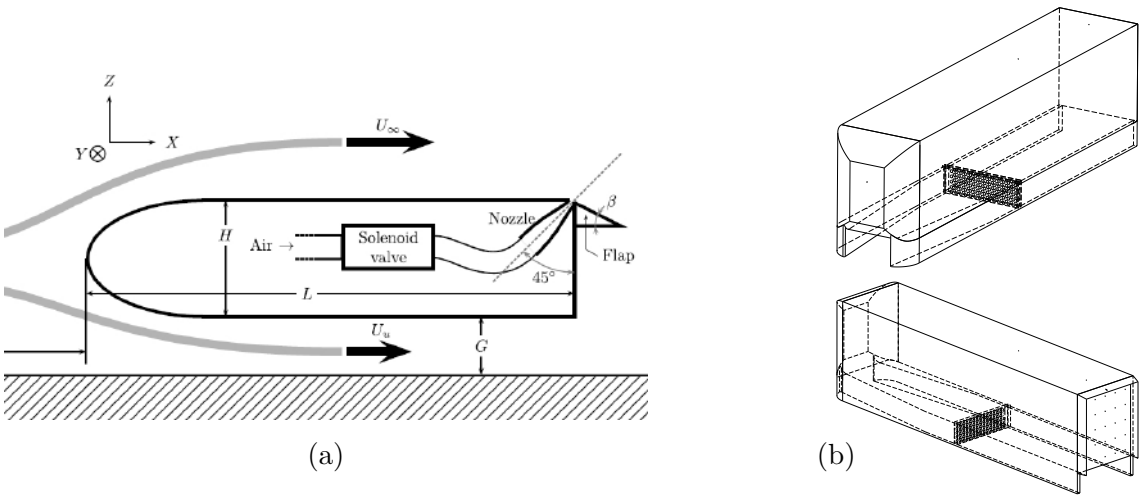

FIGURE 13 – Schéma des modélisations expérimentales successives pour l'étude du sillage d'un poids lourd : modèle 2D avec garde au sol G réduite pour limiter la valeur de vitesse de soubassement U_u (a) et modèle 3D avec jupes et intégration d'un élément poreux dans le soubassement (b).

jusqu'ici, mais des développements actuels au Laboratoire devraient permettre d'évaluer prochainement l'effet de ce paramètre sur la classification des écoulements présentée ci-avant.

4.2.2 Contrôle d'écoulement sur véhicule industriel

4.2.2.1 Application du contrôle d'écoulement sur maquette

La réglementation s'appliquant aux poids lourds a récemment évolué, permettant à terme d'installer des éléments additionnels à l'avant comme à l'arrière d'un convoi de longueur toujours limitée, pour améliorer les performances aérodynamiques. Cette possibilité ouvre la perspective de l'application pratique de systèmes intégrés à la remorque, tels que précédemment testés sur véhicule de série [27, 25]. De tels systèmes combinent typiquement des surfaces courbées ou rectilignes, appelées indistinctement dans la suite 'volet' et placées dans le prolongement des parois de la remorque à des générateurs d'écoulements secondaires à proximité des arêtes du culot, au contact des surfaces ajoutées. Ces écoulements secondaires sont dans la suite désignés par le terme 'jets de contrôle'. L'idée de ce **couplage entre volets et jets de contrôle** localisé au culot du véhicule est de forcer l'interaction avec l'écoulement qui est naturellement massivement détaché du véhicule à partir de la fin du culot. Pour des questions opérationnelles (manoeuvrabilité de la remorque et gestion de l'accostage lors des opérations de chargement/déchargement), on peut s'interroger sur la nécessité de conjuguer jets et volets, en misant sur une interaction directe entre les jets de contrôle et l'écoulement principal. De plus, la question se pose de l'intérêt de jets de contrôle continus, alors que les jets instationnaires permettent une limitation du coût du contrôle en réduisant le débit de fluide injecté et ouvrent la possibilité d'explorer la sensibilité du sillage à des perturbations instationnaires. Pour traiter la première question, l'étude préliminaire réalisée sur maquette 2D permet de montrer [20] que l'utilisation d'action-

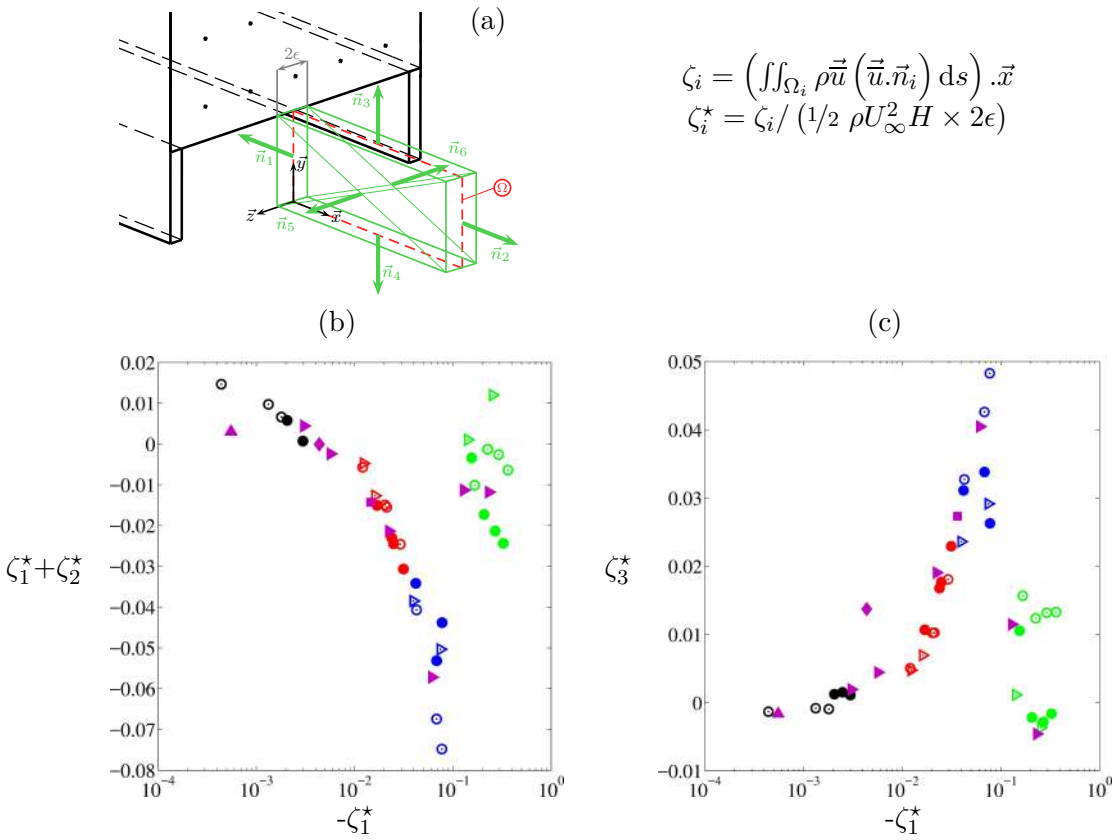

FIGURE 14 – Définition du volume de contrôle pour l'évaluation du flux de quantité de mouvement ζ_i (a) ; relations entre les flux de quantité de mouvement traversant différentes surfaces de contrôle (b,c) pour différentes configurations étudiées : maquette simplifiée 1/43$^{\mathrm{e}}$ - culot droit ($\odot$) et avec volets ($\bullet$), la couleur correspondant aux 4 classes identifiées [72], modèle réduit 1/43$^{\mathrm{e}}$ camion Renault trucks ($\blacklozenge$), maquette 1/8 ($\blacktriangleright$ thèse M.Szimigiel [72], $\blacktriangle$ thèse S.Chaligné [18]), simulation numérique par Renault Trucks d'un camion à échelle 1 avec un sol fixe ($\blacksquare$).

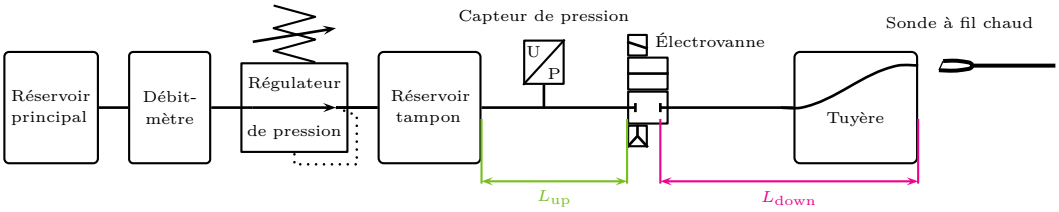

FIGURE 15 – Schéma d'une ligne pneumatique permettant la génération d'un jet pulsé. La distance L_{up} correspond à la longueur développée entre l'électrovanne et le réservoir tampon dans lequel règne une pression P_i idéalement constante sous l'effet du régulateur de pression, et la distance L_{down} à la longueur développée entre l'électrovanne et la sortie du diffuseur à pression atmosphérique. Le comportement du fluide dans la conduite en amont de l'électrovanne est traduit par le signal issu d'un capteur de pression instationnaire ; celui du fluide dans la conduite du diffuseur par une sonde à fil chaud placée en sortie de fente.

neurs instationnaires sur la configuration à culot droit entraîne une diminution de la pression moyenne au culot quelle que soit la fréquence d'actionnement utilisée (la valeur maximale de fréquence d'actionnement, 300 Hz, étant une limitation technologique du système employé). On a pu expliquer le comportement linéaire de la diminution de pression moyenne au culot quand la fréquence d'actionnement est inférieure à 10 Hz par la répétition du développement de structures tourbillonnaires induites dans l'écoulement par les jets de contrôle sans qu'il n'y ait d'interaction entre deux structures successives [19]. Au contraire, sur la même configuration agrémentée d'un volet plan d'angle 20° par rapport à l'horizontale, une **augmentation de pression moyenne au culot** est obtenue quand la **fréquence d'actionnement est élevée** ; elle peut atteindre 25% de la pression moyenne sans actionnement. La stratégie adoptée dans la suite des études menées au Laboratoire repose donc sur le couplage entre volets et jets instationnaires.

D'autre part, on souhaite identifier les mécanismes mis en jeu lors de l'interaction entre les jets instationnaires et l'écoulement à proximité du culot, en distinguant les jets pulsés (phase de soufflage suivie d'une période où la vitesse en sortie de jet est nulle) des jets synthétiques (à débit moyen nul, une phase d'aspiration suivant une phase de soufflage). Il a été montré que la modification de pression obtenue sur la configuration 2D avec des jets synthétiques est très semblable à celle obtenue avec des jets pulsés (figure D.5 de [18]). Plus qu'une insensibilité à la phase d'aspiration, ce résultat peut témoigner d'une propriété liée au choix technologique fait ici pour la génération des jets pulsés. En effet, chaque jet pulsé est formé en bout d'une ligne pneumatique allant d'un réservoir d'air comprimé à une tuyère de section de sortie rectangulaire et de grand allongement ; à cette ligne est intégrée une électrovanne pilotée à la fréquence d'actionnement souhaitée. Cet ensemble est représenté de manière schématique en figure 15. L'étude de ce **système pneumatique** a permis d'établir une propriété spécifique de ce montage pour une fréquence d'actionnement f_{act} correspondant à un mode de résonance (1/4 d'onde) de la conduite entre l'électrovanne et la sortie de tuyère de longueur développée L_{down} [55]. La vitesse maximale en sortie de fente présente dans ce cas un maximum très marqué, tel qu'illustré par la figure 16, pour une fréquence de résonance du conduit de sortie $f^d_{1/4} = c/4/L_{down}$ proche de 350

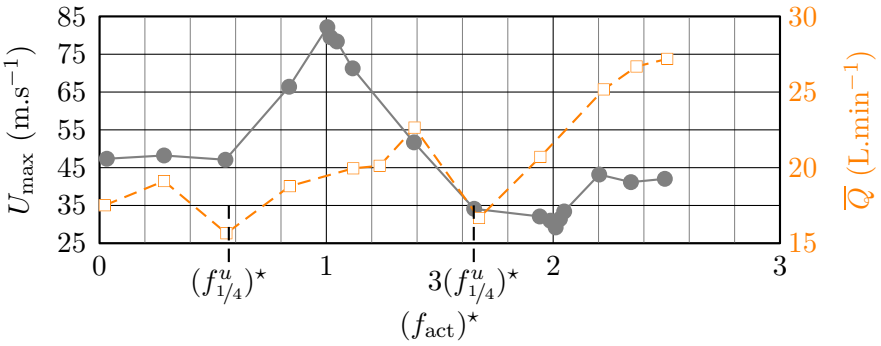

FIGURE 16 – Évolution de la vitesse maximale, au cours d'un cycle, (—●—) et du débit moyen (—□—) en sortie de fente d'un jet pulsé correspondant au montage de la figure 15 en fonction de la fréquence d'actionnement f_{act} adimensionnée par la fréquence de résonance du mode quart d'onde du conduit de sortie $f^d_{1/4} = c/(4L_{\text{down}})$. On utilise la notation $(f)^\star = f/f^d_{1/4}$.

Hz. Le débit d'air comprimé utilisé est toutefois très proche de celui consommé par exemple à très basse fréquence d'actionnement, ce qui témoigne du fait que le **mode de résonance du conduit aval** induit une aspiration significative de l'air en sortie de fente. On note également que le même phénomène de résonance acoustique dans le conduit amont (entre le réservoir secondaire et l'électrovanne) se traduit par une chute du débit parcourant la ligne pneumatique pour une fréquence d'actionnement correspondant à une harmonique impaire de $f^u_{1/4}$. Une description détaillée des propriétés de l'actionneur peut être trouvée en [30]. On pourra donc retenir ici que les jets pulsés employés peuvent présenter une phase d'aspiration selon le même principe que les jets synthétiques ; ce principe s'appuyant sur la résonance acoustique du conduit aval permet d'améliorer l'efficacité énergétique du dispositif de contrôle en limitant le débit consommé pour une valeur donnée de vitesse maximale en sortie de fente.

Cette technique de contrôle a été utilisée sur une maquette à échelle $1/8^e$ de même géométrie que celle indiquée en figure 13(b) lors de la thèse de **S.Chaligné** [18] et de **M.Szmigiel** [72]. Différents taux de porosité de la grille placée dans le soubassement du corps ont été employés au cours de ces études, dans l'objectif de représenter les différentes applications possibles, du véhicule industriel léger au poids lourd. Pour la première étude, des jets de contrôle (jets synthétiques) appliqués sur l'arête supérieure du culot d'un corps 3D ont montré qu'une recompression du proche sillage était obtenue lorsque la fréquence d'actionnement est suffisamment élevée. La deuxième étude a montré la faisabilité et l'intérêt d'un contrôle par jets pulsés tels que présentés ci-avant, répartis sur trois côtés (arêtes latérales et supérieure). On a également montré dans cette étude que, pour un volet supérieur d'angle suffisamment faible pour éviter le décollement de l'écoulement, utiliser des jets pulsés à fréquence élevée ne permet pas d'améliorer la recompression au culot déjà obtenue par la seule utilisation de volets de même inclinaison. En revanche, dans le cas où l'écoulement est naturellement décollé sur le volet supérieur, l'utilisation de jets pulsés apporte une réduction de traînée. La **comparaison quantitative** des résultats de cette **stratégie** sur trois côtés avec ceux obtenus lors de l'étude de Chaligné [18] est toutefois délicate parce que les configurations étudiées sont différentes, par les systèmes de contrôle d'une part et d'autre part par les pertes de charge placées dans le soubassement conduisant à des sillages de

classes différentes [17]. **L'intérêt d'un contrôle de l'écoulement de soubassement**, dont on sait l'influence sur la structure du sillage des corps à culot droit, y est questionné. La réponse à ces questions figure parmi les objectifs du programme ACTIV_ROAD. La maquette développée pour cette étude intègre un système de jets pulsés travaillant à une fréquence maximale de 1 kHz et orientés tangentiellement à l'écoulement incident au culot de la maquette - jusqu'ici, les jets de contrôle étaient orientés à 45° des faces latérales de la maquette tel que dans des travaux antérieurs au Laboratoire [21], ce qui permettait notamment de relaxer des contraintes d'intégration dans la maquette de l'ensemble formé par l'électrovanne, la conduite aval et le diffuseur terminal. Une évaluation fine des performances de ce type de contrôle est effectuée sur ce dispositif.

4.2.2.2 Performance des stratégies de contrôle sur modèle 3D

Un des objectifs à la base du programme ANR ACTIV_ROAD est l'étude du contrôle d'écoulement sur une maquette dont le rapport d'aspect hauteur/largeur soit adaptable, et cela sans modifier l'environnement dans lequel l'étude est effectuée. On sait en effet l'influence du rapport d'aspect sur les caractéristiques instationnaires du sillage d'un corps à culot droit à proximité du sol [29]. De plus, les études menées précédemment au LMFA sur les maquettes avec limitation du flux de soubassement montrent une influence sur la pression moyenne au culot de paramètres de contrôle (comme la fréquence d'actionnement et la quantité de mouvement injectée) qui présente des similitudes avec les résultats obtenus dans le même temps à l'ENSMA sur une maquette représentative d'un véhicule de tourisme [11]. On évaluera donc la performance de différentes stratégies de contrôle sur la manipulation du sillage d'une maquette unique qui peut être installée dans la soufflerie de telle sorte que son grand côté soit parallèle au sol (le rapport d'aspect H/W vaut ainsi 0.83) ou telle que son petit côté soit parallèle au sol (H/W=1.2) avec dans ce cas la possibilité d'intégrer un dispositif de pertes de charge similaire à celui présenté ci-avant. Les volets placés à l'arrière du corps correspondent soit à des 1/4 de rond, soit à des éléments plans. Pour la configuration H/W=0.83 associée aux 1/4 de rond étudiée dans la thèse de **Y.Haffner** [31], le développement de la vorticité induite par l'interaction entre les jets de contrôle et l'écoulement incident, très près de la sortie de la fente, dépend très significativement de la **fréquence d'actionnement** [30]. Ceci se traduit par une **recompression progressive** du sillage au fur à et à mesure que le coefficient de quantité de mouvement C_μ est augmenté pour une fréquence d'actionnement de 350 Hz (correspondant à $f^d_{1/4}$ du paragraphe précédent), tel qu'illustré en figure 17. Cette recompression est traduite par le coefficient γ_p, rapport entre la pression moyenne au culot avec contrôle et la pression moyenne dans le cas de référence ; ce rapport est d'autant plus petit que la recompression au culot est bonne. Pour la fréquence d'actionnement de 1050 Hz correspondant à $3f^d_{1/4}$, on constate que la recompression est obtenue de manière beaucoup plus marquée pour de plus faibles valeurs de C_μ, mais qu'elle est associée à une saturation que l'on ne trouve pas dans les résultats de contrôle à 350 Hz. On illustre ainsi un **effet spécifique** au caractère instationnaire de l'**écoulement pulsé** et à son couplage avec le volet ; la compréhension fine de ce phénomène et de son effet sur la recompression du sillage fait l'objet d'analyses en cours [30]. On montre aussi ici l'intérêt du soufflage pulsé par rapport

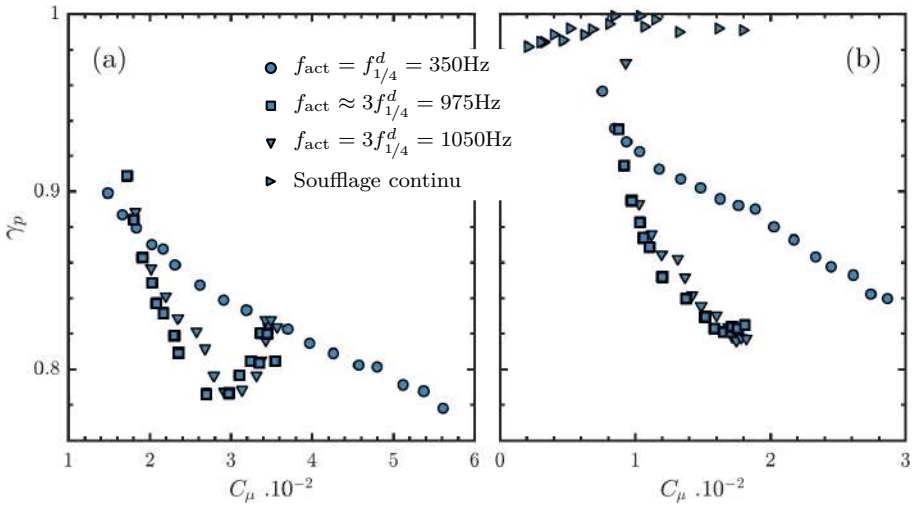

FIGURE 17 – Évolution du taux de recompression au culot γ_p en fonction de la quantité de mouvement totale injectée par le système de contrôle pour différentes fréquences d'actionnement, pour U_∞=25 m.s^{-1} (a) et U_∞=35 m.s^{-1} (b) . Les résultats présentés ici concernent la configuration $H/W = 0.83$, et les volets ont la forme de 1/4 de ronds de rayon $r = 9h$ avec h la hauteur de fente de soufflage.

au continu : on constate en effet sur la figure 17 la modification très limitée de la pression moyenne au culot de la maquette par un soufflage continu.

Pour le modèle de véhicule industriel étudié dans ACTIV_ROAD, les arêtes du culot de la maquette en configuration H/W=1.2 ont été munies de volets droits. L'angle entre ces volets et le corps de la maquette a été fixé à 25°, l'écoulement présentant ainsi naturellement un décollement massif au culot même en présence de ces volets. Cette valeur d'angle est quelque peu arbitraire, en ce sens qu'on aurait probablement pu choisir un angle de volet supérieur sans que les conclusions de l'étude n'en fussent modifiées. L'objectif de cette étude n'est pas, en effet, une optimisation aérodynamique de l'angle des volets permettant de maximiser l'efficacité de l'ensemble jets pulsés+volets, mais une **identification des mécanismes physiques** à l'œuvre dans la formation du sillage permettant une remontée de pression au culot. On s'intéresse pour cela à la recompression obtenue au culot pour différentes classes d'écoulement, telle que présentée en figure 18. On constate que le contrôle d'écoulement effectué ici sur les quatre arêtes du culot permet pour toutes les classes d'écoulement d'augmenter la pression au culot. Les évolutions de la pression moyenne au culot avec la porosité ϕ, non monotones, ont des allures semblables dans le cas de référence et dans le cas contrôlé. On a pu exploiter ce résultat pour proposer une première explication [70] de l'effet de différentes stratégies de contrôle impliquant ou non un contrôle de l'écoulement provenant du soubassement (c'est à dire impliquant ou non l'actionnement sur l'arête inférieure du culot). En effet, compte-tenu des différences de quantité de mouvement de l'écoulement de soubassement entre la classe I (faible porosité dans le soubassement) et la classe IV (forte porosité), il est intéressant d'évaluer l'influence de la vectorisation de cet écoulement sur la pression moyenne au culot pour les différentes classes

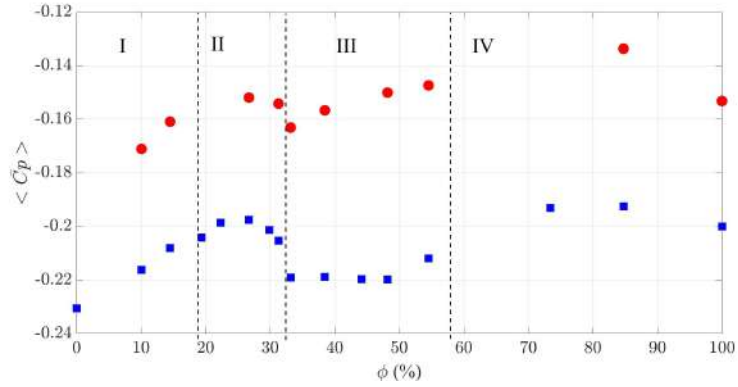

FIGURE 18 – Évolution de la pression moyenne au culot $< \overline{C_p} >$ avec la porosité ϕ de la grille perforée placée dans le soubassement de la maquette, dans le cas naturel (■) et avec contrôle à la fréquence $f^d_{1/4}$ (●).

d'écoulement.

La figure 19(a) illustre les résultats obtenus sur un écoulement de classe III (et maquette sans dérapage) en appliquant un **contrôle** impliquant l'actionnement **sur un côté ou des combinaisons de différents côtés**. On montre ainsi que pour un C_μ donné, le gain de pression peut dépendre très significativement de la stratégie choisie. En particulier, la stratégie de contrôle impliquant les 4 arêtes est moins performante que la stratégie de contrôle où sont activées les arêtes du culot à l'exception de l'arête inférieure, du point de vue de la recompression au culot et aussi du coût du contrôle. Ce résultat est retrouvé pour une configuration où la maquette présente un angle de dérapage de 5° (figure 19(b)) et pour le contrôle à une fréquence d'actionnement de 3 $f^d_{1/4}$ (figure 19(c)). Vis à vis des résultats présentés pour la configuration $H/W = 0.83$ en figure 17, on retrouve ici que le contrôle à haute fréquence (figure 19(c)) permet d'atteindre des valeurs de γ_p autour de 0.65 pour des valeurs de C_μ un peu inférieures à celles associées au contrôle à $f^d_{1/4}$ (figure 19(b)). Les tendances sont néanmoins très similaires entre les différentes stratégies pour ces deux cas, ce qui tend à montrer que pour les volets utilisés ici, l'actionnement à la fréquence $f^d_{1/4}$ ou à $3f^d_{1/4}$ implique des mécanismes physiques semblables pour la structuration du sillage.

L'examen détaillé de la figure 19(a) montre qu'il existe un **couplage significatif** entre les **couches de cisaillement contrôlées**. On constate en effet que la pénalité de pression au culot déjà constatée lorsque l'on passe de la stratégie à 3 côtés (TLR pour Top-Left-Right) à la stratégie à 4 côtés est qualitativement retrouvée sur les configurations où l'arête inférieure est actionnée seule (ii), ou en combinaison avec le haut (ii) ou avec un ou plusieurs côtés (iii). Le couplage existe aussi pour les stratégies impliquant les seuls côtés : l'actionnement sur un côté (gauche ou droit) n'a pas d'effet sur la pression moyenne au culot, mais le couplage des deux côtés a un effet significatif (iv). De même, une amélioration de la recompression par rapport au résultat obtenu par un contrôle sur l'arête supérieure uniquement est obtenue en couplant l'actionnement en haut et sur un côté (iv). Ce dernier exemple montre également, pour cet écoulement de base de classe III, que pour un coût donné (par exemple $C_\mu \approx 0.02$) un **contrôle**

asymétrique par rapport au plan médiant vertical (par exemple TR) peut être plus efficace que des stratégies de contrôle préservant la symétrie gauche/droite du sillage (par exemple LR ou TB pour Top-Bottom). Une analyse comparable [31] effectuée sur la maquette avec un rapport d'aspect $H/W = 0.83$ montre aussi que certaines stratégies avec actionnement sur 3 côtés sont plus efficaces que d'autres, mais elle indique aussi que la stratégie avec contrôle à 4 côtés reste la plus efficace, ce qui contraste avec les résultats présentés ci-avant. La sensibilité des résultats au type d'écoulement de base sur lequel le contrôle est appliqué (classe III pour la figure 19, classe IV pour [31], mais peut-être tout autant les classes I et II) et au couplage entre jets de contrôle et géométrie du volet, rappelle la grande complexité de ce problème d'aérodynamique.

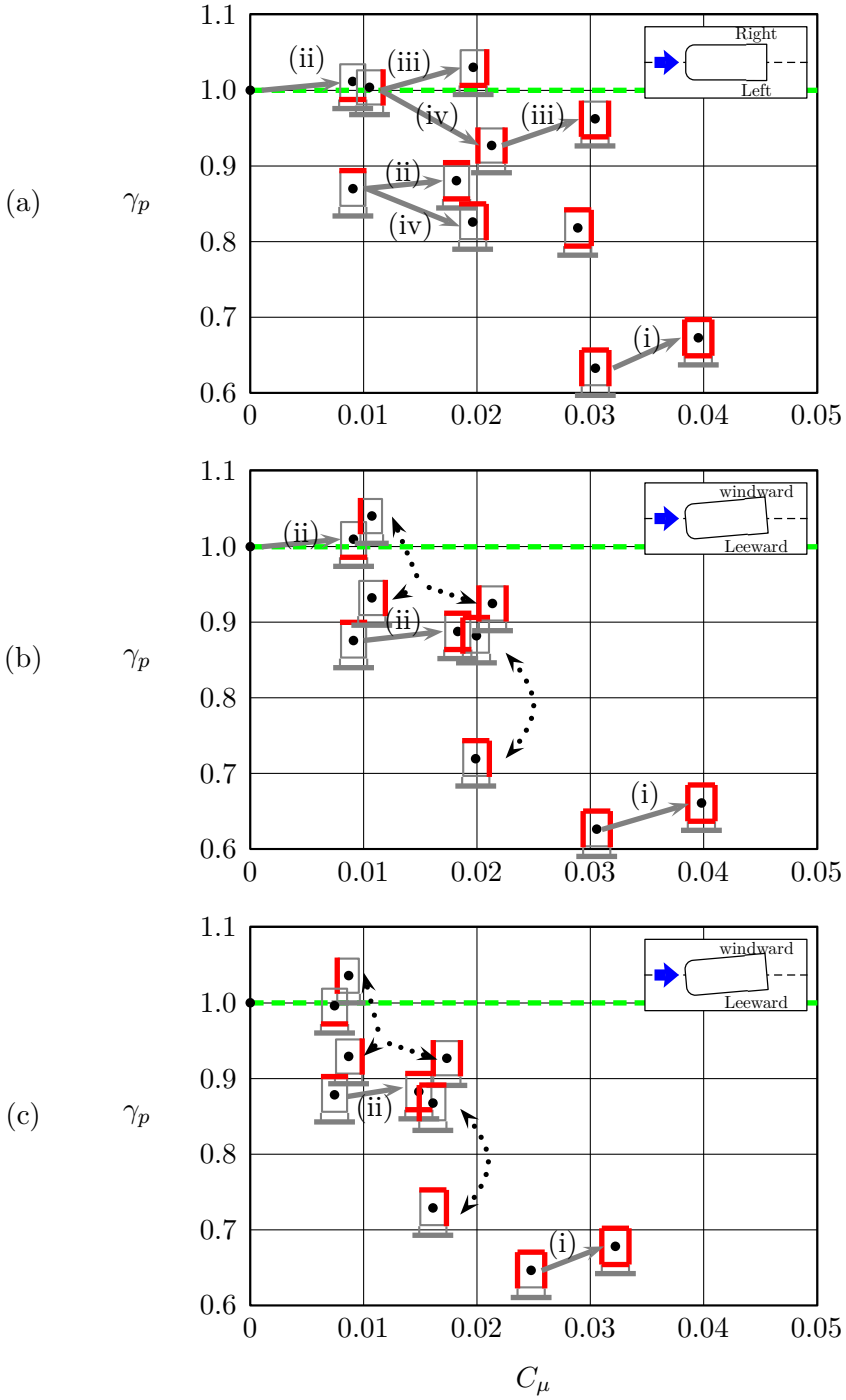

FIGURE 19 – Effet de la stratégie de contrôle employée sur la recompression au culot. Configuration de maquette $H/W = 1.2$, grille de perte de charge de porosité 42% correspondant à un écoulement de classe III. Contrôle, pour une pression d'alimentation fixée, à la fréquence $f^d_{1/4}$ (a, b) et à $3f^d_{1/4}$ (c). Angle de dérapage entre la maquette et l'écoulement de 0°(a), 5°(b, c).

4.3 Développements liés à la mesure dans les écoulements rapides

Pour appuyer les études détaillées dans ce document (sources de bruit d'origine aéroacoustique ou caractérisation de l'effet du contrôle d'écoulement), des développements métrologiques sont effectués au Laboratoire. L'objectif est ici de répondre aux besoins d'acquisition de données avec une résolution temporelle adaptée aux fréquences caractéristiques élevées des jets étudiés par exemple. De plus, pour aider à la caractérisation des sources acoustiques, on cherche préférentiellement l'utilisation de méthodes de mesure ayant un caractère non intrusif. Ainsi, idéalement, les techniques utilisées ne nécessitent pas qu'une sonde soit placée dans l'écoulement étudié, ni que des traceurs y soient introduits pour éviter les effets d'inertie pouvant induire un biais sur l'estimation du champ de vitesse fluide [7]. Le fait de privilégier ces moyens non intrusifs ne saurait toutefois pas être exclusif ; la **mesure de pression statique** en écoulement supersonique a par exemple été mise en œuvre dans la thèse de **B.André** [1]. Une synthèse du travail effectué pour le dimensionnement de ces sondes est donc présentée en premier lieu. Le (re-)développement au Laboratoire de **visualisations strioscopiques** est ensuite détaillé, dans l'objectif d'indiquer quelques-unes des exploitations quantitatives de résultats fournis par cette technique appliquée aux jets sous-détendus. Enfin, la mise en œuvre pratique de la technique de **mesure de masse volumique par diffusion Rayleigh**, développée au Laboratoire pendant la thèse de B.Mercier [46], est rappelée en cherchant à préciser les éléments techniques et fondamentaux qui doivent guider la mise en œuvre de cette technique par tout potentiel utilisateur.

4.3.1 Mesure de pression statique dans les écoulements supersoniques

La description de la structure de cellules de choc dans un jet sous-détendu, en particulier en présence d'effet de vol, a été effectuée pendant la thèse de Benoît André [1]. Nous avons pour cela décidé de réaliser des mesures de pression statique dans l'écoulement. Ces mesures locales reposent sur le développement d'une sonde dont le diamètre doit rester petit par rapport au diamètre de la tuyère employée ($D = 38$mm). La forme de cette sonde doit permettre de limiter l'**effet sur la pression mesurée du choc induit** dans l'écoulement par la sonde elle-même, et la distance entre la pointe de la sonde et le point de mesure doit être significativement plus petite que la longueur de la cellule de choc contenue dans le jet étudié. Deux géométries de sonde ont été dessinées à partir du design présenté par Pinckney [62]. Elles sont représentées en figure 20. Pour chacune de ces géométries, une pointe conique est utilisée, d'ouverture angulaire choisie ici à 10° pour l'une et 20° pour l'autre, dans l'objectif de disposer de sondes adaptées à des écoulements de Mach M_j différents. Le design générique de la sonde s'appuie sur une deuxième partie conique, d'ouverture plus faible, dans laquelle sont aménagées les prises de pression. Le raccord entre les 2 parties coniques d'une même sonde est assuré par une arête vive (figure 20 (a)) ou par une transition progressive s'étendant ici de 1.7 à 3.7mm de la pointe de la sonde (figure 20 (b)). Le dimensionnement de ce type de sondes a été effectué par Pinckney

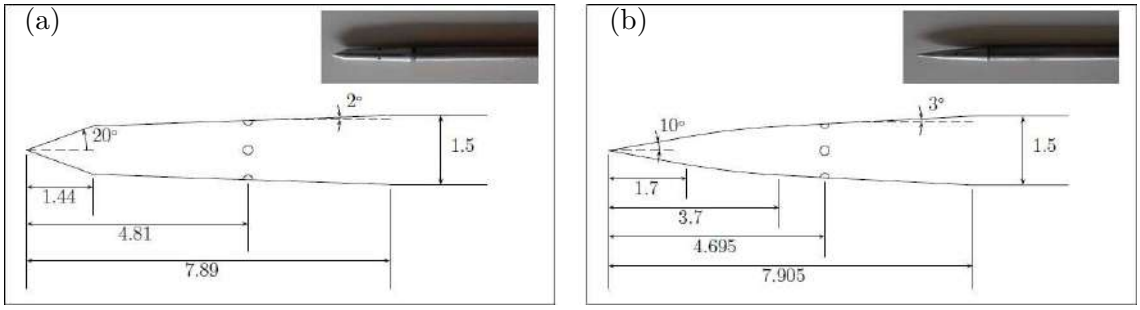

FIGURE 20 – Géométrie des sondes de pression statique utilisées pour la mesure dans les jets supersoniques. Sonde biconique (a) et sonde biconique avec raccordement C^1 entre les deux cones (b). Toutes les longueurs sont exprimées en mm.

[62] pour un écoulement (uniforme) de Mach $M_j \geq 2.5$; une calibration théorique de ces sondes a été effectuée ici jusqu'à $M_j = 1.5$, puisque cette valeur correspond à la valeur maximale pouvant être obtenue sur la soufflerie anéchoique du Laboratoire. Cette calibration s'appuie sur la description de l'écoulement conique autour de la pointe de la sonde, ce qui permet d'initier le calcul de l'écoulement sur le reste de la sonde par la méthode des caractéristiques. Ces deux approches sont à présent brièvement présentées.

4.3.1.1 Écoulements coniques

La figure 21(a) fournit une illustration des notations utilisées ci-après. La description de l'écoulement autour d'un cône infini a été réalisée par Taylor & Maccoll [76] en s'appuyant sur trois hypothèses : l'écoulement autour de l'obstacle est supposé conique et irrotationnel, et un choc oblique prend naissance à la pointe du cône. L'hypothèse d'un écoulement conique se traduit par le fait que les propriétés de l'écoulement en un point donné dépendent uniquement de l'angle ω sous lequel est vu ce point depuis la pointe du cône. À partir de l'équation d'Euler et de l'hypothèse d'écoulement irrotationnel et conique, et en introduisant la quantité adimensionnelle $u = \frac{V_r}{V_{\max}}$, avec $V_{\max}$ la vitesse maximale pour l'écoulement adiabatique et V_r la composante du vecteur vitesse selon $\vec{e}_r$, une équation différentielle portant sur u peut être établie :

$$-\frac{\mathrm{d}^2u}{\mathrm{d}\omega^2}\left(\frac{\gamma+1}{2}\left(\frac{\mathrm{d}u}{\mathrm{d}\omega}\right)^2-\frac{\gamma-1}{2}(1-u^2)\right)-\frac{\gamma-1}{2}\left(\frac{\mathrm{d}u}{\mathrm{d}\omega}\right)^3\mathrm{cotan}(\omega)-\gamma u\left(\frac{\mathrm{d}u}{\mathrm{d}\omega}\right)^2+\frac{\gamma-1}{2}\left(1-u^2\right)\frac{\mathrm{d}u}{\mathrm{d}\omega}\mathrm{cotan}(\omega)+(\gamma-1)\,u\left(1-u^2\right)=0 \quad (1)$$

La détermination de $v = \frac{V_w}{V_{\max}}$ est directe à partir de la relation obtenue par l'hypothèse d'écoulement irrotationnel :

$$v = \frac{\mathrm{d}u}{\mathrm{d}\omega} \quad (2)$$

Avoir ainsi déterminé u et v permet d'évaluer le nombre de Mach local M :

$$M(\omega) = \sqrt{\frac{2\,(u^2+v^2)}{(\gamma-1)\,(1-u^2-v^2)}} \quad (3)$$

Enfin, de part et d'autre du choc émanant de la pointe du cône, les relations dites *de choc oblique* s'appliquent, et en particulier la relation entre le nombre de Mach de l'écoulement uniforme M_1 en amont du choc et le nombre de Mach M_2 en aval du choc.

$$M_2 = \frac{1}{\sin\left(\operatorname{atan}\left(\frac{v}{u}\right)\right)} \sqrt{\frac{(\gamma-1)\sin^2(\sigma)M_1^2+2}{2\gamma\sin^2(\sigma)M_1^2+1-\gamma}}; \tag{4}$$

La résolution de l'équation (1) a été menée selon une méthode inverse, similaire à celle indiquée en [69]. À partir des conditions aux limites à la surface du cône, portant d'une part sur une valeur arbitraire de u et d'autre part sur la nullité de la composante v de la vitesse à la paroi, l'intégration de l'équation a été menée en utilisant un algorithme de Runge-Kutta (ode23 sous Matlab). La position angulaire σ de l'angle de choc est identifiée comme la valeur particulière de ω pour laquelle il y a égalité entre M et M_2, c'est à dire comme la condition pour que l'écoulement conique à cet angle ω satisfasse les relations imposées par un choc d'inclinaison ω. On en déduit la valeur de M_1 par utilisation des conditions de saut. Pour illustrer le résultat obtenu, on applique cette méthode au cas d'un cône de demi-ouverture $\delta = 12.5°$ placé dans un écoulement de nombre de Mach $M_1 = 1.84$, dont une image extraite de [79] est présentée en figure 21(b). Si les lignes de courant ne sont pas visibles sur cette observation ombroscopique, on peut néanmoins caractériser les lignes de Mach ; celles-ci correspondent en effet aux lignes de propagation des perturbations générées à la paroi du cône par la rugosité de l'objet. On remarque de plus que l'angle de choc est très proche de la valeur livrée par l'approche théorique rappelée ici.

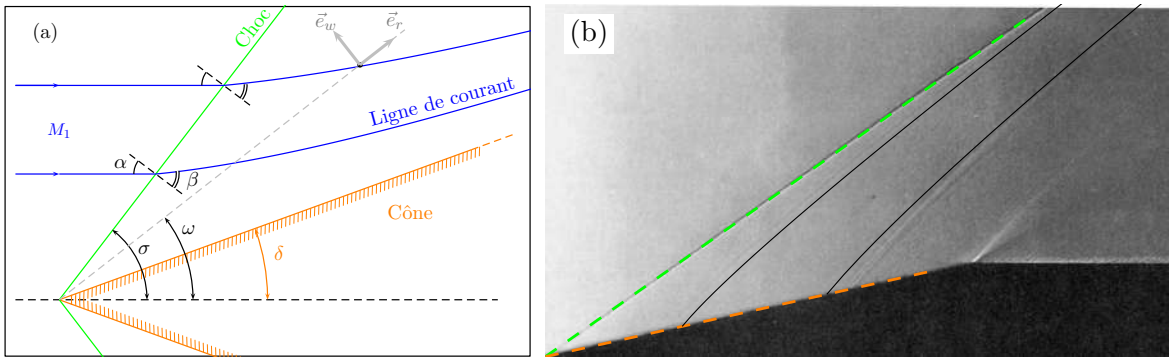

FIGURE 21 – Schéma représentatif de l'écoulement autour d'un cône (a). Écoulement autour d'un cône de demi-ouverture $\delta = 12.5°$, $M_1 = 1.84$ (reproduction de la figure 259 de [79]) ; on trace sur cette image l'angle du cône (- - -) pour vérifier l'absence de distorsion de l'image. On figure également deux lignes de Mach (——) à proximité des lignes de Mach naturellement visibles sur l'images et l'angle de choc (- - - - -), tels que prédits par le modèle de Taylor & Maccoll (b).

4.3.1.2 Méthode des caractéristiques pour les écoulements axisymétriques

Une description détaillée de la méthode des caractéristiques dans son application générale peut être trouvée notamment dans [41, 69, 54]. L'approche mise en œuvre ici, permettant la résolution de l'**écoulement autour d'un objet axisymétrique** à la condition que cet écoulement soit partout supersonique, s'appuie sur [22]. Il y est démontré que par un point donné d'un écoulement supersonique axisymétrique passent deux lignes caractéristiques, l'une formant un angle $+\alpha$ par rapport à l'orientation locale de la ligne de courant, l'autre formant un angle $-\alpha$. Y sont également établies les relations différentielles liant les propriétés de deux points de l'écoulement, supposées connues, à celle d'un troisième point qui serait situé à l'intersection de la caractéristique (+) de l'un des 2 points connus et de la caractéristique (-) de l'autre. En approximant ces relations par des différences finies il est possible de construire de manière itérative, graphiquement pour la référence [22] ou numériquement ici, un maillage de points décrivant de manière discrète l'écoulement axisymétrique étudié. Dans ce paragraphe, les **résultats des cas-test choisis** ici pour évaluer la **précision de la méthode** sont présentés, de même que la résolution de l'écoulement autour de la sonde de pression illustrée en figure 20(b) et employée dans la thèse de **B.André**.

Application à l'écoulement autour d'un cône infini

L'écoulement autour d'un cône infini est utilisé ici pour illustrer l'approche développée pendant le stage M1 de **B.Bacher**. Cette description s'appuie sur la figure 22. Le calcul est initialisé à partir des valeurs fournies par le modèle de Taylor & Maccoll le long d'une ligne de Mach construite de manière itérative et se terminant sur le choc conique d'ouverture angulaire σ. Les $(N+1)$ points le long de cette ligne servent ensuite de référence pour la **construction d'un maillage** (présenté en rouge sur la figure 22(a)) entièrement compris entre la première ligne de Mach et la surface du corps axisymétrique. Dans une dernière étape, on prolonge de manière itérative le choc en adaptant son orientation pour que la relation de saut de pression au travers du choc soit vérifiée, et on construit le maillage jusqu'au corps de sonde comme effectué lors de l'étape précédente. Pour un corps correspondant à un cône infini, on s'attend à ce que l'orientation du choc oblique soit constante, ce qui est retrouvé en figure 22(a). De même, les propriétés générales de l'écoulement conique sont bien retrouvées, et ce même pour un maillage relativement lâche ($N = 10$) comme l'illustrent les figures 22(b) pour la répartition du nombre de Mach M dans l'écoulement et (c) pour la pression à la surface du corps.

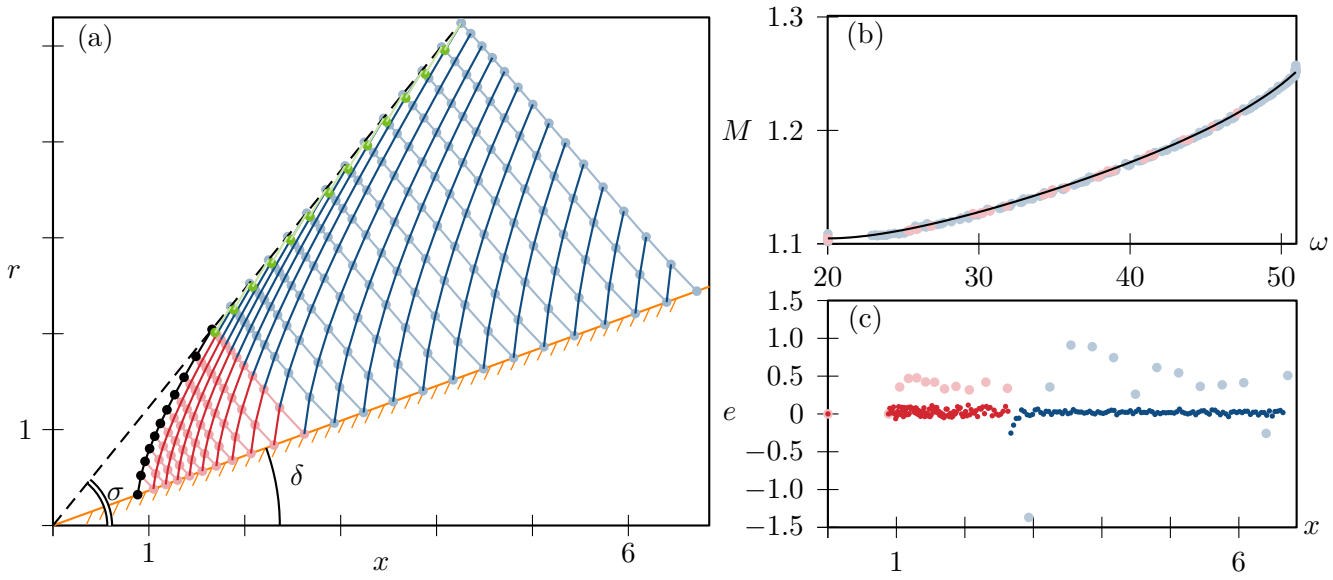

FIGURE 22 – (a) Maillage obtenu par application de la méthode des caractéristiques à un obstacle conique d'ouverture $\delta = 20°$, avec $M_1 = 1.45$.
(•) Points d'initialisation par la solution analytique de Taylor & Maccoll ($N = 10$)
(•) Maillage construit à partir des points d'initialisation
(•) Maillage construit après traitement du prolongement du choc, obtenu par les points (•)
(b) Évolution de M avec l'angle ω pour $N = 10$ (• et •) ; solution analytique de Taylor & Maccoll (—), (c) Écart relatif e (en %) entre la pression pariétale sur le cone et la valeur théorique associée à un écoulement conique, pour $N = 10$ (• et •) et $N = 100$ (• et •)

Application à un corps axisymétrique à pointe conique

L'étape suivante pour la validation du code a porté sur la détermination de la pression à la surface d'un corps axisymétrique à pointe conique. Le corps considéré correspond au missile A4V1P (tristement plus connu sous l'appellation V2) pour lequel les mesures reportées par Shapiro [69] extraites des travaux de Isenberg [34] servent de référence. On reporte en figure 23(a) une illustration du maillage issu de l'application de la méthode des caractéristiques en approximant la partie amont du corps (jusqu'en $x/L = 0.07$) à une partie purement conique sur laquelle on applique l'approche de Taylor & Maccoll. Par la méthode des caractéristiques, on retrouve bien la **courbure progressive du choc** à mesure que l'on s'éloigne de la pointe du corps (typiquement pour $0.4 < x/L < 0.6$). De plus, l'évolution de la pression à la paroi du corps n'est pas monotone, ce qui est corroboré par les résultats de l'expérience. Ceux-ci sont en effet très bien reproduits par le modèle théorique, comme illustré en figure 23(b) pour deux maillages de densité différentes ($N = 10$ et $N = 50$) pour lesquels la longueur de la pointe approchée par un cône est modifiée ($x/L = 0.07$ et x/L =0.02). La pression à la paroi est représentée ici sous la forme d'un coefficient de pression C_p défini par l'équation (5) :

$$C_p = \frac{p - p_1}{\frac{1}{2}\rho_1 U_1^2} = \frac{2}{\gamma M_1^2}\left(\frac{p}{p_1} - 1\right) \tag{5}$$

avec p la pression pariétale, p_1 la pression statique - et M_1 le nombre de Mach de l'écoulement

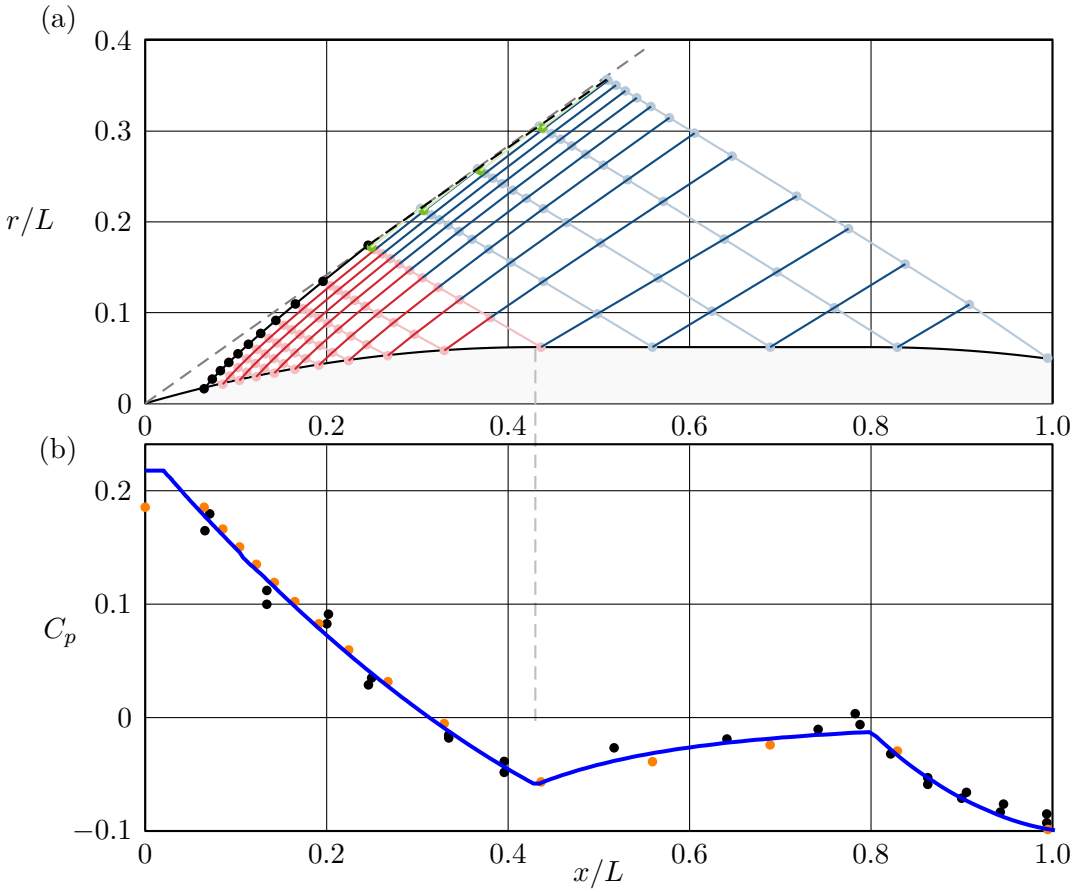

FIGURE 23 – Maillage issu de l'application de la méthode des caractéristiques au corps A4V1P pour $M_1 = 1.87$ et $N = 10$ (a) ; évolution axiale du coefficient de pression à la surface du corps (b) - résultats de Isenberg (•), résultats obtenus ici pour le maillage présenté en (a) (•) et pour $N = 50$ (—)

- en amont de la sonde. Ainsi la valeur C_p=0 correspond à un point de la paroi de la sonde où la pression est égale à la pression statique amont.

Sur la figure 23(b), l'évolution axiale de la pression pariétale est non-monotone, ce qui peut être contre-intuitif d'autant que d'autres grandeurs caractéristiques du problème, comme l'inclinaison de la paroi ou la distance entre choc et paroi du corps, ont quant-à-elles une évolution monotone. Toutefois, le rayon de courbure du corps a une évolution discontinue à la traversée du point de raccord entre la partie ogivale du corps et la partie cylindrique ($x/L = 0.43$) ; le brutal changement de courbure ainsi imposé à l'écoulement à la paroi, et par extension à l'ensemble de l'écoulement, impose le changement de monotonie de la pression à la paroi. On peut noter que C_p croît à partir de $x/L = 0.43$ mais reste négatif jusqu'à l'extrémité aval de la partie cylindrique du corps, située environ à 6.5 diamètres de corps en aval de la pointe. Prolonger la partie cylindrique de ce corps permettrait de faire tendre progressivement C_p vers 0. Cette forme de corps permettrait donc de constituer une sonde de pression statique à condition que la compacité de la sonde ne soit pas un critère de premier ordre.

Sondes de pression statique

Pour conclure cette partie, on applique la méthode décrite ci-avant à la sonde de pression bi-conique avec raccord ogival (figure 20(b)) avec pour objectif de déterminer la distribution de pression à la paroi de la sonde pour différentes valeurs de M_1 entre 1.15 et 1.5. Cette nouvelle géométrie présente de fortes similarités avec celle du paragraphe précédent ; on peut la voir comme un cas où l'on aurait cherché, plutôt qu'un arrière corps cylindrique, à imposer un arrière corps conique dont l'ouverture angulaire permettrait une remontée asymptotique de C_p à la paroi vers une valeur légèrement positive, le plus près possible du nez de la sonde. La figure 24 fournit un exemple de maillage issu de l'application de la méthode des caractéristiques, ainsi que l'évolution de C_p à la paroi avec la coordonnée axiale x pour différentes valeurs du Mach amont M_1. On trouve qu'il existe une zone de la sonde pour laquelle $C_p \approx 0$, typiquement située entre $x = 4.6$ mm et $x = 5.1$. La **position des alésages** effectués sur la sonde réelle ($x = 4.7$ mm) est donc **satisfaisante vis à vis de ces résultats**. On peut, en complément, s'interroger sur la sensibilité de ce résultat à la forme du raccord C^1 entre les deux parties coniques de la sonde. En effet, comme l'usinage de cette partie est certainement plus difficile à réaliser que l'usinage des parties coniques, on peut s'attendre à ce que cette partie de la géométrie de la sonde réelle soit différente du plan. Il peut donc être intéressant d'étudier différentes formes pour ce raccord. On montre donc en figure 25 l'évolution axiale du coefficient de pression pariétale C_p pour différentes géométries de raccord, s'effectuant autour d'un point fixe de coordonnée axiale $x = 2.7$mm et d'étendue variable allant de 0.1 mm à 1mm. Ces tracés sont fournis pour $M_1 = 1.15$ et $M_1 = 1.5$. On constate que plus l'envergure axiale du raccord est grande, plus la position axiale pour laquelle C_p revient à zéro est située en aval ; cela étant, ce décalage axial reste de faible amplitude puisqu'il correspond à 0.5mm au maximum entre les différents cas étudiés. Ce résultat est plutôt rassurant, puisque le micro-usinage des sondes de pression réalisées pour le Laboratoire est une opération complexe dont la précision est difficile à évaluer (les valeurs présentées en figure 20 étant théoriques). Les conclusions obtenues ici sont donc de nature à attester de la robustesse de la mesure de pression statique dans un écoulement uniforme ; l'utilisation de ces sondes dans les jets sous-détendus [7, 67] a toutefois montré que la position effective de la mesure correspondait en réalité à la position de la prise de pression sur le corps de sonde plutôt que la position de la pointe de sonde. La détermination de la pression pariétale sur ces sondes dans un écoulement non-uniforme, présentant par exemple un gradient axial constant pour M, permettrait de confirmer ce constat expérimental.

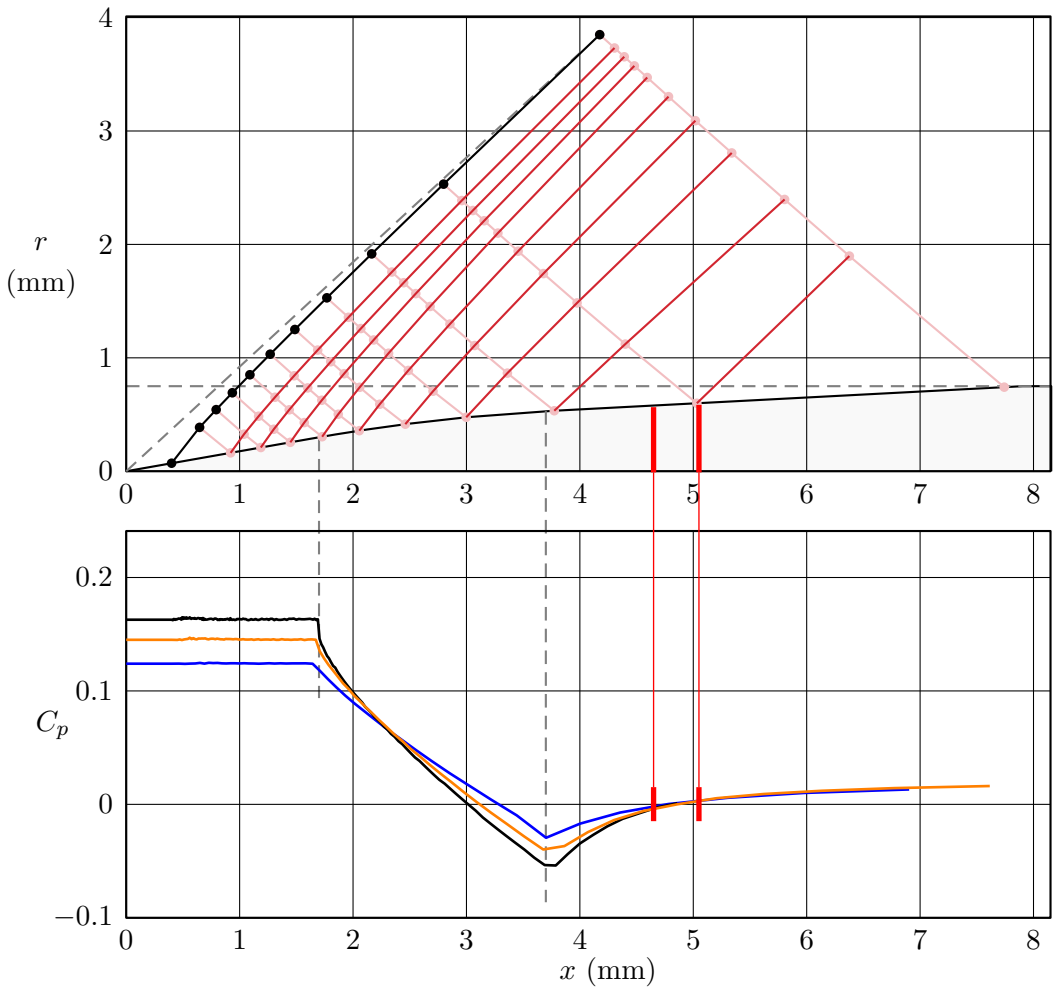

FIGURE 24 – Illustration de la géométrie de sonde et du maillage (N=10, M_1=1.5) issu de l'application de la méthode des caractéristiques à la sonde de pression statique présentée en Figure 20(b) et évolution axiale du coefficient de pression à la surface de la sonde (b), pour trois valeurs différentes de M_1 : 1.15 (—), 1.25 (—) et 1.5 (—) et $N \geq 50$. Les limites de la section de raccord entre la pointe conique de la sonde ($x \leq 1.7$ mm) et la deuxième portion conique ($x \geq 3.7$ mm) sont indiquées par les lignes discontinues verticales. La zone pour laquelle $C_p \approx 0$ est limitée par des segments verticaux.

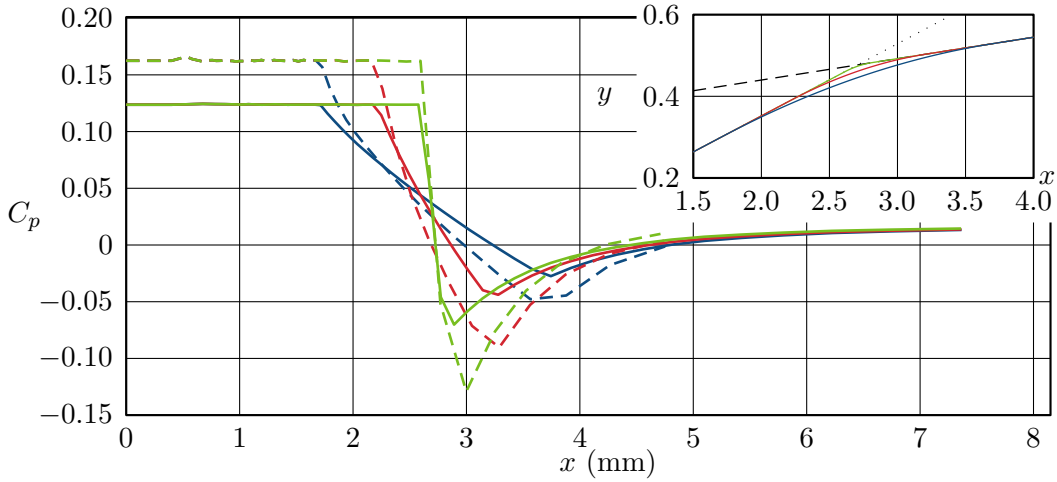

FIGURE 25 – Évolution axiale de C_p à la surface de la sonde de pression (type Figure 20(b)) pour deux valeurs différentes de M_1 : 1.15 (trait discontinu) et 1.5 (trait continu) et trois raccordements différents entre les deux sections coniques, d'envergure axiale 0.2 mm (—), 1 mm (—) et 2 mm (—) tels qu'illustrés dans l'insert

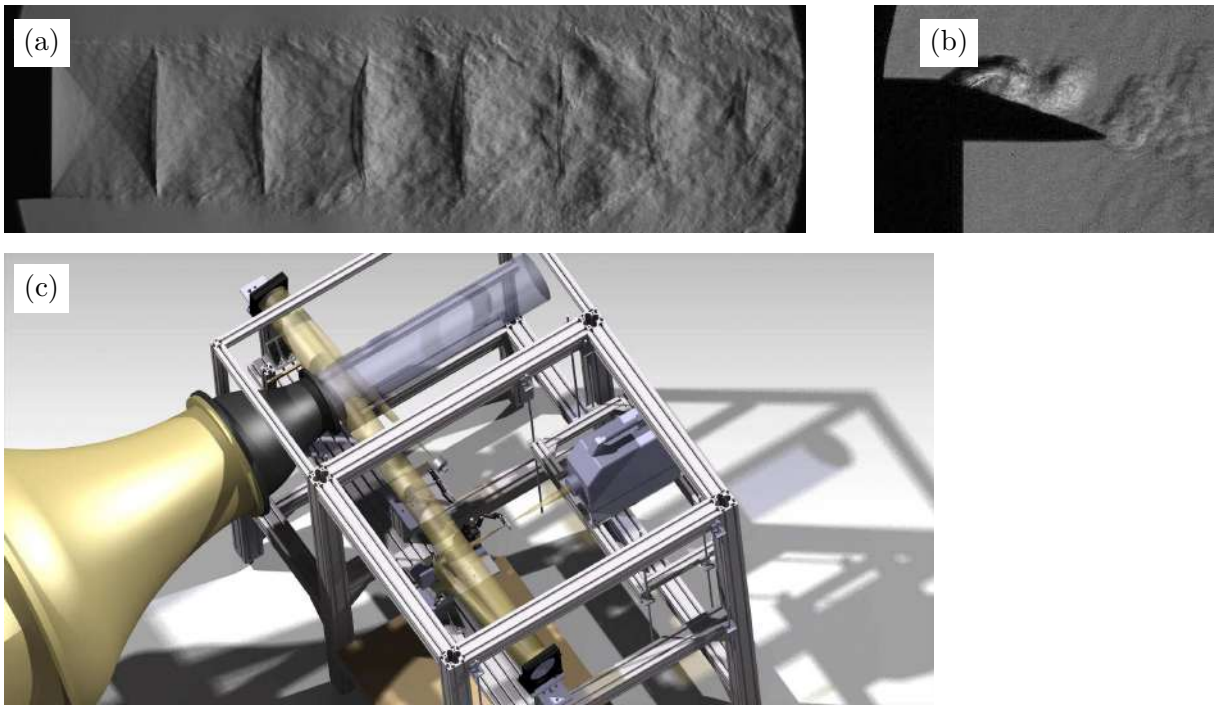

FIGURE 26 – Illustrations de visualisations schlieren réalisées au Laboratoire depuis 2010 ; Jet sous-détendu $M_j = 1.15$ (a), contrôle du sillage d'une maquette de poids lourd par jet pulsé - de CO_2 - placé à proximité du volet situé à l'arrière de la remorque (b). Montage schlieren employé sur la soufflerie d'études en intégrant les contraintes d'encombrement optique et de réglage fin de la position d'une caméra rapide (stage IUT **R.Blanc**) (c).

4.3.2 Exploitations quantitatives de visualisations schlieren

Les techniques d'ombroscopie ou de strioscopie reposent sur l'éclairage d'un milieu optiquement transparent (ici un gaz) par un faisceau de lumière d'orientation connue. La réfraction de la lumière en raison de l'inhomogénéité de l'indice optique du gaz, lié à la masse volumique tel qu'illustré par la relation de Gladstone-Dale (6), est exploitée pour former une image représentative de ces disparités [68, 33, 53] :

$$n - 1 = \kappa\rho \tag{6}$$

avec n indice optique, ρ masse volumique du gaz considéré, et κ la constante de Gladstone-Dale dont la valeur pour l'air est typiquement 0.23 $cm^3.g^{-1}$.

On peut exploiter cette relation pour caractériser expérimentalement, tel qu'illustré en figure 26, des phénomènes liés à la compressibilité du milieu (écoulements rapides, propagation d'ondes de choc) ou apparaissant alors que le milieu peut être considéré incompressible. Dans le premier cas, c'est la nature compressible du phénomène qui impose des modifications de masse volumique ρ, comme pour le jet de la figure 26(a) ; dans le deuxième, on peut introduire une inhomogénéité de masse volumique en chauffant localement ou en utilisant un mélange de gaz d'indices optiques très différents (Air et CO_2 par exemple, comme dans le cas de la figure 26(b) issue de la thèse de **S.Chaligné** [18]).

Pour illustrer l'ordre de grandeur des modifications mises en jeu pour n, on peut considérer d'abord un jet d'air à Mach $M_j = 0.9$. Pour les conditions habituelles d'utilisation de la soufflerie anéchoïque (température totale proche de 300K, température ambiante proche de 293 K), la masse volumique ρ_j dans le cone potentiel de l'écoulement est proche de 1.35 kg.m^{-3}. La variation relative d'indice optique entre l'intérieur et l'extérieur du jet est d'environ 0.004%. Pour un jet d'air à Mach $M_j = 1.55$, ce qui correspond aux conditions génératrices les plus élevées pour la soufflerie anéchoique du Laboratoire, cette variation relative atteint 0.01%. Sachant cette très faible valeur, due à la faible valeur de κ, on ne peut que souligner la performance des techniques d'ombroscopie/strioscopie pour accéder à des visualisations très détaillées de phénomènes complexes. Au Laboratoire, depuis 2010, j'ai contribué à l'utilisation de cette technique de visualisation en vue d'une exploitation quantitative des résultats dans les applications listées ci-après, souvent associées à des contraintes spécifiques d'encombrement pour lesquelles des montages adaptés ont été proposés (figure 26(c)) :

- Évaluation des fluctuations de densité dans le sillage d'un barreau chauffé placé dans un écoulement, avec pour objectif la comparaison quantitative du spectre de fluctuations de niveaux de gris de la séquence d'images enregistrée à celui des fluctuations de densité mesurée par diffusion Rayleigh [52],
- Propagation d'ondes de choc dans un milieu au repos, identification du profil de densité moyen (N-wave) et détermination de l'existence d'un pied de Mach resultant de l'interaction des ondes de choc à proximité d'une surface solide dans le cas d'ondes d'amplitude faible [36],
- Identification de l'interaction entre jets compressibles parallèles à faible Re (diamètre de l'ordre du millimètre) et de l'influence des conditions génératrices sur cette interaction (thèse de P.Laffay),
- Évaluation de la vitesse de convection de la turbulence dans la couche de cisaillement d'un jet compressible, dont la valeur est une donnée d'entrée de modèles physiques de sources de bruit de jet,
- Mesure du Mach local dans la zone supersonique d'un jet sous-détendu, par analyse directe d'images strioscopiques.
- Oscillations de la structure de cellules de choc pour un jet sous-détendu avec screech.

Pour rester concis, je choisis de ne présenter ici que les trois derniers points de cette liste, qui sont aussi ceux pour lesquels mon implication est la plus significative.

4.3.2.1 Évaluation de la vitesse de convection dans un jet compressible

En couplant un système schlieren classique à une caméra à haute fréquence d'acquisition, qui peut être fixée à une valeur comprise entre une dizaine et plusieurs centaines de kHz pour les modèles actuellement disponibles au Laboratoire (Photron SAZ et Phantom V12), il est possible d'effectuer des visualisations strioscopiques à une cadence suffisante pour **suivre la convection de la turbulence** dans la **couche de cisaillement d'un jet compressible** à

un nombre de Mach M_j de l'ordre de 1. Il est donc ainsi envisageable d'évaluer certaines caractéristiques des phénomènes en jeu, comme la **vitesse de convection de la turbulence** dans la couche de cisaillement d'un jet. Une méthode expérimentale communément utilisée s'appuie sur deux sondes fournissant l'évolution temporelle de grandeurs liées à l'écoulement en deux points distincts d'une couche de cisaillement (LDV [38], strioscopie [83], Optical Deflectometry (OD) [45, 23] reposant sur le principe de réfraction de la lumière tout comme la strioscopie, diffusion Rayleigh [58]) ; on évalue la phase de l'interspectre entre deux signaux qui permet d'évaluer l'évolution fréquentielle de la vitesse de convection. L'étude des corrélations spatio-temporelles dans la couche de cisaillement, par PIV rapide notamment [82], fournit quant à elle une estimation de la vitesse de convection moyenne, sans prise en compte de sa dépendance fréquentielle. La vitesse de convection de la turbulence est intrinsèquement un paramètre de première importance dans la **modélisation** de certaines **sources de bruit** (screech [63], BBSAN [32]) ; sa détermination précise est à ce titre intéressante, en particulier en cas d'effet de vol où l'influence de l'écoulement externe sur la fréquence du screech par exemple n'est pas facilement quantifiable.

La technique dont on propose d'étudier les résultats ici est la méthode schlieren, mais on aurait tout aussi bien pu employer la technique d'OD qui repose sur les mêmes principes physiques [39]. La visualisation schlieren a pour avantage, par rapport aux techniques PIV, LDV ou autres méthodes optiques avancées, une simplicité de mise en œuvre qui encourage son utilisation ; il est toutefois délicat de déterminer ses performances dans la détermination expérimentale de la vitesse de convection de la turbulence uniquement à partir des résultats expérimentaux.

Pour illustrer ce point, on s'appuie ici sur des résultats expérimentaux, illustrés en figure 27(a), obtenus sur un jet sous-détendu à M_j=1.50 ($Re_D \approx 2 \times 10^6$) à partir d'une séquence de 5.2 $\times 10^5$ images schlieren successives enregistrées à une fréquence d'acquisition d'environ 430 kHz. La phase de l'interspectre entre deux points situés de part et d'autre d'un point de référence situé en $r = D/2$ et au milieu de la troisième cellule de choc est présentée en figure 27(b). On déduit de ces quantités une estimation de la vitesse de convection de la turbulence à ce point de la couche de cisaillement. On constate que l'**estimation de cette vitesse de convection** fournit des **résultats significativement différents** selon la **distance ente les 2 points sonde utilisés**, ce qui n'est pas satisfaisant d'un point de vue métrologique. Plus la distance entre les deux points de mesure est grande et plus la vitesse de convection est élevée, pour une fréquence donnée. Ce biais a déjà été remarqué dans de précédentes études (e.g. [80]) sans que sa cause ne soit établie. Parmi les questions possibles à ce sujet, on peut se demander si ce biais est lié au fait que les données utilisées pour le traitement statistique soient liées aux gradients de densité ou s'il s'agit d'un effet de l'intégration spatiale des gradients de densité le long du chemin optique.

Pour aller plus loin, nous avons proposé une approche originale sur la base des résultats de simulations numériques de jets à $Re_D \approx 10^5$, subsonique ou supersonique, réalisées par **C.Bogey** et **R.Gojon**. L'idée est de **générer** une suite d'**images schlieren synthétiques** à partir du champ de densité instationnaire issu de la simulation, en intégrant les déviations subies par les rayons lumineux traversant le volume occupé par l'écoulement. On reproduit ainsi le même type d'images que celles que l'on peut obtenir expérimentalement, en tenant compte du caractère

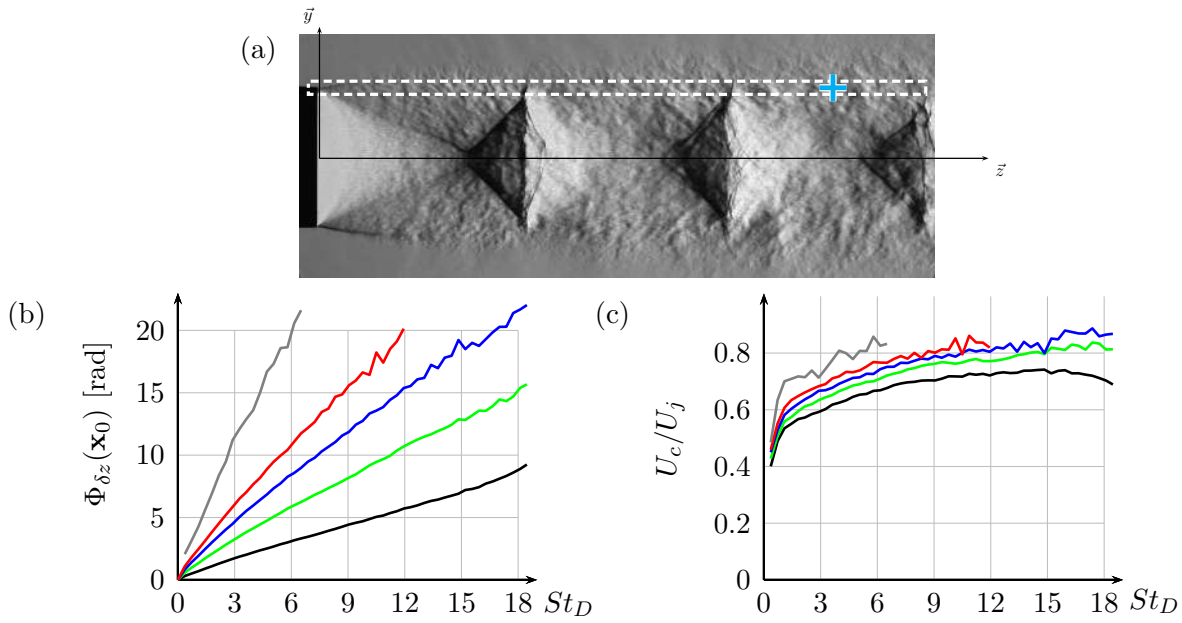

FIGURE 27 – Visualisation d'un jet sous-détendu à $M_j = 1.50$, avec illustration de la zone de couche de cisaillement supérieure sur laquelle les acquisitions à haute cadence ont été effectuées (traits discontinus blancs) ; strioscopie avec couteau perpendiculaire à l'axe du jet (a) Phase de l'interspectre entre deux points situés de part et d'autre du point de référence et distants de $2\delta z$, pour $\delta z/D = 0.055$ (—) 0.11 (—) 0.165 (—) 0.22 (—) 0.44 (—) (b) ; Vitesse de convection déduite de la phase de l'interspectre avec la même légende pour δz (c).

intégrateur de la méthode, cumulant les changements d'orientation des rayons lumineux tout le long du chemin optique. On peut ensuite appliquer à ces images les techniques de traitement de signal employées habituellement sur les mesures. L'avantage de cette approche est que l'on dispose d'une solution de référence pour la vitesse de convection, évaluée directement à partir des caractéristiques de l'écoulement lui-même (densité ou composante de vitesse). Une première approche a porté sur les données de simulation réalisée sur un jet à $M_j = 1.55$ avec un maillage cylindrique autour de l'axe du jet et comprenant 512 points dans la direction azimuthale. En figure 28, une illustration extraite de [16] montre le type d'images ainsi générées, en comparaison d'images ayant été obtenues expérimentalement à $Re \approx 10^6$. La différence d'un ordre de grandeur entre ces valeurs de Re se traduit par une différence de finesse des structures turbulentes visibles sur les images ; les caractéristiques symptomatiques des différents réglages optiques possibles sont néanmoins bien retrouvées sur les images synthétiques, de même que les caractéristiques physiques de l'écoulement (structure de cellules de choc, cohérence azimuthale des structures turbulentes dans les premiers stades de développement de la couche de cisaillement). Pour accroître la durée du signal disponible, on génère ici environ 100 images par pas de temps, en faisant virtuellement tourner l'axe optique du système schlieren synthétique, restant perpendiculaire à l'axe du jet, autour du jet. Cela revient à imaginer disposer de 100 systèmes schlieren à haute cadence indépendants et synchrones, ce qui est un luxe expérimentalement inaccessible (les systèmes BOS utilisant jusqu'à une douzaine de caméras sont sans doute les configurations expérimentales ayant employé le plus de caméras simultanément [57]), qui vient compenser le fait que les signaux temporels issus de la simulation numérique sont usuellement plus courts que leurs équivalents issus de mesures d'un facteur au moins 100 (en raison des coûts de calcul d'une part et des très bonnes performances en mémoire vive des systèmes d'acquisition utilisés). Une fois tous les pas de temps traités, on dispose ainsi de 100 séquences supposées indépendantes d'images schlieren successives ; pour chacune de ces séquences, on extrait les signaux temporel en 2 points choisis et le calcul de phase d'interspectre peut être effectué. Le résultat est enfin moyenné sur l'ensemble des séquences disponibles. L'application de cette procédure aux **résultats de simulation numérique** d'un jet à $M_j = 1.55$ [16] ou d'un jet à $M_j = 0.9$ (stage M1 d'**I.Kurek**) fournit une **estimation de la vitesse de convection** présentant des **caractéristiques similaires** dans les deux cas tels que représentées sur la figure 29. L'évaluation de U_c à partir du signal de densité est indépendante de l'espacement entre les points sondes (figure 29(a)). La seule différence entre les résultats obtenus pour plusieurs espacements est la fréquence maximale au-delà de laquelle les signaux sont trop décorrélés pour que la phase de l'interspectre soit exploitable ; ce seuil de fréquence évolue pratiquement comme l'inverse de la distance entre les points sondes. L'**évaluation de** U_c à partir des images schlieren (figure 29(b)) est quant à elle **très nettement dépendante de la distance entre les points sondes** δz ; elle augmente avec δz, comme dans les mesures issues des résultats expérimentaux (figure 27). De plus, en prenant pour référence le résultat obtenu avec le signal de densité, U_c peut être sur-estimée pour les plus grandes valeurs de δz testées ou sous-estimée pour les plus petites valeurs de δz étudiées. En conclusion, on sait donc pour l'heure reproduire à partir de données numériques ce qui a été constaté expérimentalement, mais il reste à interpréter ce phénomène en identifiant ses causes.

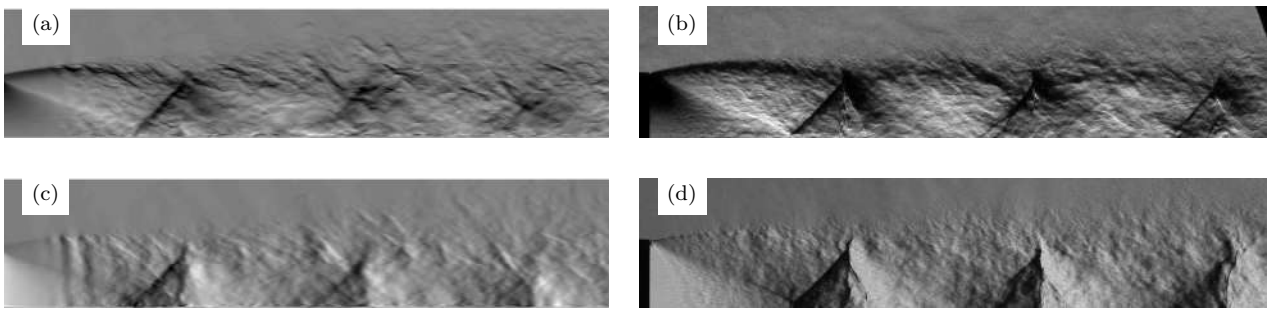

FIGURE 28 – Illustration des images schlieren synthétiques, obtenues à partir d'une simulation de jet à $M_j = 1.55$ [28] et pour un réglage optique (position du couteau) permettant une sensibilité au gradient de densité vertical (a) et horizontal (c) en comparaison d'images obtenues en soufflerie avec des réglages optiques similaires (b, d).

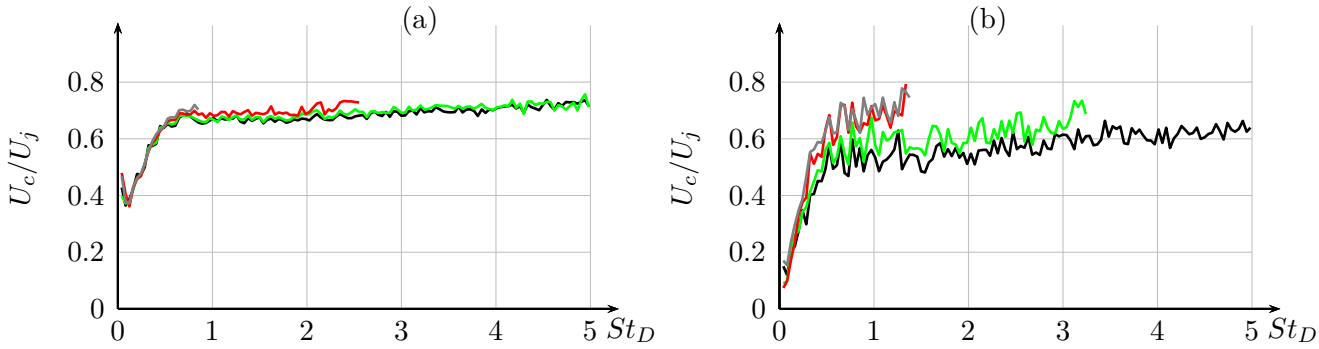

FIGURE 29 – Évaluation de la vitesse de convection U_c à partir des données de simulation numérique (jet à M_j=0.9), au point de coordonnées $r = 0.45D$ et $z = 3.5D$ et pour différents espacements de points sonde autour du point de référence : $\delta z/D = 0.059$ (—), 0.118 (—), 0.236 (—), 0.354 (—). Pour cette évaluation, on a utilisé la densité (a) ou les images schlieren (couteau perpendiculaire à l'axe du jet) générées à partir de la simulation (b).

4.3.2.2 Mesure du Mach local dans un jet sous-détendu

Durant la thèse de B.André, différentes techniques de mesure élaborées (LDV, PIV, sondes de pression) ont été mises en œuvre. Leur exploitation a notamment permis de préciser la structure du champ moyen de vitesse et de pression dans les jets sous-détendus [1, 7]. À l'issue de cette étude, nous nous sommes interrogés sur l'existence d'une méthode 'simple' de mesure permettant la **mesure du nombre de Mach local dans un jet supersonique**, en complément des mesures précédentes ; la 'simplicité' de cette méthode résiderait dans sa mise en œuvre pratique et dans l'exploitation des résultats obtenus (par exemple, pas de particules pour éviter l'effet de leur inertie). L'étude des écoulements coniques exploités précédemment pour le développement des sondes de pression statique a donné l'idée d'appliquer une méthode expérimentale certainement bien connue des collègues de combustion, et dont une application proche est mentionnée notamment dans [40] où elle est appliquée à une flamme supersonique. Elle consiste à placer un objet conique dans l'écoulement supersonique étudié ; si le nombre de Mach de l'écoulement (supposé homogène) M_1 en amont de la sonde est suffisant, il se développe à partir de la pointe du cône un choc oblique dont l'angle avec l'axe du cône dépend uniquement de M_1. En mesurant cet angle (système strioscopique), on peut donc réciproquement **obtenir la valeur de M_1 pour une géométrie de sonde connue**. C'est ce qui a été effectué ici dans le cas de jets supersoniques sous-détendus, pour lesquels la condition d'homogénéité de l'écoulement n'est pas satisfaite. On souhaite ici illustrer la performance de la méthode après avoir rappelé les conditions de mesure.

Une sonde en acier de corps cylindrique (diamètre 5 mm) comporte une extrémité usinée au Laboratoire pour former une partie conique. La demi-ouverture angulaire δ du cône, mesurée par projeteuse de profil, est de $14.83° \pm 0.22°$ et l'épaisseur de la pointe évaluée à 0.1 mm. Cette sonde est maintenue dans l'écoulement par un porte-sonde de profil triangulaire d'ouverture angulaire de 27° et dont la base est de 10 mm. L'ensemble est positionné sur un chariot de déplacement permettant des translations selon l'axe du jet, et présenté face à l'écoulement, en sortie de tuyère C38. Le calage angulaire pour limiter l'inclinaison du cône par rapport à l'écoulement est effectué en maximisant la symétrie des motifs attachés à la pointe de la sonde et vus par strioscopie. Le montage striscopique est solidaire du chariot de déplacement, de telle sorte que la pointe de la sonde se trouve à une position fixe de l'image ; on note par ailleurs x_p la distance axiale entre la pointe du cône et la sortie de tuyère. Pour l'ouverture angulaire du cône utilisé, et selon le modèle de Taylor & Maccoll, le **nombre de Mach minimum** $M_1 = M_i$ de l'écoulement incident pour qu'un choc oblique soit attaché à la pointe de la sonde est $M_i = 1.11$.

On présente à titre d'exemple en Figure 30 une visualisation de l'écoulement autour du cône sur laquelle quelques résultats issus du modèle de Taylor & Maccoll sont reportés en supposant que le nombre de Mach de l'écoulement devant la pointe du cône est $M_1 = 1.53$. L'image fait clairement apparaître le développement du choc depuis la pointe du cône, et l'état de surface permet la visualisation de lignes de Mach se développant depuis la surface du cône. **Le choc émanant de la pointe du cône** a une **inclinaison qui est bien prédite** par le modèle théorique ; toutefois, il n'est pas purement rectiligne, ce qui est une probable conséquence de l'inhomogénéité de l'écoulement dans la direction transverse. De plus, à partir du tracé de

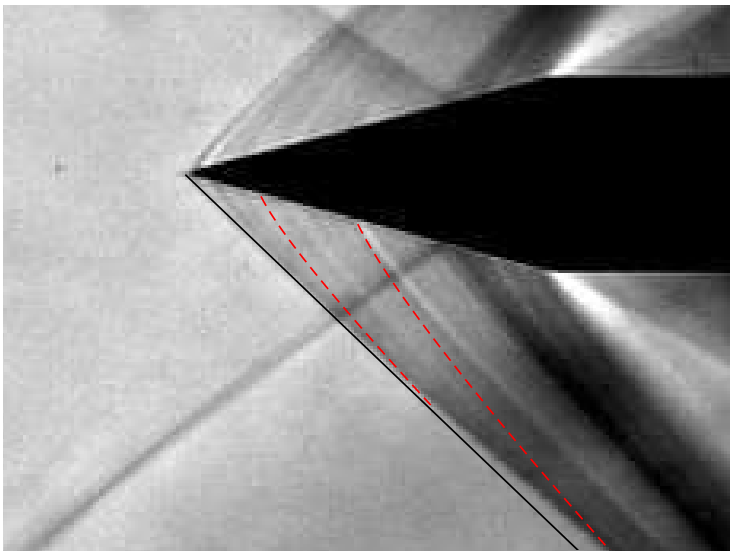

FIGURE 30 – Visualisation strioscopique de la zone de l'écoulement à proximité de la pointe du cône. Illustration des lignes de Mach (- - -) et de l'angle de choc (——) tels que prédits par la théorie de Taylor & Maccoll pour un écoulement incident homogène.

deux lignes de Mach théoriques, on constate que celle qui est la plus proche de la pointe du cône est celle qui suit le mieux la strie observée au même endroit. Pour améliorer l'accord avec ces résultats expérimentaux, une mise en œuvre de la méthode des caractéristiques dans laquelle on tiendrait compte des gradients moyens du nombre de Mach serait intéressante ; placer la sonde conique dans un écoulement parfaitement détendu et pratiquement uniforme (jet à $M_j = M_d$ correspondant à la figure 6(c)) fournirait également une validation complémentaire de l'approche.

Des acquisitions effectuées pour $M_j = 1.35$ sont présentés sur la figure 31, pour différentes valeurs de x_p. Dans certains cas, le choc est très courbé (par exemple Figure 31(b)), ce qui signifie que le nombre de Mach de l'écoulement est très proche de M_i ou que l'écoulement est très inhomogène. On se concentre donc pour cette étude sur les visualisations pour lesquelles le choc est attaché à la pointe de sonde. La figure 32(b) donne une idée des échelles mises en jeu pour cette analyse graphique ; la résolution spatiale, moyenne sur ces images, pourrait être améliorée à présent suite à un travail effectué pour la thèse de P.Laffay sur l'augmentation du grandissement optique du système schlieren. Sur ces images, on relève l'inclinaison du choc à proximité immédiate de la pointe du cône. En réalité, on relève non pas une valeur, mais un intervalle de valeurs jugées admissibles pour l'angle de choc σ. L'intervalle ainsi établi est traduit en **un intervalle de valeurs possibles pour** M, par l'intermédiaire de la courbe de calibration $M_1 = \mathcal{F}(\sigma)$ donnée en figure 32(a). Les résultats ainsi obtenus sont reportés en Figure 33, et peuvent y être comparés à la valeur de M traduite de mesures LDV effectuées dans le même jet [1], pour trois valeurs différentes de M_j. La comparaison entre ces résultats appelle différents commentaires. En premier lieu, le seuil $M_i = 1.11$ est représenté en Figure 33, où l'on constate qu'une zone axiale de l'écoulement - d'étendue limitée pour $M_j = 1.35$,

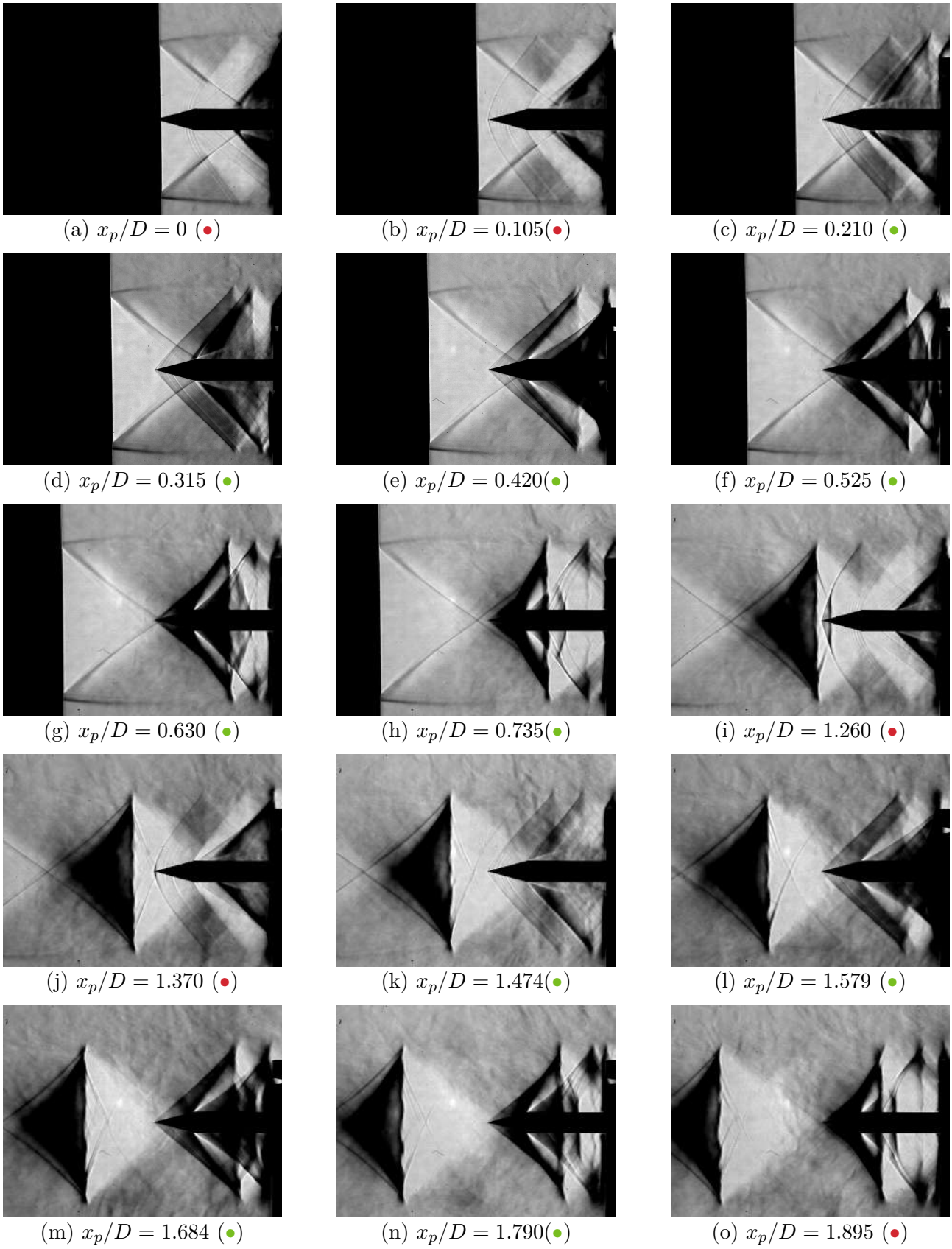

(a) $x_p/D = 0$ (●) (b) $x_p/D = 0.105$(●) (c) $x_p/D = 0.210$ (●)

(d) $x_p/D = 0.315$ (●) (e) $x_p/D = 0.420$(●) (f) $x_p/D = 0.525$ (●)

(g) $x_p/D = 0.630$ (●) (h) $x_p/D = 0.735$(●) (i) $x_p/D = 1.260$ (●)

(j) $x_p/D = 1.370$ (●) (k) $x_p/D = 1.474$(●) (l) $x_p/D = 1.579$ (●)

(m) $x_p/D = 1.684$ (●) (n) $x_p/D = 1.790$(●) (o) $x_p/D = 1.895$ (●)

FIGURE 31 – Visualisation de chocs induits par la sonde conique dans le jet ($M_j = 1.35$) en sortie de tuyère C38. Les images exploitables pour estimer le nombre de Mach local sont indiquées par le symbole (●) ; celles considérées inexploitables sont repérées par le symbole (●).

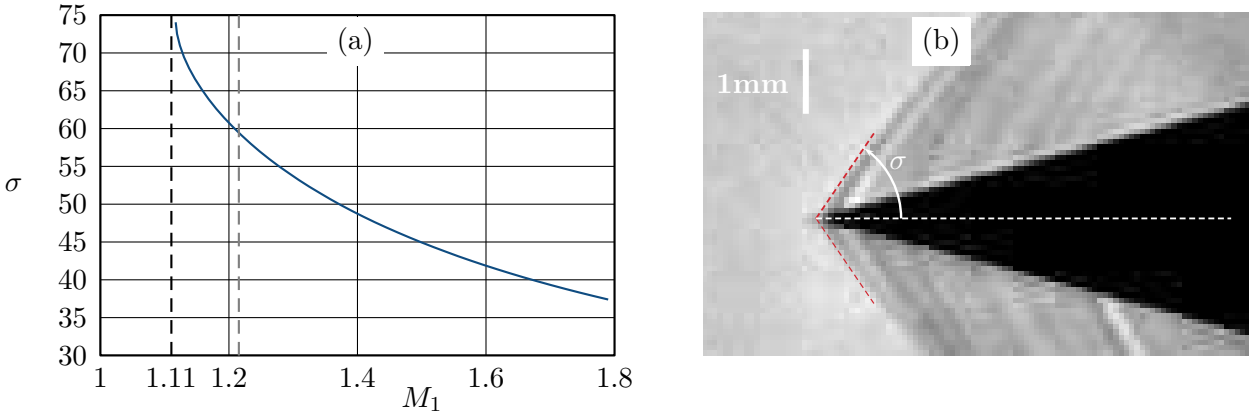

FIGURE 32 – Évolution de σ, angle du choc attaché à un cône de demi-ouverture angulaire $\delta = 14.83°$, avec M_1 (a) ; Vue grossie à proximité de la pointe du cône et matérialisation de l'angle de choc à la pointe du cône (ici $\sigma = 55°$) (b).

plus conséquente pour $M_j = 1.15$ et 1.5 - échappe à la mesure parce que le nombre de Mach local est inférieur à M_i. On peut remarquer que des **essais complémentaires avec un cône d'ouverture adaptée aux petites valeurs de** M permettraient de compléter les points manquants (et fourniraient en outre une nouvelle évaluation indépendante pour tous les points de mesure où M est plus élevé). De plus, les résultats donnés par le cône dévient fortement de ceux qu'offre la LDV en fin de zone de détente, et qui plus est autour du disque de Mach pour le cas $M_j = 1.5$. Dans ce dernier cas, on peut supposer que lorsque la pointe du cône est située en amont du disque de Mach et que la partie aval du cône est située dans la zone subsonique en aval du disque de Mach, l'hypothèse d'un écoulement conique supersonique soit remise en cause. Plus généralement, une limitation intrinsèque de la méthode réside dans sa sensibilité décroissant avec M. Ceci est clairement visible sur la courbe $\sigma = \mathcal{F}(M_1)$ présentée en Figure 32(a). Si σ diminue et si l'incertitude sur l'évaluation σ est constante, l'intervalle des valeurs possibles pour M augmente. À nouveau, adapter l'ouverture angulaire du cône aux valeurs de M à mesurer permettrait de contourner cette contrainte. Enfin, dans les plages de l'écoulement où la mesure avec le cône actuel est possible dans de bonnes conditions, l'**accord entre l'estimation de** M **par la visualisation liée au cône** et **celle par obtenue par anémométrie laser doppler** (LDV) est relativement **bon**.

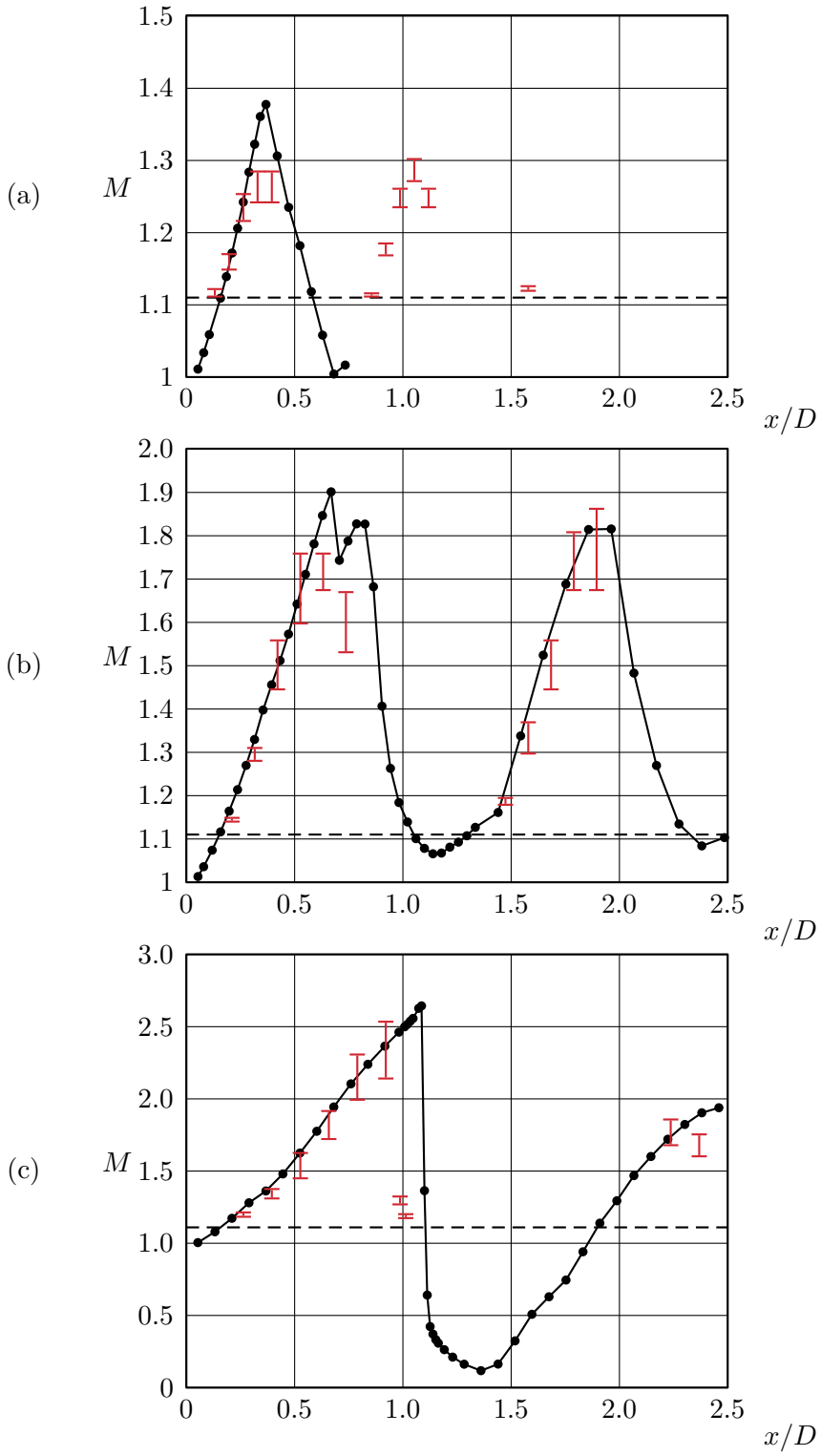

FIGURE 33 – Nombre de Mach local M sur l'axe du jet, en fonction de x/D. (•) Mesures LDV ; (I) résultats issus de la visualisation intégrant l'incertitude sur la détermination de l'angle du choc ; (- - -) seuil correspondant à $M_i = 1.11$. (a) $M_j = 1.15$, (b) $M_j = 1.35$ et (c) $M_j = 1.50$.

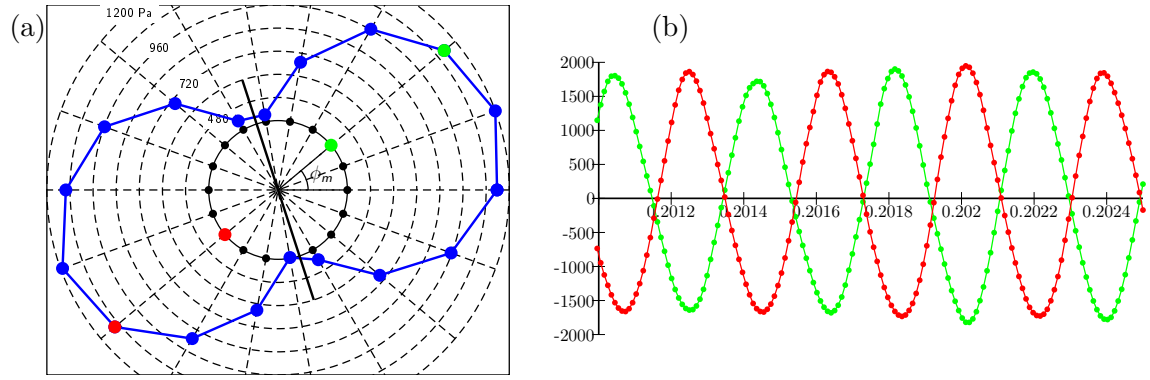

FIGURE 34 – Pression acoustique mesurée sur une antenne azimutale placée en champ proche, pour un jet sous-détendu à $M_j = 1.50$; (a) valeurs efficaces de la pression acoustique pour les différents microphones de l'antenne azimutale, (b) signaux temporels issus de deux microphones diamétralement opposés sur l'antenne (correspondant sur la fig.(a) à $\phi_m = 40°$ (●) et 220° (●).

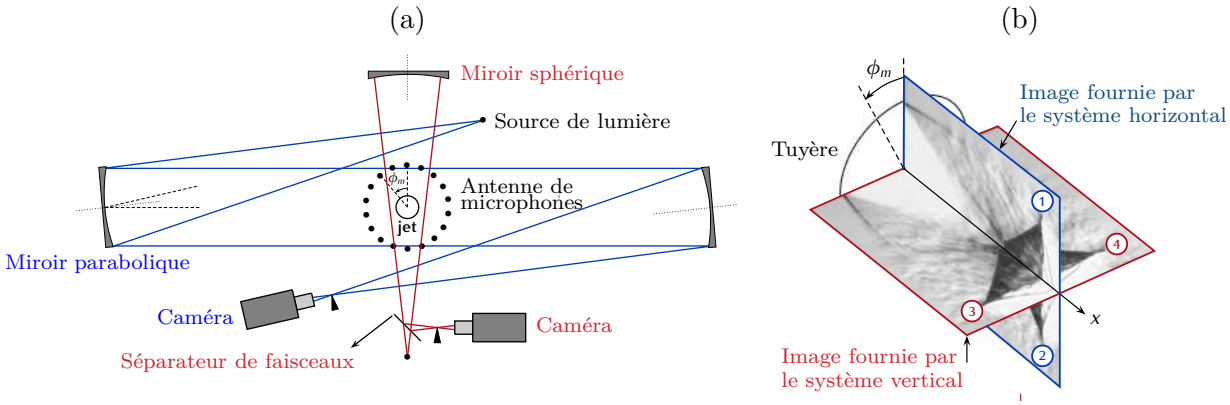

FIGURE 35 – Montage expérimental impliquant deux systèmes strioscopiques croisés (a) ; Application à un jet sous-détendu à $M_j = 1.50$ (b).

4.3.2.3 Oscillations de la structure de cellules de choc avec screech

Pour un jet sous-détendu axisymétrique, le champ acoustique associé au **screech** - s'il existe - est marqué par différents modes en fonction du M_j [64, 77], comme rappelé au paragraphe 4.1.3. La transition entre deux modes est obtenue pour des valeurs spécifiques du M_j qui peuvent dépendre des caractéristiques de l'installation expérimentale utilisée [65] ; dans notre étude, pour M_j autour de 1.50, le **mode obtenu, noté** b, a pour caractéristique un **plan de symétrie contenant l'axe du jet**. Une illustration de ce résultat est fournie en figure 34. La distribution des valeurs efficaces de pression acoustique mesurée par 18 microphones d'une antenne azimutale positionnée sur la tuyère montre la directivité azimutale du screech pour ce mode b. Il existe un plan de symétrie dans cette représentation, dont l'orientation azimutale est nominalement fixe. Le mécanisme physique à l'origine de la sélection de cette orientation n'est pas connu, et il n'est pas garanti que cette orientation soit fixe d'un enregistrement à l'autre. Une étude spécifique sur la répétabilité du positionnement de ce plan permettrait de conclure sur ce point, et l'in-

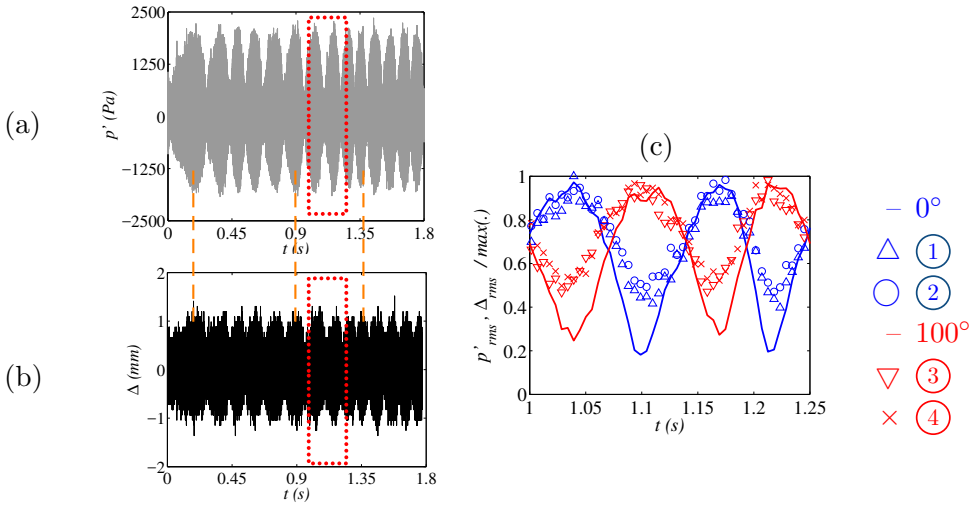

FIGURE 36 – Illustration de l'évolution temporelle de (a) la pression acoustique, (b) du déplacement axial de la pointe de choc (1) illustrée en Figure 35, dans le même plan $\phi_m = 0°$. Les bouffées visibles sur les signaux traduisent la rotation du plan d'antisymétrie ; ces bouffées apparaissent simultanément sur les deux type de signaux, ce qui traduit la synchronisation des phénomènes aérodynamiques dans le jet et l'acoustique liée au screech. (c) Evolution de la valeur rms (calculée typiquement sur $1/25^{\text{e}}$ de la période de rotation du plan d'antisymétrie) de la pression acoustique et du déplacement des pointes de chocs dans les plans $\phi_m = 0°$ et $\phi_m = 100°$.

troduction de micro-rugosités localisées en un point de la tuyère par exemple serait un moyen de déterminer si des facteurs environnementaux peuvent contribuer à fixer cette orientation ou éventuellement provoquer un basculement de mode. De plus, on constate en figure 34(b) que la pression acoustique en deux points diamétralement opposés est en opposition de phase, d'où le caractère *anti*-symétrique de ce mode b.

Au cours de la thèse de **B.André** [1], le lien entre la structure du champ acoustique dû au screech et le mouvement des cellules de choc dans le jet a été étudié. Pour cela, une méthode d'analyse quantitative de l'amplitude du mouvement des pointes choc sur la base de visualisations strioscopiques a été développée [3] et appliquée au cas d'un jet de Mach $M_j = 1.50$ [2]. Il s'est avéré nécessaire de développer un système de visualisation tel que les déplacements des chocs soient observés selon deux directions différentes, de telle sorte que l'on puisse **recomposer une vue 3D du comportement de la structure de cellules de choc**. Pour cela, on a employé de manière synchronisée l'antenne de microphones en champ proche acoustique mentionnée précédemment, et deux dispositifs schlieren, tels qu'illustrés sur la figure 35(a) issue de [4]. Chaque dispositif permet l'enregistrement d'une image contenant l'information de position axiale des deux pointes de choc que l'on peut y voir pour chaque cellule de choc. L'objectif est de comparer, dans un même plan azimutal ($\phi_m = \text{cste}$), l'amplitude du mouvement oscillatoire des pointes de choc à l'amplitude des fluctuations de pression acoustique liées au screech. On montre par cette approche, et en particulier dans le cas où le plan d'antisymétrie du mode b tourne lui-même autour de l'axe du jet (mode b dit instable), que le plan d'antisymétrie caractérisant la directivité azimuthale du screech est confondu avec un plan d'antisymétrie relatif au mouvement des chocs eux-mêmes. Il existe donc une corrélation claire entre ces deux phénomènes, comme illustré sur la Figure 36. L'existence du mode b instable et les grandeurs caractéristiques de cette instabilité (en particulier la fréquence de rotation du plan d'antisymétrie) sont du reste encore mal caractérisées et pourraient donner lieu à une étude approfondie.

4.3.3 Mesure de masse volumique par voie optique

Le phénomène de diffusion de la lumière de longueur d'onde λ par des particules de petit diamètre par rapport à λ est connu sous le nom de diffusion Rayleigh. Le modèle correspondant, décrit en détail dans [78] et dont on trouve une synthèse dans la thèse de **B.Mercier** [46], permet d'établir *in fine* l'expression de la puissance P_d de lumière diffusée par une particule :

$$P_d = V \frac{\partial \sigma}{\partial \Omega} \, \delta\Omega \, \sin^2 \psi \, I_i \tag{7}$$

où

- $\delta\Omega$ est l'angle solide sous lequel est diffusée la lumière (cet angle étant défini de manière pratique par les caractéristiques de l'optique de collection utilisée pour mesurer P_d, comme on le montre en figure 37),
- I_i est l'intensité du faisceau de lumière incidente,
- ψ est l'angle entre la direction d'observation et la direction du vecteur polarisation de la lumière incidente,

- $\frac{\partial\sigma}{\partial\Omega}$ est une caractéristique optique traduisant la faculté de la particule considérée à diffuser la lumière. Cette caractéristique dépend du type de particule (en particulier, si on considère des molécules constitutives d'un gaz, de leur caractère mono- ou poly-atomique) et de l'angle ψ. Pour les gaz considérés dans la suite (essentiellement N_2 et O_2), on considère de manière simplifiée que cette caractéristique, appelée section efficace différentielle de diffusion, est indépendante de ψ.

Pour N particules diffusantes, et dans le cas où ces diffuseurs sont les molécules d'un gaz, la relation (7) peut être mise en forme pour introduire la masse volumique ρ du gaz :

$$P_d = \frac{N_A}{M} V \frac{\partial\sigma}{\partial\Omega}\ \delta\Omega\ \sin^2\psi\ I_i\ \rho \tag{8}$$

avec N_A le nombre d'Avogadro, M la masse molaire du gaz étudié et V le volume occupé par les N molécules (et en considérant $N = \rho N_A/M$). Avec cette relation, et avec quelques précautions, on peut relier P_d à la masse volumique locale d'un gaz.

Si la section efficace différentielle de diffusion est supposée indépendante de ψ, elle évolue toutefois avec λ^{-4} [78] si bien que l'on peut écrire que pour un volume donné de gaz à caractériser (N et V fixés) avec une optique collectrice donnée ($\delta\Omega$ et ψ fixés) :

$$P_d \propto I_i \lambda^{-4} \tag{9}$$

Ce point conditionne en partie **les choix technologiques** détaillés ci-après pour l'implémentation pratique de cette technique de mesure au Laboratoire. On a ainsi tout intérêt pour maximiser la collection de lumière diffusée, pour un système collecteur donné, à opter pour une source laser de longueur d'onde petite. Toutefois, pour des raisons pratiques liées à la sécurité des utilisateurs et à la faible efficacité des capteurs photo-multiplicateurs ou photo-diode en UV, nous avons souhaité utiliser une **source de lumière visible**. Ainsi, la quantité à optimiser (P_d) correspond donc au rapport P/λ^4, avec P puissance du faisceau laser incident. Le choix de la source laser porte en premier lieu sur le caractère continu ou pulsé du laser. Une limitation d'utilisation des sources pulsées correspond à leur fréquence de fonctionnement, typiquement de l'ordre d'une dizaine de kHz pour une utilisation prolongée permettant l'acquisition de données successives dans l'optique de traitements statistiques (moyenne, écart-type et spectre du signal de masse volumique). On choisit donc ici un laser continu (CW pour *continuous wave*). La figure 38 rassemble la valeur du rapport P/λ^4 pour différents modèles commercialisés actuellement (2019), dans la limite d'une puissance P de 10W qui correspond à la borne supérieure actuelle de nombreux modèles (même s'il existe certaines références, comme par exemple Millenia eV CW 532 DPSS, annoncées à 25W pour $\lambda = 532$ nm). Ce qui peut être retenu de cette figure est que les **sources CW actuelles dans le bleu** (λ 460nm, 480nm et 488nm) **sont actuellement moins efficaces pour maximiser la puissance diffusée par diffusion Rayleigh que les sources à 532 nm par exemple**, compte-tenu de leur puissance maximale plus faible (5W pour le Genesis MX-488 contre 10W (ou plus) pour le Millenia eV CW 532 DPSS).

L'ordre de grandeur des puissances diffusées dans les conditions rencontrées au Laboratoire conditionne quant à lui le type de capteur choisi pour l'analyse de la lumière diffusée. Pour un volume sondé de longueur caractéristique 1mm, pour un faisceau laser ayant un diamètre

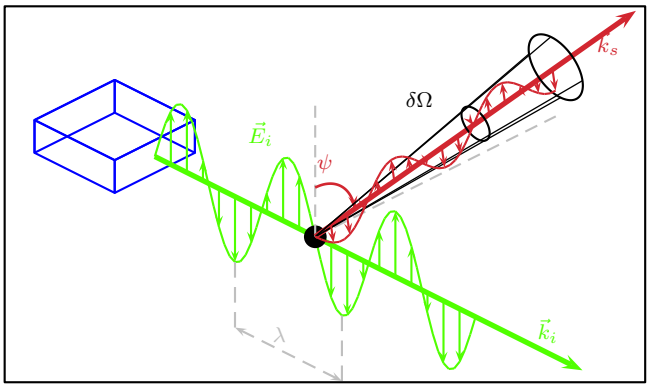

FIGURE 37 – Schéma de principe de la diffusion Rayleigh par des particules diffusantes situées en (•) et soumises à un faisceau laser incident de longueur d'onde λ

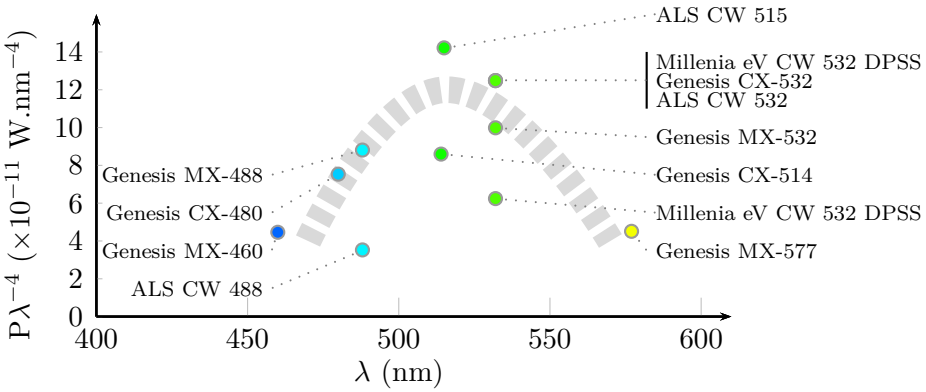

FIGURE 38 – Caractéristique $P.\lambda^{-4}$ en fonction de la longueur d'onde λ pour différents systèmes lasers monomodes (données de fournisseurs - 2019).

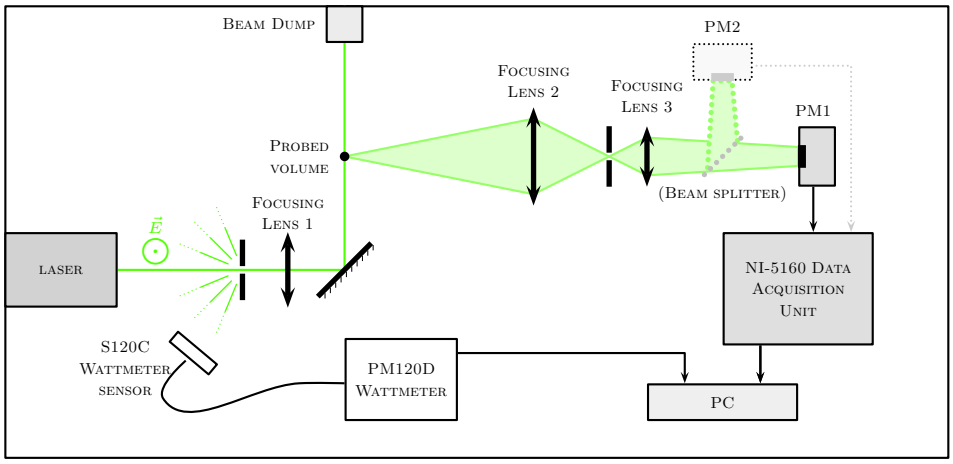

Figure 39 – Chaine de mesure pour l'évaluation de la densité en écoulement par diffusion Rayleigh

de l'ordre du millimètre et d'une puissance P=5W, pour une section différentielle de diffusion de 6×10^{-32} m^2/sr [56], pour une optique réceptrice de l'ordre de 0.1m de diamètre située à une distance de 1m du volume sondé, on obtient l'**ordre de grandeur pour la puissance diffusée** P_d de 10^{-11} W. Cet ordre de grandeur rend inopérante la mesure par un wattmètre à photodiode par exemple, dont la borne inférieure de la gamme de mesure est typiquement de l'ordre de 5×10^{-10} W, mais l'écart d'ordre de grandeur n'est pas si grand (typiquement 2 ordres de grandeur d'écart) pour imaginer qu'une évolution technologique de ce type de capteur permette d'effectuer - à terme - directement la mesure de P_d. Pour la thèse de **B.Mercier** [46], l'estimation de P_d a été effectuée par **comptage de photons** donnant une évaluation du flux de photons détectés Φ_d en développant une chaîne de mesure intégrant des photo-multiplicateurs (PM - Hamamatsu H7422P-40 sans limitation du courant de sortie) dont le signal de sortie est numérisé à haute cadence (carte NI-5160 ayant une bande passante de 500 MHz) avant d'être analysé *a posteriori* sur le PC d'acquisition. Un grand nombre de détails expérimentaux sur la configuration expérimentale et le traitement des données sont fournis dans [46], auquel le lecteur est renvoyé pour plus de précision. On indiquera simplement dans la suite de ce paragraphe, les différents éléments d'**une configuration expérimentale permettant de mesurer valeur moyenne et fluctuations de densité en écoulement**. Cette configuration, représentée en figure 39, résulte d'améliorations successives apportées au cours de différentes campagnes d'essais portant sur l'étude d'écoulements à Mach élevé (par exemple [51]) ou plus faible (par exemple [52]). Deux caractéristiques principales de ce montage expérimental sont détaillées ci-dessous.

Tout d'abord, on peut indiquer que la valeur moyenne de densité peut s'avérer plus difficile à mesurer que les fluctuations de densité. Ceci peut être contre-intuitif, mais toutes proportions gardées, on retrouve aussi cette difficulté pour d'autres méthodes de mesure comme par exemple l'anémométrie à fil chaud. Les mesures effectuées reposent sur la courbe de calibration Φ_d=$f(\rho)$, dont un exemple tiré de [46] est illustré en figure 40. On trouve une relation pratiquement linéaire entre ces deux quantités, ce qui a pour conséquence de rendre l'évaluation des fluctuations de ρ

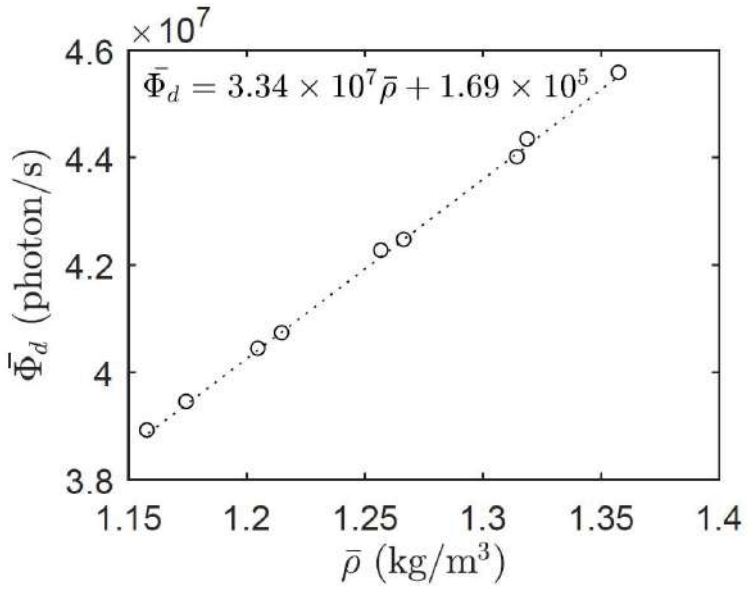

FIGURE 40 – Courbe de calibration typique d'un système de mesure de diffusion Rayleigh, donnant le flux de photons mesurés en fonction de la densité locale de l'écoulement. Résultat extrait de [46]

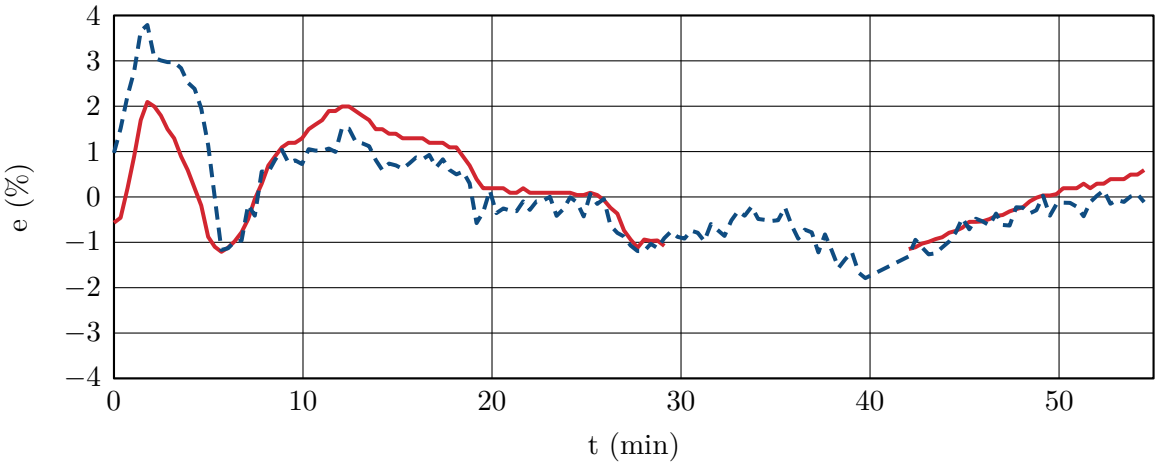

FIGURE 41 – Écart relatif à la valeur moyenne e de la puissance mesurée par le wattmètre situé à proximité de la sortie du laser, tel qu'illustré sur la figure 39 (—) et de la moyenne glissante du flux de photons en sortie de chaîne de mesure (- - -), sur environ 1h de fonctionnement après la mise en fonctionnement du laser et du PM. Deux enregistrements du signal issu du wattmètre ont été réalisés : l'un jusqu'à t=30 min et l'autre à partir de t=42 minutes.

quasiment indépendante de la puissance du laser même si celle-ci varie (lentement) avec le temps. Du reste, la stabilité de la puissance lumineuse fournie par la source laser est caractérisée par le constructeur (ici ALS) ; cette évaluation s'appuie sur des mesures effectuées après plusieurs heures de fonctionnement du laser (typiquement 10h). En soufflerie anéchoïque, le laser ne fonctionne pas sans interruption pendant des durées de cet ordre, si bien que la stabilité du laser n'est pas atteinte dans la pratique. L'objectif est donc d'avoir un suivi temporel de la puissance effective en sortie de laser, sans modifier le faisceau. Pour cela, on place un diaphragme (différentes formes ont été testées) à une distance de l'ordre de 10 cm en sortie de laser, dont l'ouverture est suffisante pour laisser passer le faisceau sans altération notable, et qui pour autant est éclairée en partie par le laser (diffraction par éléments optiques en sortie de boitier laser). On peut ainsi mesurer la puissance de ce résidu par un wattmètre placé en face du diaphragme, et comparer ce résultat au flux de photons comptés. Les résultats obtenus dans le cas où le volume de mesure est placé dans un environnement au repos sont présentés en figure 41. Une excellente corrélation existe entre les deux évolutions temporelles, ce qui permet de conclure sur 2 points. D'une part, la chaîne secondaire impliquant le wattmètre permet bien d'avoir un suivi temporel de la puissance effective du laser. D'autre part, on peut ainsi compenser la mesure du flux de photons de la variation de puissance laser pour accéder à une meilleure évaluation de la densité moyenne. Cette **correction** peut s'avérer **indispensable** compte-tenu du fait que pour un jet compressible à $M_j = 0.9$ par exemple, la valeur moyenne de la masse volumique change de typiquement 6% au maximum alors que la puissance effective du laser - et donc la puissance de lumière diffusée - peut changer pendant l'exploration du jet selon le même ordre de grandeur (figure 41).

Ensuite, la difficulté principale pour l'évaluation des fluctuations de densité est que leur effet sur le flux de photons détectés est faible devant le **bruit propre des capteurs** (PM). Pour contourner cette difficulté, Panda [59] utilise l'interspectre de 2 signaux issus de PMs différents, s'appuyant ainsi sur la compensation du bruit propre aléatoire de chaque capteur. Pour cette raison, la configuration représentée en figure 39 peut comporter 2 PMs ; dans la pratique, **Mercier** et al. [51] ont montré qu'il suffit de traiter le signal d'un seul PM, obtenu à une fréquence d'acquisition suffisante pour qu'il puisse être scindé en deux signaux complémentaires (chacun des 2 signaux comportant 1 point sur 2 du signal de départ) tout en préservant une bonne cohérence entre les deux signaux ainsi formés. Les opérations de traitement de signal spécifiques à ce procédé ont été validées d'une part par analyse critique de la physique des résultats obtenus - bien sûr !- mais aussi par la réalisation d'un banc de **calibration avec source LED simulant les fluctuations de luminosité** d'un volume de mesure qui serait situé dans une couche limite turbulente. Cette approche très originale mise en œuvre par **B.Mercier** est détaillée dans Mercier & Castelain [47].

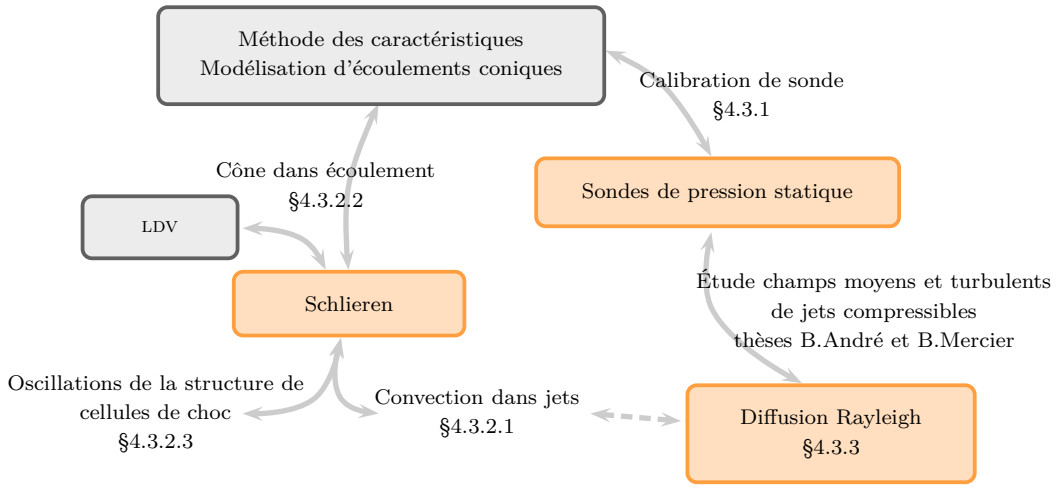

FIGURE 42 – Schéma de synthèse des différentes actions menées sur les techniques de mesure présentées ici (Schlieren, diffusion Rayleigh, pression statique en supersonique)

4.3.4 Synthèse

Dans cette partie, j'ai souhaité montrer les différentes adaptations et améliorations apportées à des techniques optiques existantes (schlieren, diffusion Rayleigh dévelopée durant la thèse de **B.Mercier**) pour lesquelles des applications innovantes ont été mises en œuvre au Laboratoire. J'ai également indiqué la procédure adoptée pour la qualification de sondes de pression statique en écoulement supersonique. Le schéma de synthèse fourni en Figure 42 a pour objectif de montrer que ces différentes études ont pu, ou pourront, partager des cibles communes ou des moyens communs. En effet, l'application au Laboratoire de la méthode des caractéristiques pour les écoulements axisymétriques (stage M1 **B.Bacher**) a servi à la fois la calibration des sondes de pression utilisées au cours de la thèse de **B.André** et l'étude quantitative d'images schlieren d'un cone placé dans un jet supersonique. De manière quantitative également, les enregistrements schlieren combinant plusieurs systèmes strioscopiques synchronisés avec le bruit émis (screech) ont permis la caractérisation de l'oscillation de la structure de cellules de choc (thèse **B.André**). On a enfin pointé certaines limites de l'analyse quantitative des images strioscopiques à l'occasion d'une étude numérique de l'estimation de la vitesse de convection dans la couche de cisaillement d'un jet rapide, en suivant la même procédure que celle d'études expérimentales précédentes. Les trois techniques de mesure complémentaires présentées ici ont été portées à un niveau de maturité suffisant pour envisager leur utilisation au Laboratoire dans des configurations variées.

5 Perspectives de recherche

5.1 Aéroacoustique des jets rapides

Les perspectives du travail présenté au paragraphe 4.1 concernant l'aéroacoustique expérimentale des jets subsoniques et supersoniques ($M_j \leq 1.55$) sont nombreuses. La liste ci-dessous distingue celles qui sont communes aux écoulements sub- et supersoniques de celles qui concernent plus spécifiquement le screech :

- Une signature (en un point de l'espace) d'un phénomène lié au bruit de mélange turbulent a été obtenue par l'association de mesures acoustiques en champ lointain et de densité dans l'écoulement par diffusion Rayleigh (paragraphe 4.1.1). Pour poursuivre l'étude de ce phénomène, il faut mesurer du champ de vorticité dans une zone spatiale étendue, en particulier en bout de cône potentiel, tout en préservant une bonne résolution temporelle de mesure. Pour cela, la technique de PIV rapide à une fréquence d'acquisition pouvant atteindre plusieurs dizaines de kHz, conditionnée par les événements acoustiques en champ lointain comme dans [49], ou en champ proche, sera mise en œuvre. Pour l'identification des sources de bruit de choc large bande, on pourra suivre cette même approche avec une antenne acoustique en champ proche et en appliquant un filtre passe-bande au signal acoustique adapté à la signature du BBSAN (autour de Sr=1.5 typiquement, selon [5]). Dans un second temps, on pourra modéliser le mouvement des chocs, sur la base de relevés expérimentaux, pour préciser l'effet du screech sur le BBSAN.
- On a rappelé qu'un plan d'antisymétrie existe dans le champ acoustique du screech en mode b. Il sera intéressant de déterminer les paramètres physiques influençant la position angulaire de ce plan d'antisymétrie : facteurs environnementaux liés à la géométrie de la tuyère, du banc d'essais, ou paramètres intrinsèques à l'écoulement (inhomogénéité azimuthale). De manière générale, la mesure fine des propriétés de l'écoulement en sortie de tuyère et le lien avec le bruit rayonné pourra faire écho aux travaux menés par simulation numérique dans l'équipe [14].
- Pour poursuivre l'étude du screech, on pourra généraliser l'analyse des caractéristiques de la boucle de rétroaction [48] au cas de jets avec effet de vol. Il est à présent possible de simuler un effet de vol par un écoulement secondaire deux fois plus rapide que lors des mesures faites dans la thèse de B.André [1], ce qui permettra de conclure sur l'effet de ce paramètre sur l'amplitude du screech sur une plage plus importante que ce qui a été étudié jusqu'ici.
- Enfin, différents modèles définissent les éléments de la boucle aéroacoustique à l'origine du screech, pour évaluer par exemple la fréquence du screech : un modèle s'appuie sur l'existence d'une onde stationnaire dans le champ proche du jet [60], l'autre sur le développement d'une onde d'instabilité dans la couche de cisaillement et expliquant la fermeture de la boucle de rétroaction par un retour des ondes de pression dans la couche

de cisaillement et dans le cône potentiel du jet [13, 24]. Dans de tels modèles pour le screech dans les jets sous-détendus, la formule prédictive de la fréquence du screech repose sur une longueur caractéristique (par exemple la distance moyenne entre chocs, ou la longueur moyenne de l'onde d'instabilité) et une vitesse de convection moyenne. Pourtant, on a montré que la distance entre les chocs change au cours d'une période de screech, et qu'elle évolue aussi en moyenne avec la distance axiale (la distance entre le choc 2 et le choc 3 est différente de la distance entre chocs 3 et 4). Le screech est un phénomène très marqué fréquentiellement mais on le décrit selon un formalisme impliquant des grandeurs moyennes qui sont en fait faiblement représentatives des conditions réelles dans lesquelles la boucle de rétroaction s'établit. Il y a donc un intérêt certain à dimensionner une expérience permettant d'obtenir les données suffisantes pour alimenter ces différents modèles et déterminer comment ils peuvent se compléter. De plus, une analyse temps-fréquence dans les premiers stades d'établissement du screech pour déterminer les mécanismes à l'œuvre dans la boucle de rétroaction pourra apporter des éléments de réponse. On a vu qu'une *tab* permet de supprimer le screech ; on envisage donc de synchroniser une mesure aéroacoustique sur un t_0 où l'on retire de manière automatisée ce dispositif placé sur la tuyère d'un jet à M_j fixé.

5.2 Contrôle des écoulements

Les perspectives à donner aux travaux présentés au paragraphe 4.2 pour l'amélioration de l'aérodynamique des véhicules industriels sont :

- pour le contrôle, d'identifier les mécanismes locaux liés à l'interaction jets/volets, notamment par l'étude de l'évolution du champ de vorticité instationnaire au cours d'un cycle d'actionnement et son effet sur l'entraînement de l'écoulement vers l'intérieur du sillage. Ce point est une clé d'une part essentielle pour interpréter la raison de la remontée de pression au culot des corps étudiés sous l'effet du contrôle, et d'autre part indispensable à l'établissement des lois d'échelle permettant de déterminer le gain sur système réel.
- pour la représentativité des maquettes étudiées face au problème réel (paragraphe 4.2.1), de déterminer la robustesse de classification des écoulements en présence de sol défilant. Un projet d'étudiants à l'IUT durant l'année 2018-2019 a porté sur la fabrication d'un tapis défilant à placer dans la soufflerie du Laboratoire ; ce mécanisme intègre les contraintes liées à la maquette 1/43eme employé jusqu'ici. Une nouvelle campagne de mesures pourra être effectuée dès 2020 pour engager cette étude.
- enfin, de prendre en compte des particularités aérodynamiques induites par la rotation des (nombreuses !) roues de la remorque, négligée jusqu'ici. Cet aspect peut donner lieu à des travaux collaboratifs dans la lignée du programme ACTIV_ROAD sur la base de travaux précédents [81]. L'étude des perturbations induites dans le soubassement par les roues en mouvement et leur effet sur le développement du sillage de la remorque

est intéressante. Elle peut être vue comme un prolongement de l'étude de l'influence du rapport entre vitesse de soubassement et vitesse infinie amont U_u/U_∞ sur le développement du sillage, en introduisant une inhomogénéité de la vitesse dans le plan de sortie du soubassement. De plus, on peut s'interroger sur l'effet de l'interaction entre la roue et l'écoulement incident sur les propriétés instationnaires de l'écoulement dans le soubassement, et en particulier si ce caractère instationnaire de l'écoulement persiste jusqu'en sortie de soubassement. Si tel est le cas, cette caractéristique est susceptible d'influencer le développement du sillage en agissant par exemple sur l'interaction entre l'écoulement de soubassement et l'écoulement provenant du toit de la remorque.

5.3 Aspects métrologiques

Enfin, au sujet des développements métrologiques en lien avec les résultats présentés dans la partie 4.3, on mentionnera :

- l'application de la méthode des caractéristiques sur un écoulement non uniforme, comportant par exemple un gradient axial du nombre M d'amplitude représentative de ce qui a pu être mesuré dans les jets sous-détendus étudiés [7]. L'objectif ainsi poursuivi est d'expliquer le nécessaire recalage axial des mesures de pression effectuées dans les jets.
- le travail de développement de la technique de mesure par diffusion Rayleigh et de sa calibration. La procédure actuelle pour calibrer ce système implique un écoulement compressible de référence ; selon les applications souhaitées, la mise en œuvre de cette procédure peut s'avérer fastidieuse. Pour autant, d'autres méthodes de calibration s'appuyant sur des propriétés purement optiques sont possibles, comme entrevu dans la thèse de B.Mercier. Leur maîtrise est indispensable pour généraliser l'utilisation de cette technique au Laboratoire dans des configurations variées. Plus généralement, la maîtrise du comptage de photons donnant accès à la densité (ou, de manière équivalente, la température dans un gaz supposé parfait à pression uniforme) est un savoir-faire important ; il est à présent nécessaire de développer une analyse - autrement plus complexe - de l'évolution spectrale de la lumière diffusée par les molécules dans un écoulement rapide. Cette analyse permettra d'accéder de manière non intrusive à la vitesse et à la température dans un écoulement compressible [61]. Des techniques récentes d'analyse spectroscopique à haute cadence font l'objet de développement dans certaines structures (CORIA, ONERA) où l'optique est une spécialité à part entière ; le développement de la vélocimétrie et thermométrie Rayleigh est à mon avis un excellent candidat pour constituer un projet transversal impliquant, en plus des expérimentateurs spécialisés en optique du Laboratoire, des collègues opticiens.

Références

[1] André, B. *Étude expérimentale de l'effet du vol sur le bruit de choc de jets supersoniques*. PhD thesis, École centrale de Lyon, N°2012-42, 2012.

[2] André, B., Castelain, T., and Bailly, C. Experimental study of flight effects on screech in underexpanded jets. *Physics of Fluids 23* (2011), 1–14.

[3] André, B., Castelain, T., and Bailly, C. A shock-tracking procedure for studying screech-induced oscillations. *AIAA j. 49* (2011), 1563–1566.

[4] André, B., Castelain, T., and Bailly, C. Shock oscillations in a supersonic jet exhibiting antisymmetrical screech. *AIAA j. 50* (2012), 2017–2020.

[5] André, B., Castelain, T., and Bailly, C. Broadband shock-associated noise in screeching and non-screeching underexpanded supersonic jets. *AIAA j. 51* (2013), 665–673.

[6] André, B., Castelain, T., and Bailly, C. Effect of a tab on the aerodynamical development and noise of an underexpanded supersonic jet. *C. R. Méc. 341* (2013), 659–666.

[7] André, B., Castelain, T., and Bailly, C. Experimental exploration of underexpanded supersonic jets. *Shock Waves 24* (2014), 21–32.

[8] André, B., Castelain, T., and Bailly, C. Investigation of the mixing layer of underexpanded supersonic jets by particle image velocimetry. *International Journal of Heat and Fluid Flow 50* (2014), 188–200.

[9] André, B., Castelain, T., and Bailly, C. Experimental study of flight effects on slightly underexpanded supersonic jets. *AIAA j. 55* (2017), 57–67.

[10] Bailly, C., and Fuji, K. High-speed jet noise. *Mechanical Engineering Reviews 3(1)* (2016), 15–00496.

[11] Barros, D., Borée, J., Noack, B. R., Spohn, A., and Ruiz, T. Bluff body drag manipulation using pulsed jets and coanda effect. *J. Fluid Mech. 805* (2016), 422–459.

[12] Berland, J., Bogey, C., and Bailly, C. Numerical study of screech generation in a planar supersonic jet. *Phys. Fluids 19(7)* (2007), 075105, 1–14.

[13] Bogey, C., and Gojon, R. Feedback loop and upwind-propagating waves in ideally expanded supersonic impinging round jets. *Journal of Fluid Mechanics 823* (2017), 562–591.

[14] Bogey, C., and Sabatini, R. Effects of nozzle-exit boundary-layer profile on the initial shear-layer instability, flow field and noise of subsonic jets. *Journal of Fluid Mechanics 876* (2019), 288–325.

[15] Camussi, R., Marco, A. D., and Castelain, T. Statistical analysis of the hydrodynamic pressure in the near field of compressible jets. *International Journal of Heat and Fluid Flow 64* (2017), 1–9.

[16] Castelain, T., Gojon, R., Mercier, B., and Bogey, C. Estimation of convection speed in underexpanded jets from schlieren pictures. In *22nd AIAA/CEAS Aeroacoustics Conference, Lyon, Paper 2984* (2016).

[17] Castelain, T., Michard, M., Szmigiel, M., Chacaton, D., and Juvé, D. Identification of flow classes in the wake of a simplified truck model depending on the underbody velocity. *Journal of Wind Engineering and Industrial Aerodynamics 175* (2018), 352–363.

[18] Chaligné, S. *Contrôle du sillage d'un corps non profilé. Application expérimentale à une maquette simplifiée de véhicule industriel.* PhD thesis, École centrale de Lyon, N°2013-50, 2013.

[19] Chaligné, S., Castelain, T., Michard, M., Chacaton, D., and Juvé, D. Fluidic control of wake-flow behind a two-dimensional square back bluff body. *Comptes Rendus Mécanique 342*, 6 (2014), 349–355.

[20] Chaligné, S., Castelain, T., Michard, M., and Juvé, D. Active control of the flow behind a two-dimensional bluff body in ground proximity. *Comptes Rendus Mécanique 341*, 3 (2013), 289–297.

[21] Chiekh, M. B., Béra, J.-C., and Sunyach, M. Synthetic jet control for flows in a diffuser : vectoring, spreading and mixing enhancement. *Journal of Turbulence 4* (2003), 32.

[22] Cronvich, L. A numerical-graphical method of characteristics for axially symmetric isentropic flow. *Journal of the Aeronautical Sciences* (1948), 155–162.

[23] Doty, M., and McLaughlin, D. Space-time correlation measurements of high-speed axisymmetric jets using optical deflectometry. *Experiments in Fluids 38* (2005), 415–425.

[24] Edgington-Mitchell, D., Jaunet, V., Jordan, P., Towne, A., Soria, J., and Honnery, D. Upstream-travelling acoustic jet modes as a closure mechanism for screech. *Journal of Fluid Mechanics 855* (2018), R1.

[25] El-Alti, M., Chernoray, V., Jahanmiri, M., and Davidson, L. Experimental and computational studies of active flow control on a model truck-trailer. In *EPJ Web of Conferences* (2012), vol. 25, EDP Sciences, p. 01012.

[26] El-Alti, M., Chernoray, V., Kjellgren, P., Hjelm, L., and Davidson, L. Computations and full-scale tests of active flow control applied on a volvo truck-trailer. In *The Aerodynamics of Heavy Vehicles III*. Springer, 2016, pp. 253–267.

[27] Englar, R. J. Improved pneumatic aerodynamics for drag reduction, fuel economy, safety and stability increase for heavy vehicles. Tech. Rep. 2005-01-3627, SAE, 2005.

[28] Gojon, R., and Bogey, C. Numerical study of the flow and the near acoustic fields of an underexpanded round free jet generating two screech tones. *International Journal of Aeroacoustics 16*, 7-8 (2017), 603–625.

[29] Grandemange, M., Gohlke, M., and Cadot, O. Bi-stability in the turbulent wake past parallelepiped bodies with various aspect ratios and wall effects. *Physics of Fluids 25*, 9 (2013), 095103.

[30] Haffner, Y., Borée, J., Spohn, A., and Castelain, T. Unsteady coanda forcing for drag reduction of a turbulent wake. In *11th International Symposium on Turbulence and Shear Flow Phenomena (TSFP11), Southampton, UK* (2019).

[31] Haffner, Y., Borée, J., Spohn, A., Castelain, T., Michard, M., Sesmat, S., and Bideaux, E. Forcing three-dimensional large-scale flow asymmetries in the wake of a blunt body : wake equilibrium and drag reduction. In *Third International Conference in Numerical and Experimental Aerodynamics of Road Vehicles and Trains (Aerovehicles 3), Milano* (2018).

[32] Harper-Bourne, M., and Fisher, M. J. The noise from shock waves in supersonic jets. In *AGARD Conference Proceedings n°131* (1973), pp. 11–13.

[33] Holder, D., and North, R. *Notes on Applied Science N°31 : Schlieren Methods*. Department of Scientific and Industrial Research - National Physical Laboratory, 1963.

[34] Isenberg, J. The method of characteristics in compressible flow : Part ib (numerical examples). Tech. Rep. N° F-TR-1173C-ND, Air Materiel Command Report, 1947.

[35] Juvé, D., Sunyach, M., and Comte-Bellot, G. Intermittency of the noise emission in subsonic cold jets. *J. Sound Vib. 71* (1980), 319–332.

[36] Karzova, M., Salze, E., S.Ollivier, T.Castelain, B.André, Yuldashev, P., Khokhlova, V., Sapozhnikov, O., and P.Blanc-Benon. Interaction of weak shocks leading to mach stem formation in focused beams and reflections from a rigid surface. In *Acoustics 2012, 11ème Congrès Français d'Acoustique & 2012 Annual IOA (Institute of Acoustics, UK), Nantes* (2012), pp. 1111–1115.

[37] Kearney-Fischer, M., Sinha, A., and Samimy, M. Intermittent nature of subsonic jet noise. *AIAA j. 51* (2013), 1142–1155.

[38] Kerherve, F., Jordan, P., Gervais, Y., and Valiere, J.-C. Aerodynamic characterization of a supersonic jet using two-point laser doppler velocimetry. In *AIAA paper 2003-3215* (2003).

[39] Kuo, C.-W., Power, R., and McLaughlin, D. K. Space-time correlation of flow and acoustic field measurements in supersonic helium-air mixture jets using optical deflectometry. In *17th AIAA/CEAS Aeroacoustics Conference, Portland, Oregon* (2011).

[40] Ladenburg, R., Lewis, B., Pease, R., and Taylor, H. *Physical Measurements in Gas Dynamics and Combustion*. Princeton University Press, 1954.

[41] Liepmann, H. W., and Pucket, A. E. *Introduction to Aerodynamics of a Compressible Fluid*. John Wiley and Sons, 1947.

[42] Mancinelli, M., Pagliaroli, T., Marco, A. D., Camussi, R., and Castelain, T. On the hydrodynamic and acoustic nature of pressure pod modes in the near field of a compressible jet. *Journal of Fluid Mechanics 836* (2018), 998–1008.

[43] Mancinelli, M., Pagliaroli, T., Marco, A. D., and Castelain, T. Wavelet decomposition of hydrodynamic and acoustic pressures in the near field of the jet. *Journal of Fluid Mechanics 813* (2017), 716–749.

[44] McArthur, D., Burton, D., Thompson, M., and Sheridan, J. On the near wake of a simplified heavy vehicle. *Journal of Fluids and Structures 66* (2016), 293–314.

[45] McIntyre, S., Stanewsky, E., and Settles, G. An optical deflectometer for the quantitative analysis of turbulent structures. In *ICIASF '91 Record., International Congress on Instrumentation in Aerospace Simulation Facilities* (1991).

[46] Mercier, B. *Développement d'une méthode de mesure de la masse volumique par diffusion Rayleigh appliquée à l'étude du bruit de jet, et contribution à l'étude du screech dans les jets supersoniques sous détendus.* PhD thesis, École centrale de Lyon, LYSEC61, 2017.

[47] Mercier, B., and Castelain, T. Dynamic analysis of a rayleigh scattering setup using synthetic light signals from a modulated led. *Rev. Sci. Instrum. 90* (2019), 063109.

[48] Mercier, B., Castelain, T., and Bailly, C. Experimental characterization of the screech feedback loop in underexpanded round jets. *Journal of Fluid Mechanics 824* (2017), 202–229.

[49] Mercier, B., Castelain, T., and Bailly, C. Experimental investigation of the turbulent density - farfield sound correlations in compressible jets. *International Journal of Aeroacoustics 17(4-5)* (2018), 521–540.

[50] Mercier, B., Castelain, T., and Bailly, C. Experimental study of the coherent vorticity in slightly under-expanded supersonic screeching jets. *International Journal of Aeroacoustics 18* (2019), 207–230.

[51] Mercier, B., Castelain, T., Jondeau, E., and Bailly, C. Density fluctuations measurement by rayleigh scattering using a single-photomultiplier. *AIAA j. 56-4* (2018), 1310–1316.

[52] Mercier, B., Jondeau, E., Castelain, T., Osawa, Y., Bailly, C., and Comte-Bellot, G. High frequency temperature fluctuation measurements by rayleigh scattering and constant-voltage cold-wire techniques. *Exp Fluids 60* (2019), 110.

[53] Merzkirch, W. *Flow Visualization.* Academic Press, 1987.

[54] Meyer, R., and Goldstein, S. The method of characteristics for problems of compressible flow involving two independent variables : Part i. the general theory. *The Quarterly Journal of Mechanics and Applied Mathematics 1-1* (1948), 196–219.

[55] Michard, M., Sesmat, S., Castelain, T., Jondeau, E., Bideaux, E., and Bourgeois, A. Unsteady pulsed jets using pneumatic valves for flow separation control : effect of internal acoustic waves on external flow structure. In *GdR Contrôle des écoulements, Polytech' Orléans, 8-9 novembre* (2017).

[56] Miles, R. B., and Lempert, W. R. Quantitative flow visualisation in unseeded flows. *Annual Review of Fluid Mechanics 29*, 1 (1997), 285–326.

[57] Nicolas, F., Donjat, D., Léon, O., Besnerais, G. L., Champagnat, F., and Micheli, F. 3d reconstruction of a compressible flow by synchronized multi-camera bos. *Exp Fluids 58*, 5 (2017), 1.

[58] Panda, J. Two point space-time correlation of density fluctuations measured in high velocity free jets. In *AIAA-2006-0006* (2006).

[59] Panda, J. Experimental investigation of turbulent density fluctuations and noise generation from heated jets. *J. Fluid Mech. 591* (2007), 73–96.

[60] Panda, J., Raman, and Zaman, K. Underexpanded screeching jets from circular,rectangular, and elliptic nozzles. Tech. rep., NASA/TM-2004-212481, 2004.

[61] Panda, J., and Seasholtz, R. G. Velocity and temperature measurement in supersonic free jets using spectrally resolved rayleigh scattering. In *AIAA paper 1999-0296.* (1999).

[62] Pinckney, S. Z. A short static-pressure probe design for supersonic flow. Tech. rep., NASA/TN-D-7978, 1975.

[63] Powell, A. The noise of choked jets. *The Journal of the Acoustical Society of America 25*, 3 (1953), 2588–2588.

[64] Powell, A., Umeda, Y., and Ishii, R. The noise of choked jets. *The Journal of the Acoustical Society of America 92* (1992), 2823–2836.

[65] Raman, G. Supersonic jet screech : half-century from powell to the present. *Journal of Sound and Vibration 225*, 3 (1999), 543 – 571.

[66] Samimy, M., Kim, J.-H., J.Kastner, I.Adamovich, and Y.Utkin. Active control of a mach 0.9 jet for noise mitigation using plasma actuators. *AIAA j. 45*, 4 (2007), 890–901.

[67] Seiner, J., Dash, S., and Wolf, D. Analysis of turbulent underexpanded. *AIAA j. 23(5)* (1985), 669–677.

[68] Settles, G. *Schlieren and shadowgraph techniques : visualizing phenomena in transparent media.* Springer, 2001.

[69] Shapiro, A. *The Dynamics and Thermodynamics of compressible fluid flow*, vol. 2. John Wiley & Sons, 1977.

[70] Sujar, P., Michard, M., Castelain, T., and Haffner, Y. Identification of efficient flow control strategies for truck model drag reduction. In *Turbulent Shear Flow Phenomena Conference TSFP11, Southampton, 30 juillet - 2 Août,* (2019).

[71] Suzuki, T., and Lele, S. Shock leakage through an unsteady vortex-laden mixing layer : application to jet screech. *Journal of Fluid Mechanics 490* (2003), 139–167.

[72] Szmigiel, M. *Étude du flux de soubassement sur la dynamique du sillage d'un corps non profilé à culot droit : Application du contrôle actif pour la réduction de traînée de véhicule industriel.* PhD thesis, École centrale de Lyon, 2017LYSEC016, 2017.

[73] Tam, C. K. W. Jet noise : since 1952. *Theoretical and Computational Fluid Dynamics 10*, 1-4 (1998), 393–405.

[74] Tam, C. K. W., Golebiowski, M., and Seiner, J. On the two components of turbulent mixing noise from supersonic jets. In *AIAA paper* (1996), pp. 1996–1716.

[75] Tam, C. K. W., Viswanathan, K., Ahuja, K. K., and Panda, J. The sources of jet noise : experimental evidence. *Journal of Fluid Mechanics 615* (2008), 253–292.

[76] Taylor, G. I., and Maccoll, J. W. The Air Pressure on a Cone Moving at High Speeds. I. *Proceedings of the Royal Society of London. Series A 139*, 838 (1933), 278–297.

[77] Umeda, Y., and Ishii, R. On the sound sources of screech tones radiated from choked circular jets. *The Journal of the Acoustical Society of America 110* (2001), 1845–1858.

[78] van de Hulst, H. *Light Scattering by Small Particles*. Dover, Dover books on physics, 1981.

[79] Van Dyke, M. *An Album of Fluid Motion*. Parabolic Press, 1982.

[80] Veltin, J. *On the Characterization of Noise Sources in Supersonic Shock Containing Jets*. PhD thesis, Pennsylvania State University, 2008.

[81] Wang, Y. *Experimental study of wheel-vehicle aerodynamic interactions*. PhD thesis, ISAE-ENSMA, 2019.

[82] Wernet, M. P. Temporally resolved piv for space-time correlations in both cold and hot jet flows. *Measurement Science and Technology 18*, 5 (2007), 1387–1403.

[83] Wilson, L., and Damkevala, R. Statistical properties of turbulent density fluctuations. *Journal of Fluid Mechanics 43* (1970), 291–303.

6 Annexe

Les travaux suivants sont joints à ce document :

- S.Chaligné, T.Castelain, M.Michard, D.Chacaton & D.Juvé. Fluidic control of wake-flow behind a two-dimensional square-back bluff body, *C. R. Méc.*, 342 :349-355, **2014**.
- T.Castelain, M.Michard, M.Szmigiel, D.Chacaton & D.Juvé. Identification of flow classes in the wake of a simplified truck model depending on the underbody velocity, *Journal of Wind Engineering and Industrial Aerodynamics*, 175 :352-363, **2018**.

- B.André, T.Castelain & C.Bailly. Investigation of the mixing layer of underexpanded supersonic jets by particle image velocimetry, *International Journal of Heat and Fluid Flow*, 50 :188-200, **2014**
- B.Mercier, T.Castelain, and C.Bailly. Experimental characterization of the screech feedback loop in underexpanded round jets, *Journal of Fluid Mechanics*, 824 :202-229, **2017**
- B.Mercier, T.Castelain & C.Bailly. Experimental study of the coherent vorticity in slightly under-expanded supersonic screeching jets, *International Journal of Aeroacoustics*, 18 :207-230, **2019**.

- B.André, T.Castelain & C.Bailly. Shock oscillations in a supersonic jet exhibiting anti-symmetrical screech, *AIAA j.*, 50 :2017-2020, **2012**.
- B.Mercier & T.Castelain. Dynamic analysis of a rayleigh scattering setup using synthetic light signals from a modulated led, *Rev. Sci. Instrum.*,90 :063109, **2019**.

C. R. Mecanique 342 (2014) 349–355

Contents lists available at ScienceDirect

Comptes Rendus Mecanique

www.sciencedirect.com

Separation flow control

Fluidic control of wake-flow behind a two-dimensional square back bluff body

Contrôle du sillage d'un corps bidimensionnel à culot droit

Sébastien Chaligné [a,b], Thomas Castelain [a,c,*], Marc Michard [a], Damien Chacaton [b], Daniel Juvé [a]

[a] *LMFA, École centrale de Lyon, 36, avenue Guy-de-Collongue, 69134 Écully cedex, France*
[b] *Volvo Group Truck Technology, Cab Engineering Lyon, 99, route de Lyon, 69806 Saint-Priest cedex, France*
[c] *Université Lyon-1, boulevard du 11-Novembre-1918, 69622 Villeurbanne cedex, France*

ARTICLE INFO

Article history:
Received 4 September 2013
Accepted 14 December 2013
Available online 5 June 2014

Keywords:
Flow control
Synthetic jet
Square-back

Mots-clés :
Contrôle d'écoulement
Jet synthétique
Culot droit

ABSTRACT

This experimental study deals with wake-flow fluidic control behind a two-dimensional square back geometry positioned close to the ground. The fluidic control system is made of pulsed jets positioned at the upper edge of the model base. The objective of the fluidic action is to modify the wake-flow development, and as a consequence the static pressure distribution over the model base and hence the pressure drag. The main concern of this study is to determine to what extent the presence of a flow confined between the model and the floor influences the effectiveness of the control. Static pressure measurements at the model base and wake-flow characteristics derived from PIV measurements at a high acquisition frequency indicate global similarities between a case where an underbody flow exists and a case where this underbody flow is absent. For low actuation frequencies, discrepancies in the way the coherent structures due to the control develop in the shear layer appear.

RÉSUMÉ

Une méthode de contrôle d'écoulement en boucle ouverte est appliquée à un écoulement de sillage d'une maquette bidimensionnelle à culot droit. Un système de jets pulsés soufflant à l'arrête du culot de la maquette est utilisé. L'objectif de l'action fluidique est de modifier le développement de l'écoulement de sillage et par conséquent la répartition de pression statique au culot de la maquette, donc la traînée de pression. Une attention particulière est portée dans cette étude à l'influence d'un écoulement de soubassement entre la maquette et le sol de la veine d'essais sur la pertinence du contrôle. Des mesures de pression statique au culot et les caractéristiques principales de l'écoulement à l'aval de la maquette, obtenues par l'analyse de mesures PIV à haute fréquence d'acquisition, indiquent des similitudes entre un cas où un écoulement de soubassement existe et un cas sans écoulement de soubassement. Pour les plus faibles fréquences d'actionnement

* Corresponding author at: LMFA, UMR CNRS 5509, École centrale de Lyon, 36, avenue Guy-de-Collongue, 69134 Écully cedex, France.
E-mail address: thomas.castelain@ec-lyon.fr (T. Castelain).

http://dx.doi.org/10.1016/j.crme.2013.12.008
1631-0721/

testées, on observe des spécificités propres à chaque cas dans la manière dont les structures cohérentes induites par le contrôle se développent dans la couche de cisaillement.

1. Introduction

Fluidic control has been experimentally tested on a two-dimensional square back geometry of height H positioned at a distance G from the ground.

The case where the ground clearance G is not null, in other words where an underbody flow develops, is of primary interest in ground vehicles aerodynamics. The aim of this study is to shed some light on the differences in the results obtained for two different configurations. The first one corresponds to a zero underbody flow condition ($G/H = 0$), thus a backward-facing step for which flow control have been previously implemented for instance in channel flows [1]. The second configuration corresponds to a ratio G/H non-null but still small. This configuration will be considered here as a reference configuration and will thus be analyzed more in details than the other one. The motivation to set G/H to a small value is twofold. It is well known that the vortex shedding present in the wake of two-dimensional blunt bodies placed in free stream no longer exists if a flat surface is sufficiently close to the body [2,3]. Also the mean drag is known to be significantly higher when a vortex shedding occurs [4]. Thus a sufficiently small value of G/H prevents vortex shedding and allows the comparative study with a backward-facing step-like flow. Furthermore, this geometrical characteristic can be found for example on the long-haul truck trailers where the ratio G/H ranges from 0.3 down to very low values, depending on the trailer type.

2. Experimental setup

Experiments are conducted in an open test section wind tunnel. The flow comes out of a nozzle with an exit square section of 500×500 mm^2. The free stream velocity U_∞ is set to 25 m.s^{-1} and constantly monitored by using a Pitot tube. The model used is a two-dimensional bluff body represented in Fig. 1. This model is positioned at a distance of 300 mm from the nozzle. Its length L, height H and width W are respectively 555 mm, 100 mm and 380 mm, resulting in a Reynolds number Re_H of 176 000. Two configurations are reported here, depending on the associated value of the ground clearance ratio G/H. The first one corresponds to $G/H = 0$, and the second one to $G/H = 0.04$. In the latter configuration, the underbody flow velocity U_u has been measured to 0.6 times the free stream velocity. Two lateral transparent plates are positioned on each side of the model to ensure two-dimensional statistical flow properties in the central part of the geometry, where pressure and velocity measurements are performed. These properties are confirmed in the central upper part of the model by comparing the velocity profiles at different locations in the Y direction, 5 mm upstream the rear edge. The velocity profiles compare well over at least 60% of the model width, the reference profile being that measured in the median plane.

The description of the control system is given in details in [5]. In brief, a pulsed jet system consisting of seven rapid solenoid valves placed upstream of circular-to-rectangular nozzles is used here. Each nozzle exit section corresponds to a rectangular slot of 0.3-mm thickness and 50-mm spanwise length. Slots are positioned at the upper rear edge of the model and are oriented so that the jet angle with respect to the free stream flow direction is equal to 45°, as illustrated in Fig. 1. The solenoid valves are driven in open loop and in phase with an actuation frequency F_{ac} and a duty cycle of 50%. The

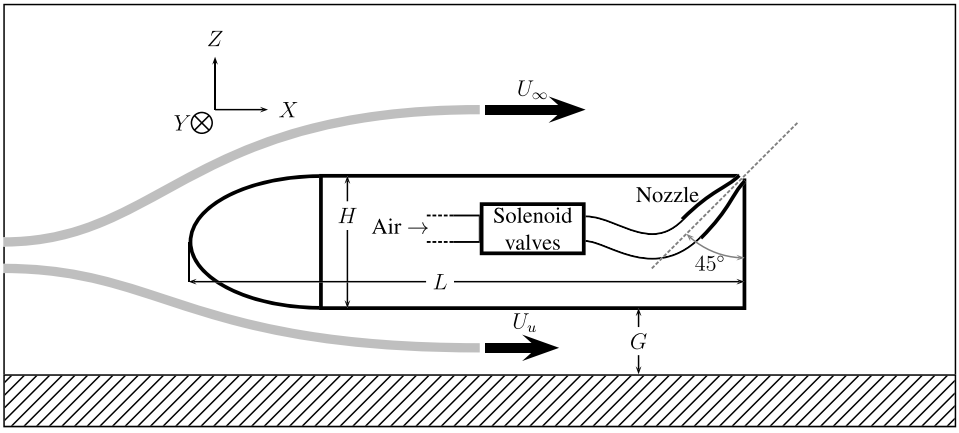

Fig. 1. Side view of the two-dimensional model with pulsed jet system. The normal to the plane of symmetry is the Y axis.

Table 1
Reference mean pressure coefficients $\overline{C_p}^{\text{ref}}$ at the model base, without control, for the two different configurations.

	$G/H = 0$	$G/H = 0.04$
$\overline{C_p}^{\text{ref}}$	−0.122	−0.180

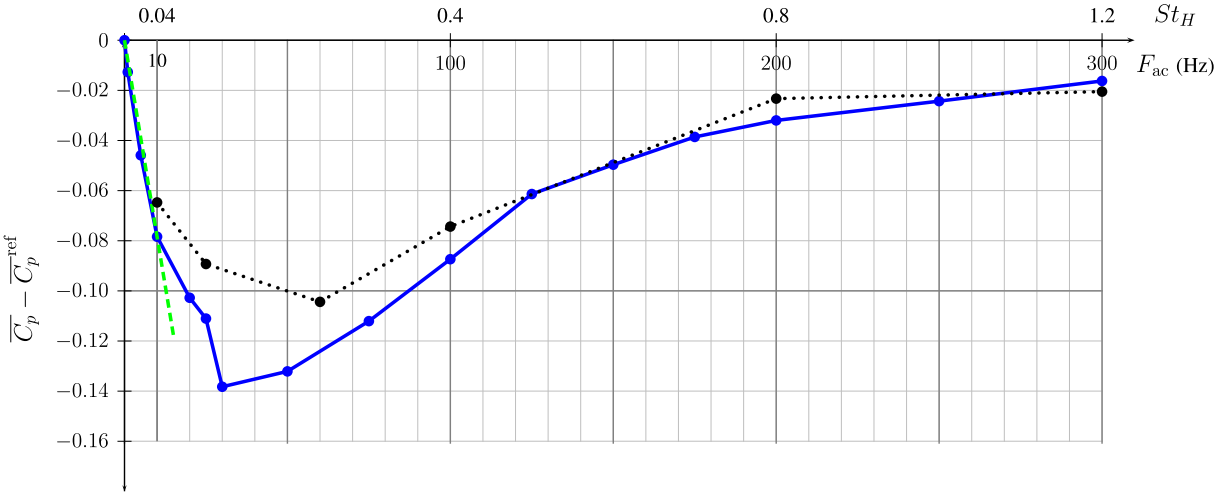

Fig. 2. (Color online.) Mean static pressure coefficient $\overline{C_p}$ measured at the base of the model function of the actuation frequency F_{ac}. The values of the pressure coefficient are relative to the reference value $\overline{C_p}^{\text{ref}}$ obtained without control (for $F_{\text{ac}} = 0$, the pulsed jet system is off). (▪▪▪▪▪) $G/H = 0$; (——) $G/H = 0.04$; (– – –) linear fit for the low-frequency actuation.

relative pressure upstream the valves is set to 1 bar. Wall pressure measurements are carried out at the base of the model. Fifteen wall pressure taps are distributed along the median plane, each being connected to a Scanivalve system coupled with a Furness 0–200-mm H_2O manometer. Time-averaged values over two seconds are collected and the spatial average of these values provides an estimate of the mean pressure $\overline{p}$ at the model base. The results are provided here in terms of mean pressure coefficient $\overline{C_p}$, defined in (1) by use of the air density ρ and the free stream static pressure p_0:

$$\overline{C_p} = \frac{\overline{p} - p_0}{1/2 \rho U_\infty^2} \tag{1}$$

Particle Image Velocimetry measurements are performed in the near-wake median plane. The PIV set-up and the processing details are described in [5]. In brief, sets of 2500 image couples are recorded at a rate of 3125 Hz. The dimensions of the field of view are $L_X/H = 2.15$ horizontally and $L_Z/H = 1.34$ vertically.

3. Results

The analysis of the mean pressure and flow-field characteristics is given first for the cases without control. On this basis, the results for controlled configurations are further discussed.

3.1. Mean pressure coefficient at the model base

The measured values of the mean pressure coefficient at the model base without control are reported in Table 1. These values are used in the following as reference values, and are therefore noted $\overline{C_p}^{\text{ref}}$. The mean pressure coefficient in the $G/H = 0.04$ case is, in absolute value, about 50% higher than that of the $G/H = 0$ case. This result is consistent with the monotonic decrease of $\overline{C_p}$ with G/H obtained in previous experimental studies [6,7]. The mean pressure coefficient values obtained with control are presented in Fig. 2 for the two values of ground clearance considered here. In each case on this figure, the corresponding reference value $\overline{C_p}^{\text{ref}}$ obtained with the pulsed jet system off is subtracted to the actual mean pressure coefficient value. In each case also, the evolution of $\overline{C_p}$ with the actuation frequency presents a minimum value for an actuation frequency around 50 Hz, the precise value of the actuation frequency depending on the configuration; for higher actuation frequencies, the mean pressure coefficient keeps increasing and seems to reach an asymptotic value below $\overline{C_p}^{\text{ref}}$. Thus, the control only decreases the base pressure with respect to the reference case, and as a consequence increases the pressure drag. The similarity in the evolution of $\overline{C_p}$ between the two configurations contrasts with the very different values of $\overline{C_p}^{\text{ref}}$ commented above. The fact that for given actuation frequencies, a doubling in the $\overline{C_p}$ values with

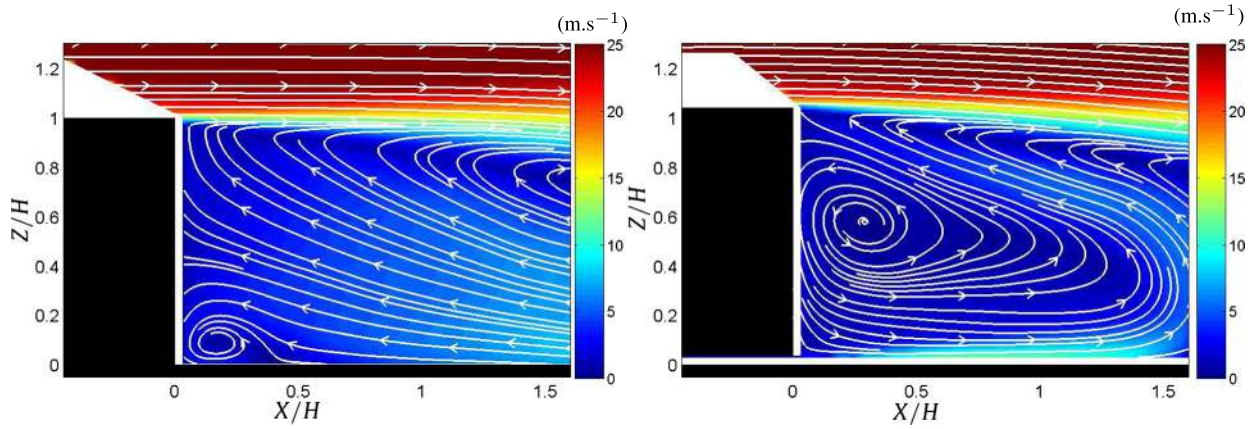

Fig. 3. (Color online.) Norm of mean velocity $\bar{u}$, without control, for (a) $G/H = 0$, (b) $G/H = 0.04$. The streamlines superimposed on the colormap are given to highlight the local flow direction.

respect to $\overline{C_p}^{\text{ref}}$ is obtained, is linked to changes in the wake flow characteristics, as will be described in Section 3.2. Moreover, the presence of a minimum in the evolution of $\overline{C_p}$ with the actuation frequency suggests that different control-induced flow phenomena contribute to a diminution of $\overline{C_p}$. Finally, one may note that, for the $G/H = 0.04$ configuration, the evolution of $\overline{C_p}$ with the actuation frequency, for the low-frequency values up to $F_{\text{ac}} = 10$ Hz, exhibits a linear behavior. It is supposed that this property also applies to the $G/H = 0$ configuration, even if the lack of data in the low-frequency region for this configuration does not permit to prove this assumption. This linear behavior is further interpreted on the basis of the wake flow characteristics.

3.2. Near wake-flow development

The analysis of the velocity flow-field is performed by use of statistical approaches. For the reference flows, the classical Reynolds decomposition allows to separate in any quantity $q(\mathbf{x}, t)$ the time-average value $\bar{q}(\mathbf{x})$ from the fluctuating part q', using Eq. (2). In controlled cases moreover, where the actuation cycles provide a periodic time basis, the triple decomposition is also used to separate in the fluctuating part of q, the contribution of periodic perturbations $\tilde{q}$ at the actuation frequency from the stochastic fluctuations q'', as illustrated in Eq. (3). The phase average $\langle q \rangle$ of the quantity q is also defined in Eq. (3), noting τ as the time delay within the period of one actuation cycle.

$$q(\mathbf{x}, t) = \bar{q}(\mathbf{x}) + q'(\mathbf{x}, t) \tag{2}$$

$$q(\mathbf{x}, t) = \bar{q}(\mathbf{x}) + \tilde{q}(\mathbf{x}, \tau) + q''(\mathbf{x}, t) = \langle q \rangle(\mathbf{x}, \tau) + q''(\mathbf{x}, t) \tag{3}$$

3.2.1. Mean-flow characteristics without control

Velocity maps given in Fig. 3 clearly highlight the fundamental differences in the wake flow between the two configurations considered. For $G/H = 0$, the wake region close to the ground is dominated by the recirculating flow coming from the region downstream the field of view; a small counter-clockwise rotating recirculation is located next to the bottom corner of the model. For $G/H = 0.04$, the underbody flow is responsible for a recirculation located at mid-height in the wake of the model and much larger than that observed in the $G/H = 0$ case. These features are thought to induce the differences in $\overline{C_p}^{\text{ref}}$ values presented in Section 3.1. In the other hand, the shear layer development is not significantly affected by the presence of the underbody flow in the $G/H = 0.04$ case, over the X/H range considered here. To illustrate quantitatively this property, an estimate of the momentum thickness δ_θ is computed by considering, for each longitudinal location X, the vertical profile above the point where the longitudinal velocity is zero. The evolution of δ_θ with X/H, presented in Fig. 4, compares well between the two cases. This being said, the δ_θ values are larger for the $G/H = 0$ case than for the $G/H = 0.04$ case; this is attributed to an installation effect consisting in a change in the boundary layer thickness over the model and is therefore not characteristic of any underbody flow effect.

3.2.2. Mean-flow characteristics with control

The effects of the control are illustrated here on the mean flow characteristics. Of particular interest are the actuation frequencies $F_{\text{ac}} = 10$ Hz and 100 Hz, which provide, for a given ground clearance, nearly the same diminution in the mean pressure coefficient, as indicated in Fig. 2. In Fig. 5 the corresponding velocity maps for $G/H = 0$ and 0.04 are presented. A recirculation region is visible in the mean wake-flow. The control has a noticeable effect on the location of the recirculation centers, that additionally depends on the ground clearance value. Indeed, one may notice that the recirculation center in the $G/H = 0$ case is considerably moved downstream when the actuation frequency varies from 10 to 100 Hz

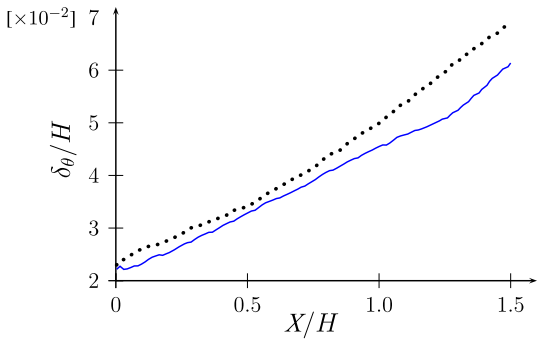

Fig. 4. (Color online.) Evolution of δ_θ with X/H. (▪▪▪▪▪) $G/H = 0$; (——) $G/H = 0.04$.

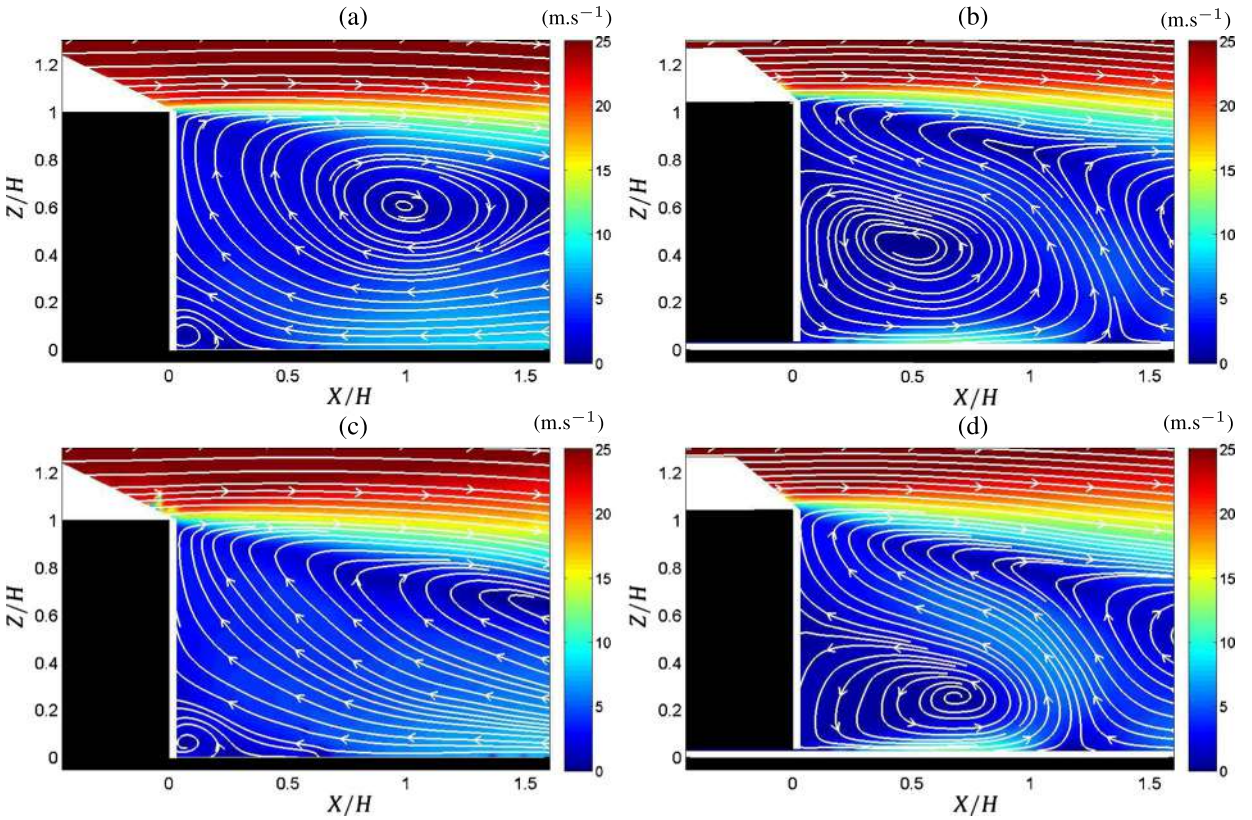

Fig. 5. (Color online.) Norm of mean velocity $\bar{u}$, with control, for (a,c) $G/H = 0$, (b,d) $G/H = 0.04$ and controlled jets actuated at (a,b) $F_{ac} = 10$ Hz and (c,d) $F_{ac} = 100$ Hz.

(Fig. 5 (a) and (c)); in the other hand, the displacement of the recirculation center visible in the velocity map in the case $G/H = 0.04$ is much less marked (Fig. 5 (b) and (d)). Moreover, in the low actuation frequency case, the velocity fluctuations (not shown here for conciseness) are comparable in magnitude to that presented in Fig. 4 of [5]. In a large part of the wake-flow, the high velocity fluctuations are a consequence of a highly non-stationary process; this process is therefore analyzed in the following by use of a triple decomposition.

3.2.3. *Phase averaging for controlled cases*

In Fig. 6 are presented the phase average of y-component vorticity, $\langle\omega_y\rangle(\mathbf{x}, \tau)$, as defined in Eq. (3) for different time delay τ covering a complete actuation cycle and for the two actuation frequencies studied in the previous section. For the control at frequency $F_{ac} = 10$ Hz (Fig. 6.I), two perturbations are induced successively in the wake-flow. One, generated when the control jets start (a), develops in the shear layer with a convection speed about $U_\infty/2$. This structure is thus visible in (b) around $X/H = 1.5$, and keeps on being convected such that it leaves the field of view in the following map. After, the phase average vorticity is mainly associated with a nearly-constant shear within the shear layer (c to e). The other

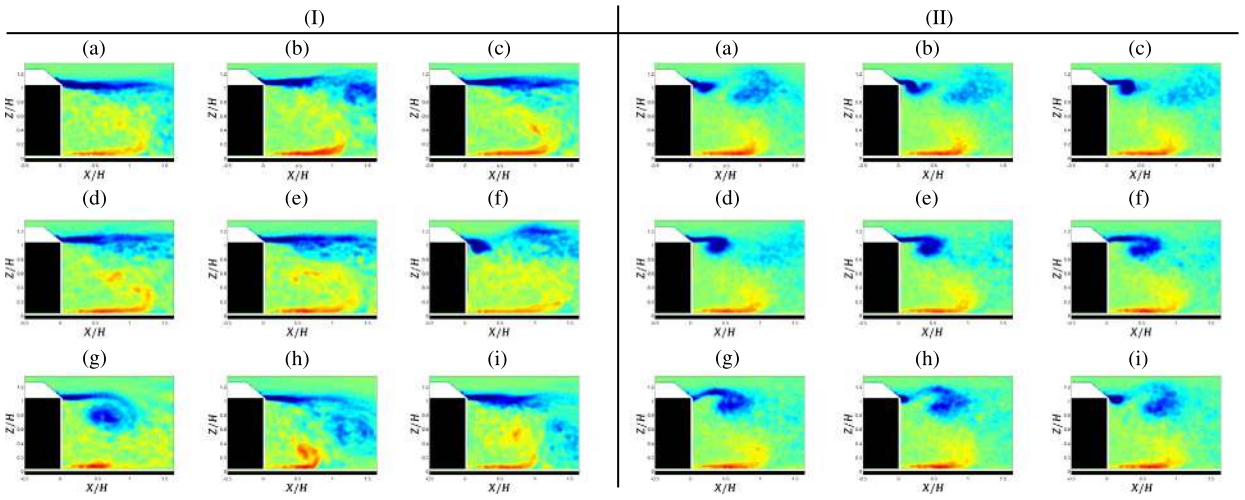

Fig. 6. (Color online.) Maps of $\langle\omega_y\rangle$ for the $G/H = 0.04$ configuration with control at $F_{ac} = 10$ Hz (I) and 100 Hz (II). The maps are equally spaced within one actuation cycle, which corresponds to a difference in time delay τ between two successive maps of $1/9/F_{ac}$; the map (a) corresponds to the beginning of blowing. For color coding, see online the color map of Fig. 7.

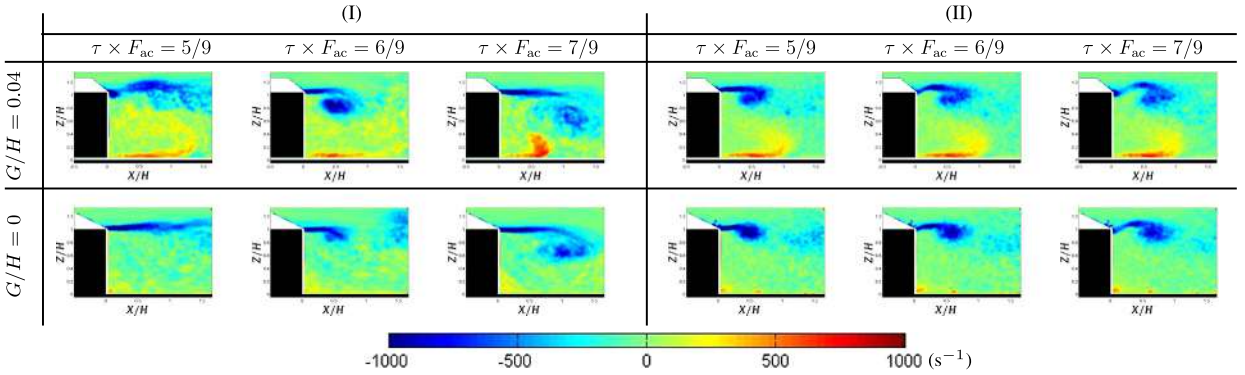

Fig. 7. (Color online.) Maps of $\langle\omega_y\rangle$ with control at $F_{ac} = 10$ Hz (I) and 100 Hz (II). The results obtained for the configurations $G/H = 0$ and 0.04 are compared at values of $\tau \times F_{ac}$ of 5/9, 6/9 and 7/9.

perturbation is associated with the stop in control jets blowing (f). This structure rolls-up in such a way that it interacts with the underbody flow and develops over a vertical dimension close to the model height (g and h). It may be assumed that such perturbations (or at least one of these perturbations) are responsible for a decrease in the mean pressure coefficient, because they may impose periodically an overall drop in the base pressure. These two perturbations apparently do not interact before $X/H = 1.6$, because their convection speed and the time delay of $1/2/F_{ac}$ corresponding to the duty-cycle of 50% imposed to the control jets are sufficiently high. Thus, it is obvious that for actuation frequencies lower than 10 Hz, these two structures during each actuation cycle will not interact close to the model base. As a consequence, the same kind of structures induced directly (at the beginning of blowing) or indirectly (at the end of blowing) is to be found for any actuation frequency at least up to 10 Hz. For an actuation frequency of 5 Hz for instance, these two perturbations will occur two times less than for an actuation frequency of 10 Hz, but with the same magnitude. This may explain the good fit between the experimental data and the linear behavior of the left part of the curves in Fig. 2, between $F_{ac} = 0$ and 10 Hz. As long as no interaction occurs, the linear behavior of $\overline{C_p}^{ref}$ with F_{ac} prevails. The analysis now concerns the data in Fig. 6.II where $F_{ac} = 100$ Hz. When the control jets start (a), a small perturbation is induced next to the top base, in the vicinity of an existing structure coming from the previous actuation cycle, as highlighted hereafter. These two structures interact (b) and the resulting pattern develops as it is convected downstream (c to f). After the stop of control jets (f), one perturbation is induced in the flow, into the form of an undulation of the shear layer (g), which partly interacts with the existing structure (g). In the same time, part of the undulation of the shear layer rolls-up around the model base, and forms the vortical structure that will interact at the beginning of the next actuation cycle with the new perturbation introduced. Thus this interaction promote a mechanism that differs from that observed at $F_{ac} = 10$ Hz.

Phase average results for the two values of ground clearance are given for $F_{ac} = 10$ Hz and 100 Hz in Fig. 7. For the highest actuation frequency (Fig. 7.II), one may note that the phase average vorticity maps present the same features in the two configurations. For example, the undulation of the shear layer associated with the stop of control jets is very well

retrieved in the $G/H = 0$ case. This is interpreted as the result of the little influence, for this actuation frequency, of the underbody flow on the development of the structures in the upper shear layer. Indeed, a closer observation of Fig. 6.II indicates that the characteristics of the phase average vorticity in the underbody flow region are quite constant from one time delay τ to another, which holds also in the configuration related to Fig. 7.II and suggests that the underbody flow does not present a significant response at the actuation frequency. The same comparison for $F_{ac} = 10$ Hz (Fig. 7.I) indicates that, to some extend, the similarity between the two configurations also holds. One may notice that the vortical patches in the maps obtained for $\tau F_{ac} = 6/9$ are a bit different in intensity and location, and that those visible in the maps obtained for $\tau F_{ac} = 7/9$ also differs in orientation. This is postulated to result from the interaction with the underbody flow in the $G/H = 0.04$ case. These results are finally used to determine possible links between the vortical structures induced by the control and the local diminution of pressure over the model base. In the $F_{ac} = 10$ Hz case, in both configurations, two noticeable vortices were induced in the flow in phase opposition by the control, and convected downstream. From a phase average point of view, it exists in this case phases during an actuation cycle where the wake-flow do not present vortical structures close to the model, but is essentially marked by mean shear in the shear layer. In the $F_{ac} = 100$ Hz case, again for both configurations, the interaction between the generated structures happen close to the model. These structures remain smaller than that observed for $F_{ac} = 10$ Hz, but they are present in the wake-flow for all the phases examined in the phase average study. Thus, the very similar values of $\overline{C_p}$ obtained for these two actuation frequencies are likely to result from a balance between the intensity of the vortical structures generated by the control and the frequency at which they are generated.

4. Conclusions

This experimental study of flow control around a square back model focuses on the influence of an underbody flow between the model and the floor on the control effects. The phase average analysis indicate that the perturbations induced by the control dominate over the natural wake-flow differences between the configurations with or without underbody flow. Striking similarities between controlled cases particularly for the high actuation frequency cases are observed. The role of the actuation frequency is also considered, by comparing pressure coefficient data and wake-flow characteristics for two actuation frequencies, chosen because they offer highly comparable values in $\overline{C_p}$ reduction. The study of the vortical structures development in each case suggests that a balance between the intensity of the vortical structures generated by the control and the frequency at which they are generated governs the $\overline{C_p}$ reduction. Further developments of the present analysis will rely on synchronized pressure–velocity measurements in the wake flow to correlate the evolution of the pressure on the model base over one actuation cycle and the generation and development of vortical structures in the main shear layer.

References

[1] K.B. Chun, H.J. Sung, Control of turbulent separated flow over a backward-facing step by local forcing, Exp. Fluids 21 (6) (1996) 417–426.
[2] G. Bosch, M. Kappler, W. Rodi, Experiments on the flow past a square cylinder placed near a wall, Exp. Therm. Fluid Sci. 13 (3) (1996) 292–305.
[3] L.L. Shi, Y.Z. Liu, H.J. Sung, On the wake with and without vortex shedding suppression behind a two-dimensional square cylinder in proximity to a plane wall, J. Wind Eng. Ind. Aerodyn. 98 (10–11) (2010) 492–503.
[4] H. Choi, W.-P. Jeon, J. Kim, Control of flow over a bluff body, Annu. Rev. Fluid Mech. 40 (1) (2008) 113–139.
[5] S. Chaligné, T. Castelain, M. Michard, D. Juvé, Active control of the flow behind a two-dimensional bluff body in ground proximity, C. R. Mecanique 341 (2013) 289–297.
[6] K.P. Garry, Some effects of ground clearance and ground plane boundary layer thickness on the mean base pressure of a bluff vehicle type body, J. Wind Eng. Ind. Aerodyn. 62 (1) (1996) 1–10.
[7] S. Chaligné, T. Castelain, M. Michard, E. Jondeau, D. Juvé, Contrôle d'écoulement autour d'un corps non profilé bidimensionnel en interaction avec le sol, in: 21e Congrès français de mécanique, Bordeaux, France, 2013.

Journal of Wind Engineering & Industrial Aerodynamics 175 (2018) 352–363

Contents lists available at ScienceDirect

Journal of Wind Engineering & Industrial Aerodynamics

journal homepage: www.elsevier.com/locate/jweia

Identification of flow classes in the wake of a simplified truck model depending on the underbody velocity

Thomas Castelain [a,c,*], Marc Michard [a], Mathieu Szmigiel [a,b], Damien Chacaton [b], Daniel Juvé [a]

[a] Université de Lyon, École Centrale de Lyon and LMFA UMR CNRS 5509, F-69134, Ecully, France
[b] Volvo Group Truck Technology, Renault Trucks SAS, Cab Engineering Lyon, 99 route de Lyon, 69806, Saint-Priest Cedex, France
[c] Université de Lyon, Université Lyon 1 and LMFA UMR CNRS 5509, F-69622, Villeurbanne, France

ARTICLE INFO

Keywords:
Aerodynamics
Experiments
Ground effect
Road vehicles
Wake

ABSTRACT

An experimental study of the near wake of a simplified truck model with an aspect ratio between the height and the width greater than one is presented. The influence of the underbody velocity at a constant ground clearance height is considered. The evolution of the model base pressure and of the near wake as a function of the underbody velocity permits to identify four classes of flow. For large values of underbody velocity, typically above 60% of the free stream velocity, the near-wake structure is similar to what obtained in bluff-body characterizations where the underbody flow momentum is sufficient to prevent its detachment from the ground. For smaller values of underbody velocity, of particular interest when considering real truck applications, base pressure mean value and near wake characteristics strongly depend on the underbody velocity; three different classes are defined through the values of time-averaged rear pressure as well as a qualitative analysis of the near-wake structure. Quantitatively, a momentum budget in the near-wake together with the characterization of the curvature of the underbody flow near the model end provide ad-hoc indicators for discriminating between the different flow classes.

1. Introduction

Medium and heavy duty vehicles can be considered as square-back bluff-bodies with an aspect ratio between their height H and width W above one. Depending on the practical use of the vehicle, the ground clearance height of the cab and the free space under the trailer can vary. This leads to various flow blockages in the underbody area and results in different wake topologies. The possible energy gains linked with a better understanding of the physical phenomena related to drag forces motivated studies at industrial scales. For instance, results on van-type vehicles (Bonnavion et al., 2017) confirmed the occurence of multistability on such a configuration, as previously obtained on a Ahmed body at industrial-scale (Grandemange et al., 2015). At smaller scale or for academic studies, simplified models of medium and heavy duty vehicles are used, among which simplified reduced-scale models of a real heavy duty vehicle, preserving the main aerodynamically significant details (simplified cooling system, indicators and vehicle registration holder plate for instance) (Hwang et al., 2016; Salati et al., 2017), or more simplified models such as the Ground Transportation System (GTS) or the Generalized European Transport System (GETS) (Croll et al., 1996; Gutierrez et al., 1996; McArthur et al., 2016; Storms et al., 2001; Van Raemdonck and Van Tooren, 2008). For these models, consisting of a rounded nose coupled with an elongated parallelepiped shape of aspect ratio $H/W > 1.3$, the ground clearance G is also a parameter of the experimental set-up, and governs the balance between the free stream and the underbody flow. When $G^\star = G/H \geq 0.14$, the bulk underbody flow velocity is very close to the free stream velocity (Croll et al., 1996; Gutierrez et al., 1996; Islam et al., 2017; Storms et al., 2001; Van Raemdonck and Van Tooren, 2008); the mean near wake is then composed of a closed recirculation bubble detached from the ground. From a qualitative point of view in this case, the wake structure is reminiscent of that obtained in passenger vehicles studies based on the Ahmed body (Ahmed et al., 1984), Windsor (Littlewood and Passmore, 2012) or ASMO models (Nakashima et al., 2008). Nevertheless, for full-scale trucks, the underbody bulk velocity ranges from 10% to 40% of the free stream velocity. As a consequence, the wake develops closer to the ground because of the limited momentum flux from the underbody flow. Previous studies already tackled the issue of handling the underbody velocity value, or proposed systems that could serve this purpose. A slanted underbody rear geometry was added by Kowata et al. (2008) to a

* Corresponding author. Université de Lyon, Université Lyon 1 and LMFA UMR CNRS 5509, F-69622, Villeurbanne, France.
E-mail address: thomas.castelain@ec-lyon.fr (T. Castelain).

https://doi.org/10.1016/j.jweia.2018.02.004
Received 29 September 2017; Received in revised form 8 February 2018; Accepted 10 February 2018

Nomenclature

$\overline{\bullet}$	Time-average value of $\bullet$
$\langle\bullet\rangle$	Spatial-average value of $\bullet$
$\bullet'$	Fluctuating part of $\bullet$
$\sigma_\bullet$	Standard deviation of $\bullet$
$\bullet^\star$	Length $\bullet$ normalized by H, or velocity component $\bullet$ normalized by U_∞
U_∞	Free stream velocity
u, v, w	Velocity components in the reference frame
U	Velocity magnitude in the longitudinal plane
U_s	Bulk underbody velocity
λ	Ratio between U_s and U_∞
$k^\star$	Turbulent kinetic energy normalized by U_∞^2
H, W, L	Model Height, Width, Length
ν	Air kinematic viscosity
Re_H	Reynolds number based on U_∞ and H
ϕ	Porosity of pressure loss system

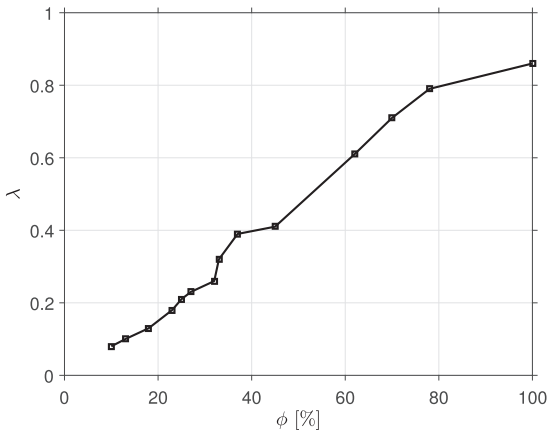

Fig. 3. Evolution of the ratio $\lambda = U_s/U_\infty$ with the porosity.

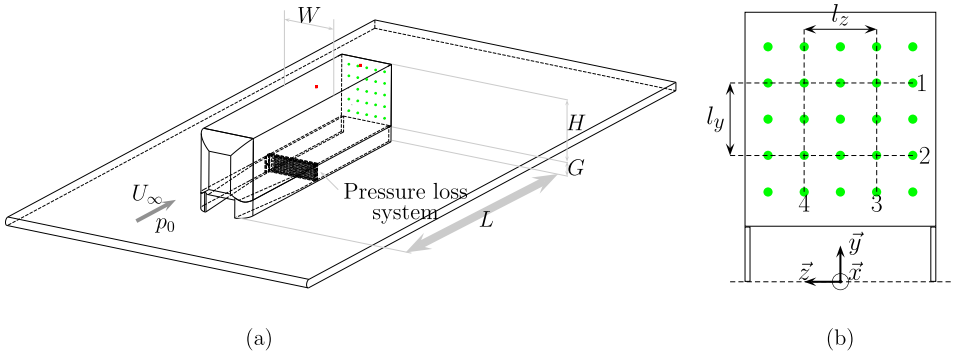

Fig. 1. Experimental set-up: (a) perspective view, (b) rear view. Locations of base pressure taps are given by •; those on the roof by ■. The pressure loss system is not represented in (b).

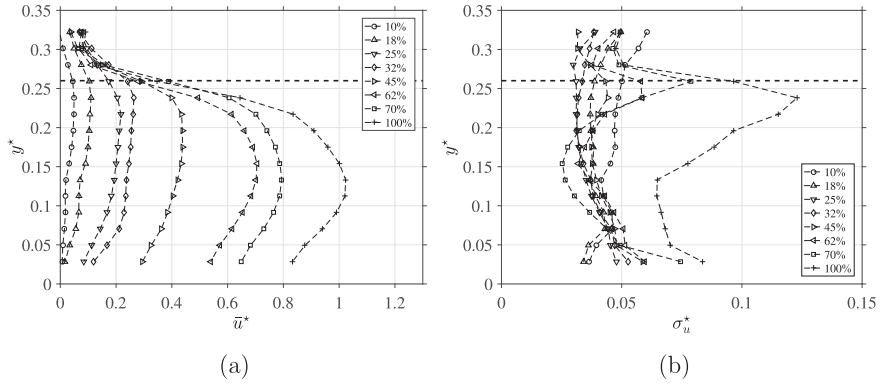

Fig. 2. Profiles at $x^\star = 0.02$ of (a) normalized mean longitudinal velocity and (b) standard deviation of the underbody flow for several pressure losses. Each symbol in the legend corresponds to a value of porosity ϕ; the black dashed line represents the ground clearance top.

square-back Ahmed body for drag reduction. Varying the angle of the slanted part would result in changing the underbody velocity at the model exit, but would consequently modify the height of the model rear. Perry and Passmore (2013) introduced roughness in the underbody area of a square-back Windsor model, which led to an underbody velocity change due to the induced pressure losses. To some extent, whether the ground displacement is reproduced or not can also influence the underbody bulk velocity, as a consequence of changes in the flow boundary condition on the ground; Garry (1996) for instance measured the base pressure of simplified bluff bodies with $H/W > 1$ for various ground plane velocities ranging from 0 to U_∞, and Krajnovic et al. (Krajnovic and Davidson, 2015) showed that the influence of the floor motion on the wake structure of a slanted surface body is qualitatively limited to the region near the floor and near the slanted surface. Finally, the ground clearance can be decreased to reduce the underbody velocity, because of the enhancement of pressure losses in the underbody area.

Barros et al. (2016) showed that, for a body of simplified geometry and with flow control, a strong connection exists between the change in base pressure and the drag evolution as a function of the actuation parameters. Grandemange et al. (2013a) studied the effect of ground

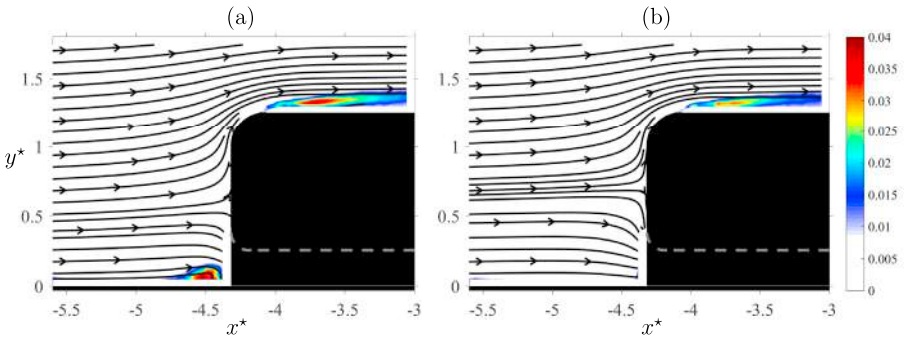

Fig. 4. Mean velocity streamlines superimposed with the maps of the normalized turbulent kinetic energy in the mid plane for $\lambda = 0.08$ (a) and $\lambda = 0.86$ (b). The dashed line is the limit of the ground clearance area.

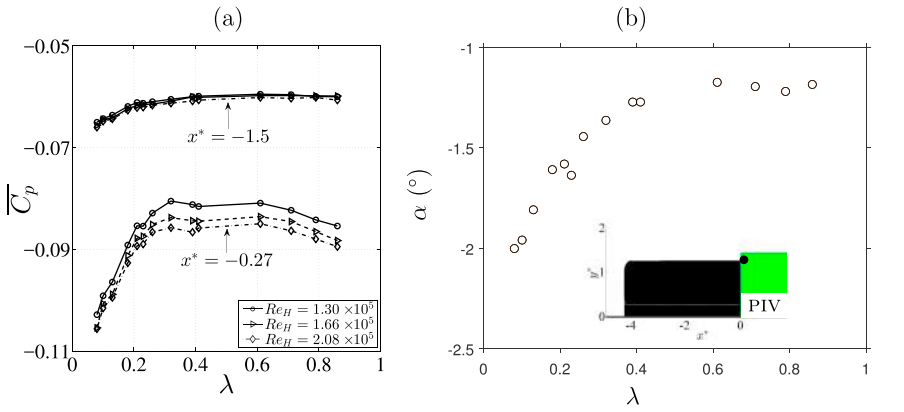

Fig. 5. Evolution with λ of (a) the mean pressure coefficient for several Reynolds numbers at $x^\star = -1.5$ and at $x^\star = -0.27$; (b) the streamline local angle with respect to $\vec{x}$ direction, at the reference point • located at $(x^\star, y^\star) = (0.06, 1.35)$.

clearance variations on the near wake of square-back bodies of different aspect ratios, including H/W = 1.34. There is no simple relationship between the mean base pressure (and drag, following (Barros et al., 2016)) and ground clearance velocity. A marked effect on mean base pressure, and drag, is obtained as G* varies. A minimum of the mean base pressure is reached for $G/W \approx 0.06$ (thus $G^\star \approx 0.045$). This value, independent of H/W, is identified as 'the transition from a backward facing step topology to a common wake topology of a simplified vehicle'. Unfortunately, velocity fields for $H^\star > 1$ are not provided. Furthermore, McArthur et al. (2016) changed progressively the ground clearance height for the GTS model, and characterized the wake for $G^\star \approx 0.14$ down to 0.03 by use of PIV measurements. Three different wake topologies were noticed in addition to that obtained for $G^\star \approx 0.14$ or higher, which is consistent with previous results (Szmigiel et al., 2016) obtained on a reduced-scale model of an industrial vehicle with flaps where 4 wake topologies were illustrated. In these different studies (Grandemange et al., 2013a; McArthur et al., 2016), the evolution of the near wake characteristics results from the combined effects of the variation of two physical parameters simultaneously. By varying the ground clearance height, viscous effects take place that limit the underbody flow momentum; the effect of the floor proximity is also modified.

The objectives of the present study are threefold: (i) determine the evolution of the near wake characteristics as the underbody flow momentum is modified while the ground clearance height is kept constant, (ii) investigate the possibility to classify these different wake structures using indicators derived from flow measurements, (iii) compare the identified flow classes to those obtained by changing the ground clearance height (Grandemange et al., 2013a; McArthur et al., 2016). Here, a simplified square-back truck model is studied. The influence of the underbody velocity on the near-wake characteristics and on the base pressure is investigated, with a ground clearance fixed to $G^\star = 0.25$. The experimental set-up is described in Section 2 together with the measurement techniques and the procedure to determine the underbody bulk velocity. The flow characteristics around the model are presented in Section 3. The base pressure distribution, the near-wake structure in terms of time-averaged velocity fields and the associated Reynolds stresses distribution are given in Section 4. Analyses based on a momentum budget, the evaluation of the underbody flow curvature in the near wake and base pressure gradients provide results compared in Section 5 to those derived from base pressure measurements.

2. Experimental set-up and underbody flow characterization

2.1. Low-scale tractor-trailer model

Experiments are carried out at École Centrale de Lyon, LMFA, in an open wind tunnel where the flow exhausts from a 500 mm-side square section. A simplified tractor-trailer model of scale 1:43 with a 90° rear slant angle, presented in Fig. 1, is studied. The length L of the bluff body is 320 mm, its height H and width W are respectively 74 mm and 66 mm. The aspect ratio H/W is thus equal to 1.12, which corresponds to a classical value encountered in European long haul vehicles. The ground clearance height G is 19 mm so that $G^\star = 0.25$ is identical to that of previous studies at larger scale (Chaligné, 2013) and close to the value of full scale long haul vehicle. The model is positioned on a flat plate, 133 mm downstream its leading edge. Results have been obtained for a free stream velocity U_∞ set to 25 m s^{-1} leading to a Reynolds number $Re_H = U_\infty H/\nu = 1.3 \times 10^5$. In some cases U_∞ was fixed to 32 m/s and 40 m/s to investigate the influence of Re_H. The peculiarities of this model are twofold: its aspect ratio and the presence of side skirts. The side skirts, fixed on the ground without gap, are used to channel the underbody flow which is forced to pass through a pressure loss system located in the ground clearance, 160 mm downstream of the model front. The effect on body drag of the side skirts, known from previous works (Hwang et al., 2016) to be beneficial in heavy trucks configurations, is not considered here but their presence is mandatory to allow for the management of the

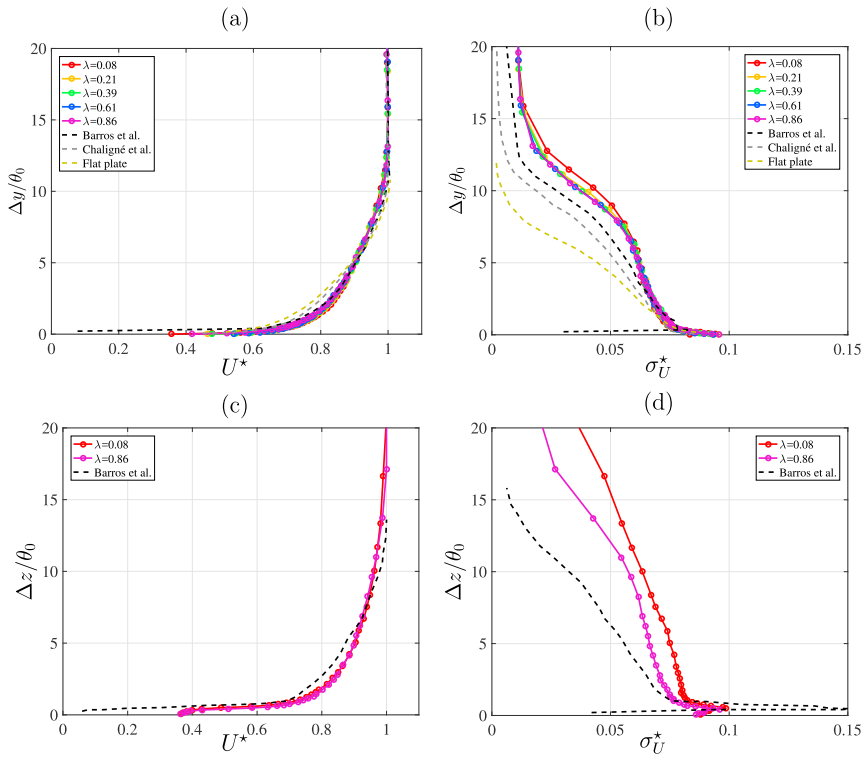

Fig. 6. Profiles of normalized mean velocity magnitude and standard deviation at $x^\star = -0.07$ in the mid plane (a,b) and at mid height on the side of the model (c,d). Comparison with results from (Chaligné, 2013; Barros et al., 2016; Klebanoff, 1955).

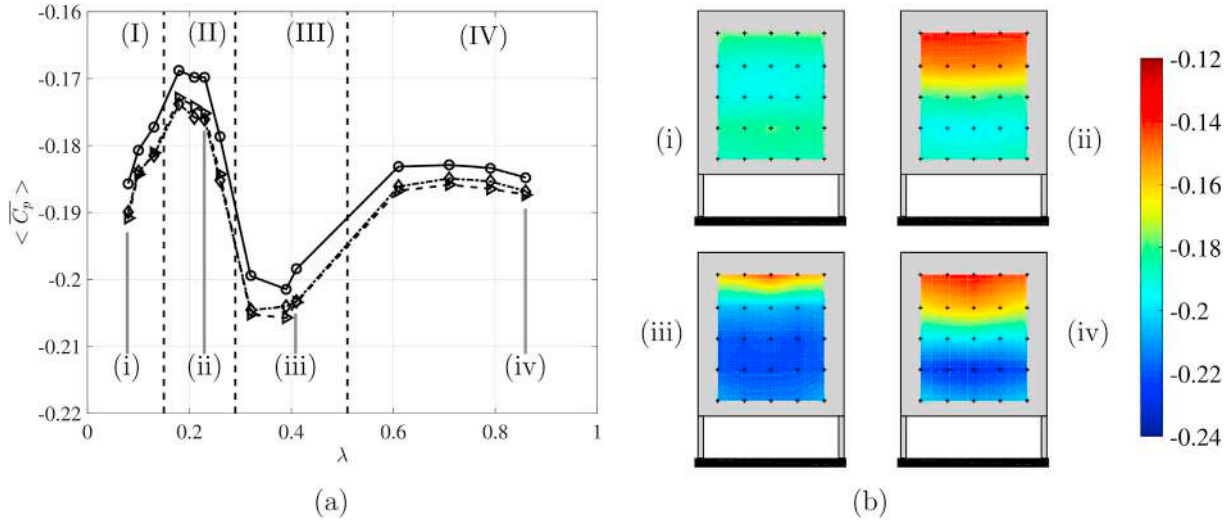

Fig. 7. (a) Evolution of the mean base pressure coefficient $\langle \overline{C_p} \rangle$ with λ for three Re_H values ((∘) 1.30×10^5, (△) 1.66×10^5, (∘) 2.08×10^5). (b) Maps of $\overline{C_p}$ on the rear surface for selected values of λ= (i) 0.08, (ii) 0.21, (iii) 0.39, (iv) 0.86.

underbody flux at constant ground clearance height. The pressure loss device, depicted in Fig. 1(a), is made of a 4 mm thick grid with a porosity ϕ adjustable between 10% and 100% of the ground clearance area. This allows for the underbody velocity to be adjusted without modifying the ground clearance height. To minimize flow separation on the upstream part of the model, a rounded shape of the model nose has been chosen. The choice of the radius for the upper and lateral edges equal to 19 mm and for the lower edge equal to 9 mm results from a previous study (Chaligné, 2013). A 5 mm-large sandpaper band of 25 μm grains is placed just after the nose on the roof and the side walls to help the transition of the boundary layers. The coordinate system is defined as the x axis directed toward the flow direction, y normal to the ground and z forming a direct trihedral. The origin of the coordinate system is defined as the point on the flat plate at the mid-span and rear end of the model. The three components of the velocity are noted u, v and w, respectively associated to the $\vec{x}$ (streamwise), $\vec{y}$ (vertical) and $\vec{z}$ (spanwise) direction.

2.2. Measurement techniques

2.2.1. Pressure measurements

Two wall pressure taps are located on the roof and 25 taps are distributed on the model base as depicted in Fig. 1. The pressure is measured using a 32-port ESP pressure scanner of 0–1000 Pa full scale interfaced to a μDAQ located outside the model. The scanner is linked to

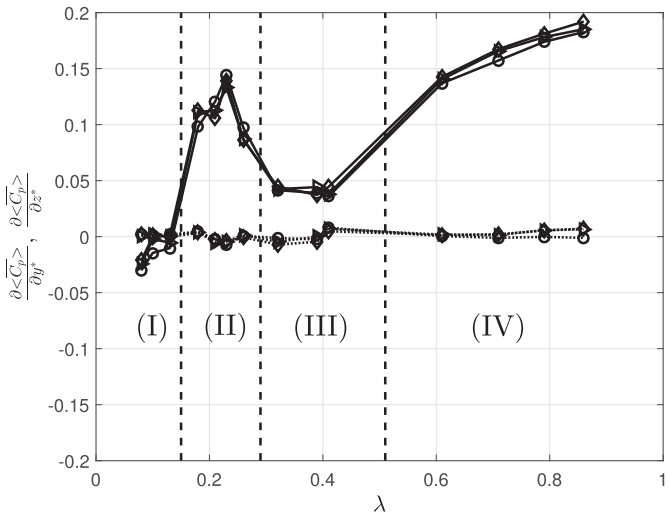

Fig. 8. Evolution of the vertical (solid lines) and horizontal (dashed lines) pressure gradients with λ for three Re_H values (see caption of Fig. 7).

each tap by tubes 270 mm long. To prevent flow disturbances, communicating wires for data transfers between the pressure scanner and the μDAQ are inserted inside the skirts. The acquisition frequency rate is set to 1 kHz. The frequency response of this set-up has been tested independently and can be considered as flat up to 400 Hz which is significantly above the bandwidth of interest here. The dimensionless pressure coefficient C_p is defined by use of the upstream static pressure p_0 and the air density ρ:

$$C_p = (p - p_0)/(1/2\rho U_\infty^2) \quad (1)$$

2.2.2. Hot-wire probe

A Dantec Dynamics 55P01 hot-wire probe, associated with a Dantec Dynamics Streamline 90N10 anemometer, is mounted on a displacement system to characterize the boundary layers developing along the roof and side walls and to perform spectral analysis in the near wake. For boundary layer measurements, signals are sampled at 12.8 kHz during 10 s.

2.2.3. Particle image velocimetry

Study of the front flow is carried out by using 2D2C particle image velocimetry (PIV). The whole wake in the mid plane and the wake in the transversal plane at $x^\star = 0.5$ are characterized by using stereoscopic PIV (SPIV). The laser system is a Nd:YAG Quantronix Darwin Duo of 2 × 18 mJ. The laser head is installed above the flow. The cameras used are CMOS Phantom V12 having a resolution of 1280 × 800 pixels. For SPIV, the cameras are placed on each side of the mid plane and inclined by an angle of 41° with respect to the direction of the upstream flow. The acquisition frequency rate of image pairs is set to 100 Hz. For each measurement, 1000 image pairs are recorded. Image processing is performed with DaVis 7.2.2 software using interrogation windows of decreasing size from 64 × 64 pixels down to 16 × 16 pixels and an overlap of 50%. The final grid resolution is 1.53 mm for the front flow, 0.99 mm for the whole wake in the mid plane and 1.08 mm for the transversal plane, this last value corresponding to 0.015 H.

2.3. Underbody velocity characterization

The flow at the underbody exit is investigated using SPIV, to determine the influence of porosity ϕ of the pressure loss system on the underbody flow homogeneity and evaluate the underbody bulk velocity for each value of ϕ. Vertical profiles of velocity $\overline{u}$ at $x^\star = 0.02$ in the mid-plane are given in Fig. 2(a) for selected grids over the investigated range of porosity. These profiles are rather symmetrical with respect to the middle of the ground clearance ($y^\star = 0.13$), as expected for a channel flow; the slight deviation from symmetry, in particular for low values of ϕ, may be attributed to differences in the boundary layers development along the ground ($y^\star = 0$) and along the model bottom ($y^\star \approx 0.26$). Profiles of velocity fluctuations are provided in Fig. 2(b). For $\phi \geq 62\%$ the maximum of velocity fluctuations is located in the shear layer downstream the underbody exit. Furthermore, the turbulence level within the ground clearance flow is rather constant as long as the pressure loss system is used ($\phi < 100\%$). This level is higher in the case $\phi = 100\%$. The bulk underbody flow velocity U_s is evaluated by integrating the vertical profiles of $\overline{u}$ (Fig. 2(a)) over the ground clearance height. The evolution of the dimensionless parameter $\lambda = U_s/U_\infty$ with ϕ is presented in Fig. 3. The evolution of λ is roughly linear in the range $\phi \in$[10%:80%]. Without underbody grid ($\phi = 100\%$), one may have expected λ to reach 1 ($U_s \approx U_\infty$); a smaller value is obtained ($\lambda = 0.85$), which is attributed to the combined effects of residual head losses in the ground clearance area, of the incoming boundary layer which develops over the ground and of a potential effect of the body in ground proximity. This last effect limits the velocity magnitude upstream of the body in a region of typical longitudinal size H; the boundary layer limits the velocity magnitude near the ground. This results in a deficit of bulk velocity in the model underbody with respect to the freestream velocity U_∞ even in the case $\phi = 100\%$.

3. Flow around the model

After having considered the bulk underbody flow velocity obtained by use of grids of different porosity in the underbody area, we describe the flow around underbody entrance at the model front, and on the model sides, where the influence of the pressure loss device is expected to be moderate.

3.1. Flow upstream of the model

The flow upstream of the body is first studied, by use of PIV in the mid plane for two underbody configurations $\lambda = 0.08$ and $\lambda = 0.86$. This last configuration is the reference case with no pressure loss grid in the

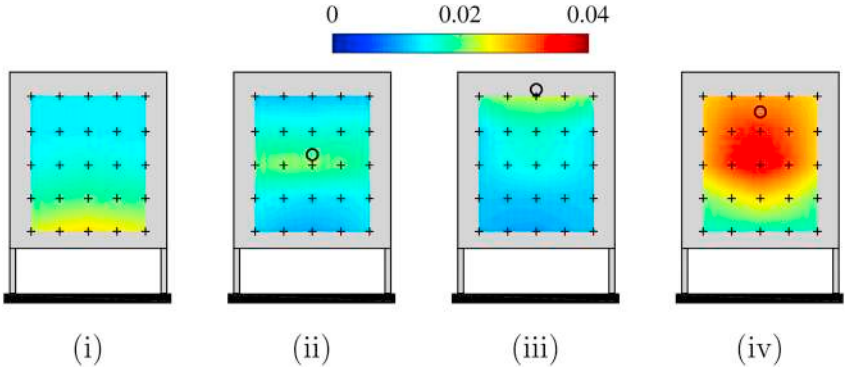

Fig. 9. Color maps of standard deviation values of C_p for selected values of λ: (i) 0.08, (ii) 0.21, (iii) 0.39, (iv) 0.86. The crosses indicate wall pressure taps and the black circles symbolize the stagnation points identified in section 4.2. (For interpretation of the references to color in this figure legend, the reader is referred to the Web version of this article.)

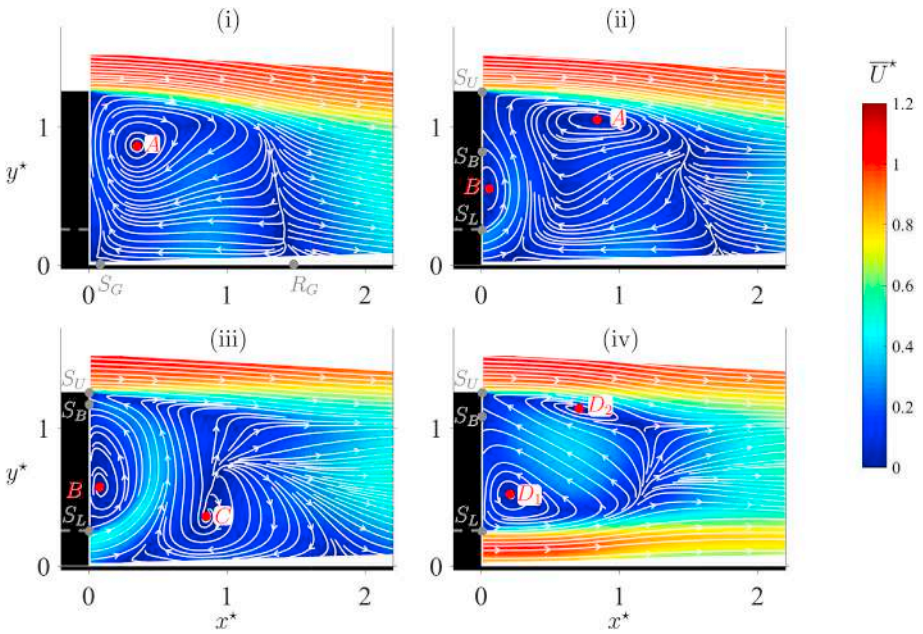

Fig. 10. Non-dimensional mean velocity magnitude in the mid plane for selected values of λ: (i) 0.08, (ii) 0.21, (iii) 0.39, (iv) 0.86.

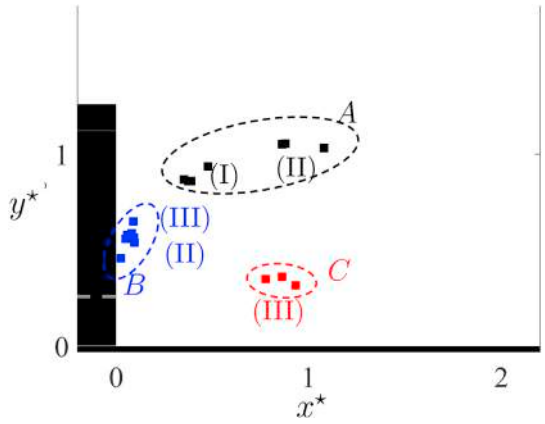

Fig. 11. Locations of the vortex centers detected in the mid-plane velocity field, for the different values of λ tested.

underbody area, while the case $\lambda = 0.08$ corresponds to the maximum pressure loss which is most susceptible to change the flow characteristics around the model. In Fig. 4, the streamlines of the time averaged velocity field together with the normalized two component turbulent kinetic energy $k^\star$ are given. The stagnation point moves towards the middle of the model nose when λ increases, as a result of a better balance between the underbody velocity and the free stream velocity. For $\lambda = 0.08$ and up to $\lambda = 0.18$, significant levels of velocity fluctuations are located in a small area near the ground, upstream of the underbody entrance where a local curvature of the streamlines is visible. In this case, the grid porosity is so small that the very limited underhood flux makes the model behave like a surface-mounted obstacle. The flow behavior around a sharp-edge surface-mounted obstacle has been previously studied (for parallelepiped obstacles in (Basara, 2015; Martinuzzi and Tropea, 1993) or cylinders (Uffinger et al., 2013) for instance), which highlighted the existence of a horseshoe vortex in the vicinity of the surface. A careful examination of the time-averaged velocity field (not provided here) confirmed here the presence of a vortical structure upstream of the ground clearance entrance. The velocity fluctuations upstream of the underbody entrance come from small variations of the location of this horseshoe vortex.

Furthermore, intermittent flow separation at the model nose induces high level of $k^\star$ over the model top. When λ decreases from 0.86 down to 0.08, the maximum of $k^\star$ on the roof increases by 15%; the area where $k^\star$ is larger than 0.01 above the model roof is not affected by the change in λ. Thus, the main features of $k^\star$ at the model front in the symmetry plane weakly depend on λ. To complement this first analysis, the wall pressure on the roof and the boundary layers on the model sides are now presented.

3.2. Wall pressure on the roof

A further assessment of the flow conditions downstream of the model nose is given by the wall pressure measurements on the roof at $x^\star = -1.5$ as illustrated in Fig. 5(a). This point is located at $2L/3$ downstream of the model front. The time averaged wall pressure is independent of Re_H and is very weakly dependent of λ, which tends to indicate that the flow modifications over the model roof downstream the nose (see section 3.1) have limited effects on the flow around the downstream part of the model. For the results obtained at $x^\star = -0.27$, thus very close to the model rear end, a dependency of $\overline{C_p}$ with λ is noticeable in Fig. 5(a). $\overline{C_p}$ increases with λ up to $\lambda = 0.3$, after which the value of the pressure coefficient remains nearly constant. At this location over the model roof, the time-averaged pressure can be affected by the modifications brought to the near-wake structure by a change in λ. To illustrate this effect, the orientation of the streamlines above the model rear end is presented in Fig. 5(b), using the velocity maps obtained by PIV. Different streamlines are considered in a region centered around the reference point located just behind the model rear and just above the shear layer where the velocity fluctuations are small, at position $(x^\star, y^\star) = (0.06, 1.35)$. The curvature of the streamlines is small in this region, and the angle α between the local streamline and the $\vec{x}$ axis has thus a value of only a few degrees. A spatial average over 0.067H centered around the reference point is performed and the estimated accuracy of the evaluation of α from the time-averaged streamlines is 0.05°; as a complement, the robustness of the trend for the evolution of α with λ has been tested against small variations of the location of the reference point. Under the reasonable assumption that these streamlines are oriented strictly along the $\vec{x}$ axis above the model (thus $\alpha = 0^\circ$ there), any change in the streamline orientation near the model end should come from a streamline curvature, which is associated with a reduction of pressure in this area. Analyzing the behavior of the evolution of α with λ in Fig. 5(b) indicates that the

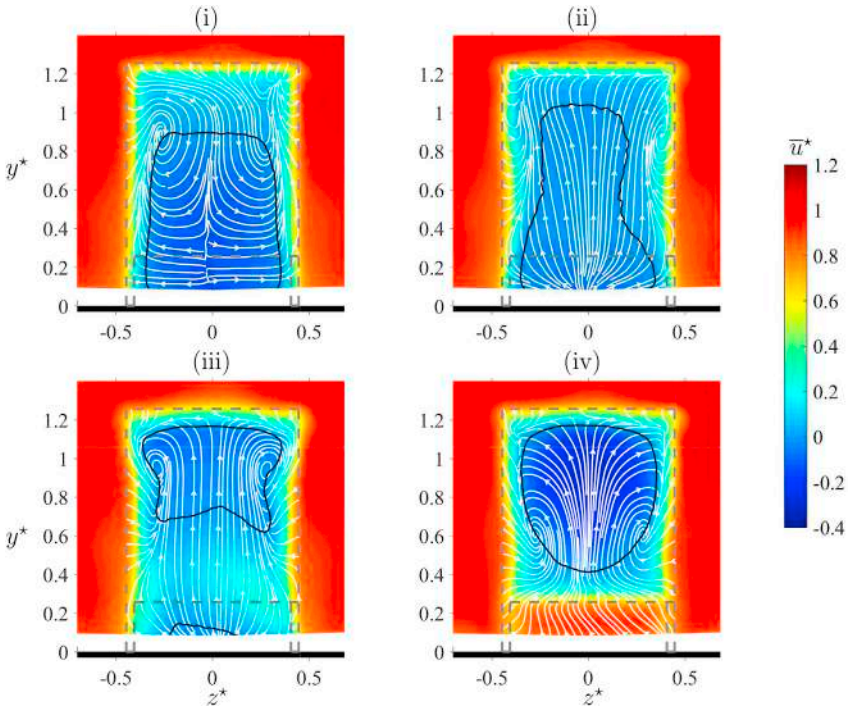

Fig. 12. Streamlines and mean streamwise velocity in a transversal plane at $x^\star = 0.5$ for λ = (i) 0.08, (ii) 0.21, (iii) 0.39, (iv) 0.86. The isoline $u^\star = 0$ is superimposed on each map.

corresponding radius of curvature tends to increase up to $\lambda = 0.3$ and is nearly constant above this value. This is fully consistent with the evolution of $\overline{C_p}$ measured near the model rear end.

3.3. Boundary layer characteristics

Hot wire measurements carried out upstream the model rear end are now considered. Mean velocity profiles and standard deviation profiles at $x^\star = -0.07$ in the mid plane are presented in Fig. 6(a and b). Normalized profiles from hot-wire measurements, on a flat plate with no pressure gradient (Klebanoff, 1955) and from a model similar to the one used in the present study but at a larger scale (Chaligné, 2013) or another model with a smaller aspect ratio H/W (Barros et al., 2016), are recalled for comparison. Considering the differences in characteristics of these various models (in particular, their length and aspect ratios), the fact that they have been tested in different wind tunnels, the turbulence levels measured from hot-wire surveys are likely not to be identical. Nevertheless, this difference in levels apart, the evolutions of the velocity fluctuations with the normal coordinate follow comparable trends. The boundary layer is turbulent for the three model walls in the downstream part of the model, as depicted by the velocity profiles and confirmed by integral parameters of these boundary layers provided in Appendix A. The influence of λ on the profiles is small with respect to the differences with reference profiles. These differences consist essentially in a slightly higher level of velocity fluctuations in the outer part of the boundary layer ($\Delta y/\theta_0 \approx 10$ typically, with θ_0 the local momentum thickness) for the measurements on models with respect to flat plate measurement. This may result from an intermittent flow separation downstream the model nose as pointed out in section 3.1. The velocity profiles on one side of the model, at mid-height, are also considered and presented in Fig. 6(c and d). The time-averaged velocity profile is similar to that obtained over the model roof. Velocity fluctuations are slightly higher in this case, in particular for $\lambda = 0.08$, which may be linked with the convection of the disturbances depicted in Fig. 4(a).

These first results indicate that the influence of λ on the flow over the model roof and the sides is limited. This ensures clean test conditions for the wake study in the different conditions of blockage ratio in the underbody area.

4. Near wake

4.1. Rear base pressure

The evolution with λ of the spatially averaged base pressure coefficient $\langle \overline{C_p} \rangle$ is given in Fig. 7(a), for three test configurations corresponding to different values of Reynolds number Re_H. The global trend of $\langle \overline{C_p} \rangle$ with λ is very slightly affected by a change in Re_H, within the range of Re_H tested. Below $\lambda = 0.61$, the base pressure is highly sensitive to λ. For very low underbody velocities, $\langle \overline{C_p} \rangle$ sharply increases with λ up to a maximum for $\lambda \approx 0.2$; for λ above 0.2, a marked decrease of $\langle \overline{C_p} \rangle$ with λ is noticed up to a minimum value for $\lambda = 0.4$. Finally, for λ above 0.4, the base pressure coefficient increases and reaches a plateau. For a given ratio H/W of a square-back Ahmed body, Grandemange et al. (2013a) showed that a decrease of the ground clearance height is related to a sharp change in base pressure for a critical value of $G/W = 0.06$. This indicates that both G/W and the underbody velocity, which changed with G/W, may influence the model rear pressure. The present study helps in separating these two effects by focusing on the influence of underbody velocity only. Fig. 7(b) gives color maps of C_p distribution over the model rear for selected values of λ. In most cases, the pressure distribution is far from homogeneous, which suggests to estimate the vertical and horizontal gradients of the base pressure distribution. These estimates are defined by equation (2) where $\langle \overline{C_p} \rangle_j$ corresponds to a spatial average on three points of line j depicted in Fig. 1(b):

$$\frac{\partial \langle \overline{C_p} \rangle}{\partial y^\star} = \frac{\langle \overline{C_p} \rangle_1 - \langle \overline{C_p} \rangle_2}{l_y/H} \tag{2a}$$

$$\frac{\partial \langle \overline{C_p} \rangle}{\partial z^\star} = \frac{\langle \overline{C_p} \rangle_3 - \langle \overline{C_p} \rangle_4}{l_z/H} \tag{2b}$$

The evolution of these pressure gradients with λ is provided in Fig. 8. The horizontal gradient remains small with respect to the values of the vertical gradient, which has been noticed earlier in similar configurations (Cadot et al., 2016; Chaligné, 2013; Grandemange et al., 2014; Gutierrez

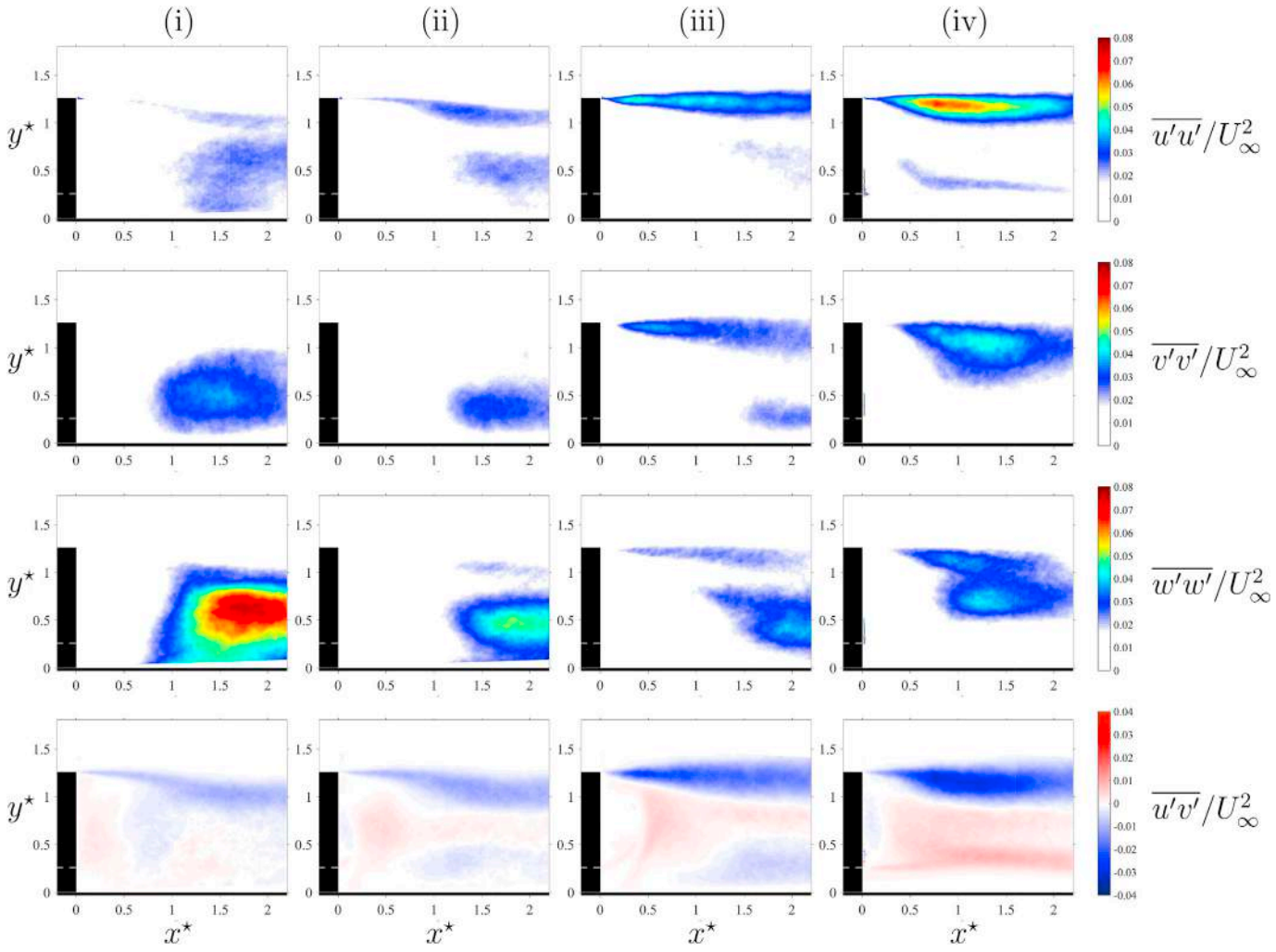

Fig. 13. Reynolds stresses in the mid plane for λ = (i) 0.08, (ii) 0.21, (iii) 0.39, (iv) 0.86.

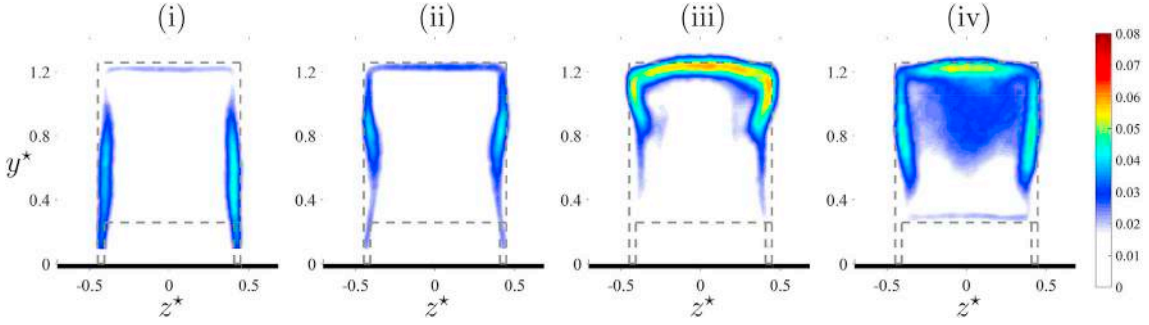

Fig. 14. Turbulent kinetic energy $k^\star$ in the $x^\star = 0.5$ plane for λ = (i) 0.08, (ii) 0.21, (iii) 0.39, (iv) 0.86.

et al., 1996; Szmigiel, 2017). The vertical gradient exhibits also a remarkable evolution with λ, being negative for very low values of the underbody velocity, peaking around 0.1 as λ reaches 0.25, and staging around 0.05 in a range of λ around 0.4. For larger values of λ, the vertical pressure gradient reaches high values again. This evolution denotes a strong influence of the underbody velocity on the near-wake and four flow classes can be distinguished. These classes, numbered from (I) to (IV) are reported on Figs. 7 and 8 together with vertical dashed lines as the estimated borders between classes. If the distinction between classes (I-II-III) and (IV) is related to a transition from a wake attached to the ground to a wake completely detached to the ground as for square-back Ahmed body as later illustrated in section 4.2, the physical interpretation governing the differences between the classes (I), (II) and (III) is less obvious. In the following, complementary analyzes are presented to better characterize of these flow classes; results obtained in particular with four selected values of λ, corresponding to those used in Fig. 7(b), will be used to illustrate representative characteristics of each of the four classes identified above.

A first complement comes with the examination of the standard deviation of the pressure coefficient on the model rear. Its evolution with the underbody velocity is presented in Fig. 9. When λ increases, the location of the maximum of pressure fluctuations moves from the bottom

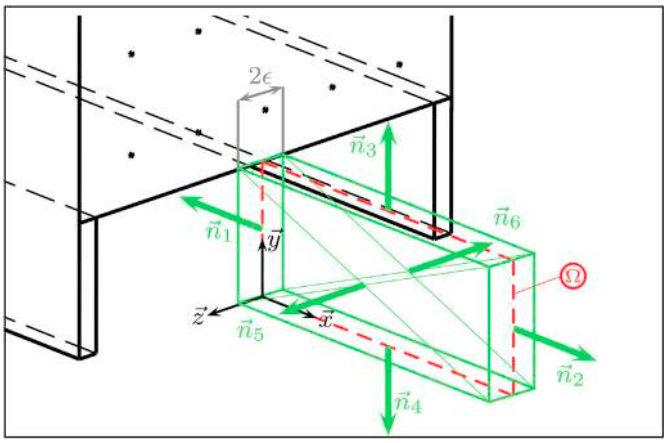

Fig. 15. Position of the closed control volume for establishing the momentum balance.

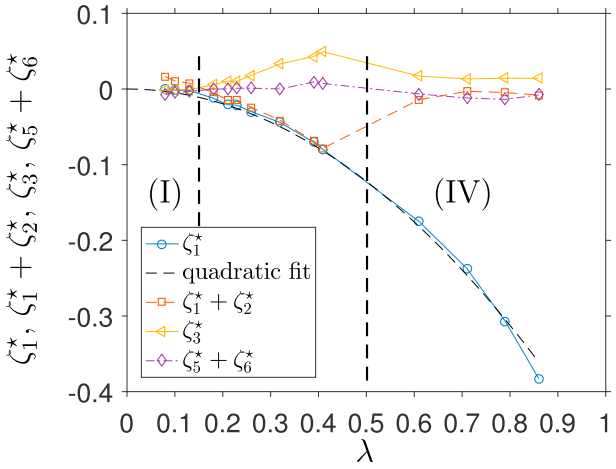

Fig. 16. Evolution with λ of the different momentum flux terms over the selected control volume.

to the top of the model rear. This result will be commented together with the analysis of the wake flow in section 4.2. The pressure fluctuations are also much larger for class (IV), as illustrated considering $\lambda = 0.86$. Bistability has been previously seen in the case $H/W > 1$ (Grandemange et al., 2013b), for values of C/W typically greater than 0.4. The result obtained here is somewhat different, because the first signs of possible bistability (not illustrated here) have been encountered only for the maximum of λ in the present set-up, $\lambda = 0.86$. For the different configurations tested here, the base pressure gradient remains positive. It is likely that, for greater values of λ, results consistent with what obtained in (Grandemange et al., 2013b) for $C/W > 0.4$ would have been observed.

4.2. Mean flow

SPIV measurements have been performed in the 14 configurations corresponding to the different λ values used here. Fig. 10 gives the mean velocity fields obtained in the mid plane of the model for the values of λ representative of the flow classes identified above. First, a major distinction can be drawn between class (IV) where the underbody flow momentum is sufficient to be convected along the ground without separation, and classes (I-II-III), where the underbody flow forms a backflow directed towards the base with separation from the ground. The results obtained here correspond to a fixed ground configuration, and are

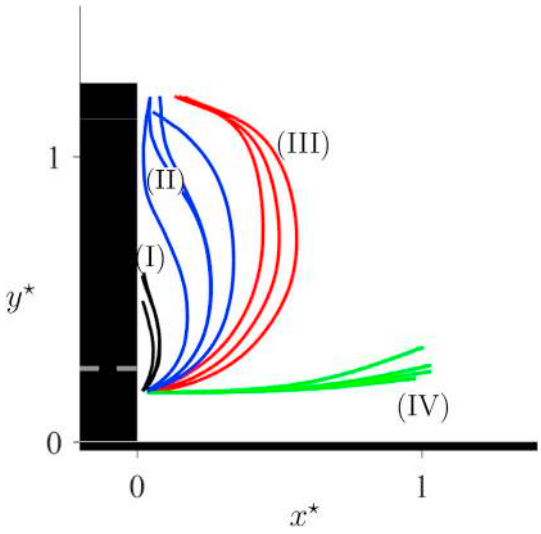

Fig. 17. Streamline starting at $(x^\star, y^\star) = (0.03, 0.2)$ for different values of λ.

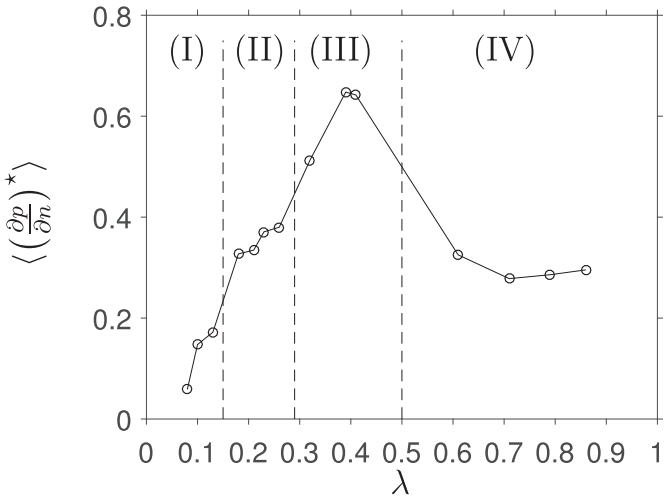

Fig. 18. Evolution with λ of the different contributions to the momentum balance over the selected control volume.

Table 1
Boundary layer characteristics at $x^\star = -0.07$ in the mid plane.

λ	δ_{99} (mm)	δ (mm)	θ_0 (mm)	Re_{θ_0}	h
0.08	18.1	1.96	1.59	2743	1.23
0.21	18.6	2.01	1.64	2810	1.22
0.32	17.9	1.95	1.60	2712	1.22
0.39	18.2	2.01	1.64	2795	1.23
0.41	17.7	2.00	1.63	2781	1.22
0.61	17.3	1.94	1.59	2694	1.22
0.86	16.6	1.92	1.55	2651	1.24

likely to be modified in the realistic case of a moving ground. Nevertheless, the same evolution of the wake characteristics with λ is expected, with a transition from one class to another possibly obtained at different values of λ. The following analyzes will focus on the flow topology in the vicinity of the base, less sensitive to the moving/fixed ground condition than the wake further downstream.

- For class (I), the wake in the mid plane is nearly similar to that of a 3D backward facing step flow with one main clockwise recirculation bubble attached to the ground, whose center denoted by A is depicted

Table 2
Boundary layer characteristics at $x^\star = -0.07$ at mid height on the side of the model.

λ	δ_{99} (mm)	δ (mm)	θ_0 (mm)	Re_{θ_0}	h
0.08	20.2	1.39	1.21	2014	1.15
0.86	21.0	1.69	1.46	2457	1.16

in Fig. 10(i). According to the boundary condition, separation and reattachment points S_G and R_G appear on the ground. R_G is located around $x^\star = 1.5$ as previously observed on a wall-mounted parallelepiped with the same aspect ratio than the present study (Martinuzzi and Tropea, 1993).

- For a higher momentum underbody flow corresponding to class (II), illustrated in Fig. 10(ii), A is progressively pushed away from the base by the backflow emanating from the underbody region. Additionally, a counterclockwise recirculating bubble of center B develops near the bottom edge of the base. A stagnation point S_B is located in the bottom part of the base, between the separation points S_L and S_U located respectively on the lower and upper edges of the base. The vertical size of the vortex corresponding to B is defined by the distance between S_L and S_B and is thus around $0.5H$.
- For class (III) depicted in Fig. 10(iii), a new clockwise recirculation bubble appears near the ground, whose center C is axially located between S_G and R_G. The stagnation point S_B is pushed upward, near S_U, and the vertical size of the vortex B trapped by the backflow scales approximately with $0.9H$. The existence, behind the base, of a vortex whose vertical size is around H, with strong curvature and velocities, potentially induces large low pressure values in the direction of B. Due to the proximity of B, the base is therefore largely contaminated by these low pressure values for class (III), in accordance with the mean wall pressure map shown in Fig. 7(b) for $\lambda = 0.39$. The reorganization of the mean flow structure, also marked with the disappearance of the vortex defined by A, coincides with a strong base pressure jump observed in Fig. 7(a) between classes (II) and (III).

The systematic existence of the structures of different types (A, B and C) for flow classes (I), (II) and (III) is illustrated in Fig. 11 that summarizes the results obtained with the different tested values for λ.

- For class (IV), as illustrated in Fig. 10(iv), the mean wake is formed in the mid plane by two counter-rotating vortices (whose centers are denoted D_1 and D_2) as observed in the wake of a classical Ahmed body as well as real square-back passenger cars or light commercial vehicles (Grandemange et al., 2014).

Maps of longitudinal velocity magnitude in the transverse $x^\star = 0.5$ plane are presented in Fig. 12, together with the streamlines in this plane. The isoline $u^\star = 0$ helps in identifying the flow area where the longitudinal velocity is negative. For classes (I) and (II), (Fig. 12(i,ii)), this area spreads from the floor to half the model height and is associated with the back-flow coming from the upper shear layer. For class (III) as depicted in Fig. 12(iii), this area is located in the upper part of the model wake and corresponds to the region where the underbody flow is directed toward the model rear. For class (IV), illustrated in Fig. 12(iv), the recirculation area with two non-symmetric recirculation bubbles dictates the form of the $u^\star < 0$ zone. Concerning the pattern of the streamlines, class (I) is clearly linked with streamlines going toward the sides of the lower part of the recirculating area, which indicates that the spanwise component of the mean velocity dominates in this region. Additionnaly, a rolling-up of the streamlines in the upper part of the near wake is noticed. On the contrary, for classes (II) and (III), the streamlines are oriented vertically on a large part of the near wake width, which corresponds to the underbody flow. Classes (II) and (III) mainly differ by the size of rolling-up of the streamlines in the upper part of the near wake and by the velocity magnitude in the underbody region. For class (IV), illustrated in Fig. 12(iv), the rolling-up of the streamlines is moved toward the lower part of the near wake.

4.3. Turbulence in the near wake

Time-averaged Reynolds stresses derived from SPIV measurements in the mid plane are given in Fig. 13. For classes (I) and (II), the normal Reynolds stress $\overline{w'w'}$ is the dominant component and is concentrated around $x^\star \approx 1.7$ at mid-height of the model. The high values of $\overline{w'w'}$ are related to strong lateral flow movements at the closure of the main vortex A. High levels of $\overline{v'v'}$ are also located in the same area. On the other hand, for classes (III) and (IV), the main contributor to turbulent kinetic energy is the normal Reynolds stress $\overline{u'u'}$ localized inside the upper shear layer, as observed on an Ahmed body (Barros et al., 2016; Grandemange et al., 2013b). For a given diagonal term of the Reynolds stress tensor ($\overline{u'u'}$, $\overline{v'v'}$, or $\overline{w'w'}$), an increase in λ leads to a decrease of its intensity in the lower region of the model wake, and an increase in the upper part of the model wake. The $\overline{u'v'}$ term reinforces with λ and is more intense in the upper shear layer.

Turbulent kinetic energy $k^\star$ measured in the transverse plane at $x^\star = 0.5$ is presented in Fig. 14. It is noteworthy that the largest velocity fluctuations are confined inside the lateral shear layers for classes (I) and (II), while they are shifted inside the upper shear layer for class (III). In this case, the interaction between the upper shear layer and the underbody flow redirected towards the model base, as observed in Fig. 10(iii), causes the increase in $k^\star$. For class (IV), high levels of velocity fluctuations are located inside the upper and lateral shear layers, and turbulence intensity is also increased in a large part of the closed recirculating bubble as observed for the base pressure fluctuations in Fig. 9. The velocity fluctuations in the lower shear layer are small for all classes of flow compared to the turbulence generated by other shear layers. Thus, peculiarities related to the identified flow classes are also qualitatively identified through turbulence intensities in a given transversal plane. Complementary spectral analyzes would help in clarifying the interaction between the back-flow and the upper shear layer for class (III) and the physical origin of large transverse velocity fluctuations downstream the main recirculation bubble for class (I). A more general distinction between the flow classes is now sought from the mean flow properties viewpoint.

4.4. Analysis of momentum flux terms and pressure gradients

The objective is to propose a quantitative analysis of the wake characteristics that helps in discriminating the classes identified from rear pressure measurements, and especially classes (I), (II) and (III). Appropriate metrics based on the velocity fields in the different configurations studied are now considered.

First, the momentum flux terms related to the time averaged velocity field are estimated over a closed volume centered around the mid-plane Ω. This volume, depicted in Fig. 15 has a length l along $\vec{x}$ and a width 2ε. The length l is chosen here to be half the model height H, but the conclusions presented here have been checked to be weakly dependent on l around this value. The bottom of the control volume coincides with the wind tunnel floor. The projection along $\vec{x}$ of the momentum flux through a surface Ω_i of normal vector $\vec{n}_i$ is noted ζ_i and expressed by:

$$\zeta_i = \left(\iint_{\Omega_i} \rho \vec{u} \left(\vec{u} . \vec{n_i} \right) \mathrm{d}s \right) . \vec{x} \tag{3}$$

The term ζ_4 is zero because of the location of Ω_4 on the wind tunnel floor. For practical reasons, the terms ζ_5 and ζ_6 are combined:

$$\zeta_5 + \zeta_6 = \iint_{\Omega_5} \rho \overline{u}(x, y, z = \varepsilon) \overline{w}(x, y, z = \varepsilon) \mathrm{d}x\mathrm{d}y$$

$$-\iint_{\Omega_6}\rho\overline{u}(x,y,z=-\varepsilon)\overline{w}(x,y,z=-\varepsilon)\mathrm{d}x\mathrm{d}y$$

and simplifying assumptions are considered to approximate the different momentum flux terms. First, the plane Ω is supposed to be a plane of symmetry for the time-averaged velocities. As a consequence, the following properties are obtained:

$$\overline{w}(x,y,z=0)=0 \tag{4a}$$

$$\frac{\partial\overline{u}}{\partial z}(x,y,z=0)=0 \tag{4b}$$

Secondly, the width 2ε of the control volume is supposed to be small enough to allow for a first order Taylor expansion of the velocity field around the mid-plane. Therefore:

$$\overline{w}(x,y,z=\varepsilon)-\overline{w}(x,y,z=-\varepsilon)\sim 2\varepsilon\frac{\partial\overline{w}}{\partial z}(x,y,z=0) \tag{5}$$

Consequently the sum of ζ_5 and ζ_6 is approximated by:

$$\zeta_5+\zeta_6\sim 2\varepsilon\iint_{\Omega}\rho\overline{u}(x,y,z=0)\frac{\partial\overline{w}}{\partial z}(x,y,z=0)\,\mathrm{d}x\mathrm{d}y \tag{6}$$

The term $\frac{\partial\overline{w}}{\partial z}(x,y,z=0)$ in eq. (6) is not measured directly, but can be estimated with help of the continuity equation and the SPIV data in the mid-plane (Ω). The terms ζ_i as defined in eq. (3) can be expressed in a condensed form, noted $\zeta_i^\star$, obtained by use of a reference momentum $\frac{1}{2}\rho U_\infty^2$ and a reference surface $H\times 2\varepsilon$, as follow:

$$\zeta_i^\star=\frac{\zeta_i}{\frac{1}{2}\rho U_\infty^2 H\times 2\varepsilon} \tag{7a}$$

$$\zeta_1^\star\sim -2\int_0^{G^\star}\overline{u^\star}^2(0,y^\star)\,\mathrm{d}y^\star \tag{7b}$$

$$\zeta_2^\star\sim 2\int_0^{G^\star}\overline{u^\star}^2(l^\star,y^\star)\,\mathrm{d}y^\star \tag{7c}$$

$$\zeta_3^\star\sim 2\int_0^{l^\star}\overline{u^\star}(x^\star,G^\star)\,\overline{v^\star}(x^\star,G^\star)\,\mathrm{d}x^\star \tag{7d}$$

$$\zeta_5^\star+\zeta_6^\star\sim 2\int_0^{l^\star}\int_0^{G^\star}\overline{u^\star}\frac{\partial\overline{w^\star}}{\partial z^\star}\,\mathrm{d}x^\star\mathrm{d}y^\star \tag{7e}$$

The terms listed in equation (7) are evaluated for different values of λ, and their corresponding evolution is presented in Fig. 16. The term $\zeta_1^\star$ represents the momentum flux of the underbody flow at the model rear; its evolution with λ is quadratic as expected. The examination of $(\zeta_1^\star+\zeta_2^\star)$ is suitable for different purposes. For $\lambda<0.15$, which corresponds to the range previously identified from pressure measurements as that of class (I), $\zeta_1^\star$ is almost zero, while the sum $(\zeta_1^\star+\zeta_2^\star)$ is positive. Thus, its corresponds to configurations where a large clockwise recirculation bubble *A* exists, typical of class (I). For larger values of λ, this sum is negative and its value is close to that of $\zeta_1^\star$, which corresponds to configurations where the momentum flux at the model rear is significantly higher than that through the control surface Ω_2. In these cases, the gradual increase of $\zeta_3^\star$ with λ is explained by the increase of the vertical back-flow intensity due to the backflow forming a curved jet and the separation from the ground. For $\lambda>0.5$, $(\zeta_1^\star+\zeta_2^\star)$ reaches zero while $\zeta_3^\star$ and $\zeta_5^\star+\zeta_6^\star$ remain small: this corresponds to configurations where the momentum flux at the model rear is preserved up to the control surface Ω_2, which is a property typical of class (IV). It is noteworthy that the sum $(\zeta_5^\star+\zeta_6^\star)$ is significantly smaller than the other terms over the range of λ tested, which indicates that it could reasonably be neglected. It is shown here for completeness purposes. As a summary, the momentum budget allows here to discriminate class (I), where $\zeta_1^\star+\zeta_2^\star$ is positive, from class (IV), where $\zeta_1^\star+\zeta_2^\star$ is zero; in-between, a region where $\zeta_1^\star+\zeta_2^\star$ is negative while $\zeta_3^\star$ is positive exists, and corresponds to classes (II) and (III). At this stage, it is not possible to discriminate between classes (II) and (III) using only the analyzis of the momentum terms. A further metric is required to distinguish these two classes by use of quantitative flow analyzes.

The main differences between classes (II) and (III) are the magnitude and the curvature of the back-flow which forms at the underbody exit and impinges the base as exhibited in Fig. 10(ii), or the upper shear layer as depicted in Fig. 10(iii). To illustrate this effect of curvature, the streamline starting at $(x^\star,y^\star)=(0.03,0.2)$, thus in the underbody flow, is plotted in Fig. 17 for the different values of λ considered. For classes (II) and (III), the marked curvature of the streamlines is suspected to induce a negative pressure gradient in the direction of the base, particularly for class (III) where the sign of the curvature is constant from the bottom to the top of the considered streamlines.

Thus, the local normal pressure gradient $\left(\frac{\partial p}{\partial n}\right)^\star$ related to the streamline curvature in the mid-plane is estimated by use of equation (8):

$$\left(\frac{\partial p}{\partial n}\right)^\star=2\frac{\overline{U^\star}^2}{R^\star} \tag{8}$$

where R is the local radius of curvature of the streamline. To limit the effects of measurement noise in the computation of R which involves second derivatives, the pressure gradient is averaged along the streamline up to the point where the local streamline angle with respect to the x direction is maximum. This angle corresponds to 90° in the cases where the underbody flow impinges the base. The result $\langle\left(\frac{\partial p}{\partial n}\right)^\star\rangle$ is presented in Fig. 18. This quantity is very small for class (I). For classes (II) and (IV), it remains around 0.35. A large increase up to 0.65 is obtained for class (III) around $\lambda=0.4$, which allows to efficiently discriminate between classes (II) and (III). It is remarkable that, despite the three dimensional character of the flow, a classification of the different flow structures can be derived with two simple indicators (flow momentum and pressure gradient) using the mean velocity field in a 2D vertical slice only.

5. Conclusion

In the present study, a simplified square-back tractor-trailer model of scale 1:43 is studied at a Reynolds number of 1.3×10^5. This model allows the ratio λ between the underbody velocity and the free stream velocity to be varied from 0.08 to 0.86, with the objective of identifying the effect of this single parameter on the near wake structure. The flow at the nose and upstream the separation point at the model rear is first characterized, and the boundary layer characteristics on the roof and the side walls are shown to be weakly influenced by λ. This ensures that modifications of the near wake by changing λ are not due to a disruption of the incoming flow conditions.

A first result of this study is that the variation of the underbody velocity at a constant ground clearance leads to various wake topologies. A classification between the different wakes for various λ has been made, leading to a distinction between four different flow classes that have different salient features. For class (I), high levels of transverse velocity fluctuations are noticed, and the momentum flux term $\zeta_1+\zeta_2$ is strictly positive. Other pecularities for class (I) correspond to a wake exhibiting a recirculating bubble in the upper part of the model base, and a very small base pressure vertical gradient. On the contrary, class (II) is characterized by high values of the base pressure vertical gradient together with high mean base pressure levels and a back flow phenomenon from the underbody region to the model base. For class (III), the intensity of the back-flow is high, which induces a large increase in the in-flow pressure gradient directed toward the model base. This feature is in-line with the decrease of the mean base-pressure noticed for configurations related to class (III). Furthermore in this case, the stagnation point on the model base is very close to the base top, and a new wake structure comprising a recirculating bubble located near the ground is observed. Finally, class

(IV) is characterized by the presence, in the model mid-plane, of two contra-rotating bubbles detached from the ground, as in previous studies of Ahmed body or GTS/GETS models. These different flow classes are in qualitative agreement with those derived from an earlier study (McArthur et al., 2016), in which the ground clearance only has been changed.

The existence of a back-flow appears to be a salient feature of the wake for full-scale heavy trucks, for which λ is likely to be small and remains typically lower than 0.5 even with a moving ground condition, as one consequence of the small gap between the tractor and the road, which will limit the flux under the trailor. In more realistic configurations, e.g. when taking the underride guard into account, the underbody flux is even more reduced. For trucks aerodynamics, the identification of the limit between class (II) and class (III) configurations is of practical interest; in this case, the difference in underbody flux may be small but the difference in mean base pressure significant.

Thus, GTS/GETS models used with a too large value of the ground clearance height are not appropriate to represent the wake of a heavy duty because of a non-realistic near-wake induced by a too high underbody velocity. The interpretation of the flow classes properties with respect to the possible existence of bifurcation and symmetry breaking modes, as studied in (Grandemange et al., 2013b) for instance, is of primary interest, and may require further experiments at various ground clearance heights. The identification of flow classes and their related properties are helpful to define the appropriate operating conditions for the application of control strategies (using flaps or fluidic control) to increase the mean base pressure, and reduce the drag of heavy-duty vehicles in practical applications.

Acknowledgements

This work was performed within the framework of the Labex CeLyA of the Université de Lyon, within the programme "Investissements d'Avenir" (ANR-10- LABX-0060/ANR-11-IDEX-0007) operated by the French National Research Agency (ANR). The funding of ANRT (CIFRE grant 2013/1446 with Renault Trucks) for the PhD thesis of M.Szmigiel is gratefully acknowledged. The authors wish to thank J.M. Perrin, E.Jondeau, N.Grosjean and P.Souchotte for their technical support during the experiments; the help of C.Sicot (Pprime) with the pressure scanner is also acknowledged.

Appendix A

The boundary layer thickness δ_{99}, the displacement thickness δ, the momentum thickness θ_0, the shape factor $h = \delta/\theta_0$ and the Reynolds number Re_{θ_0} are given for several values of λ, in Table 1 for the boundary layer on the roof and in Table 2 for the boundary layer on a side wall. The momentum thickness is smaller on the side wall than on the roof, which is attributed to the limited flow separation effect at the model nose. The momentum thickness is more dependent on λ on the side wall than on the roof, which may be due to the disturbances located at the model front in the cases of small λ values.

References

Ahmed, S.R., Ramm, G., Faltin, G., 1984. Some salient features of the time-averaged ground vehicle wake. SAE Int. Congr. Expo. https://doi.org/10.4271/840300, 840300.

Barros, D., Borée, J., Noack, B.R., Spohn, A., Ruiz, T., 2016. Bluff body drag manipulation using pulsed jets and coanda effect. J. Fluid Mech. 805, 422–459.

Basara, B., 2015. Fluid flow and conjugate heat transfer in a matrix of surface-mounted cubes: a PANS study. Int. J. Heat Fluid Flow 51, 166–174. https://doi.org/10.1016/j.ijheatfluidflow.2014.10.012.

Bonnavion, G., Cadot, O., Évrard, A., Herbert, V., Délery, J., 2017. On multistabilities of real car's wake. J. Wind Eng. Ind. Aerod. 164, 22–33.

Cadot, O., Courbois, A., Ricot, D., Ruiz, T., Harambat, F., Herbert, V., Vigneron, R., Delery, J., 2016. Characterizations of force and pressure fluctuations on real vehicles. Int. J. Eng. Syst. Model Simulat. https://doi.org/10.1504/IJESMS.2016.075529.

Chaligné, S., 2013. Contrôle du sillage d'un corps non profilé. Application expérimentale à une maquette simplifiée de véhicule industriel, Bluff-body wake control. Experimental application on a reduced-scale model of industrial vehicle. PhD Thesis. Université de Lyon, pp. 2013–2050. ECL - No.

Croll, R.H., Guttierez, W.T., Hassan, B., Suazo, J.E., Riggins, A.J., 1996. Experimental Investigation of the Ground Transportation Systems (GTS) Project for Heavy Vehicle Drag Reduction, SAE Technical Paper. https://doi.org/10.4271/960907.

Garry, K.P., 1996. Some effects of ground clearance and ground plane boundary layer thickness on the mean base pressure of a bluff vehicle type body. J. Wind Eng. Ind. Aerod. 62, 1–10. https://doi.org/10.1016/S0167-6105(96)00054-2.

Grandemange, M., Gohlke, M., Cadot, O., 2013. Bi-stability in the turbulent wake past parallelepiped bodies with various aspect ratios and wall effects. Phys. Fluids 25. https://doi.org/10.1063/1.4820372.

Grandemange, M., Gohlke, M., Cadot, O., 2013. Turbulent wake past a three-dimensional blunt body. Part 1. Global modes and bi-stability. J. Fluid Mech 722, 51–84. https://doi.org/10.1017/jfm.2013.83.

Grandemange, M., Ricot, D., Vartanian, C., Ruiz, T., Cadot, O., 2014. Characterisation of the flow past real road vehicles with blunt afterbodies. Int. J. Aerodyn 4 (1/2), 24–42.

Grandemange, M., Cadot, O., Courbois, A., Herbert, V., Vigneron, R., 2015. A study of wake effects on the drag of Ahmed's squareback model at the industrial scale. J. Wind Eng. Ind. Aerod. 145, 282–291.

Gutierrez, W.T., Hassan, B., Robert, H., 1996. Aerodynamics overview of the ground transportation systems (GTS) project for heavy vehicle drag reduction. SAE Int. Congr. Expo. https://doi.org/10.4271/960906, 960906.

Hwang, B.G., Lee, S., Lee, E.J., Kim, J.J., Lee, S.J., 2016. Reduction of drag in heavy vehicles with two different types of advanced side skirts. J. Wind Eng. Ind. Aerod. 155, 36–46.

Islam, A., Gaylard, A., Thornber, B., 2017. A detailed statistical study of unsteady wake dynamics from automotive bluff bodies. J. Wind Eng. Ind. Aerod. 171, 161–177.

Klebanoff, P.S., 1955. Characteristics of Turbulence in a Boundary Layer with Zero Pressure Gradient. NACA-TR-1247.

Krajnovic, S., Davidson, L., 2015. Influence of floor motions in wind tunnels on the aerodynamics of road vehicles. J. Wind Eng. Ind. Aerod. 93, 677–696.

Kowata, S., Ha, J., Yoshioka, S., Kato, T., Kohama, Y., 2008. Drag force reduction of a bluff-body with an underbody slant and rear flaps. SAE Int. J. Commer. Veh 1, 230–236. https://doi.org/10.4271/2008-01-2599.

Littlewood, R.P., Passmore, M.A., 2012. Aerodynamic drag reduction of a simplified squareback vehicle using steady blowing. Exp. Fluid 53, 519–529. https://doi.org/10.1007/s00348-012-1306-4.

Martinuzzi, R., Tropea, C., 1993. The flow around surface-mounted, prismatic obstacles placed in a fully developed channel flow (data bank contribution). J. Fluid Eng. 115, 85. https://doi.org/10.1115/1.2910118.

McArthur, D., Burton, D., Thompson, M., Sheridan, J., 2016. On the near wake of a simplified heavy vehicle. J. Fluid Struct. 66, 293–314. https://doi.org/10.1016/j.jfluidstructs.2016.07.011.

Nakashima, T., Tsubokura, M., Nouzawa, T., Nakamura, T., Zhang, H., Oshima, N., 2008. Large-eddy Simulation of Unsteady Vehicle Aerodynamics and Flow Structures, Bluff Bodies Aerodynamics & Applications (BBAA VI) International Colloquium, Milano, Italy, pp. 20–24. July.

Perry, A.-K., Passmore, M.A., 2013. The impact of underbody roughness on rear wake structure of a squareback vehicle. SAE Tech. Pap. https://doi.org/10.4271/2013-01-0463, 2013-01-04.

Salati, L., Schito, P., Cheli, F., 2017. Wind tunnel experiment on a heavy truck equipped with front-rear trailer device. J. Wind Eng. Ind. Aerod. 171, 101–109.

Storms, B.L., Ross, J.C., Heineck, J.T., Walker, S.M., Driver, D.M., Zilliac, G.G., 2001. An Experimental Study of the Ground Transportation System (GTS) Model in the NASA Ames 7- by 10-Ft Wind Tunnel. NASA/TM-2001–209621.

Szmigiel, M., Castelain, T., Michard, M., Juvé, D., Chacaton, D., 2016. Impact of the Underside Velocity on the Drag Reduction of a Trailer Model Using a Passive Control System, Aerovehicles II, Göteborg, Sweden. June 21–23.

Szmigiel, M., 2017. Effet du flux de soubassement sur la dynamique du sillage d'un corps non profilé à culot droit. Application du contrôle actif pour la réduction de traînée de véhicule industriel, Effect of the underbody flux on square-back body-wake dynamics. Application of active control to drag reduction on an industrial vehicle. PhD thesis. Université de Lyon, 2017LYSEC16.

Uffinger, T., Ali, I., Becker, S., 2013. Experimental and numerical investigations of the flow around three different wall-mounted cylinder geometries of finite length. J. Wind Eng. Ind. Aerod. 119, 13–27.

Van Raemdonck, G.M.R., Van Tooren, M.J.L., 2008. Time-averaged Phenomenological Investigation of a Wake behind a Bluff Body, Bluff Bodies Aerodynamics & Applications (BBAA VI) International Colloquium, Milano, Italy, pp. 20–24. July.

International Journal of Heat and Fluid Flow 50 (2014) 188–200

Contents lists available at ScienceDirect

International Journal of Heat and Fluid Flow

journal homepage: www.elsevier.com/locate/ijhff

Investigation of the mixing layer of underexpanded supersonic jets by particle image velocimetry

Benoît André [a], Thomas Castelain [a,b,*], Christophe Bailly [a,c]

[a] Ecole Centrale de Lyon, Université de Lyon, Laboratoire de Mécanique des Fluides et d'Acoustique, UMR CNRS 5509, 36, avenue Guy de Collongue, 69134 Ecully Cedex, France
[b] Université Lyon 1, 43 Boulevard du 11 Novembre 1918, 69622 Villeurbanne Cedex, France
[c] Institut Universitaire de France, 103 bd Saint-Michel, 75005 Paris, France

ARTICLE INFO

Article history:
Received 18 November 2013
Received in revised form 19 June 2014
Accepted 6 August 2014
Available online 12 September 2014

Keywords:
Underexpanded supersonic jets
Particle image velocimetry
Turbulence
Broadband shock-associated noise

ABSTRACT

The present experimental study focuses on some properties of the turbulence and the shock-cell structure in underexpanded supersonic jets, which are of practical relevance in air transport. Choked jets at fully expanded Mach numbers M_j = 1.10, 1.15, 1.35 and 1.50 are investigated using particle image velocimetry. The strength of the shock-cell structure is studied from mean velocity profiles, both in the jet core and in the mixing layer. The general geometry of the latter and its location relatively to the mean shock-cell structure are established. Furthermore, detailed accounts of mixing layer thickness, turbulence levels, spatial correlations and intrinsic turbulence length scales are given. While the mean velocity variations related to the shock-cell structure extend up to the subsonic part of the studied jets, their mixing layer is found to be mostly located in the subsonic region. Some of the observed turbulence properties, like the mixing layer thickness and turbulence levels, are close to what is found for subsonic jets. The effect of the shock-cell structure on turbulence is however visible for $M_j \geqslant 1.35$. The spatial correlations of turbulence are used to estimate intrinsic turbulence length scales and these are found to be of the order of the shock-cell length. These data are used to make some comments upon the generation mechanism of shock-associated noise, a noise component produced by imperfectly expanded supersonic jets.

1. Introduction

A large part of the current commercial aircraft is powered by a high-bypass-ratio engine, in which a hot primary stream is embedded in a cold secondary (fan) flow. At the typical subsonic cruise conditions, the secondary jet becomes underexpanded, meaning that the pressure in the nozzle exit plane is greater than the ambient pressure. This situation induces a shock-cell structure inside the flow, which brings the jet pressure down to the ambient pressure through a pattern of expansions and compressions. Another particularity of such flows compared to subsonic jets is the emission of a specific noise component called the shock-associated noise. This is made up of a tonal part, also known as screech, and a broadband part.

The shock-cell structure of underexpanded jets was much studied experimentally, especially through extensive static pressure measurements (Norum and Seiner, 1982; Norum and Shearin, 1988), and also by the authors of the present paper (André et al., 2014). However, detailed accounts of the turbulence in such jets are scarce. Seiner and Norum (1980) measured turbulence levels and spectra using a hot film probe. Panda and Seasholtz (1999) obtained the coherent part of the density fluctuations in choked jets using the Rayleigh scattering technique and related this to the screeching process. Several studies applied particle image velocimetry (PIV) to these flows. Jerónimo et al. (2002) investigated the first shock cell of an overexpanded jet showing a Mach disc. Alkislar et al. (2003) separated the random from the coherent turbulent motion in the mixing layer of a screeching rectangular jet using stereoscopic PIV, and pinpointed the relation between coherent vortices and screech generation. Bridges and Wernet (2008) applied high-speed PIV to screeching and non-screeching supersonic jets, mainly focusing on turbulence spectra.

The objective of the present experimental study is to focus on some properties of the turbulence and the shock-cell structure in the mixing layer of underexpanded supersonic jets using particle image velocimetry. To begin with, the strength of the shock-cell structure in the mixing layer is estimated. Then, a study of the turbulence of these jets is reported. It addresses the overall structure of the mixing layer, its thickness, turbulence levels, spatial correlations and turbulence length scales in the convected frame. In the

* Corresponding author. Address: Centre Acoustique, Ecole Centrale de Lyon, 36, avenue Guy de Collongue, 69134 Ecully Cedex, France. Tel.: +33 4 72 18 60 15.
E-mail address: thomas.castelain@ec-lyon.fr (T. Castelain).

http://dx.doi.org/10.1016/j.ijheatfluidflow.2014.08.004
0142-727X/

concluding remarks, some comments upon the generation mechanism of shock-associated noise are made in light of the obtained data.

2. Experimental methods

The facility employed in the present work has already been used to study single-stream supersonic jets (André et al., 2014) as well as co-axial jets (André et al., 2011). The configuration considered here is the latter one, with the outer stream set at a Mach number of 0.05 to seed the surroundings of the inner, supersonic jet, during the PIV measurements.

The supersonic jet flow originates from a continuously operating compressor mounted upstream of an air drier. It exhausts through a round, contoured and convergent nozzle of diameter $D = 38.7$ mm. Since the underexpanded jets exiting typical turbofan engines of civil aircraft do not seem to emit the tonal component of shock-associated noise (screech noise), and considering that this component has a strong impact on the jet dynamics (André et al., 2012; André et al., 2013), it appears relevant to eliminate it in the small-scale study. For that purpose, a screech-suppressing nozzle is employed, showing shallow notches carved into its lip. As indicated in André et al. (2013), this nozzle non-intrusively suppresses screech. The reservoir temperature T_t is measured upstream of the exit. Here, the jets are unheated and $T_t \approx 30$ °C. The nozzle pressure ratio (NPR), defined as the ratio between jet stagnation pressure and ambient pressure, is set by measuring the wall static pressure fifteen nozzle diameters upstream of the exit. In the following, results for jets of ideally expanded Mach numbers $M_j = 1.10$, 1.15, 1.35 and 1.50 are presented, corresponding to NPR = 2.14, 2.27, 2.97 and 3.67, respectively. The convective Mach numbers M_c of these jets are 0.49, 0.51, 0.59 and 0.63 for increasing M_j.

A conventional Z-type schlieren system is used to visualise the flow. It consists of a light-emitting diode, two 203.2 mm-diameter f/8 parabolic mirrors, a straight knife-edge set perpendicular to the flow direction and a high-speed Phantom V12 CMOS camera.

Particle image velocimetry has also been applied to measure velocity in a plane containing the jet axis and a notch. Illumination is provided by a pulsed double-cavity Nd:YLF Quantronix Darwin Duo laser and the sheet thickness is 1.7 mm (±0.3 mm). The supersonic jet is seeded with olive oil by means of custom-designed Laskin nozzle generators. The mean particle size is known to be around 1 μm. The secondary flow is seeded by smoke. Both seeding devices are mounted far enough upstream of the exit so that the particle concentration in each flow is approximately uniform. Two CMOS cameras of sensor size 1280×800 pixels^2 are set side by side to double axially the field of view available, which covers a length of about two jet diameters. In the radial direction, only one half of the jet is visualised, since the other part can be deduced by axisymmetry. The PIV set-up is mounted on a frame which can be translated in the jet direction; an axial extent of $12D$ is studied here, meaning that the entire field has been acquired in six parts. For each new location of the frame, a calibration of the camera images is performed using a three-dimensional LaVision plate, the jet operating conditions are reset and 2000 image pairs are recorded. The acquisition frequency of the image pairs is 500 Hz and the magnifying factor for each camera is about 0.05 mm.pixel^{-1}. The delay between the images of each pair is set to 3 μs for all jet conditions. Vector field calculation is performed by a multigrid FFT-based technique using the LaVison DaVis 7.2 software. In all but the last iteration of the velocity computation procedure, the calculation is a two-step process; a 25%-overlap of the interrogation windows is set and no window ponderation is used. For the last iteration, three computational steps are set, as well as a 50%-overlap and an isotropic Gaussian window ponderation. The final correlation windows are of size 8×8 pixels^2, leading to a vector density of one every 0.2 mm, or approximately 190 vectors across the supersonic jet diameter.

The behaviour of the seeding particles in imperfectly expanded jets was studied by André et al. (2014) from laser Doppler velocimetry (LDV) data. It was concluded that the particles followed accurately the flow in slightly underexpanded jets and even in the presence of a Mach disc. The mean velocity results obtained by PIV were compared to LDV profiles and a good agreement was found; the latter technique was validated in André et al. (2014). Our results were also found to be in good agreement with RANS simulations performed during a companion study (Henry et al., 2012).

In the following, the origin of the coordinates is taken on the jet axis, in the nozzle exit plane. The variable x will denote the axial direction and y the transverse direction.

3. Results

In order to introduce the shock-cell structure typical of underexpanded supersonic jets, spark schlieren images of two jets at $M_j = 1.10$ and 1.50 are presented in Fig. 1. Owing to the orientation of the knife-edge in the schlieren set-up, axial gradients of density are visualised here. The well-known quasi-periodic shock-cell pattern is visible. The light (dark) regions correspond to expansion (compression) regions, see Panda and Seasholtz (1999) and André et al. (2014) for more details about the mean shock-cell pattern. At $M_j = 1.50$, a small normal shock, called Mach disc, forms in the first shock cell. Turbulent fluctuations are also visible in these pictures. The fact that they even appear in the jet core region is a result of the integration of the density gradients across the entire jet. Other schlieren images of such jets, also with different knife-edge orientations, can be found in Powell (1953), Seiner and Norum (1979) or Panda (1999), among others.

3.1. Shock-cell structure in the mixing layer

Usually, pressure measurements are used for quantifying the strength of the mean flow gradients (Norum and Seiner, 1982; Norum and Shearin, 1988) but they are generally confined to the jet core. We focus here on the mean flow gradients near the mixing layer. To that end, the velocity gradients in the mixing layer are deduced from the mean velocity maps obtained by PIV, and compared to those existing in the jet core. The extreme values of M_j, namely 1.10 and 1.50, are considered.

A map of mean velocity for $M_j = 1.10$ is presented in Fig. 2, along with calculated mean flow streamlines. The mean velocity on these streamlines, which are almost straight at this low underexpansion, is shown in Fig. 3(a), while the computed gradients of the mean velocity along the streamlines are displayed in (b). It is visible that the gradients wear off when moving downstream or toward the mixing layer and that they remain small in the entire flow. It is also worth noting that the gradients are still present in the subsonic region of the jet.

The flow with $M_j = 1.50$ is now studied. The cartography of the mean velocity is displayed in Fig. 4. The streamlines present a curvature, which comes from the lateral expansions and constrictions of the jet plume, induced by the stronger underexpansion. Because of strong gradients both in the axial and radial directions in the Mach disc region, the velocity estimates from the particle image analysis are there only approximate. The velocity on the jet centreline is nonetheless shown in order to compare the estimated strong gradients associated with the Mach disc with those observed elsewhere in the jet. A signature of the Mach disc is the

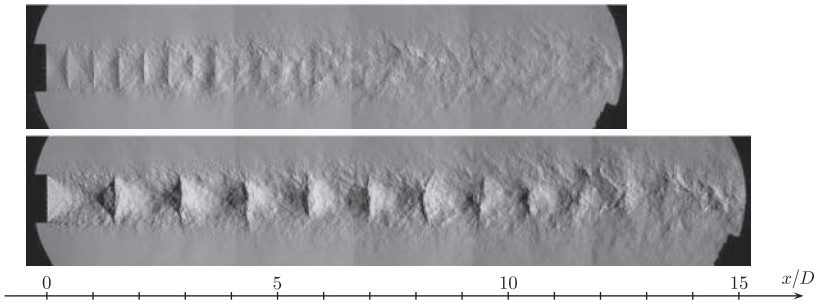

Fig. 1. Schlieren images of two jets at $M_j = 1.10$ (top) and 1.50 (bottom). Each picture is made up of several uncorrelated spark images (exposure time of 4 μs) recorded at different axial locations. The notches cut into the nozzle lip explain the ejections visible at the exit, especially for $M_j = 1.50$.

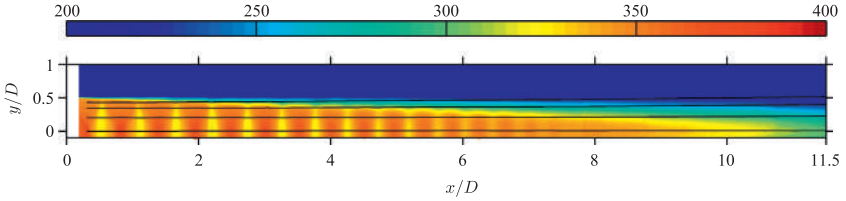

Fig. 2. Cartography of the mean velocity $u = \sqrt{\overline{u_1}^2 + \overline{u_2}^2}$ (m s^{-1}) for $M_j = 1.10$ (u_1 and u_2 are the longitudinal and transverse velocity components, respectively, and the overbar denotes the ensemble averaged value). The horizontal lines represent mean flow streamlines.

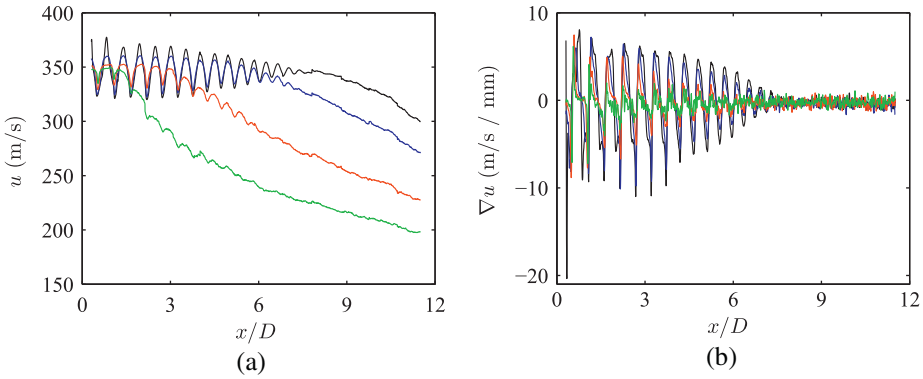

Fig. 3. (a) Mean velocity profiles measured on the mean streamlines depicted in Fig. 2, (b) velocity gradients calculated along the same streamlines; $M_j = 1.10$. The radial stations of the streamlines at their upstream location are $y/D = 0$ (—), 0.2 (—), 0.35 (—), and 0.43 (—).

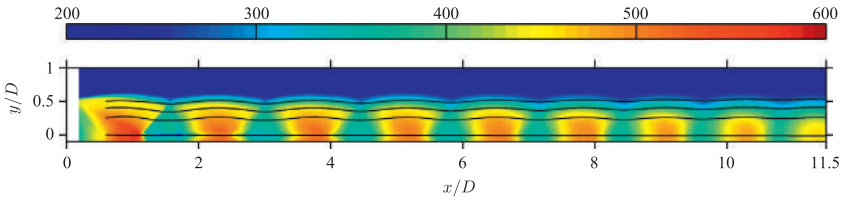

Fig. 4. Cartography of u (m s^{-1}) for $M_j = 1.50$. The horizontal lines represent mean streamlines.

strong negative peaks on the black curve in Fig. 5(b). For the other streamlines, the gradients are also sharp in the first shock cell due to the oblique shock attached to the Mach disc. However, they quickly become weaker downstream. In the second shock cell already, they are larger than, but have the same order of magnitude as, in the case $M_j = 1.10$.

3.2. Turbulence in the mixing layer

The remainder of the paper focuses on the properties of turbulence in the investigated jets. It has to be noted that such small-scale jets naturally sustain a large-scale oscillation due to the screech noise (André et al., 2011) so that it is usually relevant to separate the random fluctuations from the organised, highly energetic, ones (Alkislar et al., 2003). Here, this analysis is not needed since the screech tones, and so the associated oscillations, are suppressed, as was mentioned in Section 2.

3.2.1. General structure of the mixing layer

To begin with, an overview of the structure of the mixing layer is proposed. The mixing layer centre and boundaries are determined and compared to the mean flow pattern.

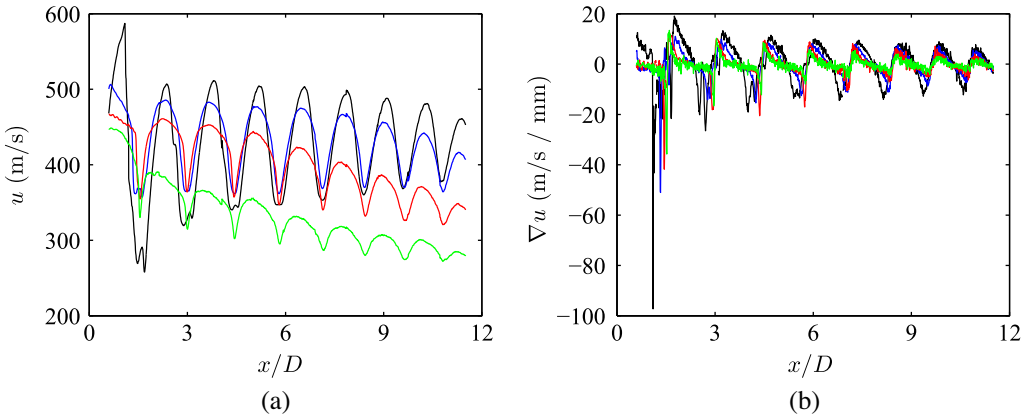

Fig. 5. (a) Mean velocity profiles measured on the mean streamlines depicted in Fig. 4, (b) velocity gradients calculated along the same streamlines; $M_j = 1.50$. The radial stations of the streamlines at their upstream location are $y/D = 0$ (—), 0.25 (—), 0.4 (—), 0.5 (—).

The mixing layer centre is simply determined as the location where the axial velocity fluctuations are the strongest. So as to properly define the mixing layer boundaries, the fluctuation data obtained by the PIV are used. For each axial station, the radial location of the maximum root-mean-square value of the axial velocity fluctuations is determined. In the high- and low-velocity side of the flow, the fluctuation minima are searched. For each side, the mixing layer boundary is defined as the location where the root-mean-square velocity has decreased to 0.1 times the difference between the maximum and the minimum of the fluctuations.

In order to have an idea of the location of the mixing layer relatively to the mean flow, it is of interest of knowing which portion of the mixing layer is supersonic and which is subsonic. Local Mach numbers can be inferred from the PIV data if it is assumed that the total temperature is uniform in the jet and equal to the reservoir temperature, by the formula

$$M = \left\{ \frac{u^2}{\gamma r T_t - u^2(\gamma - 1)/2} \right\}^{1/2} \tag{1}$$

where M is the local Mach number, u the mean velocity, T_t the reservoir temperature, $\gamma = 1.4$ and $r = 287.06\ \mathrm{J\ kg^{-1}\ K^{-1}}$. The sonic line (locus of the unit Mach numbers) is then easily deduced and can be used to separate the supersonic part of the mixing layer from the subsonic part. The total temperature uniformity can be assumed because the jets are unheated, meaning that the total temperature inside the supersonic jet is very close to that of the low-speed coflow. Furthermore, it was checked that a possible change in the total temperature only had a limited effect on the results presented in the following.

A map of the jet plume for the operating condition $M_j = 1.10$, combining local Mach number and root-mean-square axial velocity fields, is presented in Fig. 6. Also included on both cartographies are the locations of the mixing layer boundaries, of the mixing layer centre, and of the sonic line (all the lines are symmetric about the jet axis, and the line of the mixing layer centre has been smoothed for better readability). It can be said from this figure that all lines are almost straight; hence, no influence of the shock-cell structure is visible. Furthermore, the inner boundary of the mixing layer reaches the jet axis around $x/D = 9$, which marks the end of the potential core; downstream of this axial station, the mixing layer has grown across the entire jet. The supersonic core, being the region of supersonic flow, extends of course beyond the potential core, up to $10.5D$. Note also that the outer boundary of the mixing layer reaches the outermost measured location near $x/D = 10$, meaning that past this point, the real outer boundary extends actually still further outward than it is shown here. More importantly, it is obvious from Fig. 6 that most of the mixing layer is at subsonic conditions, and that the supersonic part is very thin. In particular, the mixing layer centre lies well inside the subsonic region of the jet. These observations remain true if the transverse velocity fluctuations are considered instead of the axial ones.

Similar results for $M_j = 1.50$ are proposed in Fig. 7. The lines are only drawn on the relevant half for easier reading. Compared to $M_j = 1.10$, the mixing layer centre and the sonic line are clearly undulating periodically, which is related to the succession of lateral expansions and constrictions induced by the stronger underexpansion at this operating condition. Note also the secondary ejection through a notch, visible near the nozzle exit.

A direct comparison between the two jets is proposed in Fig. 8, where the locations of mixing layer centre and boundaries relatively to the sonic line are shown. The locations of the sonic line and of the centre, inner boundary and outer boundary of the mixing layer are denoted by y_s, y_c, y_i and y_o, respectively. The curves are truncated at $x/D = 8$ for $M_j = 1.10$ since the shock-cell structure ends approximately there. It is clearly illustrated by these plots that the mixing layer centre lies in the subsonic part for both jets and that the mixing layer is mostly subsonic. It seems however

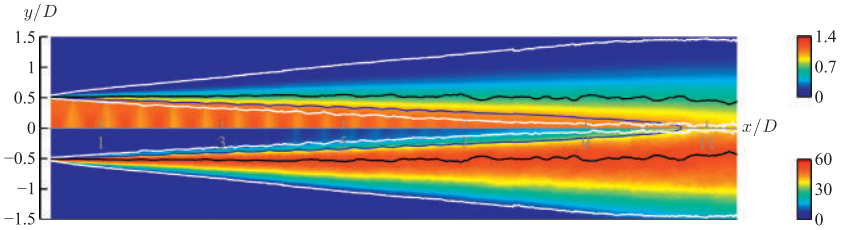

Fig. 6. Combined maps of local Mach number M on the top half and root-mean-square axial velocity fluctuations on the bottom half (in $\mathrm{m\ s^{-1}}$), $M_j = 1.10$. Superimposed on both maps are: (white lines) mixing layer inner and outer boundaries, (black line) mixing layer center, (blue line) sonic line. For reference, the spatial mean centreline velocity for the supersonic jet is $345\ \mathrm{m\ s^{-1}}$. (For interpretation of the references to colour in this figure legend, the reader is referred to the web version of this article.)

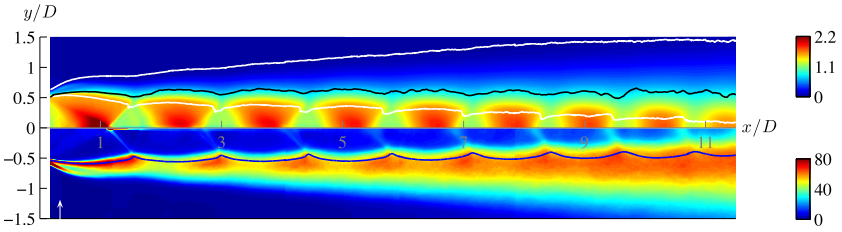

Fig. 7. Same legend as in Fig. 6, but for $M_j = 1.50$. The arrow on the bottom map pinpoints the ejection through the notch contained within the measurement plane. For reference, the spatial mean centreline velocity for the supersonic jet is 423 m s^{-1}.

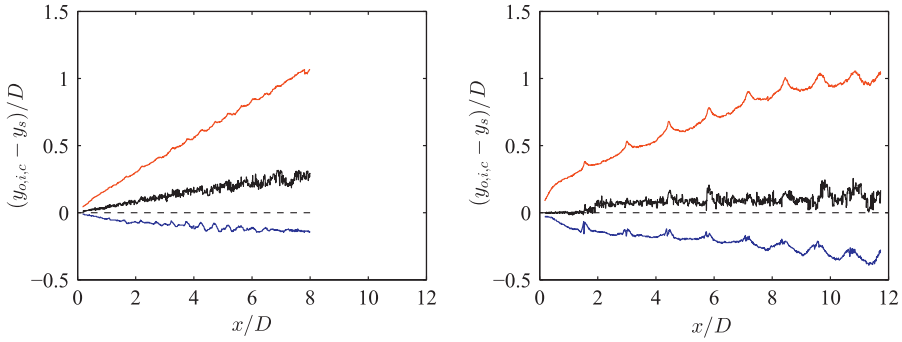

Fig. 8. Location of the mixing layer boundaries and mixing layer centre relatively to the sonic line. (a) $M_j = 1.10$, (b) $M_j = 1.50$. — $(y_c - y_s)/D$, — $(y_i - y_s)/D$, — $(y_o - y_s)/D$. The dashed horizontal line marks the sonic line location ($y = y_s$).

that the three curves tend to move down when M_j is increased, which is confirmed by the results at the intermediate values of M_j (not shown here). This means in particular that the mixing layer centre moves closer to the sonic line for increasing M_j, while the supersonic part of the mixing layer thickens.

An interesting feature of the jet at $M_j = 1.50$ can also be seen in Fig. 7. The axial stations of the turbulence maxima are not perfectly aligned with the end of the mean shock cells. The shift between the upper and lower map of the figure is made clear by the drawing of the sonic line on the lower map: the turbulence maxima are slightly ahead of the mean velocity minima, and even more so when moving downstream. This situation entails deep incursions of pockets of high turbulence intensity inside the supersonic region of the jet. This adds up to the relative closeness of the mixing layer centre to the supersonic region of the jet, as compared to the jet at $M_j = 1.10$, and constitutes a noticeable difference between the jets at $M_j = 1.10$ and $M_j = 1.50$.

3.2.2. Mixing layer thickness

The mixing layer momentum thickness is now assessed, as it is the relevant parameter for studying the stability of shear layers (Michalke, 1965). It will also provide a useful length scale for the following analysis.

Usually, the momentum thickness δ_θ is defined as

$$\delta_\theta = \int_{y_0}^{\infty} \frac{\overline{\rho u_1}}{(\overline{\rho u_1})_0}\left[1 - \frac{\overline{u_1}}{(\overline{u_1})_0}\right] dy \qquad (2)$$

for compressible flows (White, 1974). In Eq. (2), ρ and u_1 are the density and the axial component of velocity, y is the radial coordinate and y_0 a reference location. The subscript 0 means that the variables are taken at $y = y_0$ and the overbar denotes the mean value. This definition is used for instance by Ponton and Seiner (1992) and Cheng and Lee (2005) in the case of imperfectly expanded supersonic jets. They define different reference positions y_0 though. Cheng and Lee (2005) perform the integral (2) from the jet axis ($y_0 = 0$). Since the velocity on the axis is not always the maximum velocity of a radial profile owing to the shock-cell structure (typically, near the end of the compression regions), negative contributions will occur in the integral. Therefore, the computed momentum thickness oscillates across the shock cells, and can even take on negative values. In order to avoid this problem, Ponton and Seiner (1992) perform the integration from the radial location of the maximum velocity. However, it happens that the maximum velocity be located well inside the jet, again due to the shock-cell structure (typically, near the end of the expansion regions). In such an event, some integrated components do not belong to the mixing layer and its thickness is overestimated.

The incompressible version of Eq. (2) is employed here, since only the velocity is measured. It reads

$$\delta_\theta = \frac{1}{[\overline{u_1}(y_i) - \overline{u_1}(y_o)]^2} \int_{y_i}^{y_o} [\overline{u_1}(y) - \overline{u_1}(y_o)][\overline{u_1}(y_i) - \overline{u_1}(y)] dy \qquad (3)$$

In order to avoid the above-mentioned issues concerning the selected integration limits, they are chosen here as y_i and y_o, the inner and outer mixing layer boundaries defined in Section 3.2.1. In the event that negative contributions to δ_θ would be integrated, which happens when the inner boundary is closer to the jet axis than the velocity maximum in the radial direction, δ_θ is not computed. This explains some blanks in the curves displayed hereafter. In Fig. 9 is shown a comparison between the estimations of δ_θ obtained by the different definitions of the integration limits introduced above. It is clear that integrating over the present boundaries induces a disappearance of the trace of the shock-cell structure altogether and that the evolution of δ_θ becomes linear, for this operating condition.

Another mixing layer thickness can simply be defined as

$$\delta = y_o - y_i$$

It has been found that it closely corresponds to 7.5 times δ_θ for all values of M_j investigated. This relation is exemplified in the case $M_j = 1.10$ in Fig. 10.

The evolution of δ_θ until the end of the potential core of each jet is shown in Fig. 11 for all values of M_j. The extent of the potential core is determined from the centreline mean velocity profiles. Only

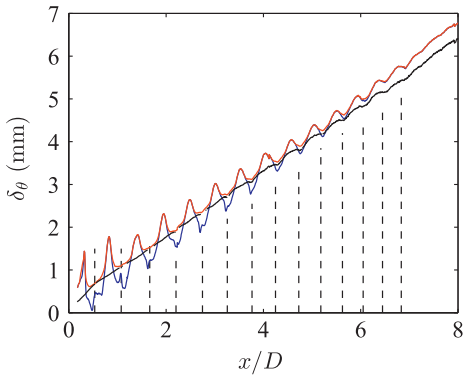

Fig. 9. Comparison of different calculation techniques for δ_θ (M_j = 1.10). For each curve, Eq. (3) is used, with — y_i = 0 and y_o the furthest location acquired, — y_i the location of maximum velocity and y_o the furthest location acquired, — y_i and y_o defined by the method proposed here. The dashed lines mark the end of the shock cells (end of the compression regions).

in the case of M_j = 1.50 does it extend beyond the measured field of view.

Firstly, it has to be noted that in the case of M_j = 1.35 and 1.50, the computation of the outer mixing layer boundary suffers from the limited radial extent of the field of view, as can be seen in Fig. 7: sufficiently far downstream, it is constrained to remain in the measured domain, while it should exit it. This situation should have a limited effect on δ_θ though, for the integrand in Eq. (3) is small near the mixing layer boundaries. The deviation from linearity observed on δ_θ for M_j = 1.35 and 1.50 far enough downstream can probably be explained by this effect. Secondly, it is visible that the very beginning of the mixing layer is thickening at a faster rate than further downstream, and even more so when M_j increases. This is due to the presence of a notch in the measurement plane, which entails a secondary ejection through it and thus a thicker mixing layer (indeed, measurements with a plain nozzle do not show this feature). When M_j is increased, the NPR also becomes larger and the secondary ejection is more pronounced, which explains the larger effect observed at high M_j. Thirdly, the mixing layer growth is linear beyond the first diameter for all conditions, which is characteristic of fully turbulent mixing layers (Troutt and McLaughlin, 1982). The slope of this linear growth decreases when M_j increases. This can be mostly explained by the reduced mixing efficiency induced by increased compressibility (Papamoschou and Roshko, 1988) (compressibility effects are often parametrised by convective Mach numbers, whose values have been indicated for the studied jets in Section 2.). The decrease in mixing layer growth rate entails the well-known potential core lengthening when M_j increases (Lau, 1981). The numerical values of the slopes are gathered in Table 1. As a comparison, the growth rates measured by Fleury et al. (2008) in subsonic jets at Mach numbers of 0.6 and 0.9 are 0.0289 and 0.0265, respectively. The present results are thus consistent with subsonic values. Finally, an effect of the shock-cell structure on the mixing layer thickness can only be identified at the highest underexpansions (M_j = 1.35 and 1.50) in the form of an increase of δ and δ_θ at the end of the shock cells. This cannot be seen on Fig. 11 due to the blanks explained earlier but it is readily visible in Fig. 7.

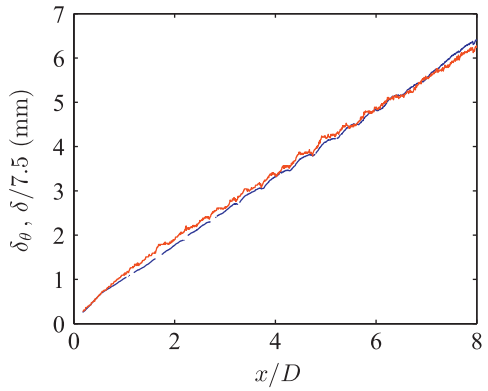

Fig. 10. Relationship between δ_θ and δ, M_j = 1.10. — δ_θ, — $\delta/7.5$.

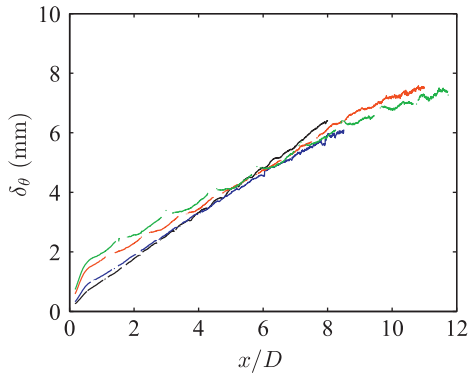

Fig. 11. Evolution of δ_θ with axial distance. — M_j = 1.10, — M_j = 1.15, — M_j = 1.35, — M_j = 1.50.

3.2.3. Turbulence levels

The turbulence levels measured in the mixing layer of the four jets studied are now analysed. Turbulence being mainly produced by velocity gradients, the ratios of the root-mean-square velocity fluctuations (written σ_1 and σ_2 for u_1 and u_2, the velocity components in the longitudinal and transverse direction) over the velocity difference ΔU between the supersonic jet and the low-speed co-flow are formed to provide indicators of turbulence levels. Since underexpanded supersonic jets are not uniform, it is not obvious which velocity is to be considered to compute ΔU. A spatial mean velocity is chosen here, about which the axial velocity oscillates in the shock-cell structure.

Turbulence levels are plotted in the following on the lines of peak fluctuations for u_1. The results for M_j = 1.10 and 1.15 are shown in Fig. 12. The turbulence intensities are seen to be quite flat; the higher values near the nozzle exit are an effect of the notch located in the plane of visualization. They reach 16% for the longitudinal velocity for both conditions, while the levels associated with the transverse component are between 10% and 11%. These values are in good agreement with what is observed in subsonic jets. Davies et al. (1963) measured with a hot wire probe peak turbulence levels of 16% in the mixing layer of round jets of Mach numbers lower than 0.6. Fleury (2006) obtained longitudinal profiles of turbulence intensity which are also flat and show about the same values as the present ones, for jet Mach numbers of 0.6 and 0.9. The results of Jordan et al. (2002) and Kerhervé et al. (2004), obtained by laser Doppler velocimetry for a jet Mach number of 0.9 and in a perfectly expanded jet at M_j = 1.2, respectively, also suggest the same behaviour for the axial evolution of the velocity fluctuations. It seems therefore that the shock-cell

Table 1
Growth rate of δ_θ as a function of M_j.

M_j	1.10	1.15	1.35	1.50
$d\delta_\theta/dx$	0.0199	0.0175	0.0158	0.0141

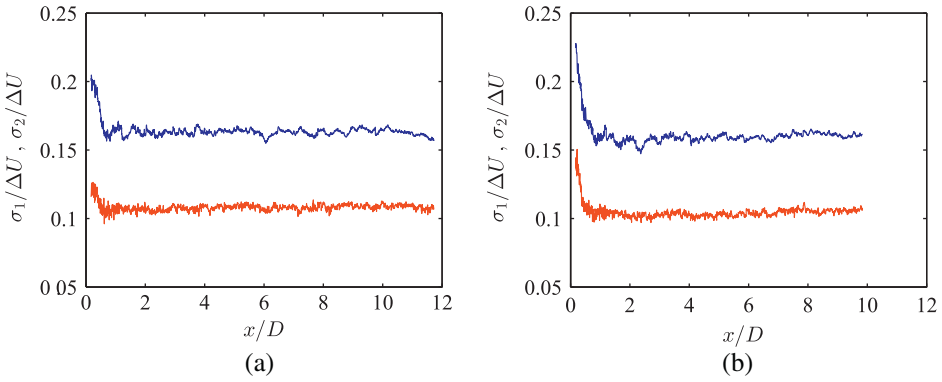

Fig. 12. Longitudinal and transverse turbulence levels in the mixing layer. (a) M_j = 1.10, (b) M_j = 1.15. — $\sigma_1/\Delta U$, — $\sigma_2/\Delta U$.

structure has little influence on the turbulence levels at these small degrees of underexpansion. This conclusion has already been reached by Seiner and Norum (1980) from the comparison of fluctuation spectra between one underexpanded jet and a fully expanded jet of same M_j.

At M_j = 1.35, and even more at M_j = 1.50, the line of the maxima of fluctuation in the mixing layer undulates slightly, as it is visible in Fig. 7. The turbulence intensities on the lines of peak values for σ_1 are shown in Fig. 13. In the first shock cell, the fluctuation levels remain approximately constant, before dropping sharply at the beginning of the second shock cell. Still further, the transverse turbulence intensities lie close to 10%, as for the slightly underexpanded jets, but start from a slightly lower value and tend to increase in the downstream direction. As for σ_1, an obvious oscillation of the levels can be observed, where the maxima are reached near the end of the compression regions (but slightly upstream of the shock-cell ends, as pinpointed in the comments of Fig. 7) and the minima occur near the end of the expansion regions (middle of the shock cells). This undulating behaviour is in agreement with the hot film measurements performed by Seiner and Norum (1980), Seiner and Yu (1984) and Seiner et al. (1985) in underexpanded jets, as well as with the numerical simulations included in this latter reference. Bridges and Wernet (2008) found the same evolutions by PIV for the fluctuations of the axial component of velocity. Interestingly, the *maxima* of the axial velocity fluctuations are near 16% for both jets, as is emphasized in Fig. 13 by the horizontal dashed lines. Recalling that it was the levels measured for M_j = 1.10 and 1.15, it seems that the shock-cell structure has a role of suppressor of turbulent fluctuations at higher underexpansion. When this structure weakens downstream, the minima of fluctuations accordingly rise while the maxima remain around 16%.

It is interesting to note that Panda and Seasholtz (1999) measure oscillations in the fluctuations of density showing *minima* near the end of the shock cells. Upon examining the profiles of σ_2, a very slight oscillation of these fluctuations appears, but it is opposite to those of σ_1. They would therefore match the modulations of the density fluctuations.

If the oscillation of the turbulence levels related to the shock-cell structure is omitted, their general evolution is quite flat for all values of M_j considered here. Some of the studies quoted earlier confirm this property, but others show a large increase of the fluctuations with downstream distance (Seiner and Norum, 1980; Panda and Seasholtz, 1999; Bridges and Wernet, 2008). This tendency comes from vanishing fluctuation levels near the nozzle exit, which can probably be explained by considering that the turbulence levels are measured on a straight line in these references. For example, the lipline (y/D = 0.5), chosen by Seiner and Norum (1980) and, with some modification, by Bridges and Wernet (2008), quickly moves out of the mixing layer for highly underexpanded jets because of the initial lateral expansion of the flow, while it is reached again by the mixing layer further downstream. The same remark holds for the measurements by Panda and Seasholtz (1999), performed on the line y/D = 0.63. Furthermore, it is possible that the presence of screech tones in some of these works induces an increase of the fluctuations in the downstream direction.

3.2.4. Spatial correlations

Spatial correlations are computed from the instantaneous velocity fields in order to obtain information on the size, shape and orientation of the turbulent structures in the mixing layer. The coefficient of space–time correlation is written

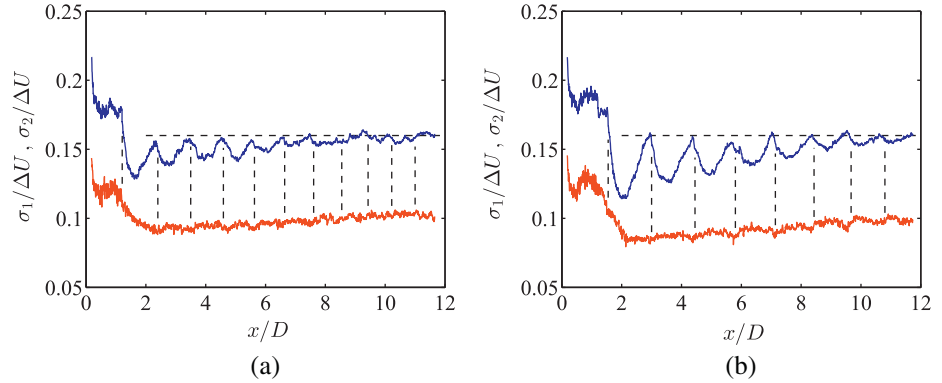

Fig. 13. Longitudinal and transverse turbulence levels in the mixing layer. (a) M_j = 1.35, (b) M_j = 1.50. — $\sigma_1/\Delta U$, — $\sigma_2/\Delta U$. The vertical lines mark the end of the shock cells; the horizontal lines denote 16%, which is the approximate value of $\sigma_1/\Delta U$ at M_j = 1.10 and 1.15.

$$R_{ij}(\boldsymbol{x},\xi,\tau)=\frac{\overline{u_i'(\boldsymbol{x},t)u_j'(\boldsymbol{x}+\boldsymbol{\xi},t+\tau)}}{\sigma_i(\boldsymbol{x})\,\sigma_j(\boldsymbol{x}+\boldsymbol{\xi})} \tag{4}$$

where the indexes i and j represent the velocity component, u_i' denotes the fluctuations of u_i, $\boldsymbol{x}$ is the reference point, $\boldsymbol{\xi}$ is the separation vector and τ is the time delay. Ensemble averages are calculated over the 2000 fields acquired. In the following, only spatial correlations are calculated, so that $\tau = 0$.

Cross-correlations R_{11} and R_{22} have been estimated while moving the reference point on the horizontal line $y/D_j = 0.5$, with D_j the fully expanded jet diameter, slightly larger than D. This is done to account for the expansion of underexpanded jets. It has been checked however that the precise location of the reference points did not have a strong influence on the results. Examples of correlation plots are shown in Fig. 14 for $M_j = 1.15$.

From $R_{ii},\ i \in (1,2)$, it is possible to calculate the integral length scale of u_i' in the direction $k,\ k \in (1,2)$, by

$$L_{ii}^{(k)}(\boldsymbol{x})=\frac{1}{2}\int_{-\infty}^{+\infty}R_{ii}(\boldsymbol{x},\xi_k)\mathrm{d}\xi_k \tag{5}$$

where ξ_k is the separation distance in the direction k. In practice, the integration is performed over a finite interval. Here, it is done down to the correlation contour of level 0.1 to avoid the low correlation domain which can be noisy; in any case, the integration limit has no large influence on the numerical values, and it has to be noted that integral length scales are merely order-of-magnitude estimates. The vertical cut ($\xi_1 = 0$) of the correlation coefficient R_{11} shown in Fig. 14(a), is represented in Fig. 15 and the integration domain is emphasized on that curve. It has been checked that the various integral length scales had converged when using 2000 velocity fields for the estimation.

The various length scales for all values of M_j are shown in Fig. 16. They are seen to grow linearly with the downstream distance, as it is the case for subsonic jets (Laurence, 1956; Davies et al., 1963; Fleury et al., 2008). The estimates of $L_{22}^{(2)}$ are noisier than the other ones and seem to show two different slopes. Some data in the curve of $L_{11}^{(1)}$ are missing because no scale estimate is produced when the curve of the coefficient of correlation, an example of which is shown in Fig. 15, is truncated. This is the case near the edges of the fields of view, and this effect becomes more pronounced as the structures grow. Striking resemblances are visible between the different operating conditions. The agreement between the $L_{11}^{(1,2)}$ curves is remarkable, while the scales $L_{22}^{(1,2)}$ grow more slowly when M_j is increased. Furthermore, a small undulation of $L_{11}^{(2)}$ and $L_{22}^{(1)}$ is visible at $M_j = 1.50$. These curves are reproduced in Fig. 17, along with the position of the end of the shock cells. The oscillations seem thus to originate from the stronger shock-cell pattern.

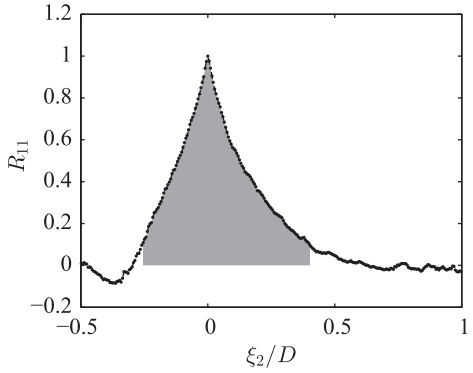

Fig. 15. Transverse profile of the correlation coefficient R_{11} for the case presented in Fig. 14 (a). The shaded area represents the region of integration for determining the integral length scale of turbulence ($L_{11}^{(2)}$ here).

Since the growth of the length scales and the mixing layer thickness is linear, the ratio of the slopes of these quantities is formed. The numerical values are gathered in Table 2 (the scale $L_{22}^{(2)}$ is left out because of the non-uniqueness of the slope). The approximate ratios observed by Fleury et al. (2008) are also recalled. Here as well, $L_{11}^{(1)}/\delta_\theta$ and $L_{11}^{(2)}/\delta_\theta$ are close to 2 and 1, respectively. However, our ratio $L_{22}^{(1)}/\delta_\theta$ is significantly smaller than 1. Furthermore, a noticeable growth of the ratios between $M_j = 1.10$ and 1.50 is identified. This means that the growth rate of the mixing layer thickness decreases quicker with M_j than that of the integral length scales, which is clear when comparing Table 1 and Fig. 16.

The shape of the correlation contours is now examined. The contours shown in Fig. 14 suggest that the turbulent structures have an elliptical shape, which has already been pinpointed by Mahadevan and Loth (1994) or Fleury et al. (2008). In order to quantitatively analyse the contours, ellipses have been fitted to them. The result of this can be viewed in Fig. 14. In the following, only contours of levels 0.3 to 0.8 are considered. Indeed, the contours of lower correlation level are generally more irregular and those of higher correlation are too small for a proper analysis. For each fitted contour, the inclination, the axis sizes and the excentricity of the ellipse have been obtained. The inclination is defined as the angle between the jet axis and the ellipse major axis. Noting a and b the length of the major and minor axes, the ellipse excentricity is

$$e=\frac{\sqrt{a^2-b^2}}{a}$$

e near one means that the ellipse is flat, while $e = 0$ for a circle.

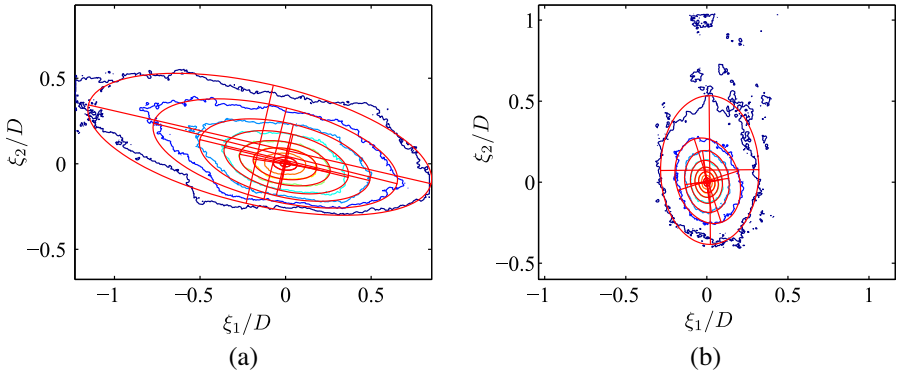

Fig. 14. Correlation contours for $M_j = 1.15$, $y/D_j = 0.5$ and $x/D = 9$. (a) R_{11} ; (b) R_{22}. ξ_i is the separation distance in the direction i. The contours represent the correlation levels 0.1–0.9 in 0.1 step. The elliptical fits, in red, will be used below. (For interpretation of the references to colour in this figure legend, the reader is referred to the web version of this article.)

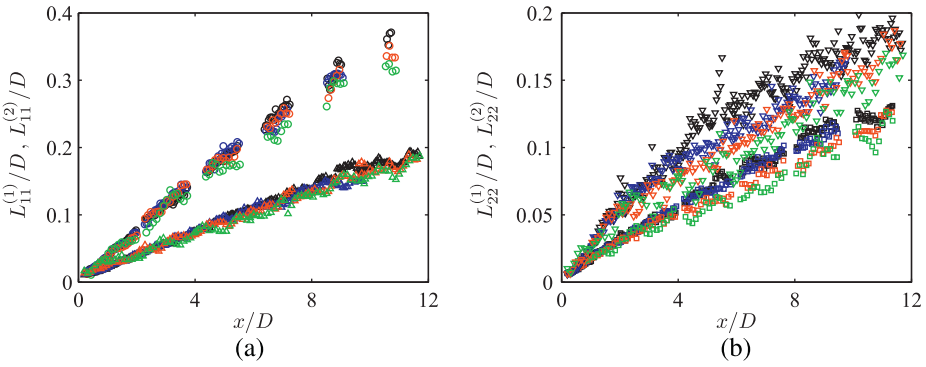

Fig. 16. Integral length scales for all values of M_j, non-dimensioned by the nozzle diameter. (a) $L_{11}^{(1)}$ and $L_{11}^{(2)}$, (b) $L_{22}^{(1)}$ and $L_{22}^{(2)}$. $\circ$ $L_{11}^{(1)}$, $\triangle$ $L_{11}^{(2)}$, $\square$ $L_{22}^{(1)}$, $\triangledown$ $L_{22}^{(2)}$. Black: $M_j = 1.10$, blue: $M_j = 1.15$, red: $M_j = 1.35$, green: $M_j = 1.50$. (For interpretation of the references to colour in this figure legend, the reader is referred to the web version of this article.)

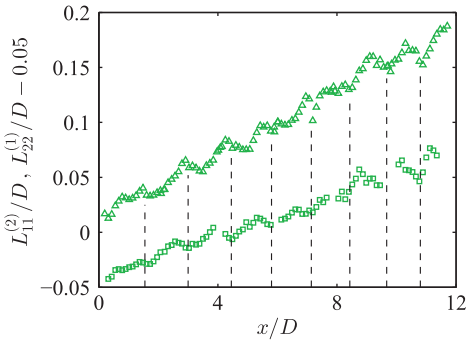

Fig. 17. $\triangle$ $L_{11}^{(2)}/D$ and $\square$ $L_{22}^{(1)}/D - 0.05$ for $M_j = 1.50$ (reproduced from Fig. 16). The vertical lines mark the locations of the shock-cell ends.

Table 2
Ratios of the growth rates between the integral length scales and the mixing layer thickness.

	$L_{11}^{(1)}/\delta_\theta$	$L_{11}^{(2)}/\delta_\theta$	$L_{22}^{(1)}/\delta_\theta$
$M_j = 1.10$	1.76	0.83	0.56
$M_j = 1.15$	1.95	0.89	0.66
$M_j = 1.35$	2.06	0.97	0.64
$M_j = 1.50$	2.15	1.03	0.67
Fleury et al. (2008)	2	1	1

Firstly, the properties of the ellipses as a function of the correlation level are mentioned for $M_j = 1.10$. The inclination and the minor axis size are shown for R_{11} in Fig. 18. It can be seen that the inclination of the ellipses depends on the correlation level, and decreases (in absolute terms) when the level increases. Mean inclinations span between $-15°$ and $-6.5°$ for the levels 0.3 to 0.8, respectively. The structures are bent toward the high-speed flow, as it has already been noted (Mahadevan and Loth, 1994; Fleury et al., 2008). The minor axis size obviously increases when the correlation level of the contour decreases. When non-dimensioned by the mixing layer momentum thickness, a constant value is found, which is in agreement with the linear growth of the turbulent length scales obtained above. The same features are also true for the major axis (not shown here). The axis lengths deliver another estimation for the size of the turbulent structures. For the contour of level 0.5, the ratios a/δ_θ and b/δ_θ are found to be 3 and 1.4, respectively. Translating this into a fraction of the mixing layer thickness δ ($\delta \approx 7.5\delta_\theta$) leads to ratios of 0.4 and 0.19. Thus, the turbulent structures can be described as *large*, in the acceptance of Papamoschou and Roshko (1988), since their size is of the same order of magnitude as the mixing layer thickness, but they do not extend over its entire width. The excentricity, not shown here, decreases when the correlation level increases, meaning that the contours of higher correlation level are closer to a circle than those of lower level. The excentricity values span from 0.91 to 0.83 for contour levels 0.3 to 0.8.

The results for R_{22} are not shown here for brevity. As compared to the case of R_{11}, the excentricity is smaller and the inclination is close to 90° (see Fig. 14 and Fleury et al., 2008). Also, the axes of the ellipses are smaller, which is in agreement with the relation found between the different integral length scales.

Secondly, the same analysis has been done for the different jets investigated here and some results are compared in Fig. 19. The contour of level 0.5 is chosen. No noticeable difference can be identified between these jets with respect to the excentricity (not shown here) or the *mean* inclination of the ellipses, while a/δ_θ and b/δ_θ tend to decrease when M_j is increased. Here again, the jets of conditions $M_j = 1.10$ and 1.15 are very similar overall, and no trace of the shock-cell structure can be found in either case. This is not true for $M_j = 1.35$ and 1.50, where the curves oscillate quasi-periodically. The modulation of the axis lengths reflects that of the integral length scales mentioned above. To understand the oscillation of the inclination, the curve for $M_j = 1.50$ is plotted in Fig. 20 alongside the inclination of the local mean streamlines going through each point of the $y/D_j = 0.5$ straight line. The location of the shock-cell ends is also indicated. Both oscillations are in phase with the shock-cell pattern, and we can verify that the inclination of the streamlines goes through 0° at the end of each cell. More importantly, the inclination of the correlation contours relatively to the local streamlines is almost constant. This means that the turbulent structures rotate while being advected by the flow, when the shock-cell pattern is strong enough to induce a notable lateral motion of the mean flow.

3.2.5. Turbulence scales in the convected frame

The intrinsic time scale of turbulence, or time scale in the convected frame of reference, measures the time a structure remains coherent in its motion. It is a very significant piece of information, especially for the broadband component of shock-associated noise (BBSAN). Harper-Bourne and Fisher (1973), who proposed the first model of this noise component, made use of turbulence measurements obtained with the crossed-beam schlieren technique to determine the level of correlation of turbulence from one shock cell to the subsequent ones. They found that the turbulence retained a high level of correlation over several shock cells. They adapted the phased array model developed by Powell (1953) for screech in taking into account this level of correlation between adjacent acoustic sources, supposed to be located at the end of each shock cell. In the end, the sources of BBSAN were thought to partially interfere, which decided the far field directivity. A success of this modelling

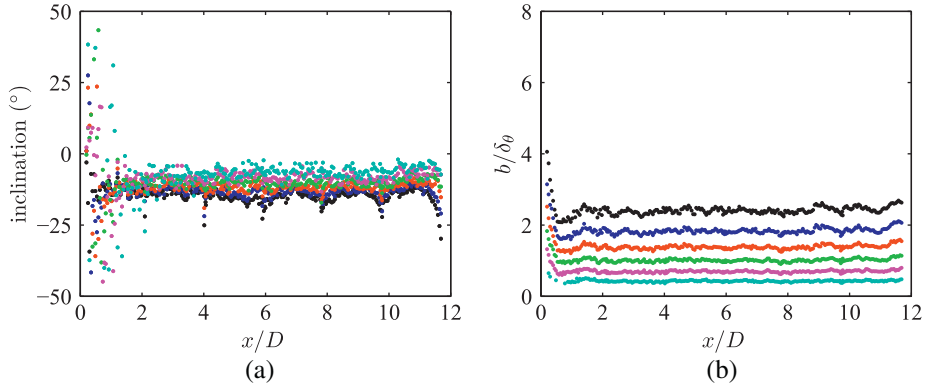

Fig. 18. Evolution of the properties of the ellipses fitted to the correlation contours R_{11} (M_j = 1.10). (a) Inclination, (b) minor axis over δ_θ. Contour levels: ● 0.3, ● 0.4, ● 0.5, ● 0.6, ● 0.7, ● 0.8.

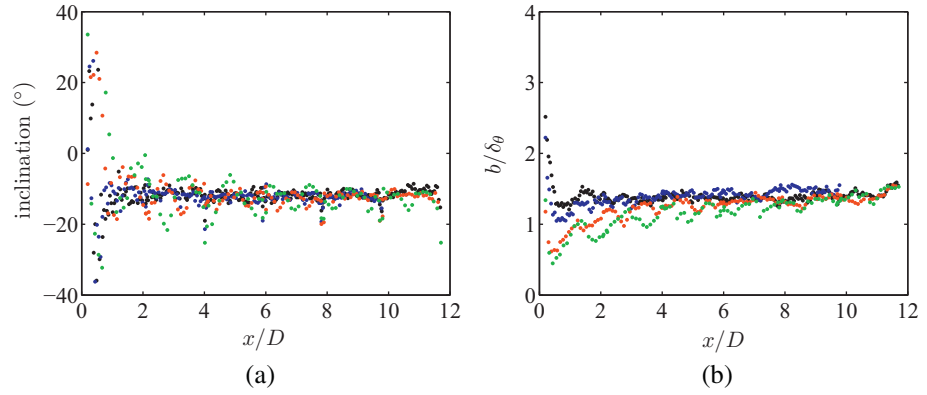

Fig. 19. Properties of the ellipses fitted to the correlation contours R_{11} of level 0.5 for all M_j. (a) Inclination, (b) minor axis over δ_θ. ● M_j = 1.10, ● M_j = 1.15, ● M_j = 1.35, ● M_j = 1.50.

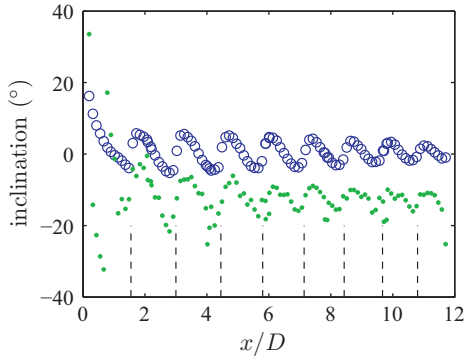

Fig. 20. Evolution of the inclinations of the local mean streamline (○) and of the R_{11}-contour of level 0.5 (●, reproduced from Fig. 19 (a)) along the line y/D_j = 0.5, at M_j = 1.50. The vertical lines mark the end of the shock cells.

is the explanation of the Doppler factor arising in the dependence of the broadband hump peak frequency on the polar angle. Another approach was later proposed by Tam and Tanna (1982) and Tam (1987). It lay on the modelling of turbulence by instability waves, which were supposed to be coherent over many jet diameters. Hence, turbulence coherence over several shock cells is also an important ingredient for this alternative model.

The intrinsic time scale of turbulence has rarely been measured in shock-containing flows, so it is interesting to estimate them and determine the corresponding axial extent of correlation. Such time scales can be defined by

$$T_{cii} = \int_0^{\tau_{0i}} R_{ii}(\boldsymbol{x}, \boldsymbol{\xi} = \boldsymbol{U_c}\tau, \tau)\mathrm{d}\tau \tag{6}$$

where τ_{0i} is the limit of integration of the coefficient of correlation R_{ii}, $\boldsymbol{U_c}$ is the convection velocity vector, and $i \in (1,2)$. The acquisition frequency in the present experiment is of course much too low to compute relevant space–time correlation coefficients, so an empirical relation observed for grid turbulence, and checked also by Fleury et al. (2008), has been used. They showed that

$$T_{cii} \approx \frac{L_{ii}^{(1)}}{\sigma_i}$$

for subsonic jets. Both quantities in the right-hand side have been obtained, and owing to the similarities found between the underexpanded jets and subsonic ones, it is believed that such a rule can still be used to estimate the correlation times. The obtained intrinsic time scales T_{c11} are shown in Fig. 21. Lau, 1980, Kerhervé et al. (2004), Panda (2006) and Fleury et al. (2008) measured such a time scale of turbulence in jets and their results are compared here with ours. The values obtained for the supersonic jets are summarised in Table 3. It has to be noted that these jets are *perfectly expanded*. Firstly, the present estimate of T_{c11} decreases with increasing M_j, which is in agreement with the quoted studies. Secondly, our estimates are in very good agreement with the measurements by Lau (1980), but are smaller than those of Kerhervé et al. (2004) and Panda (2006). Anyway, these comparisons prove that the present estimations have the right order of magnitude.

The reader will have noticed that the time scales presented in Fig. 21 and Table 3 are not non-dimensionalised. Such data are sometimes made dimensionless with the nozzle diameter D as

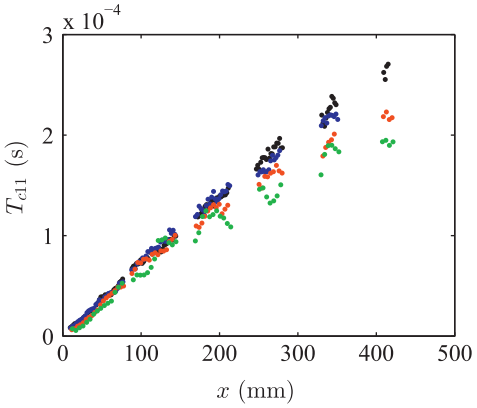

Fig. 21. The time scale in the convected frame T_{c11} against the distance to the nozzle exit for ● M_j = 1.10, ● M_j = 1.15, ● M_j = 1.35 and ● M_j = 1.50.

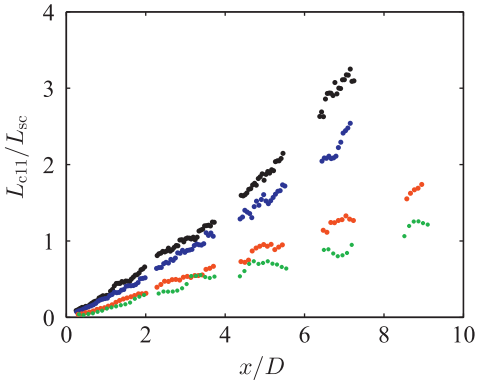

Fig. 22. L_{c11}/L_{sc} against axial location for ● M_j = 1.10, ● M_j = 1.15, ● M_j = 1.35 and ● M_j = 1.50.

Table 3
Values of time scale in the convected frame available in the literature for perfectly expanded supersonic jets. The jets are isothermal for Lau (1980) and unheated for Kerhervé et al. (2004) and Panda (2006). These estimates come from measurements of velocity for Lau (1980) and Kerhervé et al. (2004) and density for Panda (2006).

	M_j	x (mm)	Time scale (μs)
Lau (1980)	1.37	101.6	80
		203.2	120
Kerhervé et al. (2004)	1.2	52	96
		312	299
Panda (2006)	1.4	76.2	75

reference length scale and the ratio D/U_c as reference time scale (Lau, 1980), with U_c being an estimate of the convection velocity of the turbulent structures. However, it is believed that D is not a relevant scale for the early mixing layer. A better one could be the value of δ_θ near the nozzle exit plane, but this value cannot be found in the quoted papers. For further reference, the values of U_c and δ_θ for the present jets are gathered in Table 4. U_c is estimated as $0.7\,U_j$ (Harper-Bourne and Fisher, 1973; Tam and Tanna, 1982), U_j being the perfectly expanded flow velocity; δ_θ is read from Fig. 11 at the middle of the first shock cell, in order to avoid the inaccurate near-nozzle region, which is here also disturbed by the ejections through the notch.

From T_{cii}, a correlation length in the convected frame is estimated by

$$L_{cii} = U_c T_{cii}$$

where U_c is again taken as $0.7\,U_j$. L_{cii} is then non-dimensioned by the local shock-cell length L_{sc}, deduced from the PIV results. Local values of L_{sc} are considered in order to take into account the cell shortening with the axial distance; they are calculated as the mean length of two adjacent cells.

Results for L_{c11}/L_{sc} as a function of the axial location are presented in Fig. 22 for the values of M_j investigated. The curves of L_{c22}/L_{sc} (not presented here) are quite similar, since the ratio L_{c22}/L_{c11} tends to 1/2 a few diameters downstream of the nozzle exit (see also Fleury et al., 2008). The linear increase of $L_{11}^{(1)}$ with x makes L_{c11} rise linearly for all conditions tested, at least initially. For M_j = 1.10 and 1.15, the significant shortening of the shock-cell structure near the end of the pattern is responsible for the steeper rise further downstream. At the higher M_j, the axial extent of measurement did not cover the entire shock-cell structure, which explains the absence of noticeable increase in the slope of L_{c11}/L_{sc}. The important point here is that the rapid increase of L_{sc} with M_j entails a decrease of the ratio L_{c11}/L_{sc}. While it is apparently possible to consider that the turbulent structures remain coherent over several shock cells for low values of M_j, this does not seem to be the case any more for higher Mach numbers, and even less so for values of M_j greater than those investigated in the present experiment. One may argue that the shortening of the shock cells at the very end of the pattern could still allow the turbulent structures to be correlated over several cells, but the shock-cell strength is quite low there and the noise emission should not be as effective. As a consequence, the present results seem to support the suggestion uttered by Pao and Seiner (1983) that the noise mechanism could be different between low and high M_j.

Table 4
Estimates of U_c and measured values of δ_θ around the middle of the first shock cell of each jet, as reference for non-dimensionalising the values of time scale in the convected frame.

M_j	1.10	1.15	1.35	1.50
U_c (m s^{-1})	242	251	284	306
δ_θ (mm)	0.41	0.71	1.51	1.81

However, since the present estimates merely provide wideband orders of magnitude for the intrinsic time scales of turbulence, it would be of interest to directly measure these time scales in an imperfectly expanded jet in order to refine the results shown here, and gain access to a frequency dependence. Indeed, it is clear from Panda (2006) that in some frequency bands, the lifetime of turbulence can be much larger than the wideband estimate suggests. Therefore, the turbulence may still be coherent over several shock cells at the higher Mach numbers, for a range of frequencies.

4. Concluding remarks

Particle image velocimetry has been applied to four choked jets of fully expanded Mach numbers M_j = 1.10, 1.15, 1.35 and 1.50. The strength of the shock-cell structure has been estimated on mean flow streamlines. It has been found that the velocity gradients inside the jet plume wear off toward the mixing layer and in the downstream direction. In a jet containing a Mach disc, the gradients downstream of the first shock cell have been seen to be of the same order of magnitude as those encountered in slightly underexpanded jets. The velocity gradients have then been found quite moderate everywhere in these flows, and in particular in the region of production of broadband shock-associated noise, which is believed to be approximately located between the third and the eighth shock cell (Seiner and Yu, 1984). Furthermore, velocity gradients typical of the shock-cell structure have still been observed in the subsonic part of the mixing layer.

The main part of this paper focused on the properties of turbulence. Overall, it has been found that slightly underexpanded jets (M_j = 1.10 and 1.15 here) behave very similarly to jets at high subsonic Mach numbers, while the shock-cell structure more noticeably affects jets at higher values of M_j.

The location of the sonic line comparatively to the mixing layer centre and boundaries shows that for all M_j investigated, the layer centre is located in its subsonic part. At low M_j, only a very small portion of the layer is at supersonic condition, while this fraction rises when M_j is increased. Considering that BBSAN comes from the interaction between turbulence and flow gradients, it seems that a non-negligible part of shock-associated noise could be produced in the subsonic region of the mixing layer; for the higher values of M_j, this situation is attenuated by incursions of pockets of turbulence inside the supersonic region of the jet. This belief contrasts with the modellings of the BBSAN mechanism proposed by Harper-Bourne and Fisher (1973), Seiner and Norum (1980) or Seiner and Yu (1984), who explained the shock-associated noise emission by the interaction between oblique shocks and the turbulence in the supersonic part of the mixing layer. Obviously, the above argumentation on the source location of BBSAN is very qualitative. In order to locate the sources of BBSAN more precisely, a volumetric model of the sound sources, like that of Morris and Miller (2010), could be applied after estimation of some of the inputs not provided by our PIV measurements. Other ways of tackling this issue could be by means of acoustic array measurements or correlation between the signal of a probe inside the flow and near field acoustic measurements (Seiner and Yu, 1984).

A simple method, adapted to the particularities of imperfectly expanded supersonic jets, has been presented to compute the mixing layer momentum thickness δ_θ. Its evolution is fairly linear with the downstream distance, like for subsonic jets, and its growth rate decreases with increasing M_j. At the higher values of M_j, the mixing layer has been seen to thicken near the end of each shock cell.

The turbulence levels of slightly underexpanded jets have been found to be approximately constant with downstream distance and very similar to those observed in subsonic jets. For higher M_j values, the first shock cell seems to behave differently, showing higher fluctuation levels. Further downstream, a modulation of the turbulence levels by the shock-cell pattern has been identified, with maxima reached near the cell ends. Comparing these jets to the lower values of M_j, it has been concluded that the cell system acts as a turbulence suppressor.

Spatial correlations of the velocity fluctuations have been computed. A linear growth of the integral length scales has been found. The ratios of the growth rates of these scales to δ_θ take on similar values to those typical of subsonic jets. At high M_j, an undulation of the scales, which is in accordance with the shock-cell structure, has been found. The correlation contours have also been analysed as ellipses. The size of the structures thus defined is of the same order of magnitude as the local mixing layer thickness. At high M_j, a rotation of the turbulent structures in their advection has been observed, which is induced by the shock-cell pattern.

Finally, time scales of turbulence in the convected frame, crucial in connection with the BBSAN generation process, have been indirectly estimated. The corresponding correlation length of the turbulent structures has been found to become increasingly small relatively to the shock-cell length when M_j increases. However, it would be of interest to directly measure these time scales to refine the present conclusion. Especially, a frequency-dependent estimate of the intrinsic length scales of turbulence would be needed to determine if the dependence of L_c/L_{sc} on M_j found from the wideband estimates still holds.

Acknowledgements

The authors wish to thank Airbus Operations SAS (Mauro Porta) and Snecma (Guillaume Bodard) for their joint financial support, as well as Jean-Michel Perrin and Nathalie Grosjean for their help in setting up the experiment and the PIV measurement system.

Appendix A. Supplementary material

Supplementary data associated with this article can be found, in the online version, at http://dx.doi.org/10.1016/j.ijheatfluidflow.2014.08.004.

References

Alkislar, M.B., Krothapalli, A., Lourenco, L.M., 2003. Structure of a screeching rectangular jet: a stereoscopic particle image velocimetry study. J. Fluid Mech. 489, 121–154.
André, B., Castelain, T., Bailly, C., 2011. Experimental study of flight effects on screech in underexpanded jets. Phys. Fluids 23, 1–14.
André, B., Castelain, T., Bailly, C., 2012. Shock oscillations in a supersonic jet exhibiting antisymmetrical screech. AIAA J. 50 (9), 2017–2020.
André, B., Castelain, T., Bailly, C., 2013. Broadband shock-associated noise in screeching and non-screeching underexpanded supersonic jets. AIAA J. 51 (3), 665–673.
André, B., Castelain, T., Bailly, C., 2014. Experimental exploration of underexpanded supersonic jets. Shock Waves 24 (1), 21–32.
Bridges, J.E., Wernet, M.P., 2008. Turbulence associated with Broadband Shock Noise in Hot Jets. NASA Technical Memorandum 215274.
Cheng, T.S., Lee, K.S., 2005. Numerical simulations of underexpanded supersonic jet and free shear layer using WENO schemes. Int. J. Heat Fluid Flow 26 (5), 755–770.
Davies, P.O.A.L., Fisher, M.J., Barratt, M.J., 1963. The characteristics of the turbulence in the mixing region of a round jet. J. Fluid Mech. 15, 337–367.
Fleury, V., 2006. Superdirectivité, bruit d'appariement et autres contributions au bruit de jet subsonique. PhD Thesis, Ecole Centrale de Lyon.
Fleury, V., Bailly, C., Jondeau, E., Michard, M., Juvé, D., 2008. Space–time correlations in two subsonic jets using dual particle image velocimetry measurements. AIAA J. 46 (10), 2498–2509.
Harper-Bourne, M., Fisher, M.J., 1973. The noise from shock waves in supersonic jets. AGARD CP, 131.
Henry, C., Bailly, C., Bodard, G., 2012. Statistical Modeling of BBSAN including Refraction Effects. AIAA Paper 2012-2163.
Jerónimo, A., Riethmuller, M.L., Chazot, O., 2002. PIV application to Mach 3.75 overexpanded jet. In: 11th International Symposium on Applications of Laser Techniques to Fluid Mechanics, Lisbon.
Jordan, P., Gervais, Y., Valière, J.-C., Foulon, H., 2002. Jet Exhaust Aerodynamics and Noise. E.U. Research Project Jean Deliverable 3.4.
Kerhervé, F., Jordan, P., Gervais, Y., Valière, J.-C., Braud, P., 2004. Two-point laser Doppler velocimetry measurements in a Mach 1.2 cold supersonic jet for statistical aeroacoustic source model. Exp. Fluids 37 (3), 419–437.
Lau, J.C., 1980. Laser velocimeter correlation measurements in subsonic and supersonic jets. J. Sound Vib. 70 (1), 85–101.
Lau, J.C., 1981. Effects of exit Mach number and temperature on mean-flow and turbulence characteristics in round jets. J. Fluid Mech., 105.
Laurence, J.C., 1956. Intensity, Scale, and Spectra of Turbulence in Mixing Region of Free Subsonic Jet, NACA Report 1292.
Mahadevan, R., Loth, E., 1994. High-speed cinematography of compressible mixing layers. Exp. Fluids 17 (3), 179–189.
Michalke, A., 1965. On spatially growing disturbances in an inviscid shear layer. J. Fluid Mech. 23 (3).
Morris, P.J., Miller, S.A.E., 2010. Prediction of broadband shock-associated noise using Reynolds-Averaged Navier–Stokes computational fluid dynamics. AIAA J. 48 (12), 2931–2943.
Norum, T.D., Seiner, J.M., 1982. Measurements of Mean Static Pressure and Far Field Acoustics of Shock Containing Supersonic Jets. NASA Technical Memorandum 84521.
Norum, T.D., Shearin, J.G., 1988. Shock Structure and Noise of Supersonic Jets in Simulated Flight to Mach 0.4, NASA Technical Paper 2785.
Panda, J., 1999. An experimental investigation of screech noise generation. J. Fluid Mech. 378, 71–96.
Panda, J., 2006. Two Point Space–Time Correlation of Density Fluctuations measured in High Velocity Free Jets. AIAA Paper 2006-0006.
Panda, J., Seasholtz, R.G., 1999. Measurement of shock structure and shock-vortex interaction in underexpanded jets using Rayleigh scattering. Phys. Fluids 11 (12), 3761–3777.
Pao, S.P., Seiner, J.M., 1983. Shock-associated noise in supersonic jets. AIAA J. 21 (5), 687–693.
Papamoschou, D., Roshko, A., 1988. The compressible turbulent shear layer: an experimental study. J. Fluid Mech. 197 (1), 453–477.

Ponton, M.K., Seiner, J.M., 1992. The effects of nozzle exit lip thickness on plume resonance. J. Sound Vib. 154 (3), 531–549.
Powell, A., 1953. On the mechanism of choked jet noise. Proc. Phys. Soc. Lond., Sect. B 66 (12), 1039–1056.
Seiner, J.M., Norum, T.D., 1979. Experiments on Shock Associated Noise of Supersonic Jets. AIAA Paper 79-1526.
Seiner, J.M., Norum, T.D., 1980. Aerodynamic Aspects of Shock Containing Jet Plumes. AIAA Paper 80-0965.
Seiner, J.M., Yu, J.C., 1984. Acoustic near-field properties associated with broadband shock noise. AIAA J. 22 (9), 1207–1215.
Seiner, J.M., Dash, S.M., Wolf, D.E., 1985. Analysis of turbulent underexpanded jets. Part II: Shock noise features using SCIPVIS. AIAA J. 23 (5), 669–677.
Tam, C.K.W., 1987. Stochastic model theory of broadband shock-associated noise from supersonic jets. J. Sound Vib. 116 (2), 265–302.
Tam, C.K.W., Tanna, H.K., 1982. Shock associated noise of supersonic jets from convergent–divergent nozzles. J. Sound Vib. 81 (3), 337–358.
Troutt, T.R., McLaughlin, D.K., 1982. Experiments on the flow and acoustic properties of a moderate-Reynolds-number supersonic jet. J. Fluid Mech., 116.
White, F.M., 1974. Viscous Fluid Flow. McGraw Hill.

J. Fluid Mech. (2017), *vol.* 824, *pp.* 202–229.
doi:10.1017/jfm.2017.336

Experimental characterisation of the screech feedback loop in underexpanded round jets

Bertrand Mercier[1,†], **Thomas Castelain**[2] **and Christophe Bailly**[1]

[1]Université de Lyon, Ecole Centrale de Lyon and LMFA UMR CNRS 5509, F-69134 Ecully, France

[2]Université de Lyon, Université Lyon 1 and LMFA UMR CNRS 5509, F-69622 Villeurbanne, France

(Received 10 December 2016; revised 6 April 2017; accepted 15 May 2017)

Near-field acoustic measurements and time-resolved schlieren visualisations are performed on 10 round jets with the aim of analysing the different parts of the feedback loop related to the screech phenomenon in a systematic fashion. The ideally expanded Mach number of the studied jets ranges from $M_j = 1.07$ to $M_j = 1.50$. The single source of screech acoustic waves is found at the fourth shock tip for A1 and A2 modes, and at either the third or the fourth shock tip for the B mode, depending on the Mach number. The phase of the screech cycle is measured throughout schlieren visualisations in the shear layer from the nozzle to the source. Estimates of the convective velocities are deduced for each case, and a trend for the convective velocity to grow with the axial distance is pointed out. These results are used together with source localisation deduced from a two-microphone survey to determine the number of screech periods contained in a screech loop. For the A1 and B modes, four periods are contained in a loop for cases in which the radiating shock is the fourth, and three periods when the radiating shock tip is the third, whereas the loop of the A2 mode contains five periods.

Key words: acoustics, aeroacoustics, jet noise

1. Introduction

Noise produced by imperfectly expanded supersonic jets differs from subsonic jet noise by the emergence of shock noise. Major knowledge about supersonic jet noise is available in comprehensive reviews, for example in Tam (1995), Raman (1999) or Bailly & Fuji (2016). The present paper focuses on the screech, a strong tonal contribution of shock noise. Attention will be paid particularly to the structure of the resonant loop sustaining this phenomenon. One mechanism of screech tone generation was first proposed by Powell (1953), and has been the subject of many studies until the present day. Powell observed the staging behaviour of the screech frequencies produced by round jets, and identified four modes: A, B, C and D. Mode A was later separated into A1 and A2 by Merle (1957) after investigation based on stroboscopic schlieren visualisation. Davies & Oldfield (1962) have shown using two microphones on either side of the jet that the A1 and A2 modes are axisymmetric, whereas the B

† Email address for correspondence: bertrand.mercier@doctorant.ec-lyon.fr

and C modes are helical. The B and D modes were later recognised as flapping in nature by Powell, Umeda & Ishii (1992) and by Ponton & Seiner (1995), who carried out a survey with 10 microphones distributed around the jet. Ponton & Seiner (1995) found that the B and D modes comprise two oppositely rotating helices.

Theoretical knowledge about screech tone generation was supported by the model of a resonant loop developed by Powell (1953), which predicts the screech frequency f_s as a function of the convective velocity U_c of the turbulent structures, the shock cell length L_{sc} and the ambient speed of sound c_0:

$$f_s = \frac{U_c}{L_{sc}(1 + U_c/c_0)}. \tag{1.1}$$

Harper-Bourne & Fisher (1973) considered an array of equally spaced sources distributed along the lip line. The sources are shifted in phase by a lag corresponding to the time spent by the structures to be convected between two consecutive sources. By assuming that all the sound waves interfere constructively at the nozzle exit, a necessary condition on screech frequency to enhance the feedback loop was obtained, identical to (1.1). Later, Tam, Seiner & Yu (1986) derived the same equation for f_s by considering the upstream propagating wave produced by the interaction between the periodic shock cell pattern and an instability wave. Powell, Umeda & Ishii (1990) revised his model by including a phase lag to take into account the phase changes at the source or nozzle interactions, but this correction does not seem to be widely used.

Powell *et al.* (1992) observed by means of schlieren visualisations that the acoustic feedback emanated from a single source. Umeda & Ishii (2001) and Tam, Parrish & Viswanathan (2014) conducted similar schlieren visualisations that also led them to observe a single source. Suzuki & Lele (2003) performed a direct numerical simulation of a problem representative of an underexpanded jet shear layer. They observed that the passage of an eddy at a shock position may cause the shock to leak out from the mixing layer. Shariff & Manning (2013) observed the same phenomenon from a ray tracing study. Shock leakage has also been recognised as being the screech acoustic feedback generation mechanism by Berland, Bogey & Bailly (2007) by means of a large-eddy simulation of a planar jet. Based on unsteady Reynolds-averaged Navier–Stokes simulations, Gao & Li (2010) proposed a generalisation of (1.1) considering a unique source by introducing three parameters: the number of shock cells N between the nozzle and the source, the total number of wavelengths m involved in the screech loop and the convective velocity U_c:

$$f_s = \frac{mU_c}{NL_{sc}(1 + U_c/c_0)}. \tag{1.2}$$

In this model as well as in (1.1), the staging behaviour of screech tones is not accounted for. To overcome this problem, Gao & Li (2010) characterised each mode by a specific set of parameters m and N, and by the ratio of convective velocity to jet velocity. The latter is the only variable in (1.1). This ratio U_c/U_j, where U_j is the jet exhaust velocity of an equivalent perfectly expanded jet, is in general found to be between 0.55 and 0.7 (Powell *et al.* 1992; Panda 1996; Massey & Ahuja 1997; Gao & Li 2010). Nonetheless, keeping U_c/U_j constant for a given mode requires the ratio to be independent of the Mach number and constant along the jet shear layer. This statement is in contradiction with measurements performed four diameters downstream of the nozzle in jet shear layers by Veltin & McLaughlin (2008). They observed a dependence of the convective velocity on Mach number,

Reference	Source location	Mode considered	Method
Powell *et al.* (1992)	$z \simeq 5D$	A1, A2, B	Schlieren
Powell *et al.* (1992)	$z \simeq 6D$	C	Schlieren
Umeda & Ishii (2001)	Rear edge of 3rd s.c.	A1, B, C	Schlieren
Tam *et al.* (2014)	5–6 s.c. downstream	$M_j = 1.58$, $M_d = 2.0$	Schlieren
Panda (1999)	Between 3rd and 4th tip	A2	Acoustics
Gao & Li (2010)	Between 2nd and 4th s.c.	A1, A2, B, C	CAA
Edgington-Mitchell *et al.* (2014)	Between 2nd and 4th s.c.	C	PIV

TABLE 1. Localisation of screech source for circular jets: s.c. = shock cell; CAA = computational aeroacoustics; PIV = particle image velocimetry.

resulting in variation of U_c/U_j from 0.7 at $M_j = 1$ to 0.57 at $M_j = 1.56$, where M_j is the equivalent ideally expanded jet Mach number. A spatial dependence was also pointed out by Gojon, Bogey & Marsden (2015), who reported from a numerical simulation that the convective velocity increases with the downstream distance z from the nozzle. Equation (1.1) also requires that the shock cell length be constant, whereas it decreases with the axial distance from the nozzle exit z (Tam, Jackson & Seiner 1985; Tam *et al.* 1986). However, this is not an issue in (1.2) since the source is unique.

Following from these conclusions, understanding the screech mechanism, and the associated mode switching, requires first localising the acoustic source, and investigating the screech loop considering the proper convective velocity. With this purpose, Panda (1999) carried out a near-field mapping of the pressure fluctuations in phase with the screech phenomenon. He found the sound to be emitted somewhere in between the third and the fourth shock tip for mode A2. From successive spark schlieren photographs, Umeda & Ishii (2001) found the dominant source at the rear edge of the third shock cell. Gao & Li (2010) took advantage of numerical simulations to recognise the first five shocks as effective sources for A1, A2, B and C modes, but the dominant source was found between the second and the fourth shock cells. Edgington-Mitchell *et al.* (2014) investigated the C mode, and suggested that acoustic waves are more likely to be emitted somewhere in between the second and the fourth shock cells wherein the coherent vorticity undergoes the largest fluctuations. Raman (1997) also experimentally localised the sound source by using two microphones for a phase evolution survey of screech acoustic waves emitted from a rectangular jet. He figured out that the third shock is responsible for sound radiation at $M_j = 1.45$ and the fourth is involved at $M_j = 1.75$. The results on the localisation of the screech source from the mentioned studies are summarised in table 1.

The aim of the present study is to localise in a systematic fashion the unique source of screech feedback with respect to different modes, and at various setting points within the range of a given mode. The knowledge of the source position permits the estimation of the time spent for an instability to be convected from the nozzle to the source, and for the feedback to reach back to the nozzle. From this, the convective velocity and the period of a screech loop are determined. This experimental investigation is based on measurements of near-field acoustic and schlieren visualisations at high frame rate that provide complementary insights into the features of the acoustic and hydrodynamic phenomena related to screech. In § 2, the experimental set-up is described; then schlieren records are exploited to characterise the screech-associated phenomena near the shear layer in § 3.

M_j	NPR	f_s (Hz)	St_s	Mode	U_j (m s^{-1})	Re_j
1.07	2.06	6508	0.74	A1	335	1.16×10^6
1.10	2.14	5882	0.65	A1	342	1.21×10^6
1.13	2.22	5397	0.59	A1	350	1.26×10^6
1.15	2.27	6024	0.64	A2	355	1.29×10^6
1.23	2.52	3761	0.38	B	374	1.44×10^6
1.32	2.84	3295	0.32	B	394	1.61×10^6
1.35	2.97	3270	0.31	B	401	1.68×10^6
1.37	3.05	3114	0.30	B	406	1.72×10^6
1.45	3.42	2827	0.25	B	422	1.90×10^6
1.50	3.67	2712	0.24	B	432	2.02×10^6

TABLE 2. Setting points of the present study where $St_s = f_s D/U_j$ and $Re_j = \rho_j U_j D/\mu$. NPR and f_s are measured; U_j is calculated.

The localisation of the screech acoustic source is presented in § 4, which leads to a description of the screech loop structure for each mode considered in § 5. Concluding remarks are finally provided.

2. Experimental set-up

2.1. *Facility*

The studied jets exhaust from a convergent nozzle into the 10 m × 8 m × 8 m anechoic room of the Laboratoire de Mécanique des Fluides et d'Acoustique at École Centrale de Lyon. Compressed dry air is supplied by a centrifugal compressor, which allows continuous operation at a maximum flow rate up to 0.85 kg s^{-1}. The maximum nozzle pressure ratio (NPR) is 3.9, corresponding to $M_j = 1.54$. The nozzle diameter is $D = 38$ mm, its nozzle lip is 0.5 mm thick and the contraction ratio is 4.4 : 1 (André 2011). Static pressure is measured in the inlet duct 15 diameters upstream of the nozzle, and is combined with ambient pressure measurements and isotropic flow relations to evaluate M_j. These flow conditions are monitored to ensure that, once set, M_j remains constant within $\pm 0.2\,\%$. The total temperature is monitored by a K-type thermocouple protruding into the inlet pipe. After a run-time of half an hour, the air supply system is such that the total temperature stabilises at $30\,^{\circ}\mathrm{C} \pm 2\,^{\circ}\mathrm{C}$ depending on day-to-day variation of air temperature at the compressor inlet. The ambient temperature in the anechoic room is also monitored by a thermocouple probe located in a region at rest. Results obtained with two different experimental techniques are reported here: high-speed schlieren visualisations of the jet shear layer and its surroundings, and near-field acoustic measurements. These techniques are applied to 10 jets whose corresponding Mach numbers and characteristics are provided in table 2. The screech Strouhal number St_s and the jet Reynolds number Re_j are based on the equivalent fully expanded jet velocity U_j and density ρ_j. Those setting points are chosen to cover the axisymmetric modes A1 and A2, as well as the flapping mode B. Three setting points relate to the A1 mode. Only one deals with the A2 mode because it tends to coexist with another mode as soon as it moves apart from $M_j = 1.15$. Above $M_j = 1.23$, a flapping mode is obtained and is studied through six different setting points, which allows one to assess a potential effect of M_j on the screech loop characteristics for this given mode. These modes are illustrated in appendix A, on the basis of schlieren visualisations.

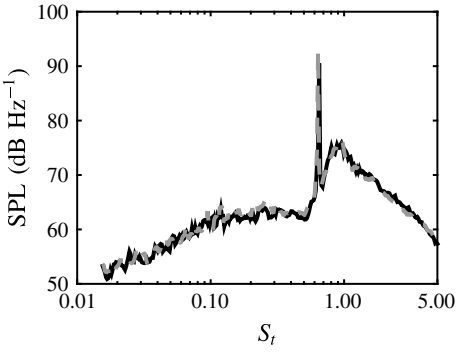

FIGURE 1. Acoustic spectrum for the $M_j = 1.15$ jet measured at a distance of $55D$ from the nozzle, with an angle of 130° from the jet axis, in 2011 (——) and 2016 (– – –).

2.2. *Apparatus*

The near-field acoustic measurements are performed using two 1/8-inch B&K 4138 microphones, with a Nexus 2692 conditioner. The first reference microphone is mounted fixed to the nozzle rig; the second is mounted on a motorised rig allowing for axial and radial traverses. The same rig is also used to support the conventional Z-type schlieren system set-up built up from two 200 mm f/8 parabolic mirrors spaced by 2.5 m. The light source is a focused high-power Cree XP-L light-emitting diode (LED). Comparative tests on data post-processing specific to this study led to the knife edge being set perpendicular to the jet axis. Axial density gradients are thus observed. The knife edge cut-off is set to approximately 50 %. Grey-scale images are recorded by a Phantom V12 CMOS camera; the grey-level field is denoted by $g(y, z, t)$. The collecting optics is a Sigma 120–400 mm f/4.5–5.6.

The schlieren films recorded as part of this study arise from two test campaigns. Cases at $M_j = 1.10$ and $M_j = 1.35$ were acquired in 2011 by André, Castelain & Bailly (2011*a*); other cases were acquired in 2016 with identical experimental set-ups. The $M_j = 1.15$ jet is available from the 2011 and 2016 campaigns, so it can be used for checking consistency. Far-field noise spectra measured in 2011 and 2016 at 130° with respect to the jet axis are compared in figure 1. The screech frequency and amplitude are found to be in good agreement in the two campaigns. The peak frequency and the sound pressure level of the broadband shock-associated noise also compare very well with each other. The similarity of the hydrodynamic structure of the $M_j = 1.15$ jets measured in 2011 and in 2016 can also be verified in figure 2 through the juxtaposition of the time-averaged schlieren images. They are also compared in figure 3 by superimposing the profiles along the jet axis of time-averaged grey levels $\overline{g}$. In these two figures, the grey levels are normalised to get around the different light and camera settings. The distance between the leading edge of the second shock cell and the leading edge of the seventh is found to be 1.3 % longer in 2016 than in 2011. This difference may be attributed to the uncertainties emerging from the calibration of the scaling factor, the precision of the setting points, and possible small modifications of the rig undergone between the two campaigns.

2.3. *Schlieren measurement procedure*

Five parameters are taken into account for acquiring the schlieren visualisations. The first one is the spatial extent of the field of view. The second one is the

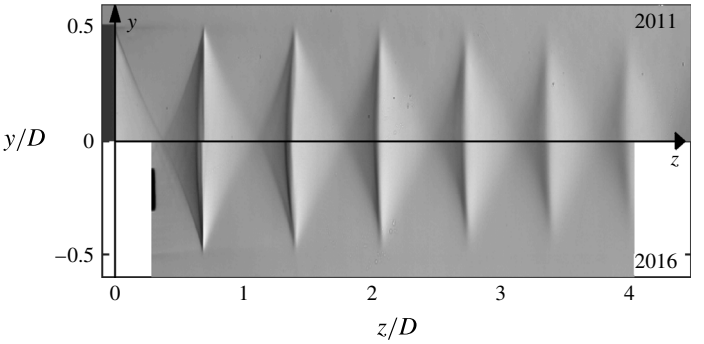

FIGURE 2. Time-averaged grey-level field $\bar{g}(y, z)$ of schlieren images of a $M_j = 1.15$ jet captured in 2011 (top) and in 2016 (bottom).

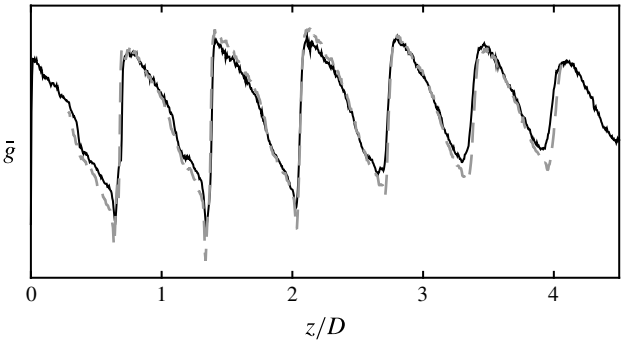

FIGURE 3. Normalised profile of $\bar{g}(z)$ (arbitrary units) on the jet axis computed from schlieren images of a $M_j = 1.15$ jet, in 2011 (——) and 2016 (– – –).

desired sampling rate. These two parameters determine the maximum frame size and the corresponding magnification factor. Finally the exposure time is set by the sampling period and the light intensity. The use of the schlieren visualisation is twofold: to study the turbulent flow in the shear layer and the screech-associated phenomena in the region surrounding the jet. Therefore, two sets of records are available from each campaign. The corresponding camera settings are provided in table 3. One puts priority on the extent of the field of view, and the other prioritises the sampling rate. The minimum acquisition frequency for analysing some flow properties was determined after the work of Veltin, Day & McLaughlin (2011), who found satisfactory results by sampling at 15 times the jet characteristic frequency $f_c = U_j/D_j$, with U_j and D_j the exit velocity and diameter of the equivalent fully expanded jet. For the worst case, $M_j = 1.50$, f_c is approximately 10 kHz, so the sampling rate is chosen higher than 150 kHz. This frequency is reached by reducing the size of the frames in the radial direction while keeping a large axial size. Previous studies summarised in table 1 recognised the source of screech to be located between the second and the fifth shock tips. Consequently, the frame used for this study is chosen to contain at least the first five shock cells. However, this measurement is not achievable on one single frame when M_j is higher than 1.23 because the spatial extent is limited by the mirror diameter. For these cases, the camera is shifted by an increment of 100 mm ($2.6D$) until the fifth shock cell is filmed. The dataset is thus

	Rate (fps)	Exposure (μs)	Size (pixel)	Length (z/D)	Radial limit (y/D)
2011 Shear layer	430 769	2.8	640×16	4.2	[0.44; 0.55]
2011 Surroundings	7 200	4.0	1280×656	5.2	[−1.48; 1.59]
2016 Shear layer	220 472	4.0	1024×24	4.9	[0.44; 0.55]
2016 Surroundings	18 000	2.0	704×424	3.8	[−0.61; 1.67]

TABLE 3. Setting of the camera and the lens for the different datasets: fps = frames per second.

composed of several films. Schlieren images must be interpreted with some caution because they are altered by integration effects along the optical path. These artefacts are, however, weaker when the flow is characterised by a strong azimuthal and radial coherence, as with screech.

3. Schlieren visualisations analysis

3.1. *Overview*

A snapshot and time-averaged picture of the schlieren visualisation of the $M_j = 1.15$ jet are presented in figure 4(*a*,*b*). These images clearly show the quasi-periodic pattern of shock cells consisting of compression and expansion waves. The mean spatial period of this pattern is called the shock cell length L_{sc}. The average image shows the decrease of the shock cell intensity with increasing downstream distance from the nozzle. For each pixel, a time signal $g(y, z, t)$ of grey levels acquired at a high sampling rate is available, and the amplitude of its Fourier transform at the screech frequency, denoted by $G_s(y, z)$, is reported in figure 4(*c*). High values of this coefficient correspond to the darkest regions, and are obtained next to the shock themselves. This high level of fluctuation is attributed to shock oscillation at the screech frequency (Panda 1998; André, Castelain & Bailly 2011*b*). Another remark concerns the presence of lobes in the near field that can be linked to the standing-wave pattern observed by Westley & Woolley (1969). They interpreted this phenomenon as the resultant effect of the interaction between the instability wave convected with the flow and the screech acoustic waves. More details about the lobed pattern can be observed in figure 5, which represents the axial profiles of grey-level fluctuations at the screech frequency. These profiles are measured at a radial position chosen to display the maximum of instability wave features, and therefore as close as possible to the lip line. However, if the measure is conducted too close to the jet, shocks periodically cross the probed line and sharp discontinuities appear in the profile; therefore the interpretation of those results becomes complicated. A convenient position for the measurement line is found along the line at $y/D = 0.55$ for M_j lower than 1.32, and along the line at $y/D = 0.75$ for higher M_j. A look into these profiles shows similarities between all cases. The first observation concerns the lobed shape of the curves, which is similar to the observation in figure 4(*c*) for the $M_j = 1.15$ jet. Considering only the midline of the profiles by putting aside the undulations, a second similarity comes out. The wavy pattern is supported by a bell-shaped curve that points out the amplification rate of instability waves. They first grow with increasing distance from the nozzle, then saturate, and finally decay further downstream.

The wavenumber k_{sw} of the lobed pattern was derived by Panda (1999) from the acoustic and hydrodynamic wavenumbers k_s and k_h, by considering upstream-propagating acoustic and downstream-propagating instability waves. This corresponds

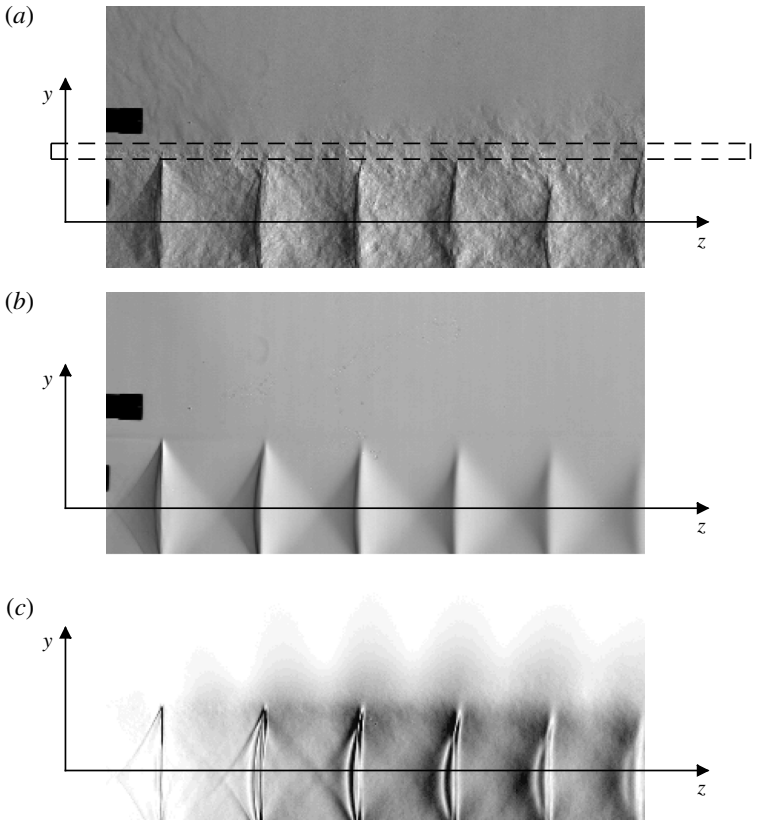

FIGURE 4. (*a*) Instantaneous schlieren image $g(y, z, t)$ (4 μs time exposure). The dashed rectangle shows the field of view of the high-speed records. (*b*) Averaged field $\overline{g}(y, z)$. (*c*) Fluctuating field $G_s(y, z)$ at the fundamental screech frequency from schlieren measurement of a jet at $M_j = 1.15$, mode A2.

to the region upstream of the screech acoustic source, but both waves travel in the same direction downstream of the source. Here we choose to denote by k_{sw}^- the wavenumber of the wave pattern where acoustic is retrograde, and k_{sw}^+ where acoustic is propagative, giving

$$k_{sw}^- = k_h + k_s, \tag{3.1a}$$

$$k_{sw}^+ = k_h - k_s. \tag{3.1b}$$

By convention, all wavenumbers are chosen positive. The corresponding wavelengths $L_{sw}^- = 2\pi/k_{sw}^-$ and $L_{sw}^+ = 2\pi/k_{sw}^+$ can be expressed as a function of the screech frequency f_s, the convective velocity at screech frequency U_c and the speed of sound c_0 in the jet surrounding:

$$L_{sw}^- = \frac{U_c}{f_s(1 + U_c/c_0)}, \tag{3.2a}$$

$$L_{sw}^+ = \frac{U_c}{f_s(1 - U_c/c_0)}. \tag{3.2b}$$

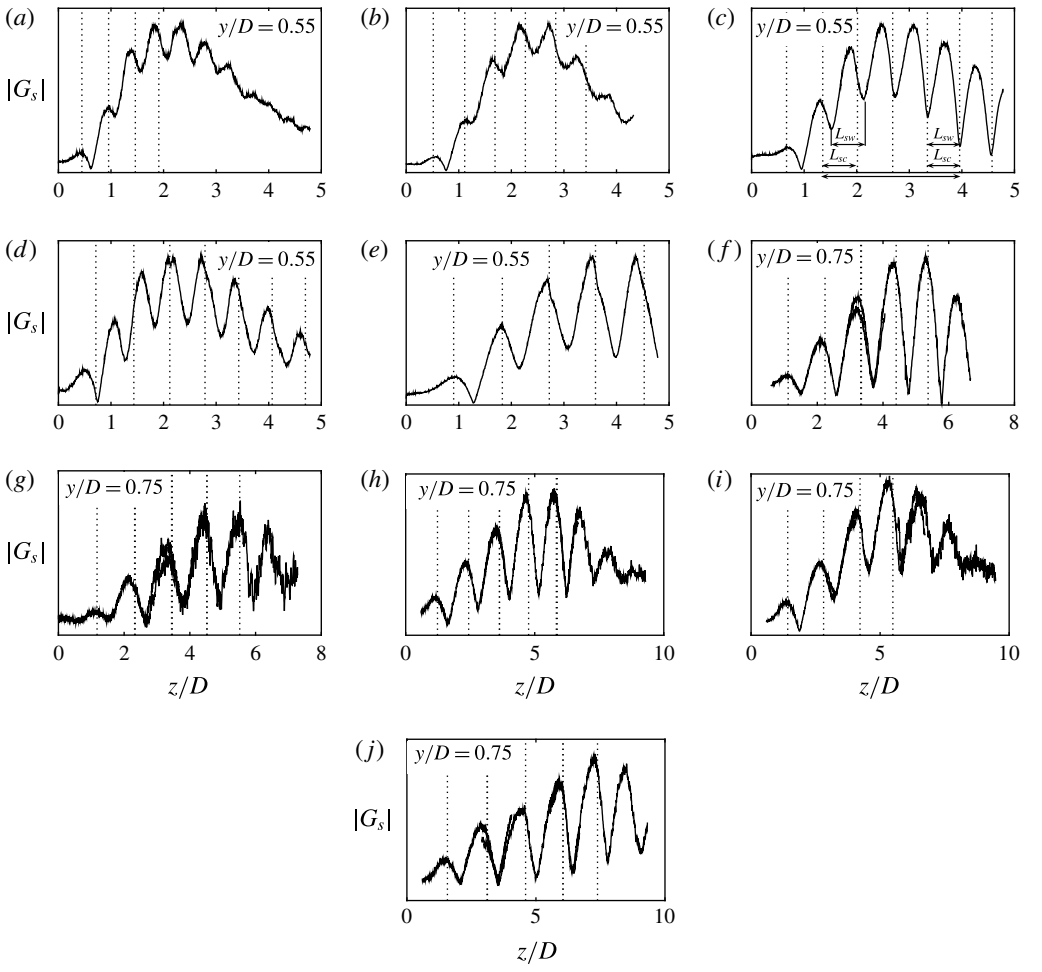

FIGURE 5. Modulation of the grey-level field G_s at the screech frequency (arbitrary scale) along a line at $y/D = 0.55$: (*a*) $M_j = 1.07$, (*b*) $M_j = 1.10$, (*c*) $M_j = 1.13$, (*d*) $M_j = 1.15$, (*e*) $M_j = 1.23$, (*f*) $M_j = 1.32$, (*g*) $M_j = 1.35$, (*h*) $M_j = 1.37$, (*i*) $M_j = 1.45$ and (*j*) $M_j = 1.50$. Shock locations are indicated by vertical dotted lines.

As an illustration, if the convective velocity is approximated to $0.6U_j$, these relations provide $L_{sw}^- = 0.63D$ and $L_{sw}^+ = 2.68D$ for the case $M_j = 1.13$, and $L_{sw}^- = 1.20D$ and $L_{sw}^+ = 7.26D$ for the case $M_j = 1.37$.

The profile of $G_s(z)$ for the $M_j = 1.13$ case shown in figure 5(*c*) covers the first seven shock cells of the jet. Since the source is expected to be located between the second and the fifth shock tips, the source is somewhere within the profile. The lobes, however, are spaced by a distance similar to L_{sw}^-, and there is no clear experimental evidence of a L_{sw}^+ length scale. More generally, the transition from L_{sw}^- to L_{sw}^+ is not visible for all 10 cases, and the observed wavelength is closer to L_{sw}^- than to L_{sw}^+.

Nonetheless, the $M_j = 1.13$ jet presents a notable characteristic that delimits two regions. Upstream of the fourth shock, the lobed pattern wavelength is smaller than the shock cell length, whereas both length scales are equal downstream. The $M_j = 1.15$ jet exhibits the same features: upstream of a region in between the third and the fourth

shocks, the lobes are spaced by a length L_{sw}^{-} smaller than L_{sc}, and these lengths are equal downstream. These jets are the only two having L_{sw}^{-} different from L_{sc}. All other cases present only a single wavelength, which appears to be equal to the shock cell length everywhere. Moreover, the similarity between L_{sw}^{-} and L_{sc} is consistent with Tam's theoretical conclusions about these length scales. According to Tam *et al.* (1986, 2014), a necessary condition for the screech feedback mechanism to be self-sustained is

$$k_h - k_{sc} = -k_s. \tag{3.3}$$

By comparison with (3.1*a*), $k_h - k_{sw}^{-} = -k_s$, Tam's theory straightforwardly imposes that $L_{sw}^{-} = L_{sc}$. This statement is not supported by the present experimental results for both $M_j = 1.13$ and $M_j = 1.15$ cases. However, the difference between L_{sw}^{-} and L_{sc} is small, although it is clearly observable, which indicates that the condition (3.3) is overly rigid, and the screech conforms with a slightly different condition provided by (3.1*a*). The behaviour of the modulation upstream of the source can thus be explained by the theoretical model relying on the wave superposition.

Downstream of the source, the lobes are not spaced by the distance expected from (3.1*b*). The period of the pattern seems to be equal to the shock cell length. This feature is likely to result from the modulation of the instability wave by the shock cells, and from the weak amplitude of acoustic waves because of the upstream directivity of screech. The role of shock cells in the existence of the lobed pattern can be demonstrated by considering the jets at $M_j = 1.07$, 1.37 and 1.45. For these three Mach numbers, the field of view of the schlieren visualisation is large enough to cover the mixing layer farther downstream from the last detectable shock tip. In each case, the amplitude of lobes starts decaying downstream of the last noticeable shock cell. In addition, the ability of shock cells to modulate the turbulence has been pointed out by André (2012, in his figure 5.33) throughout particle image velocimetry (PIV) measurements in underexpanded screeching or non-screeching jets. Moreover, the absence of the wavelength L_{sw}^{+} involved in the acoustic–hydrodynamic interaction downstream of the source can be explained by two reasons. Firstly, k_h and k_s are expected to be close, in particular for the jets at highest Mach numbers, so $k_{sw}^{+} = k_h - k_s$ is small and may not be noticeable in the spatial extent of the images. Secondly, far-field measurement at the fundamental screech frequency shows a strong upstream directivity (Norum 1983; Berland *et al.* 2007); thus, even in the near field, screech acoustic waves are likely to be weaker downstream of the source.

Finally, the features of the overall profile can be explained as follows. All along the jet, the instability wave is modulated by the shock cell pattern. This phenomenon could explain by itself the presence of lobes spaced by L_{sc} in the near-field map of screech-associated fluctuations, but jets at $M_j = 1.13$ and $M_j = 1.15$ are characterised by a modulation wavelength L_{sw}^{-} different from L_{sc} in the first three or four shock cells. This remark suggests that acoustics also plays a role in explaining the lobes where its contribution is strong, but since L_{sw}^{-} is expected to be close to L_{sc}, the difference between them is not perceptible for all other jets. However, downstream of the source, the acoustic contribution is too weak in comparison to the instability wave, preventing any observation of L_{sw}^{+}. If L_{sc} coincides with L_{sw}^{-} in the region upstream of the source, then from (3.1) and (3.3),

$$k_h - k_{sc} = k_h - k_{sw}^{-} = -k_s = -\frac{\omega_s}{c_0}. \tag{3.4}$$

This identity will be tested from the analysis of the screech-associated wavenumbers in the next section.

3.2. *Wavenumber–frequency spectrum analysis*

An attempt is made to experimentally determine the different wavenumbers involved in the screech feedback loop. This is carried out through a one-dimensional spatial Fourier transform applied to Fourier coefficients $G_s(z)$ at the screech frequency along the axial direction at $y/D = 0.55$, themselves computed from the high-speed schlieren films. A first analysis is performed in a region located upstream from the source, namely $0 \leqslant z \leqslant z_N$, where z_N denotes the coordinate of the source location. The determination of this position is detailed in the next section, which benefits from the general overview given in the present section. The source is found either at the third or at the fourth shock tip. As a consequence, the discrete Fourier transform is performed over a short extent that contains only two to four wavelengths depending on the case, so the resolution is low in the wavenumber space. The spatial signal $G_s(z)$ used as input to the spatial Fourier transform is weighted by a Gaussian function of width five standard deviations. The wavenumber resolution is improved by doubling the length of the signal by adding zeros. This process is undertaken in order to better distinguish between lobes and randomness, but tests have been performed to ensure that zero padding has no effect on the characterisation of the two main peaks described hereafter.

The result is shown in figure 6 as a solid line. It consists of a pair of dominant peaks, one characterised by a positive wavenumber and a second characterised by a negative wavenumber. The locations of local maxima are estimated using a method from Gasior & Gonzalez (2004) to improve the wavenumber resolution. This method takes advantage of the Gaussian shape of the spectrum calculated from a single-frequency signal windowed by a Gaussian function. The method can be extended to a signal containing more frequencies if their respective Fourier transforms do not overlap. As a consequence, the location of the maximum of a peak can be estimated from the Gaussian function that best fits the peak. The three points on the top of the peaks are used for fitting in this study. Gasior & Gonzalez (2004) reported a maximum error of less than 1 % of the frequency resolution. In the present study the worst resolution is found to be 80 rad m^{-1} for the $M_j = 1.07$ jet without zero padding. An error of less than 1 % would lead to an error of less than 0.8 rad m^{-1}. In order to assess the method, the spatial spectra along all the available radial positions have been computed. The results are found to be weakly dependent on the considered radial position, except for $M_j = 1.45$, probably because the distance between the peaks in the wavenumber space is small. In addition, this case exhibits strong shock oscillations that intercept the probed line, causing large discontinuities that produce a significant amount of harmonics. These are likely to influence the determination of the maximum of peaks. The same problem is observed for the $M_j = 1.50$ jet. In general, the error observed from the lowest peaks is found to be larger, because the effect of overlapping is more significant.

The maxima of the peaks are marked by crosses in figure 6, and are tabulated in table 4. The wavenumber corresponding to the retrograde screech acoustic wave $-k_s = -\omega_s/c_0$ is represented by a dotted line. The comparison between this prediction and the maximum of the peak in the negative wavenumber range shows a good agreement, as also reported in table 4. It provides some confidence to state that this peak is related to the upstream-propagating acoustic wave. As for the peak in positive wavenumbers, it is expected to be $k_h = \omega_s/U_c$; the corresponding convective velocity is provided in table 4 normalised by U_j, and is indeed roughly equal to $0.6U_j$ for all cases. This result is consistent with many studies, for instance those by Powell *et al.* (1992), Massey & Ahuja (1997) or Panda & Raman (1997).

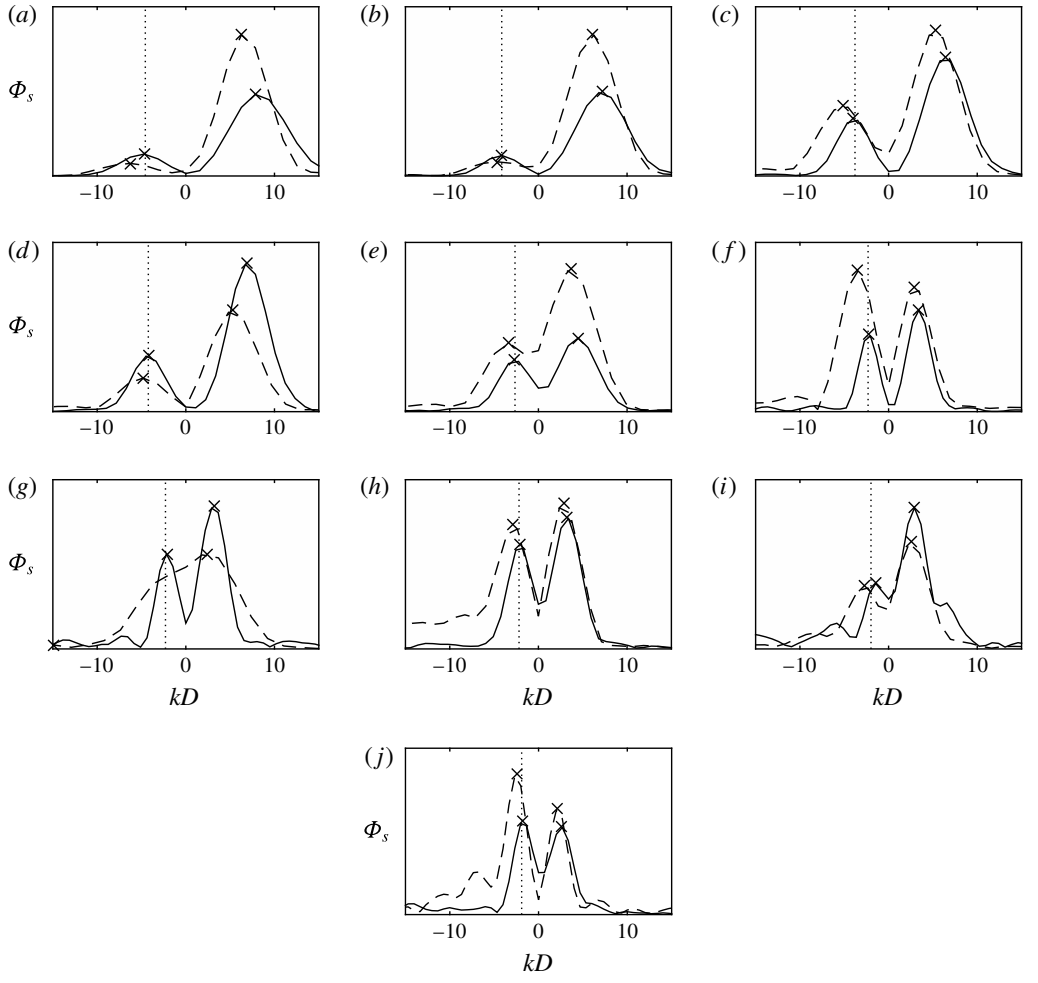

FIGURE 6. Wavenumber spectrum at screech frequency Φ_s (arbitrary linear scale) upstream of the source (——) and downstream (– – –): (*a*) $M_j = 1.07$, (*b*) $M_j = 1.10$, (*c*) $M_j = 1.13$, (*d*) $M_j = 1.15$, (*e*) $M_j = 1.23$, (*f*) $M_j = 1.32$, (*g*) $M_j = 1.35$, (*h*) $M_j = 1.37$, (*i*) $M_j = 1.45$ and (*j*) $M_j = 1.50$. The wavenumber $k_s = -\omega_s/c_0$ is indicated by the vertical dotted line.

The speed of sound tabulated in table 4 is not equal to the speed of sound of 337 m s^{-1} expected from the ambient temperature measured during the experiment. An error of 5 % or less is observed for seven of the 10 cases. A larger error is noticed for the $M_j = 1.35$, 1.45 and 1.50 jets, in particular for $M_j = 1.45$, whose validity has already been examined and called into question. Unfortunately, that dispersion prevents us from providing evidence for the existence or absence of an eventual other type of feedback mentioned by Shen & Tam (2002), Chatterjee, Ghodake & Singh (2009) or Edgington-Mitchell, Honnery & Soria (2015).

Finally, the last column of table 4 compares the wavenumber $k_{sw}^- = k_h + k_s$ associated with the lobed pattern, see (3.1*a*), to the shock cell wavenumber averaged over $0 \leqslant z \leqslant z_N$. The shock positions are measured from the centreline grey profiles of the averaged schlieren images with an accuracy of $\pm 0.007D$ arising from the width of the shocks, and an additional error of $\pm 0.04z$ from the scaling factor of pixels, but these

M_j	Range (z/D)	$-k_s$	k_h	$c_0=\omega_s/k_s$	$U_c/U_j=\omega_s/(k_hU_j)$	$(k_h+k_s)/k_{sc}$
1.07	[0, 2.0]	−128	215	319	0.57	1.03
1.10	[0, 2.3]	−111	188	334	0.57	1.03
1.13	[0, 2.7]	−103	169	328	0.57	1.10
1.15	[0, 2.8]	−111	184	340	0.58	1.28
1.23	[0, 2.8]*	−70	116	337	0.54	1.05
1.32	[0, 4.6]	−60	89	347	0.59	1.04
1.35	[0, 4.3]**	−56	83	367	0.61	1.01
1.37	[0, 3.7]*	−55	85	355	0.57	1.04
1.45	[0, 4.3]*	−36	77	493	0.55	0.97
1.50	[0, 4.7]*	−45	67	379	0.59	1.05
M_j	Range (z/D)	$-k_d^-$	k_h	$U_c/U_j=\omega_s/(k_hU_j)$	$(k_h+k_d^-)/k_{sc}$	
1.07	[2.0, 4.0]	−168	174	0.70	—	
1.10	[2.3, 4.3]	−122	161	0.67	0.99	
1.13	[2.7, 4.7]	−136	139	0.70	1.05	
1.15	[2.8, 4.7]	−128	141	0.75	1.04	
1.23	[2.8, 4.7]*	−87	99	0.64	1.02	
1.32	[4.6, 7.3]	−93	78	0.67	1.07	
1.35	[4.3, 6.3]	—	—	—	—	
1.37	[3.7, 7.3]*	−77	73	0.66	1.08	
1.45	[4.3, 7.3]*	−73	69	0.61	1.16	
1.50	[4.6, 9.3]*	−65	53	0.74	0.96	

TABLE 4. Wavenumbers of peaks in amplitude of the spatial Fourier transform applied along a line at $y/D=0.54$ over the given axial range on high-speed schlieren records that correspond to the region from the nozzle to the fourth shock tip, except for cases marked by *, which denotes the third shock tip. In the case marked **, the extent was limited by the field of view of the record. The shock cell wavenumber is determined from shock cells contained within the range given in the second column.

uncertainties are insignificant in comparison to the margin of error pointed out on k_s. The modulation wavenumber is found to be larger than the shock cell wavenumber by a few per cent, except for the case $M_j=1.15$ that exhibits k_{sw} 28 % larger than k_{sc} because of the jump in frequency, whereas no change in aerodynamic characteristics of the jet is observed (Clem, Zaman & Fagan 2016). The second largest k_{sw}^- in comparison to k_{sc} is found for case $M_j=1.13$: k_{sw}^- is 10 % larger than k_{sc}. The case $M_j=1.45$ should not be considered because of the problem of peak overlapping mentioned above. These results are consistent with the conclusions of § 3.1: k_h-k_s is actually close to k_{sc}, so L_{sw}^- is close to L_{sc}, for all but the $M_j=1.13$ and $M_j=1.15$ cases.

A procedure similar to the one outlined for the region upstream of the source is applied for $z_N \leqslant z \leqslant z_{max}$, where z_{max} is the maximum reachable distance with respect to the schlieren record. The results are plotted as a dashed line in figure 6. The peak in positive wavenumbers is still associated with the instability wave. The corresponding convection velocity is summarised in table 4. Its value is found to be close to $0.7U_j$, hence slightly higher than upstream of the source. A trend of rising convective velocity with axial location was observed by Gojon *et al.* (2015) from a numerical study, and from the same experimental data as the present study but using a different method by Mercier, Castelain & Bailly (2016). Regarding the peak

in negative wavenumbers denoted by k_d^-, the distance between this peak and k_h is compared to k_{sc} in the last column of table 4, with k_{sc} estimated from the shock cells visible in the range of the spatial spectral analysis. Since the shock cell structure fades out with downstream distance, the estimation of k_{sc} can only be approximate by comparison with the accuracy mentioned for the first few shocks. Nonetheless, the comparison highlights the similarity of these two values in most cases. The $M_j = 1.45$ case again shows a surprising result in terms of both k_h and $(k_h + k_d^-)/k_{sc}$ values. In addition to the peak overlapping, the absence of clearly detectable shocks downstream of the fourth one must be pointed out. Thus, comparing $(k_h + k_d^-)$ to k_{sc} might not be relevant. For all other cases, the peak in negative wavenumbers $k_d^- \simeq k_{sc} - k_h$ is recognised as the interaction between the shock cell pattern and the instability wave. The corresponding phase velocity ω_s/k_d^- is subsonic for all cases. No wavenumber peak associated with a retrograde acoustic wave is observed, which is consistent with the determination of the source location z_N. No propagative acoustic wave is detected; this is likely to be attributed to the screech directivity, weaker in the jet axis direction with respect to the upstream direction (Norum 1983; Berland *et al.* 2007).

4. Source localisation through near-field acoustic measurements

Schlieren measurements provide information about screech-associated phenomena in a region where the hydrodynamic contribution is predominant. Regarding the objective of localising the screech source, it is interesting to gain insight into screech-associated fluctuating pressures in the jet near field, where the hydrodynamic pressure field is faded enough so that acoustics becomes the dominant contribution. To this end, two types of near-field measurements are set up. The first is a microphone traverse along a line perpendicular to the jet axis within the nozzle exit plane for Mach numbers 1.13, 1.15 and 1.35 only. The second is a microphone traverse along a line parallel to the jet, and distant by $1.5D$ from the axis (or $2D$ for cases $M_j = 1.45$ and 1.50, to avoid microphone overload). This is repeated for all cases of table 2. For these axial and radial surveys, two microphones are used; one is fixed and constitutes the reference signal, the second is moved by increments of 3–5 mm so as to measure approximately 20–30 points per screech acoustic wavelength. The signals of the two microphones are sampled synchronously at 204 800 Hz for 2 s. The radial traverse is conducted from $y/D = 0.5$ to $y/D = 8$. In the axial direction, the moving microphone travels between $z/D = -0.1$ and $z/D = 6$ for M_j up to 1.23, and down to $z/D = 8$ for higher Mach numbers.

The post-processing of the axial and radial near-field surveys is performed for the same purpose. The phase difference at screech frequency between the moving and the fixed microphones is compared to the expected phase difference if the acoustic source were located at a given position. This method was used by Raman (1997) to determine the source of screech noise in rectangular jets. According to the literature on screech radiation that is summarised in table 1, the screech is likely to be emitted from one predominant source; under this assumption, and if this source can be regarded as a simple monopole, the expected phase lag $\Delta\phi$ between two microphones located at distances r and r_0 from the source is given by

$$\Delta\phi = k_s(r - r_0). \tag{4.1}$$

Two more assumptions are chosen here to constrain the study: the virtual source is located on the lip line in the radial direction, and at a shock tip in the axial direction.

4.1. *Radial traverse*

In the radial configuration, the reference microphone is fixed at $z = -1.8D$ and $y = 1.8D$ considering the centre of the grid as a reference with a precision of $\pm 0.03D$. The mobile microphone moves along the y direction by steps of 3–5 mm from $y = 0.5D$ to $y \simeq 8D$. The position of the rig is accurately measured at each step. Both microphones are in a region upstream of the jet in which screech is strong, and there is no contribution from the hydrodynamic pressure field; the signals are therefore clean and the phase lag variation along the probed line is expected to be smooth. The relative phase is deduced from the cross-spectrum of the two signals at the screech frequency. It is then unwrapped by adding 2π at the corresponding jumps, and finally compared with the predicted phase lags. Results for Mach numbers 1.13, 1.15 and 1.35 are presented in figure 7, through the entire spatial range in figure 7(*a*,*c*,*e*), and zoomed in closer to the nozzle in figure 7(*b*,*d*,*f*). The predicted phase lag is superimposed onto experimental results for three different source locations: the third, the fourth and the fifth shock tips.

Two regions of different behaviour can be observed in these results. For y/D between 0.5 and 4, the phase follows a pattern in fairly good agreement with the results predicted from (4.1). Farther, for y/D between 4 and 8, the phase draws unexpected patterns, particularly for the jets at $M_j = 1.13$ and 1.35. The choice of the shock corresponding to the screech acoustic source is not straightforward. There is no clear demarcation that would designate unambiguously the source location – the choice might change according to whether the considered region is only y/D between 0.5 and 4, or all the available spatial domain. Nevertheless, the interpretation of the results must be discussed when the distance to the nozzle increases. In fact, the fourth shock is located at $z/D = 2.7$, 2.9 and 4.8 for $M_j = 1.13$, 1.15 and 1.35 respectively. When the moving microphone is at $y/D = 4$, the angle formed between the jet axis and the lines linking the microphone to the source is 124°, 126° and 140°. Norum (1983) investigated the directivity of screech for B and C modes. He observed for the B mode a maximum of screech amplitude at angles close to 170°, and a drop of 10 dB at an angle of 133°, and again a 10 dB drop to reach 123°. These observations were made in the far field, and are therefore not directly applicable in the near field. Nevertheless, measurements of the screech pressure level across the moving microphone path are presented for the case $M_j = 1.35$ in figure 8. They exhibit the same sharp decrease of amplitude with increasing distance from the nozzle as expected from far-field data. The level is decreased by 20 dB at $y = 5.5D$. The lower the amplitude of the screech acoustic wave, the higher the influence of reflection and other contributions to phase measurement. For this reason, the result of this experiment must be considered with caution when y goes up. After these remarks, the results should not be regarded in the entire domain, and a look back at figure 7(*b*,*d*,*f*) leads us to conclude that the source is located between the third and the fifth shock tips. A better precision in source localisation cannot be obtained with the present method because the displacement of the source does not induce a sufficient phase shift between the two microphones. Better results would be obtained if one of the two microphone phases was less sensitive to the source location. In this configuration, a displacement of the source would involve a larger variation in phase for one microphone than for the other. This is obtainable by placing the reference in the plane perpendicular to the jet axis that passes through the expected source, so r_0 in (4.1) would be only slightly sensitive to the variation of source location, and $\Delta\phi$ would mostly be dependent upon r. This method requires *a priori* knowledge of the result, but this problem is circumvented by moving a microphone along a line parallel to the jet.

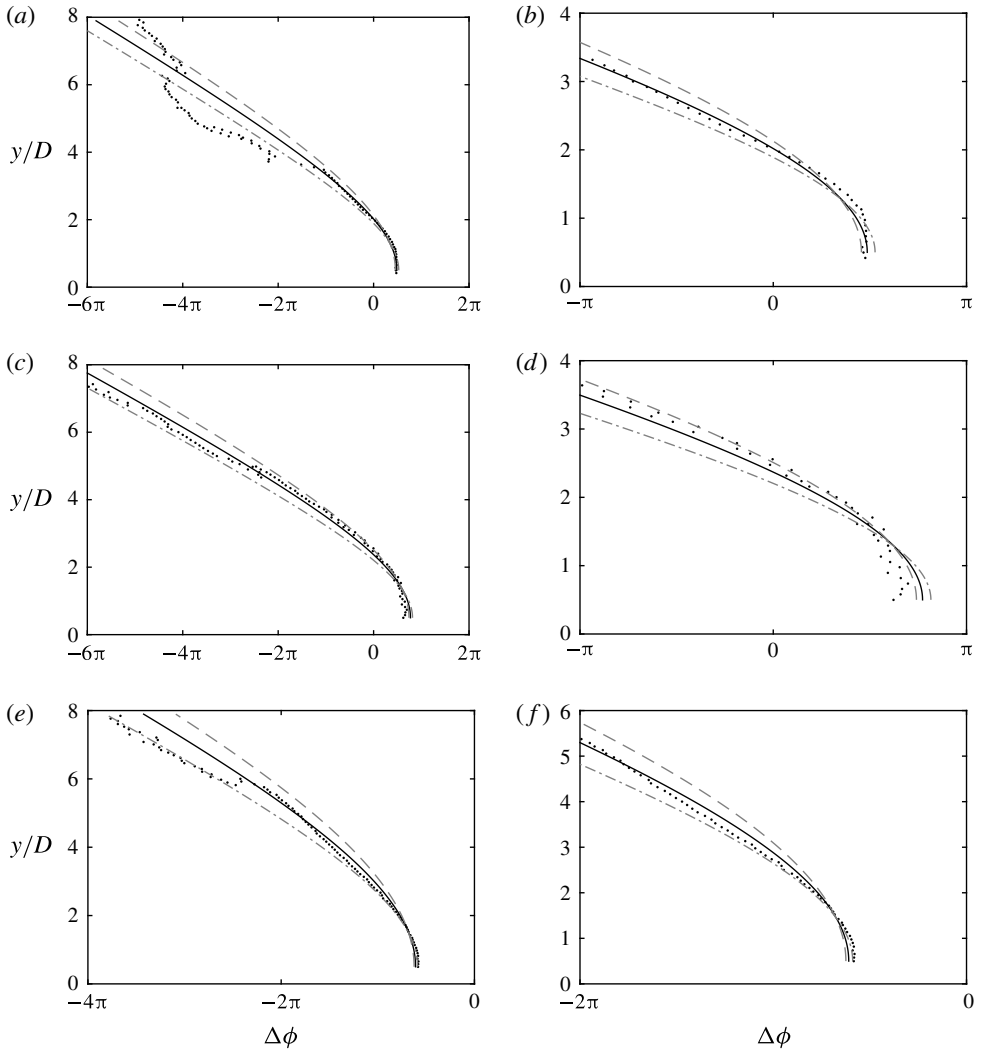

FIGURE 7. Comparison between the experimental and the expected phase lag between a reference microphone and a microphone moving along a line perpendicular to the jet axis in the nozzle exit plane. Graphs on the right are the same as graphs on the left but focused close to the nozzle. Curves: ——, fourth shock tip; – · –, third shock tip; – – –, fifth shock tip; · · · · · ·, measurements. Jet Mach number: (*a*,*b*) $M_j = 1.13$, (*c*,*d*) $M_j = 1.15$, (*e*,*f*) $M_j = 1.35$.

4.2. *Axial traverse post-processing*

In the axial configuration, the reference microphone is fixed at $y = 2.4D$ and $z = 0.4D$ with the same precision of $\pm 0.03D$ as mentioned for the radial traverse. The moving microphone measures the fluctuating pressure along the z direction by steps of 3–5 mm from $z = -0.1D$ to $z = 6D$ or $8D$. In contrast to the radial traverse, in this configuration the microphone is moved along a line close to the jet, and the fluctuating pressure results from the contribution of the acoustic and of the hydrodynamic pressure fields. The interaction between these two waves modulates the

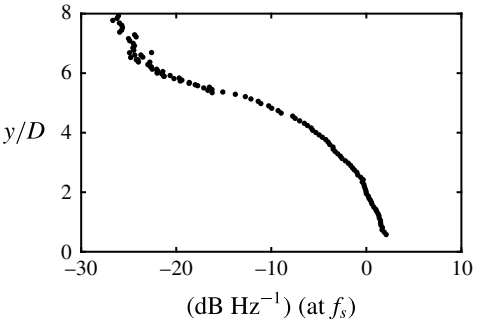

FIGURE 8. Sound pressure level (SPL) measured by the moving microphone SPL normalised by the reference microphone SPL in dB Hz^{-1} at f_s, for $M_j = 1.35$ along the radial traverse in the nozzle exit plane.

amplitude, the phase velocity and the spatial phase evolution of the resultant wave. This modulation makes it difficult to distinguish the 2π phase jumps from regular sharp variations in the region where the hydrodynamic pressure field is strong. This is a source of ambiguity for the unwrapping process; the problem is exacerbated because strong hydrodynamic fluctuations are expected to occur near the screech radiation source. For this reason we chose not to use classical methods for phase analysis such as cross-spectrum or cross-correlation, but to extract the screech coherent signal from random fluctuations by performing a phase average analysis. Such an analysis allows for tracking a single phase-averaged wavefront, and as a consequence avoids the 2π indeterminacy problem.

The phase average is performed for all probed locations along the measurement line. At each location, two synchronous signals are available, one from the reference microphone and the other from the moving microphone. The aim of the first step is to extract the phase at screech frequency provided by the fixed microphone, which will serve as the reference. The signal from the moving microphone will be sorted according to this reference in a second step. To this purpose, the signal measured on the fixed microphone is bandpass-filtered around the screech frequency. The filter is a finite impulse response (FIR) type with cut-off frequency at $\pm 10\,\%$ of f_s and a drop of 30 dB at $\pm 30\,\%$ of f_s. This filter is applied with a zero-lag method to ensure that the phase of the filtered signal does not become frequency-dependent, so there is no bias in the case of slight drift of the screech frequency. The resulting clean signal is the phase reference, and its maxima delimit the periods of screech. All periods of the record are then discretised into 20 bins of equal length that correspond to 20 increments of phase in a screech period. The samples of the moving microphone record that are in the same bin with respect to a period, and thus in phase, are averaged. This process is repeated for all longitudinal locations of the experiment. A complementary sketch presenting the method is provided in figure 9. In this figure, the phase axis is displayed between 0 and 4π; the phase average is performed over two consecutive periods because the wavefront tracking requires that the followed wavefront has enough time to travel from the source to the limits of the measured domain, here $z = 0$ and $z = 6$ or $8D$.

Phase-averaged results of all probed locations are in phase with the same reference; the spatial wave can therefore be rebuilt for each phase step. The spatial distribution of the coherent fluctuating pressure p_s against the phase with respect to the screech

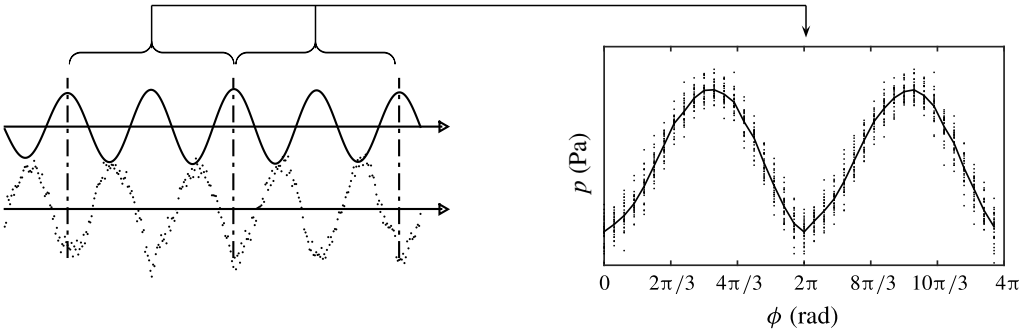

FIGURE 9. Example of phase average process. On the left: ——, reference bandpass filtered signal; · · · · · ·, moving microphone signal; |, period marks. On the right: · · · · · ·, data from the moving microphone sorted with respect to their phases; ——, phase-averaged signal.

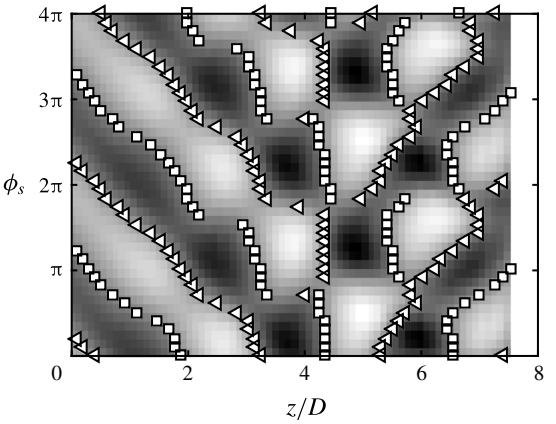

FIGURE 10. Coherent fluctuating pressure along a line at $y = 1.5D$ against the phase with respect to screech cycle in the jet $M_j = 1.32$ near field. The locations of the wavefronts are reported for the 40 phase steps: □, rising edges; ◁, falling edges.

cycle ϕ_s is provided in figure 10 for the $M_j = 1.32$ jet. The zero crossing points of the coherent fluctuating pressures are marked by squares or triangles depending on whether they correspond to a rising or a falling edge. These zero crossing points form a pattern which depicts curved lines representing the wavefronts of screech-associated waves. The direction of propagation of these waves is reversed near $z = 5D$. Considering the rising and the falling edges, four wavefronts can be observed in each direction. Both upstream and downstream of the slope inversion position, one of the wavefronts is found to be continuous from the source to the limits of the domain, and is selected to be compared with the expected phase variation $\Delta\phi$ calculated from (4.1).

4.3. *Experimental results on source location*

The spatial phase evolution of the screech phenomenon is studied across an axially oriented measurement line. This survey aims at investigating the axial evolution of the

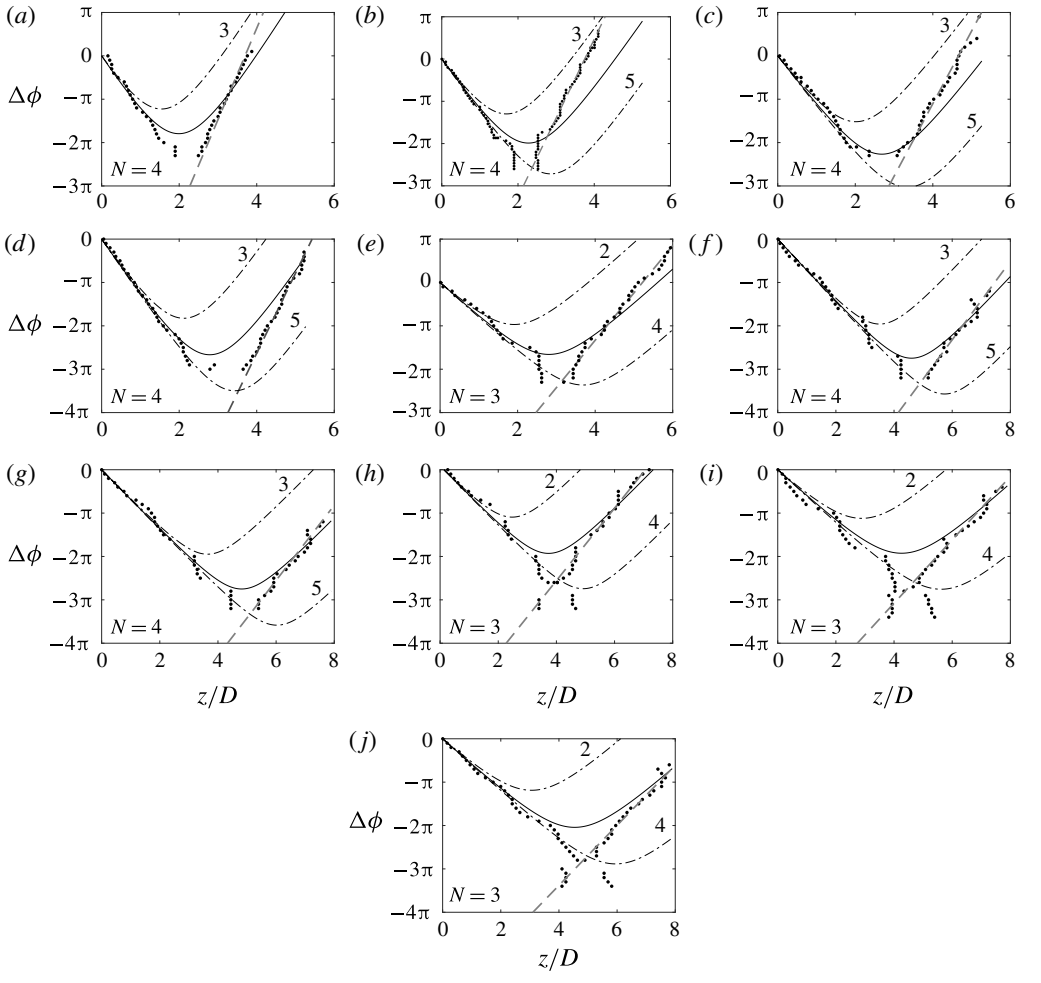

FIGURE 11. Comparison between the experimental and the expected phase lag between a reference microphone and the microphone moving parallel to the jet at (*a–f*) $y = 1.5D$ and (*g–j*) $y = 2D$: ·····, $\Delta\phi$; – – – $\mathrm{d}\phi_s/\mathrm{d}z = 2\pi f_s/(0.7U_j)$; ——, the expected result for the source at the shock N; and $-\cdot-$, at the labelled shock. Jet Mach number: (*a*) $M_j = 1.07$, (*b*) $M_j = 1.10$, (*c*) $M_j = 1.13$, (*d*) $M_j = 1.15$, (*e*) $M_j = 1.23$, (*f*) $M_j = 1.32$, (*g*) $M_j = 1.35$, (*h*) $M_j = 1.37$, (*i*) $M_j = 1.45$ and (*j*) $M_j = 1.50$.

phase lag. It concerns all the cases defined in table 2. The experimental results are compared with the corresponding expected phase lag in figure 11. A first look at this figure shows that the experimental results exhibit a slope sign inversion at a certain location as well as the expected phase lag. The slope $\mathrm{d}\phi_s/\mathrm{d}z$ is inversely proportional to the phase velocity of the wave projected onto the line along which the microphone is moved. The inversion of the sign of the slope translates to the inversion of the direction of wave propagation. In the present study, upstream of the location of slope inversion, the wave propagates upstream and conversely downstream. The study of the slopes of the upstream and downstream branches of the phase evolution provides information about their nature.

Considering only the upstream branch, the measured and the expected phase variations are similar. It is then concluded that the wavenumber of the measured phenomenon is the same as used in the model given in (4.1), k_s, for a speed of sound $c_0 = 337$ m s^{-1}. The wave detected in this region corresponds to the screech acoustic wave.

The measurement across the downstream branch diverges from the prediction. This divergence comes from a difference of slope, that is, a different speed of propagation. The slope of the measured axial phase evolution is higher than the predicted slope for an acoustic wave; the phase velocity of the phenomenon is thus lower than the speed of sound. The near-field pressure at the screech frequency is composed of acoustic and hydrodynamic contributions. The hydrodynamic convective velocity is subsonic for all the cases and is therefore eligible for explaining the slope of the downstream branch. This is also consistent with the conclusion of § 3 stating the absence of acoustic signature downstream of a given region. The slope of the measured phase evolution is compared to the expected slope considering a convective velocity $U_c = 0.7U_j$, which corresponds to estimation from the wavenumber analysis in § 3. This slope is

$$\frac{\mathrm{d}\phi}{\mathrm{d}z} = \frac{\omega_s}{U_c}. \tag{4.2}$$

The hydrodynamic pressure field is attached to the coherent structures that travel inside the mixing layer almost parallel to the jet axis, and to the line of measurements; thereby, there is no effect of projection. The hydrodynamic phase velocity measured by the microphone traverse is directly equal to the convective velocity. A line of slope corresponding to $U_c = 0.7U_j$ is added as a grey dashed line in figure 11. This line fits the experimental results well, demonstrating that the downstream-propagating branch is dominated by hydrodynamic near-field pressure. The instability wave at the screech frequency is recognised in § 3.1 to be strongly modulated by shock cells, resulting in nodes and antinodes of its amplitude. Thus, the relative acoustic and hydrodynamic amplitudes are dependent upon z. For a given acoustic pressure level, hydrodynamics might dominate at antinodes of the instability wave, and might be dominated by acoustics at nodes. Upstream of the source, the slope of acoustic associated phase lag is negative, and turns positive downstream of the source. The slope of hydrodynamic associated phase lag is positive everywhere. Therefore, wherever the slope is negative, the acoustic pressure field dominates, and the source is necessarily located downstream. This observation sets an upstream limit for the source location, but the downstream limit is still not defined. The source is assumed to be located at a distance of one shock cell or more downstream from the position where the negative slope turns positive. Then, between the inversion location and the source, the positive slope would be sustained by the dominance of the hydrodynamic contribution. Yet, since this contribution is modulated with a wavelength of one shock cell, acoustic should become stronger than hydrodynamic at a certain location upstream of the next shock, so the slope would turn negative again, in contradiction with our first hypothesis. Therefore, the source must be located somewhere in between the last place of negative slope and one shock cell downstream. Constraining the screech source to be located at a shock tip, the shock tip number N corresponding to the source is selected for being the first shock downstream of the last negative slope location. The expected phase lags obtained from the previous and the next shock tips are also included in figure 11 in order to show that there is no ambiguity in finding which agrees better. The fourth shock is found to be the source for all cases except $M_j = 1.23$, 1.37, 1.45 and 1.50. The source is the third shock tip for these four cases.

M_j	Mode	N	m	z_N/D	$\overline{U_c}/U_j$ (from table 4)	$\overline{L_{sc}}/D$
1.07	A1	4	4	2.0	0.53 (0.57)	0.48
1.10	A1	4	4	2.3	0.55 (0.57)	0.57
1.13	A1	4	4	2.7	0.58 (0.57)	0.67
1.15	A2	4	5	2.8	0.56 (0.58)	0.70
1.23	b	3	3	2.7	0.52 (0.54)	0.90
1.32	B	4	4	4.5	0.57 (0.59)	1.13
1.35	B	4	4	4.8	0.59 (0.61)	1.20
1.37	b	3	3	3.8	0.56 (0.57)	1.25
1.45	b	3	3	4.3	0.59 (0.55)	1.43
1.51	—	3	—	4.8	— (0.59)	1.61

TABLE 5. Summary of results about the screech loop structure: n = number of the radiating shock tip; m = number of screech periods per loop; z_N/D = location of the source; $\overline{U_c}/U_j$ = mean convective velocity from the nozzle to the source derived from the phase analysis and, in brackets, from the wavenumber analysis; $\overline{L_{sc}}/D$ = mean shock cell length upstream of the source.

The source locations and the associated shock tips are summarised for all cases in table 5. Since acoustic sources are identified, the screech loop is delimited in space, and can be examined in a suitable domain as discussed in § 3.

5. Screech loop

The screech loop is composed of the instability wave convected from the nozzle to the source, and of the acoustic feedback from the source to the nozzle. The travel along this loop takes time T_{loop} given by

$$T_{loop} = \frac{z_N}{\overline{U_c}} + \frac{z_N}{c_0}, \tag{5.1}$$

with z_N the distance from the nozzle to the shock tip N recognised as the screech source, and $\overline{U_c}$ the mean convective velocity between the nozzle and the source. Assuming that a new structure is triggered exactly when the acoustic wave reaches the nozzle, acoustic and hydrodynamic must be in phase at the nozzle exit. In other words, the total time spent along the loop T_{loop} is necessarily a multiple m of the screech period T_s. In terms of phase, this statement requires the total phase spent along a loop $\phi_{loop} = 2\pi T_{loop}/T_s$ to be a multiple of 2π. The phase of the screech-associated phenomena ϕ_s is calculated along the line $y/D = 0.55$ from high-speed schlieren records. A series of cross-spectra are computed between the grey-level signal of a pixel at the nozzle exit $g(0.55D, 0, t)$ and the signal of another point moving along the z direction $g(0.55D, z, t)$. For each cross-spectrum, the phase at the screech frequency ϕ_s is extracted. The result is then unwrapped to obtain a continuous curve and, if needed, is shifted by increments of 2π to ensure that the prolongation of the positive slope part of the curve downstream approximately crosses $z = 0$ at $\phi_s = 0$. This curve is finally displayed on a (z, ϕ_s) plane in figure 12.

Two characteristics common to all cases, except for $M_j = 1.50$, are noticed in figure 12. The first feature is the inversion of the slope of the curve upstream of the second shock. This observation is related to the local ratio of the amplitude of the hydrodynamic and acoustic waves: close to the nozzle, the hydrodynamic wave

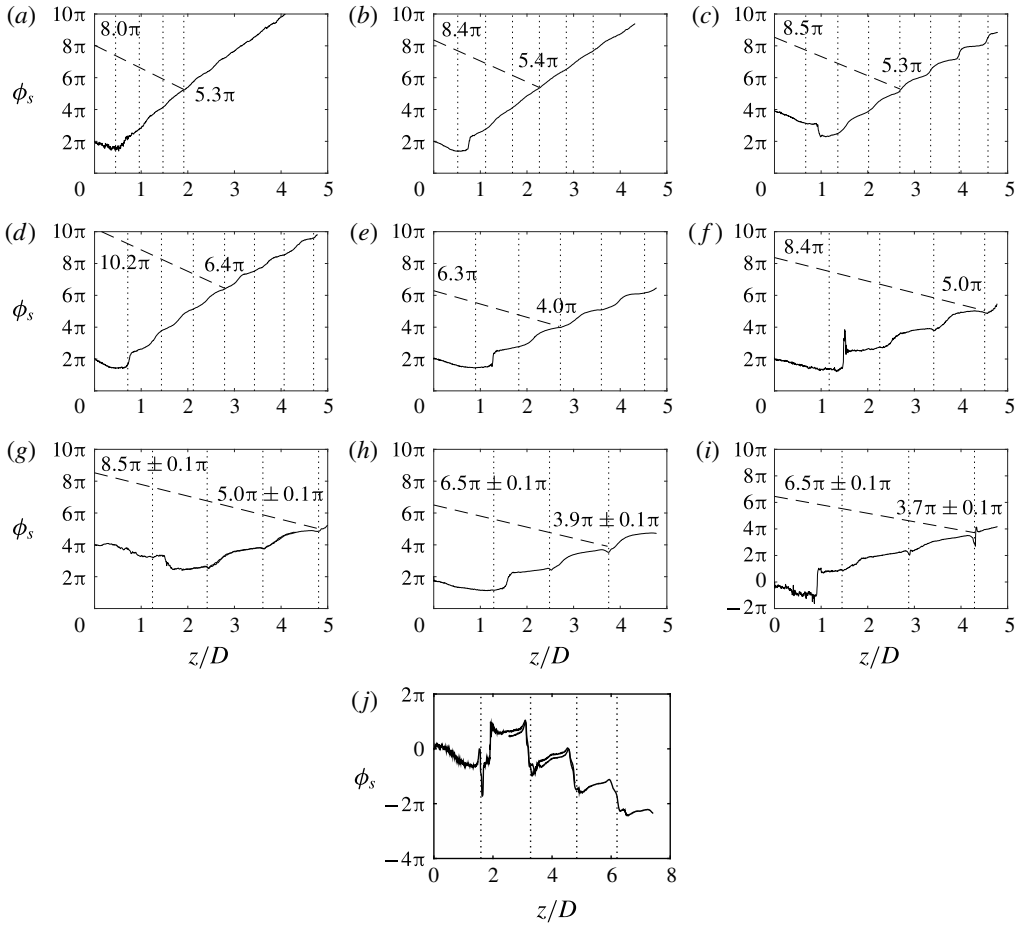

FIGURE 12. Phase evolution $\phi_s = 2\pi t/T_s$ extracted from the cross-spectrum between a pixel at the nozzle and a pixel moving along the line $y/D = 0.55$: – – –, acoustic feedback at 337 m s^{-1}; shock locations are indicated by vertical dotted lines. Jet Mach number: (*a*) $M_j = 1.07$, (*b*) $M_j = 1.10$, (*c*) $M_j = 1.13$, (*d*) $M_j = 1.15$, (*e*) $M_j = 1.23$, (*f*) $M_j = 1.32$, (*g*) $M_j = 1.35$, (*h*) $M_j = 1.37$, (*i*) $M_j = 1.45$ and (*j*) $M_j = 1.50$.

grows, but is weak compared to the acoustic feedback. This is the receptivity region, characterised by a negative slope corresponding to a wave propagating upstream. The case depicting the earliest slope inversion is $M_j = 1.07$; the inversion occurs at $z/D \simeq 0.5$; and the latest occurs at $z/D \simeq 2$ for $M_j = 1.35$. Downstream of some location, the hydrodynamic wave overcomes the acoustic, and the slope of the curve turns positive. This slope inversion is not visible for the case $M_j = 1.50$, which must be considered jointly with the shape of the wavenumber spectrum in figure 6(*j*): the $M_j = 1.50$ jet is the only case exhibiting a higher peak in negative wavenumber than in positive, which means a predominant upstream-propagating contribution. This observation is currently not understood. The second feature common to all cases is the wavy shape of the curve, resulting from the interaction between the instability wave, the acoustic wave and the shock cell pattern as discussed in § 3.1, with more details in Panda (1999). In addition to the hydrodynamic wave, the acoustic feedback is represented in figure 12 by a dashed line of negative slope $-\omega_s/c_0$ plotted from the point at which the hydrodynamic wave crosses the shock recognised as the acoustic

source. The modulation prevents the hydrodynamic wave from being localised with precision, but the latter is assumed to go along the line of best fit, calculated from the data between $z_N - L_{sc}/2$ and $z_N + L_{sc}/2$. The shock oscillation during a screech cycle (Panda 1998; André *et al.* 2011*b*) should also be considered. The amplitude of shock motion is estimated from the profile of $g(0.50D, z, t)$ fluctuations. Locations affected by the passage of the shock show the significantly largest level of fluctuations. The full width at half maximum of the peak associated with shock passage is considered as a reasonable estimation of the uncertainty of shock position, and is turned into a phase error.

The acoustic wave reaches the nozzle at the phase ϕ_{loop} expected to be a multiple of 2π. For all cases, ϕ_{loop} is indeed found to be close to an even multiple of π. The largest difference is 0.5π away from a 2π multiple, and all are positive. Although the modulation may play a role in these discrepancies, it might also be connected to an observation by Mitchell, Honnery & Soria (2012) in a comparable feedback process. Their experimental results point out the generation of an incited vortex ring in the mixing layer $0.25D$ downstream from the nozzle, suggesting that the trigger position of the instability could be slightly shifted. Phase ϕ_{loop} is considered to determine the number of screech cycles that compose the full screech loop, and to check for consistency between cases of the same mode.

The acoustic feedback is not expected to travel inside the mixing layer wherein convection slows down retrograde acoustics. The present model may underestimate the propagation time from the source to the nozzle. A pessimistic upper bound of the error is estimated by calculating the time spent by an acoustic wave to cross the shear layer half-thickness. This corresponds for the worst case $M_j = 1.15$ to a phase increment of 0.4π. Nevertheless this additional phase will not introduce ambiguity in defining the closest 2π multiple from ϕ_{loop}.

Cases $M_j = 1.07$, 1.10 and 1.13 are all the A1 mode, the acoustic source is located at the fourth shock tip, and the screech loop is made of four screech periods. Case $M_j = 1.15$ is the A2 mode; it differs from A1 by the number of screech periods in a loop – it is made of five periods. Higher-Mach-number jets all exhibit a flapping mode: $M_j = 1.23$, 1.37 and 1.45 emit acoustic from the third shock tip and their loops are composed of three periods, whereas $M_j = 1.32$ and 1.35 generate acoustic from the fourth shock tip and their loops are made of four periods. According to the Mach number of these different cases, the first set could show the characteristics of the b mode defined by Powell as a secondary mode (Powell *et al.* 1992), and the second set could be representative of the B mode. Nevertheless, Powell described secondary modes as modes coexisting with a dominant one – the b mode coexists with the A2 and C modes – but all the present cases manifest a single screech tone, and the C mode is not observed.

The convective velocity $\overline{U_c}$ averaged between the nozzle and the source at $z = z_N$ is deduced from the phase at the source ϕ_N by the relation

$$\overline{U_c} = f_s \frac{2\pi}{\phi_N} z_N. \tag{5.2}$$

The average shock cell length $\overline{L_{sc}}$ is calculated by

$$\overline{L_{sc}} = \frac{z_N}{N}. \tag{5.3}$$

Those results are summarised in table 5 and the convective velocity estimated from the wavenumber analysis is repeated for comparison. To better show the sensitivity of

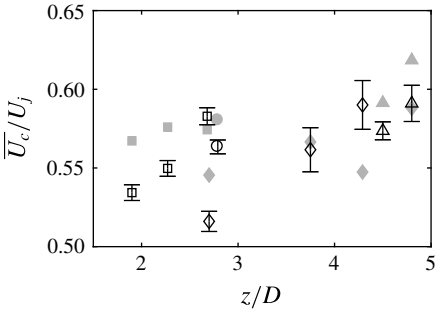

FIGURE 13. Spatially averaged convective velocity from the nozzle to the acoustic source normalised by the jet fully expanded velocity $\overline{U_c}/U_j$, against the acoustic source location z_N: □, A1 mode; ○, A2 mode; ◇, b mode; △, B mode; filled markers are from the wavenumber analysis; empty markers are from the phase analysis.

the convective velocity to Φ_s, error bars have been determined. They correspond either to the uncertainty linked to the shock motion, or to a floor of $\pm 0.05\pi$ representing the unknown third digit of Φ_s. The convective velocities estimated by the two methods are very close. The worst comparison concerns the cases $M_j = 1.07$ and $M_j = 1.45$; their convective velocities from wavenumber analysis differ respectively by $-8\,\%$ and $+7\,\%$ from phase evolution analysis. The good agreement between the results from the two different methods provides confidence for the interpretation of these figures. The main feature to be noted is the evolution of the convective velocity within a given mode – a fixed convective velocity cannot be attributed to a mode. The convective velocities are presented in figure 13 against the source location. Looking, for instance, at results for the mode A1, the convective velocity tends to rise when the position of the source is shifted downstream. This phenomenon is expected from the wavenumber analysis showing that the convective velocity is found close to $0.6U_j$ upstream of the source, and close to $0.7U_j$ downstream, so the convective velocity of the screech instability wave increases along its travel within the mixing layer. This can also explain why, with the exception of the $M_j = 1.13$ and $M_j = 1.45$ cases, all velocities calculated from wavenumber analysis are found to be higher than those from a phase analysis. The result of the spatial Fourier transform is somehow weighted by the local amplitude of the instability wave that grows along its travel within the mixing layer. The contribution coming from the region of low speed near the nozzle is underestimated in comparison with the influence of the high-convective-speed region near the source, resulting in an overestimation of the velocity averaged between the nozzle and the source. The convective velocity of the case $M_j = 1.23$ is equal to $0.52U_j$, against $0.56U_j$ for the case $M_j = 1.15$. However, the sources of these two cases are located very close to each other. The noticeable difference of U_c results from mode switching. It could also result from a compressibility effect due to the change of Mach number. Nevertheless, convective velocities are very similar for the two jets whose sources are located at $z/D = 4.6$ and $z/D = 4.7$, but whose Mach numbers are $M_j = 1.35$ and $M_j = 1.50$. In this case, the convective velocity seems not to be affected by compressibility effects. The mean convective velocity $\overline{U_c}$ is an input in screech frequency prediction models; therefore improving the screech frequency prediction requires a better understanding of the evolution of convective velocity with axial distance.

6. Conclusion

Acoustic and hydrodynamic properties of screech are investigated over 10 underexpanded supersonic jets of Mach number ranging from 1.07 to 1.50. Near-field acoustic measurements are achieved and schlieren visualisations of the jet near field and the shear layer are recorded. The two stages of the screech cycle that set the screech period are examined, namely the convection of the instability wave within the jet shear layer and the acoustic feedback. If it seems reasonable to consider the speed of sound as a constant along the feedback path, it is not the case for the convective velocity of the instability wave. The spatial dependence of U_c might involve a difficulty in predicting screech frequency; this velocity must be seen as an averaged value. Such an averaging must be calculated on a given spatial domain, which is bounded by the nozzle on one side and the screech acoustic source on the other side. The localisation of the source is therefore a major concern in understanding the screech loop and in predicting the screech frequency. An examination of the spatial evolution of the phase at the screech frequency of pressure signals has been conducted. The axial phase evolution survey provides the location of the source. It is found at the fourth shock tip for modes A1 and A2, and at either the third or the fourth shock tip for the B mode. The phase at the screech frequency is also measured within the shear layer from the schlieren records. In this region, the hydrodynamic contribution overcomes the acoustic, and, since the location of the source has been found, the convective velocity can be estimated by looking at the time spent by the instability wave to travel from the nozzle to the source. Its value varies from $0.54U_j$ to $0.61U_j$ with a tendency to rise when the distance between the nozzle and the source is increased.

Wavenumber spectra are also computed from the Fourier coefficients at the screech frequency of the schlieren data calculated along axially oriented lines. When considering results obtained upstream of the source, two peaks are identified in the spectra: one corresponds to the instability wave propagation, and the other to the acoustic feedback. The convective velocity is also estimated from these results, and is found to be in good agreement with the results obtained from the first method. The acoustic feedback wave propagation speed is estimated to be at $\pm 10\,\%$ of the speed of sound.

The screech loop is finally examined by measuring the phase of the screech-associated wave along the mixing layer down to the source, and by considering a feedback straight to the nozzle at the speed of sound. The time taken to travel the full loop is found to be equal to four periods for the A1 mode, five periods for the A2 mode, and either three or four periods for the B mode.

Acknowledgement

This work was performed within the framework of the Labex CeLyA of the Université de Lyon, within the programme 'Investissements d'Avenir' (ANR-10-LABX-0060/ANR-11-IDEX-0007) operated by the French National Research Agency (ANR), and is also partially supported by the industrial Chair ADOPSYS co-financed by Safran Aircraft Engines and the ANR (ANR-13-CHIN-0001-01).

Appendix

The real part of the Fourier transform at the screech frequency is calculated at all pixels of the schlieren films and normalised in amplitude. The results are

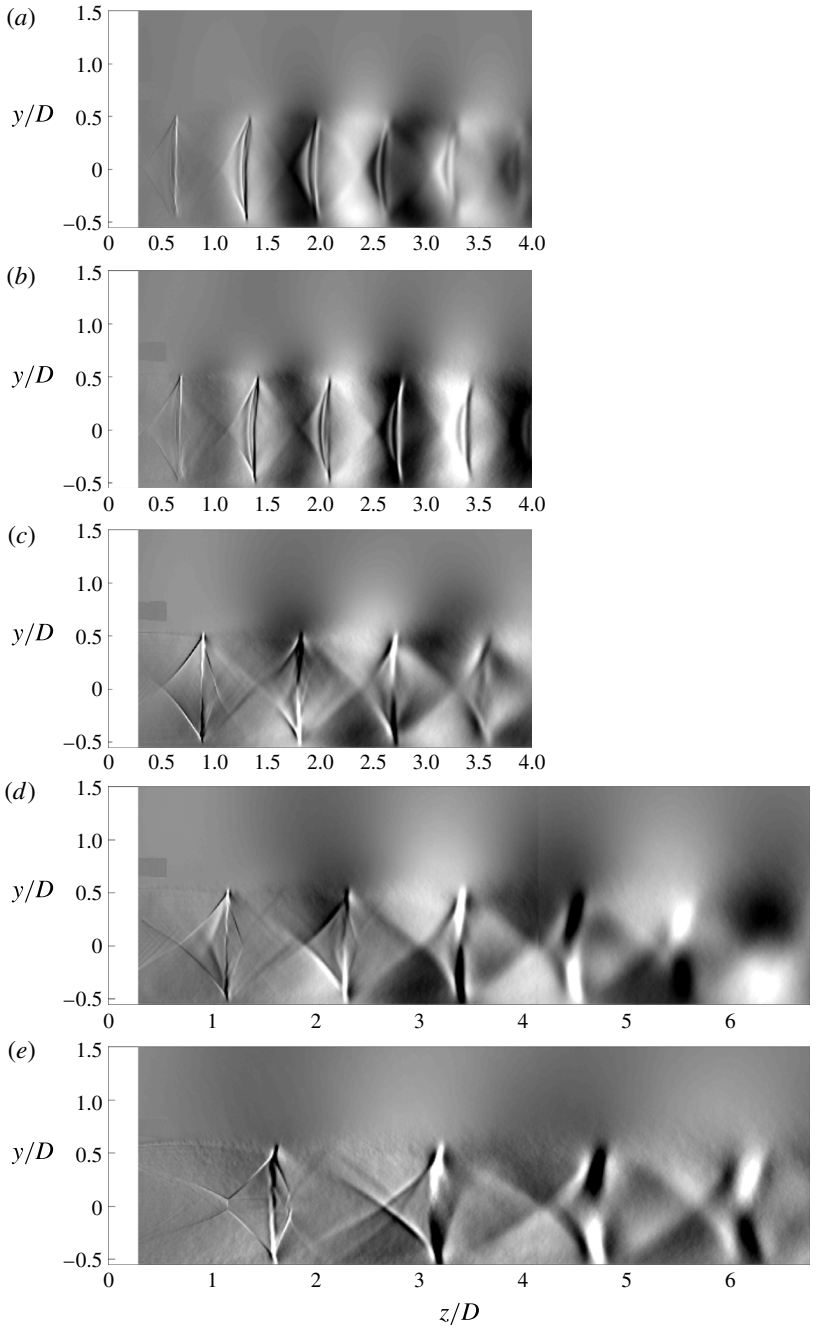

FIGURE 14. Real part of the Fourier transform at the screech frequency calculated from schlieren films: (*a*) $M_j = 1.13$ mode A1, (*b*) $M_j = 1.15$ mode A2, (*c*) $M_j = 1.23$ mode b, (*d*) $M_j = 1.32$ mode B, (*e*) $M_j = 1.50$ mode b. Results from two schlieren records are juxtaposed in (*d*) and (*e*).

provided in figure 14. Axisymmetric modes A1 and A2 are respectively represented in figure 14(*a*,*b*). Antisymmetric modes b and B are shown in figure 14(*c*,*e*) and figure 14(*d*). An azimuthal modal decomposition has been performed from the

signals of an azimuthal array of nine microphones following the method proposed in Massey & Ahuja (1997), and showed that all antisymmetric modes are flapping (B and b modes).

REFERENCES

André, B. 2011 Nozzle geometry. Available at: http://acoustique.ec-lyon.fr/jetnoise_uk.php.

André, B. 2012 Etude expérimentale de l'effet du vol sur le bruit de choc de jets supersoniques sous-détendus. PhD thesis, No. 2012-42, Ecole Centrale de Lyon.

André, B., Castelain, T. & Bailly, C. 2011*a* Experimental study of flight effects on screech in underexpanded jets. *Phys. Fluids* **23** (12), 126102.

André, B., Castelain, T. & Bailly, C. 2011*b* Shock-tracking procedure for studying screech-induced oscillations. *AIAA J.* **49** (7), 1563–1566.

Bailly, C. & Fuji, K. 2016 High-speed jet noise. *Mech. Engng Rev.* **3** (1), 1–13.

Berland, J., Bogey, C. & Bailly, C. 2007 Numerical study of screech generation in a planar supersonic jet. *Phys. Fluids* **19** (7), 075105.

Chatterjee, A., Ghodake, D. & Singh, A. 2009 Screech frequency prediction in underexpanded axisymmetric screeching jets. *Intl J. Aeroacoust.* **8** (5), 499–510.

Clem, M. M., Zaman, K. B. M. Q. & Fagan, A. F. 2016 Variation of shock-spacing during screech stage-jumps. *Intl J. Aeroacoust.* **15** (3), 324–335.

Davies, M. G. & Oldfield, D. E. S. 1962 Tones from a choked axisymmetric jet. II. The self excited loop and mode of oscillation. *Acustica* **12** (4), 267–277.

Edgington-Mitchell, D., Honnery, R. D. & Soria, J. 2015 Staging behaviour in screeching elliptical jets. *Intl J. Aeroacoust.* **14** (7–8), 1005–1024.

Edgington-Mitchell, D., Oberleithner, K., Honnery, D. R. & Soria, J. 2014 Coherent structure and sound production in the helical mode of a screeching axisymmetric jet. *J. Fluid Mech.* **748**, 822–847.

Gao, J. H. & Li, X. D. 2010 A multi-mode screech frequency prediction formula for circular supersonic jets. *J. Acoust. Soc. Am.* **127** (3), 1251–1257.

Gasior, M. & Gonzalez, J. L. 2004 Improving FFT frequency measurement resolution by parabolic and Gaussian spectrum interpolation. *AIP Conf. Proc.* **732** (1) 276–285.

Gojon, R., Bogey, C. & Marsden, O. 2015 Large-eddy simulation of underexpanded round jets impinging on a flat plate 4 to 9 radii downstream from the nozzle. *AIAA Paper* 2210-2015.

Harper-Bourne, M. & Fisher, M. J. 1973 The noise from shock waves in supersonic jets. *AGARD CP* 131.

Massey, K. C. & Ahuja, K. K. 1997 Screech frequency prediction in light of mode detection and convection speed measurements for heated jets. *AIAA Paper* 97-1625.

Mercier, B., Castelain, T. & Bailly, C. 2016 A schlieren and nearfield acoustic based experimental investigation of screech noise sources. *AIAA Paper* 2016-2799.

Merle, M. 1957 Nouvelles recherches sur les fréquences ultrasonores émises par les jets d'air. *Annales des Télécommunications* **12** (12), 424–426.

Mitchell, D., Honnery, D. R. & Soria, J. 2012 The visualization of the acoustic feedback loop in impinging underexpanded supersonic jet flows using ultra-high frame rate schlieren. *J. Vis.* **15** (4), 333–341.

Norum, T. D. 1983 Screech suppression in supersonic jets. *AIAA J.* **21** (2), 235–240.

Panda, J. 1996 An experimental investigation of screech noise generation. *AIAA Paper* 96-1718.

Panda, J. 1998 Shock oscillation in underexpanded screeching jets. *J. Fluid Mech.* **363**, 173–198.

Panda, J. 1999 An experimental investigation of screech noise generation. *J. Fluid Mech.* **378**, 71–96.

Panda, J. & Raman, G. 1997 Underexpanded screeching jets from circular, rectangular, and elliptic nozzles. *AIAA Paper* 97-1623.

Ponton, M. K. & Seiner, J. M. 1995 Acoustic study of b helical mode for choked axisymmetric nozzle. *AIAA J.* **33** (3), 413–420.

Powell, A. 1953 On edge tones and associated phenomena. *Acustica* **3**, 233–243.

POWELL, A., UMEDA, Y. & ISHII, R. 1990 The screech of round choked jets, revisited. *AIAA Paper* 90-3980.

POWELL, A., UMEDA, Y. & ISHII, R. 1992 Observations of the oscillation modes of choked circular jets. *J. Acoust. Soc. Am.* **92** (5), 2823–2836.

RAMAN, G. 1997 Cessation of screech in underexpanded jets. *J. Fluid Mech.* **336**, 69–90.

RAMAN, G. 1999 Supersonic jet screech: half-century from Powell to the present. *J. Sound Vib.* **225** (3), 543–571.

SHARIFF, K. & MANNING, T. A. 2013 A ray tracing study of shock leakage in a model supersonic jet. *Phys. Fluids* **25** (7), 076103.

SHEN, H. & TAM, C. K. W. 2002 Three-dimensional numerical simulation of the jet screech phenomenon. *AIAA J.* **40** (1), 33–41.

SUZUKI, T. & LELE, S. K. 2003 Shock leakage through an unsteady vortex-laden mixing layer: application to jet screech. *J. Fluid Mech.* **490**, 139–167.

TAM, C. K. W. 1995 Supersonic jet noise. *Annu. Rev. Fluid Mech.* **27** (1), 17–43.

TAM, C. K. W., JACKSON, J. A. & SEINER, J. M. 1985 A multiple-scales model of the shock-cell structure of imperfectly expanded supersonic jets. *J. Fluid Mech.* **153**, 123–149.

TAM, C. K. W., PARRISH, S. A. & VISWANATHAN, K. 2014 Harmonics of jet screech tones. *AIAA J.* **52** (11), 2471–2479.

TAM, C. K. W., SEINER, J. M. & YU, J. C. 1986 Proposed relationship between broadband shock associated noise and screech tones. *J. Sound Vib.* **110** (2), 309–321.

UMEDA, Y. & ISHII, R. 2001 On the sound sources of screech tones radiated from choked circular jets. *J. Acoust. Soc. Am.* **110** (4), 1845–1858.

VELTIN, J., DAY, J. B. & MCLAUGHLIN, K. D. 2011 Correlation of flowfield and acoustic field measurements in high-speed jets. *AIAA J.* **49** (1), 150–163.

VELTIN, J. & MCLAUGHLIN, D. K. 2008 Noise mechanisms investigation in shock containing screeching jets using optical deflectometry. *AIAA Paper* 2008-2889.

WESTLEY, R. & WOOLLEY, J. H. 1969 The near field sound pressures of a choked jet during a screech cycle. *AGARD CP* **42**, 23.1–23.13.

Article

aeroacoustics

International Journal of Aeroacoustics
2019, Vol. 18(2–3) 207–230

DOI: 10.1177/1475472X19834530
journals.sagepub.com/home/jae
SAGE

Experimental study of the coherent vorticity in slightly under-expanded supersonic screeching jets

Bertrand Mercier[1], Thomas Castelain[2] and Christophe Bailly[1]

Abstract

The noise generation mechanism of screech tone by shock leakage in underexpended round jets is experimentally investigated by means of phase-averaged velocity fields. Two jet flows at Mach numbers 1.10 and 1.15 are measured by a particle image velocimetry apparatus simultaneously with their near acoustic fields and sorted according to their phase with respect to a screech period. The coherent vorticity fields are then computed and analyzed. They depict two distinct regions of high level of vorticity fluctuations. Thanks to the knowledge about shock leakage gathered in previous studies, the role of both regions in the acoustic generation process is identified and a region of the flow is recognized as suitable for emitting acoustic waves. Phase-averaged schlieren visualizations are also computed and used to determine the motion of the first five shocks over a screech period. For both jets, the peak shock motion is found at the fourth shock tip. This shock is also located in the region recognized as favorable for the shock leakage to be observed.

Keywords

Underexpanded jet, screech, experimental study, particle image velocimetry, schlieren

Date received: 8 February 2019; accepted: 8 February 2019

Introduction

Screech noise is a tonal component produced by imperfectly expanded supersonic jets. It was first identified by Powell[1] as a phenomenon emerging from an acoustic feedback

[1]Univ Lyon, Ecole Centrale de Lyon and LMFA UMR CNRS 5509, Ecully, France
[2]Univ Lyon, Université Lyon 1 and LMFA UMR CNRS 5509, Ecully, France

Corresponding author:
Bertrand Mercier, Laboratoire de Mécanique des Fluides et Acoustique, Ecole Centrale de Lyon, LMFA UMR CNRS 5509, Ecully, France.
Email: B.H.Mercier@tudelft.nl

mechanism. From this pioneering work, it has been accepted that the feedback loop can be split into hydrodynamic structures convected in the jet mixing layer, and acoustic waves propagating upstream that initiate the generation of new structures when reaching the nozzle. Acoustic waves are produced by the interaction between the hydrodynamic structure and the periodic shock-cell pattern. The principle of this loop is now widely accepted in aeroacoustics, but the complex mechanisms causing the acoustic radiation and the acoustic receptivity of the mixing layer remain an ongoing research topic. Fairly accurate models[2–5] indeed allow for screech frequency prediction, but the understanding of the process in terms of gain is necessary for predicting screech intensity. The receptivity has been indirectly investigated by modifying the acoustic field through the use of reflectors[6–9] and absorbent panels[10,11] near the nozzle, and the flow itself with different shapes of nozzle lip,[12–15] but has not yet been modeled. Several theoretical approaches have nevertheless been developed over time. Tam's theory[16,17] rests upon the linear interaction between the screech instability waves, and the periodic shock-cell pattern that produces an upstream propagating wave at screech frequency which travels at the speed of sound. A second theory[18–21] relies on the acoustic emission by shock leakage across the mixing layer, but suffers from a lack of quantitative data to be fully established. The aim of the present work is to provide such data complementary with those proposed by Edgington-Mitchell et al.[22] for the helical mode. In particular, the study focuses on the experimental characterization of the coherent vorticity field that plays a critical role in shock leakage.

Screech displays various modes associated with different frequency stages that depend upon the nozzle pressure ratio (NPR). These modes are axisymmetric, flapping, or helical and described in Ramanib's review[23] for round jets. The present study will focus on under-expanded jets exhausted from a convergent nozzle at low supersonic Mach number, for which only the axisymmetric modes called A1 and A2 are observed. For two jets, the velocity and vorticity fields coherent with the screech tone are extracted from particle image velocimetry (PIV) measurements of the planar velocity field, thanks to phase averaging post-processing. A mechanism for screech radiation based on the shock leakage is proposed, and a region of possible upstream propagating acoustic radiation is identified. These results are finally put together with the shock dynamics determined from phase-averaged schlieren measurements on the same jets to provide a complete picture of screech.

Experimental setup

The present experiments were conducted in the 10 m × 8 m × 8 m anechoic wind tunnel of the Center for Acoustic at École Centrale de Lyon. The wind tunnel is equipped with a high pressure compressor and a high flow rate centrifugal fan. In the present experiment, the high pressure supply is connected to a convergent nozzle[24] of exit diameter $D = 38$ mm. A secondary convergent nozzle coaxial to the primary one of diameter 236 mm is also used and fed by the fan. The exit plane of this secondary nozzle is located 135 mm upstream of the exit plane of the primary one. For this study, the NPR of the jets generated by the primary nozzle are NPR = 2.14 and NPR = 2.27 that correspond to fully expanded jet exhausted at a Mach number $M_j = 1.10$ and $M_j = 1.15$ and to Reynolds numbers of $Re_D = 8.5 \times 10^5$ and $Re_D = 8.9 \times 10^5$, respectively. The NPR is monitored during experiments and was found to remain constant within ±0.3%. The secondary flow is only used for flow seeding purpose during PIV measurement, with an exit velocity of approximately 10 m/s.

PIV was applied to measure planar velocity fields of the two jets. Illumination is provided by a Litron Bernoulli 200–15 laser at 532 nm wavelength with 2×200 mJ pulse energy. The laser sheet crosses the jet through its axis and covers a usable field of $3D$ in the axial direction, and $\pm 1.5D$ around the jet axis in the radial direction. Particle images are acquired by a PCO.edge 5.5 camera mounted perpendicular to the laser sheet at a distance of 1 m. It is equipped with a 135 mm lens and an additional 20 mm extension ring. The images contain 2560 × 2160 pixels covering a field centered on the jet axis of axial and radial extents $2.9D$ (110 mm) and $2.4D$ (90 mm). The images are separated by 2 μs at a repetition rate of 15 Hz. For each studied case, data are made of three set of acquisitions shifted by $2.5D$ that results in a field of physical size $7.4D \times 2.4D$. The primary jet is seeded by an oil droplet generator, and the secondary flow is seeded with smoke. The relaxation time of the particles has been recognized as satisfactory in André et al.[25] for this configuration. The post-processing is performed by LaVision DaVis 7 with initial interrogation windows of 32 × 32 ($0.04D \times 0.04D$) pixels decreasing to 8×8 ($0.01D \times 0.01D$) with 50% overlap and two passes per window size.

A conventional Z-type schlieren apparatus was also used to visualize the flow. It consists of two $f/8$ parabolic mirrors of diameter 200 mm separated by 2.5 m, a high-power Cree XP-L LED as light source, and a knife edge set perpendicular to the jet axis. Images are recorded at a sampling rate of 18,000 frames per second by a Phantom V12 CMOS camera equipped with a Sigma 120–400 mm $f/4$–5.6 lens. The exposure time of the images is 4 μs, which is approximately equal to 1/40th of the screech period for both jets.

Phase averaging

Particle image velocimetry

Phase-averaged flow description consists in determining the evolution of an arbitrary quantity with its phase with respect to a given periodic phenomenon. A first method consists in triggering the acquisition of data from a reference signal. This method has for instance been used in the investigation of the screech phenomenon by Westley and Wolley,[26] Panda[27] or Alkislar et al.[28] from schlieren visualization, near field pressure, density measurements, or PIV measurements. The quality of the phase reference, however, rests upon the reference signal that must be cleaned from any noise contamination. For the screech tone, the reference signal can be the acoustic pressure measured in the upstream direction of the jet which is already a well demarcated peak in the spectrum. This is illustrated in Figure 1 by an example of pressure spectra measured in the nearfield and farfield of the two jets considered in this study. Nevertheless, even though in the nearfield the screech tone emerge by 26 dB for $M_j = 1.10$, and by 34 dB for $M_j = 1.15$, the broadband noise contribution to the signal cannot be neglected. Therefore, this signal is in general bandpass filtered to increase the phase trigger precision. The bandwidth of the filter must be as narrow and as steep as possible, which requires the use of a high-order filter. Such a filter is associated with a strong frequency dependent phase lag. As a consequence, a shift of frequency during measurement results in a shift of the phase of the reference signal. PIV measurements involve long records during which a slight screech frequency drift is likely to occur, due for instance to a possible small change in flow exhausting conditions. In order to avoid this difficulty, it is here chosen to record simultaneously the acoustic pressure near the nozzle, and the trigger signal of the laser Q-switch, as performed by Henderson et al.[29] for impinging jets. The phase in the screech loop at which the Q-switch is triggered is random and can be

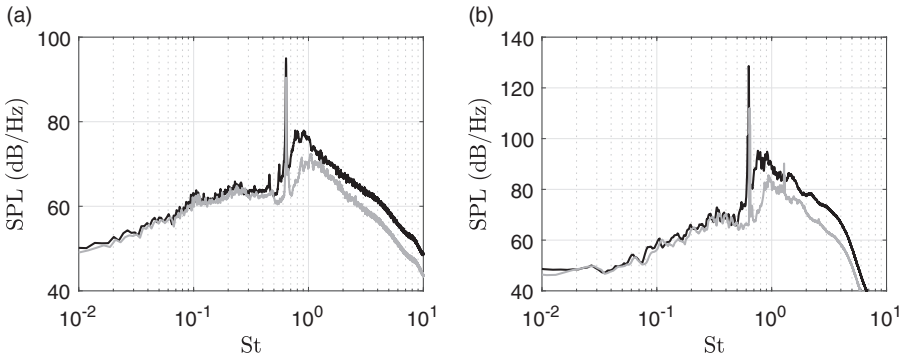

Figure 1. (a) Acoustic spectrum at 140° with respect to the jet axis and at a distance of 50*D*. (b) Acoustic spectrum measured at 110° and 5.5*D*. — $M_j = 1.15$, — $M_j = 1.10$.

determined from the recording. Similarly to the first method, the reference signal is obtained from the acoustic pressure signal through a bandpass filtering. However, the signal is numerically filtered during the post-processing. It is therefore easier to design a high-order filter which can be applied in a zero phase lag way, ensuring no dependency of the reference with regard to the measured screech frequency. Only an insignificant error remains from the associated drift in the acoustic wavelength since both the acoustic source and the microphone are fixed. The filter used is a 10th-order IRR bandpass filter centered on the screech frequency with a bandwith equal to 3% of the screech frequency. The filtered reference pressure signal p_{ref} is an almost prefect sinewave from which the phase reference Φ_{ref} is extracted as follows

$$\Phi_{ref} = \arctan\left(\frac{\mathcal{H}(p_{ref})}{p_{ref}}\right) \tag{1}$$

where $H(p_{ref})$ is the Hilbert transform of p_{ref}. The phase resolution is determined by the sampling frequency of the acoustic signal, namely 1 MHz in this study, corresponding to a resolution as small as 4×10^{-2} rad for the phase. The number of bins to divide the screech period is arbitrarily set to 18. All Q-switch events, namely velocity fields, are sorted in those bins with respect to their phase in the reference signal, and finally, all fields in a given bin are averaged resulting in velocity fields cleaned from most of the random turbulence contribution. All the phase-averaged quantities $\tilde{q}$ of a given variable q results in

$$\tilde{q} = \bar{q} + q^{sc}(\Phi_k) \tag{2}$$

where $\bar{q}$ is the time-averaged value of $q = \bar{q} + q'$, q^{sc} is the screech associated, or coherent component, and $\Phi_k = 2\pi i/18$ for $i = 0, \ldots, 17$. In total, 3500 images were recorded per case to ensure a good convergence for the phase averaging.

Schlieren

Schlieren visualizations do not require an external signal to perform the phase averaging since the chosen field of view already contains some region of the flow at rest where the

screech is mostly the only contribution. The gray-level signal taken at the point $z = 0.7D$ and $y = 1.0D$ serves as the reference. The sampling frequency of the record is only approximately three times the screech frequency which is insufficient for estimating the phase with a satisfying precision by means of the Hilbert transform method. The phase Φ in the screech cycle is therefore determined by another mean. For each image, only a short sequence of the reference signal is considered. It starts three images before the one whose phase must be determined, and finishes three images after, making a seven-point long signal. This short signal is fitted by the function

$$A\sin(2\pi f_s t_k - \Phi) + C, \qquad t_k = (-3, -2, \ldots, 3)/f_{acq} \tag{3}$$

from which A, C, and Φ have to be determined, and f_s is the screech frequency obtained from the schlieren film. When the phase is known for all images, the same sorting and averaging process is applied as with PIV data.

Results

Time-averaged flow features

An overview of the flow structure is first offered through the time-averaged velocity, the fluctuating velocity, and the spanwise vorticity component $\omega = \partial u/\partial y - \partial v/\partial x$. These fields are presented in Figure 2, remembering that $q = \bar{q} + q'$ with $q_{rms}{}' = \overline{q'^2}^{1/2}$. The mean velocity fields are marked by the shock-cell pattern that characterizes the structure of non-ideally expanded jets. The end of the first five shock cells where the compression waves are reflected into expansion waves is indicated by a dashed line. This reflection occurs at the sonic line[30] represented by a solid line, whose position is determined by estimating the local static temperature T following the Crocco-Busemann relation[31]

$$\frac{T}{T_j} = \frac{T_{amb}}{T_j} + \left(1 + \frac{(\gamma - 1)}{2} M_j^2 - \frac{T_{amb}}{T_j}\right)\frac{u}{U_j} - \frac{(\gamma - 1)}{2}\frac{u^2}{a_j^2} \tag{4}$$

where T_{amb} is the ambient static temperature, $M_j = U_j/a_j$ is the jet Mach number based on the velocity U_j and on the speed of sound $a_j = \sqrt{\gamma r T_j}$ with T_j the jet static temperature. The index j denotes the value of a quantity corresponding to the perfectly expanded jet. Among the other assumptions for its derivation, equation (4) holds for an isentropic flow and is thus used along the subsonic region frontier to determine the sonic line position. Nevertheless, the flow across the weak shocks contained in the supersonic jet plume is also expected to be isentropic, and conditions to use equation (4) might also been satisfied there. By examining the mean transverse velocity field in Figure 2, it may be observed that the location of the sonic line is found in good agreement with the position of the shock cell structure.

The axial velocity fluctuations reach a constant value close to $0.2U_j$ in the shear layer for $M_j = 1.15$ against $0.16U_j$ for $M_j = 1.10$. A similar trend is observed for the radial velocity fluctuations, as it may be better observed in Figure 3. These higher fluctuations must be linked to the higher acoustic pressure level at screech frequency, refer to Figure 1.

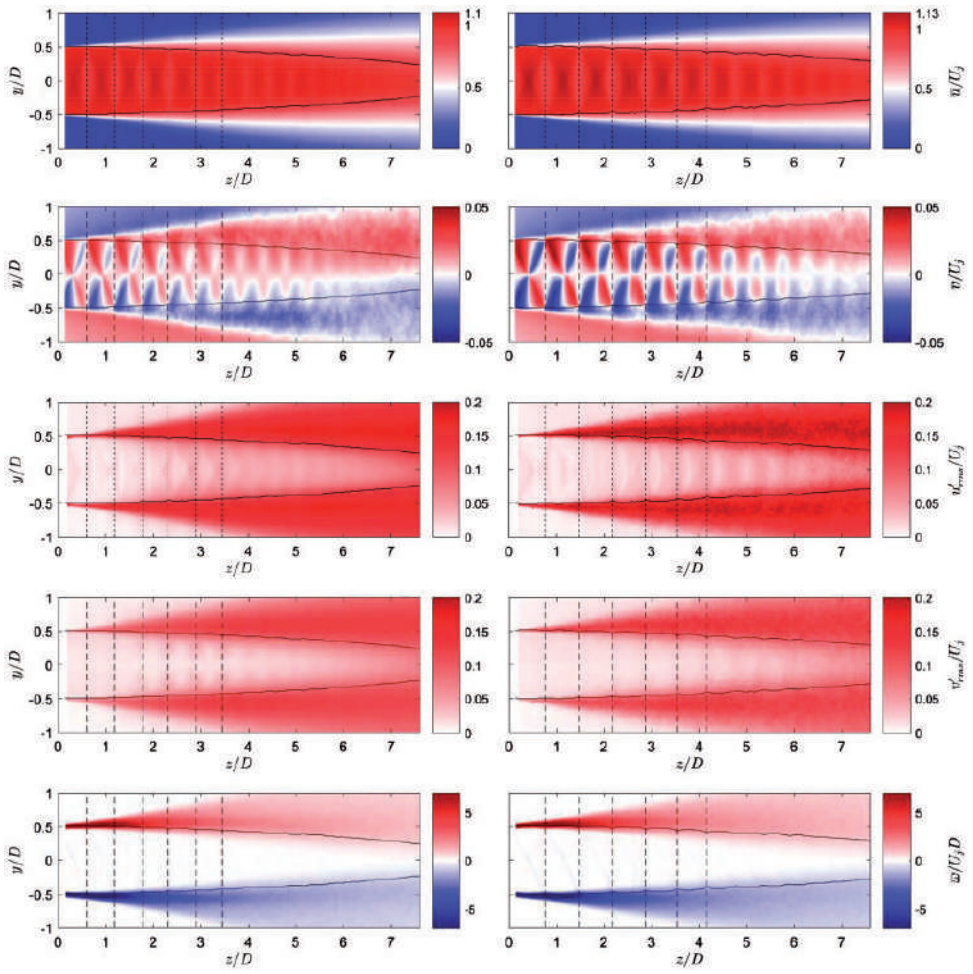

Figure 2. Contour of the mean and fluctuating velocity components and the mean vorticity for $M_j = 1.10$ (left) and $M_j = 1.15$ (right). The vertical dashed lines indicate the first five shock positions, and the solid line indicates the sonic line.

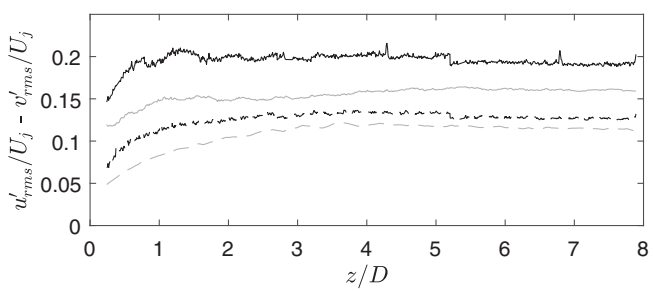

Figure 3. Evolution of the axial (—) and radial (- - -) peak velocity fluctuations along the mixing layer. — $M_j = 1.15$, — $M_j = 1.10$.

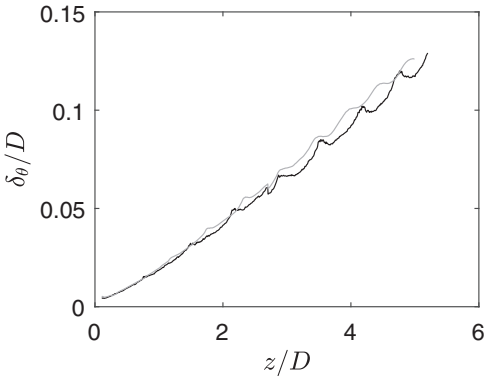

Figure 4. Evolution of the momentum thickness along the mixing layer. — $M_j = 1.15$, — $M_j = 1.10$.

Krothapalli et al.[32] have shown in their experimental study that fluctuations in the mixing layer of screeching rectangular jets increase with the screech amplitude. This is also observed in the PIV measurements by André et al.,[33] who used a notched nozzle to remove the screech component, and in the experiment results by Edgington-Mitchell et al.[22] and Tan et al.[34] for similar Mach numbers. A turbulence intensity close to $0.16U_j$ is reported in the former study, while a turbulence intensity beyond $0.20U_j$ was found by the latter study. The time-averaged vorticity is also represented in Figure 2, and no significant difference between the two jets can be highlighted.

Both jets are forced by screech tone at a Strouhal number approximately equal to $St_D = 0.65$, which meets the range of frequencies causing instability waves amplification, and promoting turbulent mixing. The spatial evolution of the jet momentum thickness computed following the method proposed in André et al.,[25] is plotted in Figure 4. The spreading rate is found to be $\mathrm{d}\delta_\theta/\mathrm{d}z \simeq 0.046$, which is a higher value than for unforced jets.[35]

Phase-averaged flow features

Coherent velocities

It has been observed in the previous section that the two jets have a similar structure, but they differ by their velocity fluctuation levels. The screech associated contribution (2) of the velocity fluctuations is now investigated independently from turbulent fluctuations. Figure 5 displays the coherent axial and radial velocity fluctuations, and the coherent vorticity. For all these quantities, the magnitude is found lower for the $M_j = 1.15$ jet than for the $M_j = 1.10$. It is not expected to observe a direct simple link between the coherent fluctuations, and the screech tone level. The latter is indeed determined by a complex generation mechanism; moreover, the screech forcing does not correspond to a classical configuration of excited flows.[36]

A second general observation concerning the velocity fluctuations is the noticeable modulation of u^{sc}_{rms} and v^{sc}_{rms} by the shock cells, already described in the literature.[22,37–40] Besides, u^{sc}_{rms} is found to be maximum inside a region bounded by the sonic line, to be minimum at the lip line, and to be weak in the low-speed region of the mixing layer. Conversely, v^{sc}_{rms} is maximum near the lip line and decreases beyond. These two features are the signature of a

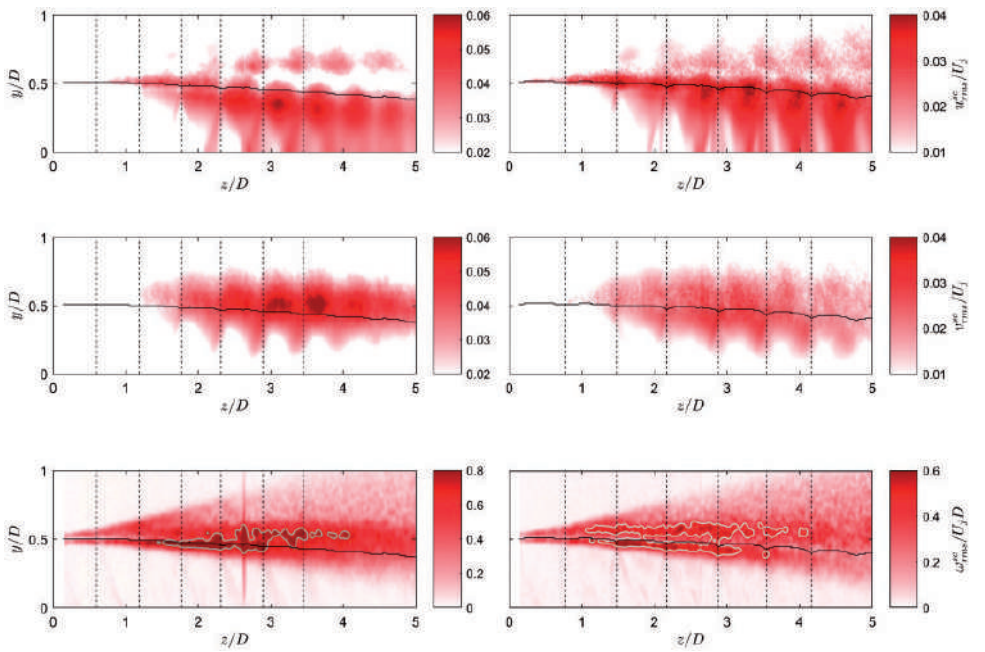

Figure 5. Statistics of the coherent component in the $M_j = 1.10$ (left) and the $M_j = 1.15$ (right) jets. Note the change in scale between the $M_j = 1.10$ and $M_j = 1.15$ jets. The vertical dashed lines indicate the first five shock positions and the solid line corresponds to the sonic line.

convected vortex of size close to the local mixing layer thickness. The tilting of the shock cells also produces coherent fluctuations in both directions that appear in the jet core. Additionally, the potential core is affected by coherent fluctuations induced by the passage of the large structures in the mixing layer. It should finally be noted that the modulation of u^{sc}_{rms} is not spatially synchronized in the inner and the outer mixing layer regions. Indeed, except for the first three shock cells of the $M_j = 1.15$ jet, in the supersonic region maximum levels of u^{sc}_{rms} occur barely in the middle of the shock cells with respect to the streamwise direction, whereas they are aligned with the shock tips in the low-speed region. This behavior is similar with the experimental observations by Ecker et al.[39] in a $M_j = 1.4$ overexpended jet, or by Edgington-Mitchell et al.[22] in a $M_j = 1.45$ jet, even though the maximum is found shifted toward the center of the shock cells in the present case in comparison with the two latter studies. This difference possibly arises from the difference in screech mode between these two studies in which helical mode is observed, whereas A1 and A2 modes of the present study are axisymmetric.

Coherent vorticity

Two regions in the shear layer where ω^{sc}_{rms} exhibits large values can be observed in the fluctuating vorticity map in Figure 5 (refer to white contours). They correspond either to high-velocity regions or lower velocity regions. For $M_j = 1.10$, the maximum of ω^{sc}_{rms} is first obtained in the high-velocity region for $z/D < 3$. In the same axial range, high values of ω^{sc}_{rms} are also visible as local maxima in the lower velocity region. For $z/D > 3$, values in the high-

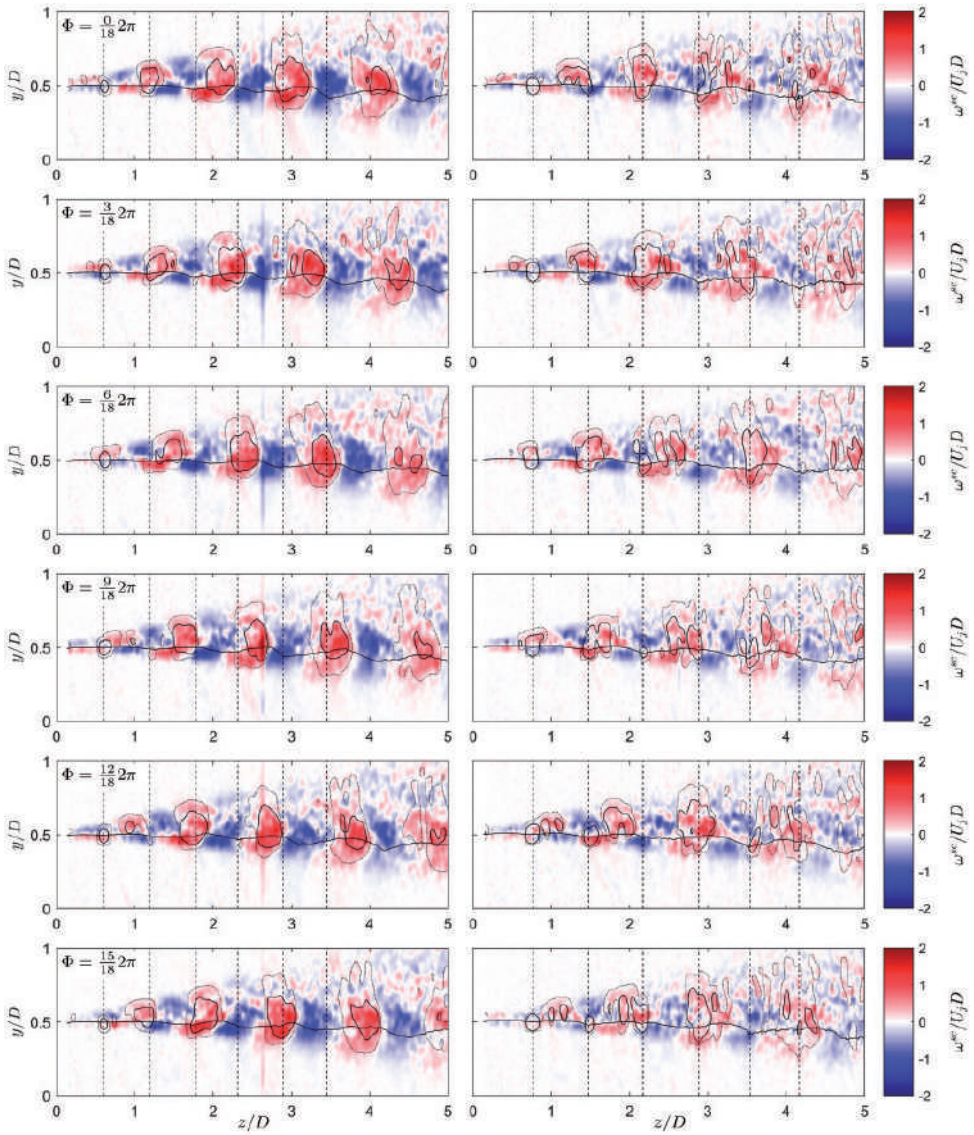

Figure 6. Snapshot of the coherent vorticity $\omega^{sc}(\Phi)$, for $M_j = 1.10$ (left) and $M_j = 1.15$ (right). The vertical dashed line indicates the first five shock positions, the solid line corresponds to $u = 0.85U_j$, and the isocontours are provided by the Q-criterion.

velocity region decrease, and the maximum is located in the lower velocity region. For $M_j = 1.15$, the two regions of local maximum for ω^{sc}_{rms} are again observed. The region in the low-speed side appears to extend further downstream than that in the high-speed side. The same pattern is also visible in recent results obtained by Edgington-Mitchell et al.[41]

The time evolution of the coherent vorticity ω^{sc} over of the screech period is shown in Figure 6. A low-pass Gaussian filter of standard deviation two grid points ($0.02D$) has been applied to the images in order to improve the readability. A well-organized pattern of

positive and negative vorticity spots can be seen. The positive vorticity here corresponds to vortex cores whereas the negative vorticity must be associated with saddle points since the mean flow is not included.

The line corresponding to $\bar{u} = 0.85U_j$, that is close to the sonic line, is also superimposed. Following the path of this line, the flow is deflected toward outside in region of high vorticity, and toward the core of the jet at the saddle points. This behavior can be observed with more details in the films provided in supplementary material for both jets. The time evolution of the high coherent vorticity $\omega^{sc}(\phi)$ spots is shown, in addition with the coherent velocity field ($u^{sc}(\phi)$, $v^{sc}(\phi)$), and with time-averaged axial velocity contours. In order to better identify the flow deflection, the line at which $\bar{u} = 0.85U_j$ is also plotted in green and the line at which $\bar{u} + u^{sc}(\phi) = 0.85U_j$ is plotted in blue.

Near the nozzle, the vorticity spots are in opposition of phase in the inner and the outer part of the mixing layer for both jets. Downstream, this phase shift tends to decrease with increasing z/D. The varying phase shift indicates a difference of phase velocity in the two regions of high vorticity fluctuations shown in Figure 5. The next paragraphs are dedicated to the analysis of these two regions.

A first analysis consists in comparing the Q-criterion and the vorticity field, as illustrated in Figure 6. The Q-criterion can only be calculated in the PIV plane, which yields

$$Q = (\Omega_{ij}\Omega_{ij} - S_{ij}S_{ij})/2 = -\frac{\partial u^{sc}}{\partial y}\frac{\partial v^{sc}}{\partial x} - \frac{1}{2}\left(\left(\frac{\partial u^{sc}}{\partial x}\right)^2 + \left(\frac{\partial v^{sc}}{\partial y}\right)^2\right) \tag{5}$$

where Ω_{ij} and S_{ij} are the anti-symmetric and symmetric components of the velocity gradient tensor. The contour in solid line corresponds to a convenient Q-criterion value, and the dotted line corresponds to the contour of a tenth of that value. As well illustrated by the $M_j = 1.10$ jet between $z/D = 1$ and $z/D = 3$, the high level of vorticity in the supersonic region is not connected to the vorticity in the low speed region by contours of Q-criterion. The same feature is also observed in the $M_j = 1.15$ case, but the lower signal-to-noise ratio prevents from providing an unambiguous result. Beside, this observation is supported by the spatial distribution Q_{rms} of the rms fluctuation of the Q-criterion presented as a contour superimposed to the vorticity fluctuations in Figure 7. This figure also depicts phase contours that will be analyzed later. The relevant point to observe at this step is the symmetrical expansion of Q_{rms} around the high vorticity region located in the low speed side of the mixing layer, but that does not include the inner high vorticity region.

High values of Q-criterion indicate that the outer region of high vorticity is associated with the screech coherent structures. The second region of high vorticity appearing in inner side of the mixing layer is less immediate to interpret. To address this question, the analysis is focused on the flow features around vortices. At this stage, the phase-averaged results still contain too much noise for the maps to be unambiguously interpreted. Therefore, we propose a dedicated data treatment to provide smoother vorticity fields that consists in averaging the flow field around an arbitrary chosen vortex over different phases in the screech period. This processing is carried out by defining a rectangular window that contains the chosen vortex. For the first phase step the window is centered around the vortex. For the next phase step, a second window initially at the same position as the first one is considered. A 2D cross-correlation is then computed between the coherent vorticity field ω^{sc} in each window. The position of the maximum of correlation indicates the spatial shift to apply to

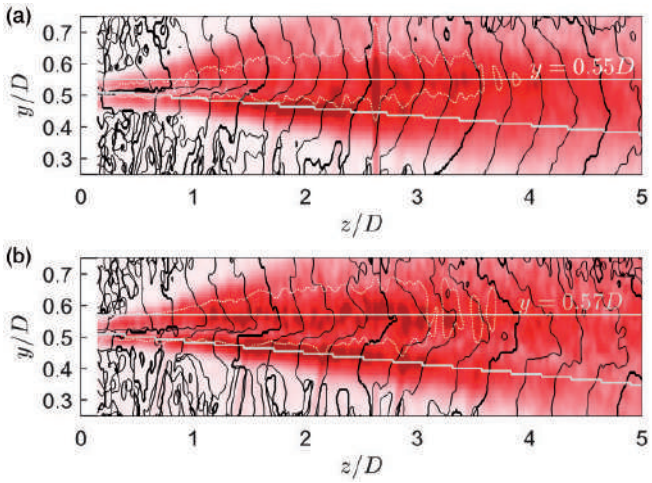

Figure 7. Contours of the phase $\Phi_{\omega^{sc}}$ every $\pi/2$ superimposed on ω^{sc}_{rms}. The dotted line is an isocontour of the Q-criterion fluctuations Q_{rms}, and the white lines indicate the location of maximum ω^{sc}_{rms}. (a) $M_j = 1.10$ and (b) $M_j = 1.15$.

the second window to track the vortex. The process is repeated for the following phase steps by considering each time the window of the previous phase step as new reference. The result of the procedure is a set of flow fields, all containing the same vortex at different phase steps, and approximately at the same position in the window. This set of fields is averaged to obtain smoothed flow features denoted by $< >$. The average resulting from this process is intrinsically biased by the spatial growth of the vortex, but this bias can be reduced by considering areas where the spatial evolution of the vortices pattern is weak. For both jets, vorticity maps displayed in Figure 6 show that this constraint is roughly respected between $z = 1.5D$ and $z = 3D$. The vortex tracking will therefore be restricted to this region. The bias introduced by the spatial growth of the vortex is estimated by performing averages across 6, 12, and 18 phase steps which corresponds to tracking the vortex over 1/2, 3/4, and 1 wavelength. The three results which are not presented here are similar, indicating that the effect of the spatial growth of the vortex can be neglected. Only the Q-criterion for $M_j = 1.15$ is found to strongly vary with the number of steps, and the initial position of the vortex. This lack of convergence can be linked together with the poor signal-to-noise ratio already observed in Figure 6. In the following, the first window is initially centered around $z = 1.5D$ and $y = 0.55D$, its axial and radial extents are $1.30D$ and $0.45D$.

The averaged axial and radial coherent velocities $< u^{sc} >$ and $< v^{sc} >$ are shown as vector plots superimposed on the averaged coherent vorticity $< \omega^{sc} >$ in Figure 8. In addition to the coherent vorticity and velocities, the mixing layer is delimited from region of potential flow by gray lines at position where $\bar{\omega} + < \omega^{sc} > = 0.1\max(\bar{\omega} + < \omega^{sc} >)$. For both jets, the maximum of $\bar{\omega} + < \omega^{sc} >$ is close to 9 U_j/D_j and found at the center of the mixing layer in the upstream limit of the domain. Finally, contours of the Q-criterion are added for $M_j = 1.10$ only, $M_j = 1.15$ being omitted for clarity. Results shown in Figure 8 for $M_j = 1.10$ and $M_j = 1.15$ jets are very similar, and their main features are summarized in the sketch Figure 8(e). The flow consists of a vortex turning anti-clockwise, associated with a stagnation point upstream and downstream. The stagnation points are equivalent to

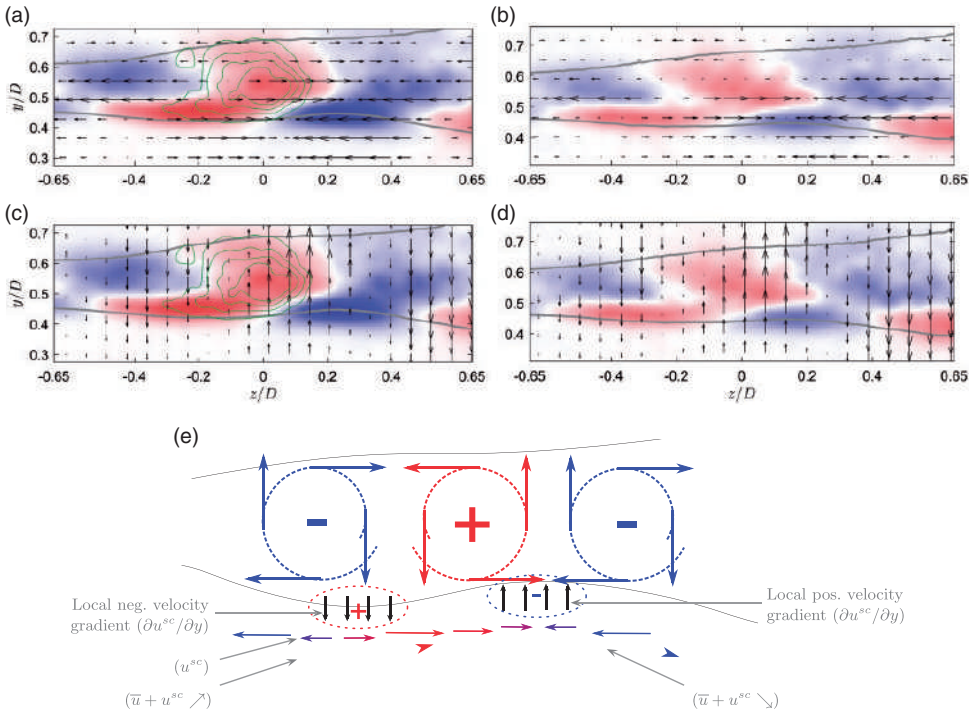

Figure 8. Spatially averaged vorticity around a vortex initially centered at $z/D = 1.5$. (a) and (b) $M_j = 1.10$. (c) and (d) $M_j = 1.15$. Arrows represent u^{sc} in their respective directions. Gray lines show the iso-vorticity contour $\bar{\omega} + \omega^{sc} = 0.1\mathrm{Max}(\bar{\omega} + \omega^{sc})$. Green lines show Q-criterion contours. (e) Diagram of the phenomenon.

vortices turning clockwise when the time-averaged vorticity is removed, as in the present case where only $< \omega^{sc} >$ is considered. According to the contours of Q-criterion, and to the analysis proposed in the previous paragraphs, the vortex lays near the lip line at the center of the mixing layer. The vortex also deforms the boundary of the mixing layer. The convection velocity of this deformation is linked with the vortex convection velocity, and is close to $0.55U_j$.[40] The relative velocity between the flow in the potential core and the vortex in the mixing layer is thus around $0.45U_j$. Therefore, in the field of view displayed in Figure 8, positive curvature of the mixing layer boundary implies potential core flow acceleration, whereas negative curvature implies flow deceleration. When the average value of the velocity is removed, to only examine $< u^{sc} >$, low speed and high speed, respectively, turn into positive and negative value for $< u^{sc} >$. The combination of the vortex associated rotating flow in the mixing layer, and of its effect in the potential core, gives rise to two regions of strong axial velocity gradients in the radial direction near the inner boundary of the mixing layer, between the vortex core and the stagnation points. At the same positions, the radial velocity gradient is far weaker. Thus, gradients of the axial velocity component come in the form of vorticity in the inner part of the mixing layer, shifted by approximately a quarter of the screech hydrodynamic wavelength apart from the vortex core.

The phase shift between the two regions of high vorticity tends to decrease when z increases, as already mentioned above. In order to bring a quantitative analysis of this

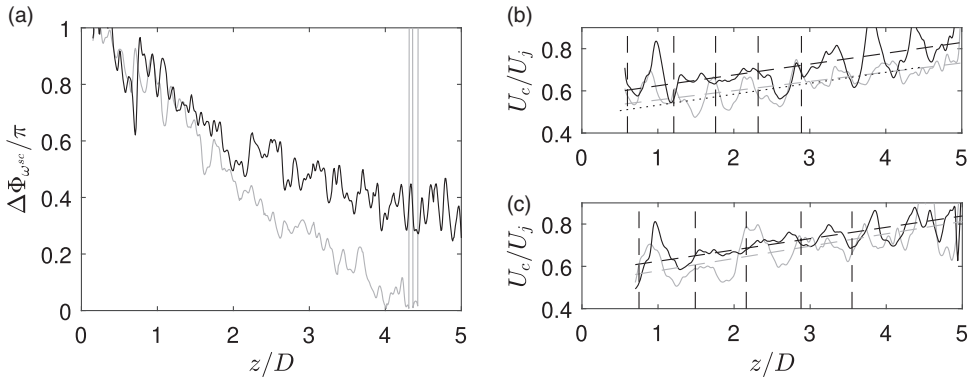

Figure 9. (a) Vorticity phase lag between the low- and high-speed regions for — $M_j = 1.10$, — $M_j = 1.15$, (b) $M_j = 1.10$, and (c) $M_j = 1.15$: convective velocity derived from the spatial phase evolution of the vorticity. — Low-speed side, — high-speed side, – – – fitted convective velocity, ··· schlieren data from Mercier et al.[40]

phase shift evolution, and of the associated convection velocities, the phase $\Phi_{\omega^{sc}}$ is introduced as the argument of the second term of the Fourier series of the vorticity field at every position. The result is presented in Figure 7 as a contour superimposed on the coherent fluctuations of the vorticity through lines separated by $\pi/2$. For $M_j = 1.10$, there is a sharp jump of phase across the shear layer that tends to decrease in magnitude with increasing z/D. For $M_j = 1.15$, this same strong jump decreases from $z = 1.5D$ to $z = 3.5D$ and increases again downstream. The existence of such a sharp jump sustains that the evolution of the vorticity associated with the screech related structures in the mixing layer is in some ways independent from the vorticity spots laying in the supersonic region, which interact with the shock tips. Two lines that follow the maximum of the coherent vorticity fluctuations are defined for each case in Figure 7. The phase difference $\Delta\Phi_{\omega^{sc}}$ between the coherent vorticity along the two lines is shown in Figure 9(a). At the nozzle exit, the vorticity is in opposition of phase between the outer and the inner sides of the jet. The difference decreases monotonically with the axial distance indicating that the phase velocity of the vorticity is greater inside than outside the mixing layer. A convective velocity can be computed from the differentiation of the phase $d\Phi_{\omega^{sc}}(z)/dz$ through a linear regression of $\Phi_{\omega^{sc}}$ within the moving window $[z - L_{sc}/4,\ z + L_{sc}/4]$, where L_{sc} is the shock cell length. It yields

$$U_c(z) = \frac{2\pi f_s}{d\Phi_{\omega^{sc}}/dz} \tag{6}$$

Here, the filter width is chosen to keep the oscillation related to the shock-cell pattern as shown in Figure 9(b) and (c) with the resulting convective velocity. The ripple is more intense on the convective velocity measured in the low-speed region upstream of the third to the fourth shock tip. Beside, this ripple increases downstream of this region when the high-speed convective velocity is considered. Contrary to what is observed from density measurements by Rayleigh scattering in Panda[38] or by Schlieren measurements[42,43] on the phase velocity that partially arises from the modulation of the hydrodynamic perturbation by the acoustic field, the present convective velocity calculated from the vorticity only

represents the hydrodynamic component. It is therefore demonstrated here that even in the supersonic region, where the mean flow undergoes compressions and expansions induced by the shock cells, the screech associated component remains unaffected when passing across the shock tips. The axial evolution of U_c is also provided in dashed line by a linear fit computed over the whole domain. The convective velocity increases with the axial distance as already observed in Mercier et al.,[40] with a similar rate in the low and high-speed regions. In addition, the linear trend of the phase velocity computed from schlieren data obtained by the authors in a previous study[40] is presented for the $M_j = 1.10$ jet in dotted line. This trend compares well with that obtained in the low speed side. The result for the $M_j = 1.15$ case derived from the previous schlieren visualizations is not presented since it is found strongly sensitive to the range of the derivative computation due to the high level of modulation of the hydrodynamic wave by the shock cells and the acoustic field.

In the end, two regions of high vorticity, which are related to two distinct phenomena induced by the screech feedback loop, are identified. The vorticity region that lays near the lip line in the low-speed side seems to correspond to the structures that dominate schlieren visualization and that are generally accounted for in the frequency prediction models. However, the coherent vorticity spots convected in the inner part of the mixing layer are more likely to interact directly with the shock tips.

A noise generation mechanism for screech

The interaction between the coherent structures and the shock-cell pattern that leads to the generation of the screech tone has already been investigated by many authors. The mechanisms identified in these studies can be divided into two main classes. The acoustic radiation would result from the shock leakage across the mixing layer,[18–22,44–46] or the interaction between the instability wave and the shock-cell pattern would give rise to supersonic phase velocity perturbation, and therefore acoustic generation in the upstream direction.[16,47,48] This second point of view brings up some issues if, for instance, the broadening of the wave number spectrum due to the growth and decay of the instability wave was considered and confronted to the narrowness of the screech tone observed in acoustic spectra. Similarly, the A2 mode does not meet the requirement of this theory in terms of wave numbers as pointed out in Mercier et al.[40] On the other hand, the mechanism by which the compression wave of the shock cell leaks across the mixing layer has been analyzed numerically and appears to be eligible for modeling the screech acoustic source. Suziki and Lele[19] obtained satisfactory results by using a direct numerical simulation combined with geometrical acoustics on an idealized mixing layer. Berland et al.[20] directly observed the shock leakage phenomenon in their large eddy simulation of a planar jet.

In what follows, the hypothesis of screech tone radiation induced by a shock-leakage process is favored. From Suziki and Lele[19] and Shariff and Manning,[21] the shock leakage occurs in supersonic flows convecting vorticity spots, and in particular at the saddle points between two vortices as also shown in Berland et al.[20] The periodic passages of vorticity spots are directly associated with the coherent flow depicted in Figure 6. Two regions of high coherent vorticity have been identified above, near the lip line in the low speed region, and in the supersonic region. This second component directly interacts with the shock tips in a similar fashion as the idealized academic cases[19,21] and would therefore be considered as responsible for the shock leakage. Suziki and Lele[19] also demonstrated that the acoustic wave front is bended toward the upstream direction by passing across positive

vorticity spots. This second mechanism can be applied to the acoustic wave emerging from the shock leakage and that propagates into the high coherent vorticity region located near the lip line. This interaction would consequently increase the upstream directivity of the screech acoustic waves. As such a directivity is a necessary condition of the screech, this bending of wavefronts is supposed here to play a significant role in the screech phenomenon. In order to efficiently bend the wave front, the wave leaking at the saddle point of the inner high coherent vorticity region must meet a maximum of coherent vorticity near the lip line. A necessary phase shift between these two regions should therefore be around π if the shock leakage was omnidirectional, or to a smaller phase shift if an upstream directivity already resulted from the shock leakage as it is observed by Suzuki and Lele[19] or Shariff and Manning.[21]

Based on this proposed mechanism, the feedback of the screech resonant loop rests upon high vorticity fluctuations ${}^{i}\omega^{sc}_{rms}$ in the inner region of the mixing layer defined by the inner white line in Figure 7, high vorticity fluctuations ${}^{o}\omega^{sc}_{rms}$ in the outer region, and a suitable phase shift $\Delta\Phi_{\omega^{sc}}$ given in Figure 9. In order to evaluate the local ability of the shear layer to sustain this mechanism, the following function C is introduced

$$C(z) = G_i({}^{i}\omega^{sc}_{rms})G_o({}^{o}\omega^{sc}_{rms})G_\phi(\Delta\Phi_{\omega^{sc}}) \tag{7}$$

where G_i, G_o, and G_ϕ are respectively three gain functions associated with the inner vorticity, the outer vorticity, and the phase shift between them. Gain functions are unknown, but in a first guess, one may simplify the shock leakage phenomenon by assigning a linear dependency to these functions. This is probably oversimplified, but more cases than available in this study would be required to identify these gain function. Following this principle, G_i can be $G_i = {}^{i}\omega^{sc}_{rms}$ and G_o be $G_o = {}^{o}\omega^{sc}_{rms}$. It seems reasonable to guess that G_ϕ should be maximum for $\Delta\Phi_{\omega^{sc}} \lesssim \pi$ and minimum for $\Delta\Phi_{\omega^{sc}} \simeq 0$. Since in the present case, $\Delta\Phi_{\omega^{sc}}$ varies between 0 and π, G_ϕ can simply be $G_\phi = \Delta\Phi_{\omega^{sc}}/\pi$.

The spatial evolution of the function $C(z)$ with these gains is shown in Figure 10. For both jets, C takes low values near the nozzle, then rises to a plateau, and finally decreases downstream of a given position. The plateau is comprised between the second and the fifth shock tip for $M_j = 1.10$ and between the first and the fourth for $M_j = 1.15$.

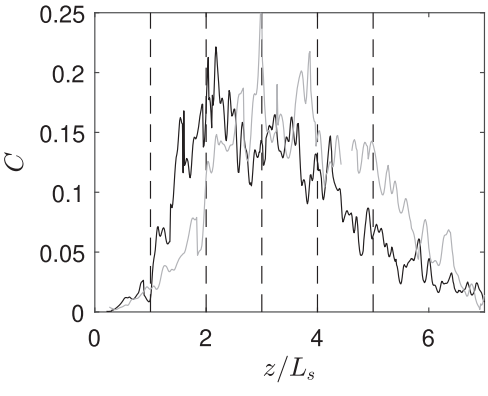

Figure 10. Spatial evolution of the function C (7) arbitrarily normalized. — $M_j = 1.10$, — $M_j = 1.15$.

The range of maximum C is interpreted as the region where shock leakage is most likely to occur, and where the upstream directivity of the radiated acoustic waves should be maximum. The range found in this study is consistent with those determined in the literature for similar jets.[4,5,18,40,41,49]

The results here presented, and obtained from phase-averaged vorticity fields, constitute a restricted sample of flows hosting the screech phenomenon. Despite that, original phenomena are pointed out, in particular the presence of a vorticity layer directly interacting with the shock tips, and convected at a velocity higher than that of the screech associated large structures. To the knowledge of the authors, this layer has not been considered in frequency prediction models even though they all rest upon the convection velocity of the hydrodynamic wave interacting with the shock-cells. It would be of great interest, regarding screech modeling purposes, to reproduce such results for more Mach numbers, and not only for axisymmetric modes. A larger database would allow to assess models fed by each of the two convective velocities and could bring up correlations between the screech amplitude and the vorticity field.

Shock motion

PIV measurements are well suited to study the vorticity and other flow features relying on the velocity field. However, a second essential contributor to the shock leakage is the shock cell structure of the jet. A very convenient method to observe shocks in flows is the schlieren visualization that emphasis density gradients. Furthermore, coupled with a high-speed camera, schlieren apparatuses allow to study the dynamic of the shocks. In the following, we take advantage of the periodic nature of the screech phenomenon to investigate the screech associated shock motion through phase averaging, following the method described in section *Phase averaging*.

The dynamic of the shock cells in a screeching jet was first studied by Panda[50] through schlieren visualizations and a dedicated instrumentation capable of detecting the passage of a shock into a light beam. The phase-averaged displacement of the first four shock tips of two jets exhibiting axisymmetric, and flapping screech modes were measured. The displacement was found to increase with the axial position of the shock tip. The complex and large motion of the core of the shock cells was also pointed out. More recently, the shock tip motion was measured by André et al.[51] who showed a positive correlation between the amplitude of the shock motion and the screech sound level. These two studies provide accurate data on the shock motion for a given shock cell, but do not easily offer a global picture of the shock motions and of the vorticity field. There is nevertheless a clear interest, for modeling purpose, to determine the phase relationship between the shock motions and the coherent vorticity. Consequently, a shock-tracking procedure is developed and applied on the phase-averaged schlieren visualizations for both jets at $M_j = 1.10$ and $M_j = 1.15$. Outcomes of the shock tracking are phase-averaged shock tip positions that will be synchronized with the phase-averaged PIV results.

Shock tracking procedure

The shock tracking procedure is based on the phase-averaged schlieren visualizations. An example of schlieren results at six phases over a screech period are presented for the $M_j = 1.15$ jet in Figure 11. This figure also aims at describing the tracking procedure.

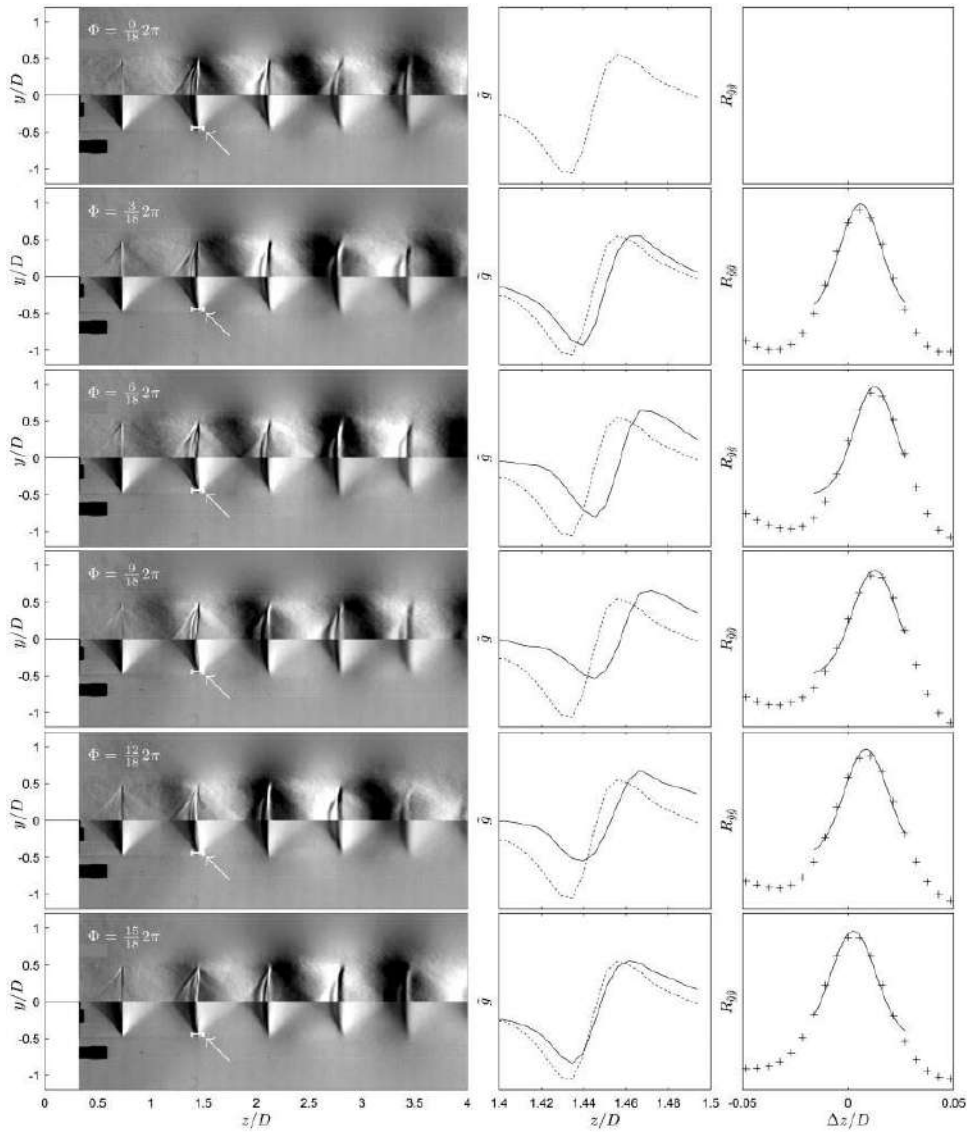

Figure 11. Left: snapshot of the phase average schlieren gray level, g^{sc} (top) and $\tilde{g}$ (bottom), over a screech period. Center: gray level across the white line. Right: + cross-correlation function between the instantaneous and the reference gray levels, — Gaussian fit.

For each tracked shock, a probed line plotted in white in the figure is defined. According to equation (2), the gray-level profile $\tilde{g} = \bar{g} + g^{sc}$ is extracted for each value Φ_k of the phase along this line. The profile obtained for $k = 0$ is arbitrarily defined as the reference. Then, the cross-correlation function of each profile with the reference one is computed to determine the axial position of the shock Δz relative to this reference. The cross-correlation is determined with a resolution of one pixel, which is of the same order as the amplitude of the

shock motion. To increase this cross-correlation resolution, the top of the correlation function is fitted with a Gaussian curve from which the position of the maximum correlation can be obtained, as illustrated in Figure 11.

Results

The positions of the first five shocks are displayed in Figure 12 with respect to their average position over a screech period. This figure depicts the phase lag between the motion of the shocks and their amplitudes. For a quantitative analysis, a fitting sinusoidal function is computed in each case and superimposed in dashed line on the phase average results. A nearly perfect match between the actual shock motion and the sinusoidal function is observed for all shocks except the fifth shock of the $M_j = 1.10$ jet that would require to consider also the first harmonic to obtain a better agreement. At this stage, it would be interesting to conduct a complementary study for the following shocks to observe if this property also arises for the $M_j = 1.15$ jet and if it could be linked with the acoustic radiation of the screech first harmonic. Table 1 summarizes the measured amplitudes of the shock

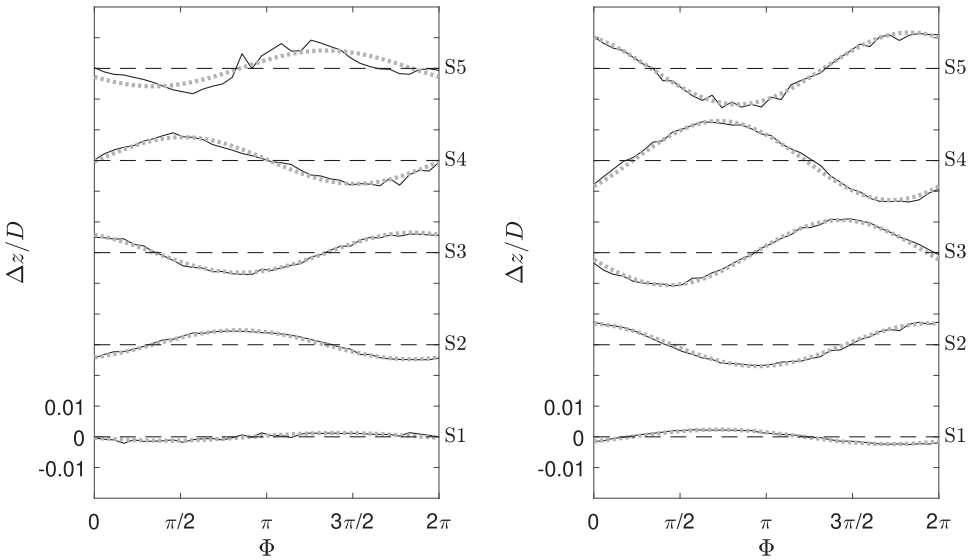

Figure 12. Position of the first five shock tips S_N during a screech period. Left: $M_j = 1.10$, right: $M_j = 1.15$. — measured position, ··· sine-fitted position.

Table 1. Peak to peak amplitude of the shock motion for the first five shock cells.

	$\Delta z^{pp}/D$ $(\times 10^{-3})$				
M_j	S1	S2	S3	S4	S5
1.10	2.5	9.5	13	15	12
1.15	4.7	14	21	26	24

motions. The motion amplitude of the first shock for $M_j = 1.15$ is found identical as the one measured by André et al.[51] for the same jet, but using a different method. However, the amplitude of the second shock is found 25% lower in the present study, perhaps because of the phase averaging that smooth the shocks and reduces the contribution of the extremum events. The value obtained in the present study is also found one order of magnitude lower than those obtained by Panda[50] for the same screech mode, but neither the same Mach number nor the same experimental conditions, that turns into a screech amplitude of 149.5 dB against 144 dB measured by André et al.[51] at a similar position. The amplitude of the shock motion is found to be maximum at the fourth shock for both jets. This shock location falls in the range of highest values taken by the C function plotted in Figure 10 which is consistent with the hypothesis that this region of the flow sustains the feedback loop.

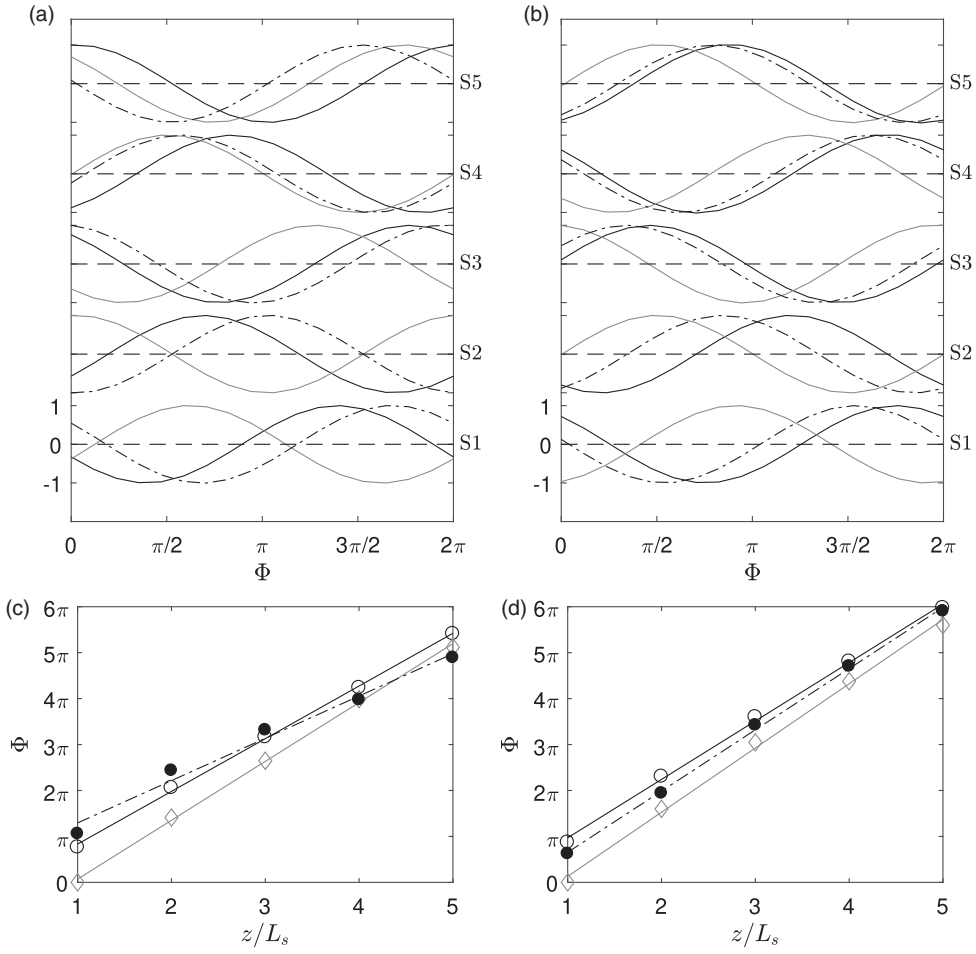

Figure 13. Left: $M_j = 1.10$ and right: $M_j = 1.15$. (a) and (b) Fitted sine of the normalized vorticity ω^{sc} in the high-speed (—) and low-speed (—) regions and the shock position (— · —) over a screech period at the first five shock tip stations. (c) and (d) Phase of the vorticity in the high-speed (◦) and low-speed (◇) regions and the shock position (•) against the axial position. The straight lines are the best fitted lines.

In addition, the noisiest screeching jet also corresponds to the jet exhibiting the largest shock motion. All the present findings are in agreement with the previous study by Mercier et al.,[40] where the fourth shock has been identified as the screech source from an analysis of the near acoustic field, without excluding that other shocks may also produce lower amplitude acoustic waves.

In order to put against each other the shock motion and the vorticity field, the same procedure as for shock tracking from schlieren data has been applied to the phase-averaged axial velocity field form PIV measurements. Due to limitations in data processing, only the motion of second and third shocks has been properly captured and is used to synchronize the phase-averaged fields calculated from the PIV data with those obtained from schlieren visualizations. The evolution during a screech period of the shock position and of the vorticity along the lines of maximum vorticity defined in Figure 7(a) and (b) is superimposed in Figure 13 for each shock location. For the sake of readability, only the fitted sinusoidal functions of the phase-averaged data are presented after being normalized in amplitude. The phase of these three quantities has been extracted for each shock position, and is presented in Figure 13(c) and (d) with an arbitrary reference so that the phase of the vorticity in the low-speed region is zero at the first shock. Firstly, the phase lag between the vorticity in the high-speed and low-speed regions decreases with the axial distance as already noticed in Figure 10. Secondly, it appears clearly that in the case of the $M_j = 1.10$ jet, the phase of the shock motion is not synchronized with the vorticity. The same remark also holds for the $M_j = 1.15$ jet but with a smaller phase shift. The complexity of the shock motion, which results from the interaction between the aerodynamic field and the shock-cell pattern, but also from the acoustic field surrounding the jet that imposes unsteady boundary conditions, is well illustrated with this analysis.

Conclusion

The understanding of screech acoustic radiation is a major concern in aeroacoustics for establishing a model able to predict the screech amplitude. The shock leakage mechanism is here considered as the most probable process for describing screech radiation. Previous works have shown that shock leakage arises in mixing layers that contain a strong level of coherent vorticity, but this flow component has been little investigated in the past. In order to offer a better view of the coherent vorticity field, a phase averaging processing has been applied to the velocity fields acquired with a PIV system in the present study.

A complex structure of the spanwise vorticity field has been pointed out in mode A1 and A2 jets. It can be divided in two regions of high coherent vorticity levels that are convected at distinct phase velocities: one is located in the supersonic region of the flow and the other is located near the jet lip line in the subsonic region. The phase shift between these two regions is close to π near the nozzle and decreases further downstream. This phase shift may play an important role in the generation of the acoustic feedback of screech. The high vorticity region in the supersonic region might be responsible for shock leakage, and the vorticity near the lip line might be responsible for the upstream directivity. Those two statements lead to determine a region between the shock tip numbers 3 and 5 for $M_j = 1.10$ and numbers 2 and 4 for $M_j = 1.15$, where acoustic waves responsible for screech feedback are most likely to be emitted. A similar phase averaging is also carried out with schlieren visualizations from which the periodic motion of the shock tips is determined. For both jets, the fourth shock is found to have the largest motion amplitude. These observations together with that

obtained for the same jets in Mercier et al.[40] provide a strong confidence in stating that for the A1 and A2 modes, the shock number four has a major role in the acoustic feedback of screech.

Acknowledgments

This work was performed within the framework of the Labex CeLyA of Université de Lyon, within the program "Investissements d'Avenir" (ANR-10-LABX-0060/ANR-11-IDEX-0007) operated by the French National Research Agency (ANR).

Declaration of conflicting interests

The author(s) declared no potential conflicts of interest with respect to the research, authorship, and/or publication of this article.

Funding

The author(s) disclosed receipt of the following financial support for the research, authorship, and/or publication of this article: This work was partially supported by the industrial Chair ADOPSYS co-financed by Safran Aircraft Engines and ANR (ANR-13-CHIN-0001–01).

ORCID iD


Bertrand Mercier http://orcid.org/0000-0003-3468-8176

References

1. Powell A. On edge tones and associated phenomena. *Acustica* 1953; 3: 233–243.
2. Powell A. On the mechanism of choked jet noise. *Proc Phys Soc B* 1953; 66: 1039–1056.
3. Massey KC and Ahuja KK. Screech frequency prediction in light of mode detection and convection speed measurements for heated jets. In: *3rd AIAA/CEAS Aeroacoustics Conference*, 1997, Atlanta, GA, U.S.A., AIAA paper no. 97–1625.
4. Panda J. An experimental investigation of screech noise generation. *J Fluid Mech* 1999; 378: 71–96.
5. Gao JH and Li XD. A multi-mode screech frequency prediction formula for circular supersonic jets. *J Acoust Soc Am* 2010; 127: 1251–1257.
6. Nagel RT, Denham JW and Papathanasiou AG. Supersonic jet screech tone cancellation. *AIAA J* 1983; 21: 1541–1545.
7. Norum TD. Control of jet shock associated noise by a reflector. In: *9th Aeroacoustics Conference*, 1984, Williamsburg, VA, U.S.A., AIAA paper no. 84–2279.
8. Ahuja KK. Some unique experiments on receptivity. In: *Shear Flow Control Conference*, 1985, Boulder, CO, U.S.A., AIAA paper no. 85–0533.
9. Raman G, Panda J and Zaman KBMQ. Feedback and receptivity during jet screech: influence of an upstream reflector. In: *35th Aerospace Sciences Meeting and Exhibit*, 1997, Reno, NV, U.S.A., AIAA paper no. 97–0144.
10. Harper-Bourne MJF. The noise from shock waves in supersonic jets. Noise mechanisms. In: *AGARD Proceedings*, 1974, Brussels, Belgium, paper no. CP 131.
11. Kweon YH, Tsuchida M, Miyazato Y, et al. The effect of reflector with sound-absorbing material on supersonic jet noise. *J Therm Sci* 2005; 14: 22–27.
12. Tanna H. An experimental study of jet noise part i: turbulent mixing noise. *J Sound Vib* 1977; 50: 405–428.
13. Norum TD and Seiner JM. Broadband shock noise from supersonic jets. *AIAA J* 1982; 20: 68–73.

14. Bridges JE and Wernet MP. Turbulence associated with broadband shock noise in hot jets. In: *14th AIAA/CEAS Aeroacoustics Conference*, 2008, Vancouver, Canada, AIAA paper no. 2008–2834.
15. André B, Castelain T and Bailly C. Broadband shock-associated noise in screeching and non-screeching underexpanded supersonic jets. *AIAA J* 2013; 51: 665–673.
16. Tam C, Seiner J and Yu J. Proposed relationship between broadband shock associated noise and screech tones. *J Sound Vib* 1986; 110: 309–321.
17. Tam CK. Supersonic jet noise. *Annu Rev Fluid Mech* 1995; 27: 17–43.
18. Umeda Y and Ishii R. On the sound sources of screech tones radiated from choked circular jets. *J Acoust Soc Am* 2001; 110: 1845–1858.
19. Suzuki T and Lele SK. Shock leakage through an unsteady vortex-laden mixing layer: application to jet screech. *J Fluid Mech* 2003; 490: 139–167.
20. Berland J, Bogey C and Bailly C. Numerical study of screech generation in a planar supersonic jet. *Phys Fluids* 2007; 19: 075105.
21. Shariff K and Manning TA. A ray tracing study of shock leakage in a model supersonic jet. *Phys Fluids* 2013; 25: 076103.
22. Edgington-Mitchell D, Oberleithner K, Honnery DR, et al. Coherent structure and sound production in the helical mode of a screeching axisymmetric jet. *J Fluid Mech* 2014; 748: 822–847.
23. Raman G. Supersonic jet screech: half-century from Powell to the present. *J Sound Vib* 1999; 225: 543–571.
24. André B. http://acoustique.ec-lyon.fr/jetnoise_uk.php, 2011
25. André B, Castelain T and Bailly C. Experimental study of flight effects on slightly underexpanded supersonic jets. *AIAA J* 2016; 55: 57–67.
26. Westley R and Woolley J. The near field sound pressures of a choked jet during a screech cycle. *Agard Cp* 1969; 42: 23-1–23-13.
27. Panda J and Seasholtz R. Density measurement in underexpanded supersonic jets using Rayleigh scattering. In: *36th AIAA Aerospace Sciences Meeting and Exhibit*, 1998, Reno, NV, U.S.A., paper no. 98–0281.
28. Alkislar MB, Krothapalli A and Lourenco LM. Structure of a screeching rectangular jet: a stereoscopic particle image velocimetry study. *J Fluid Mech* 2003; 489: 121–154.
29. Henderson B, Bridges J and Wernet M. An experimental study of the oscillatory flow structure of tone-producing supersonic impinging jets. *J Fluid Mech* 2005; 542: 115–137.
30. Seiner J and Norum T. Aerodynamic aspects of shock containing jet plumes. In: *6th Aeroacoustics Conference*, 1980, Hartford, CT, U.S.A., AIAA paper no. 1980–965.
31. White F. *Viscous fluid flow*. *McGraw-Hill International Edition*. New York, NY: McGraw-Hill Higher Education, 2006. ISBN 9780071244930.
32. Krothapalli A, Hsia Y, Baganoff D, et al. The role of screech tones in mixing of an underexpanded rectangular jet. *J Sound Vib* 1986; 106: 119–143.
33. André B, Castelain T and Bailly C. Investigation of the mixing layer of underexpanded supersonic jets by particle image velocimetry. *Int J Heat Fluid Flow* 2014; 50: 188–200.
34. Tan DJ, Soria J, Honnery D, et al. Novel method for investigating broadband velocity fluctuations in axisymmetric screeching jets. *AIAA J* 2017; 55: 2321–2334.
35. Hussain AKMF and Zaman KBMQ. The free shear layer tone phenomenon and probe interference. *J Fluid Mech* 1978; 87: 349–383.
36. Crighton DG. Acoustics as a branch of fluid mechanics. *J Fluid Mech* 1981; 106: 261–298.
37. Raman G and Rice EJ. Instability modes excited by natural screech tones in a supersonic rectangular jet. *Phys Fluids* 1994; 6: 3999–4008.
38. Panda J and Seasholtz RG. Measurement of shock structure and shock-vortex interaction inunderexpanded jets using Rayleigh scattering. *Phys Fluids* 1999; 11: 3761–3777.

39. Ecker T, Brooks DR, Lowe KT, et al. Development and application of a point Doppler velocimeter featuring two-beam multiplexing for time-resolved measurements of high-speed flow. *Exp Fluids* 2014; 55: 1819.
40. Mercier B, Castelain T and Bailly C. Experimental characterisation of the screech feedback loop in underexpanded round jets. *J Fluid Mech* 2017; 824: 202–229.
41. Edgington-Mitchell DM, Weightman JL, Honnery DR and Soria J. Sound production by shock leakage in supersonic jet screech. In: *2018 AIAA/CEAS Aeroacoustics Conference*, Atlanta, GA, U. S.A., AIAA paper no. 2018–3147.
42. Westley R and Woolley J. An investigation of the near noise fields of a choked axisymmetric air jet. Technical Report, National Aeronautical Establishment (Canada) Aero, 1968.
43. Mercier B, Castelain T and Bailly C. A schlieren and nearfield acoustic based experimental investigation of screech noise sources. In: *22nd AIAA/CEAS Aeroacoustics Conference*, 2016, Lyon, France, AIAA paper no. 2016–2799.
44. Manning T and Lele S. A numerical investigation of sound generation in supersonic jet screech. In: *6th Aeroacoustics Conference and Exhibit*, 2000, Lahaina, HI, U.S.A., AIAA paper no. 2000–2081.
45. Lui C and Lele S. Sound generation mechanism of shock-associated noise. In: *9th AIAA/CEAS Aeroacoustics Conference and Exhibit*, 2003, Hilton Head, SC, U.S.A., AIAA paper no. 2003–3315.
46. Fujimatsu N and Misu I. Numerical investigation of sound generation in supersonic jet screech. In: *43rd Aerospace Sciences Meeting and Exhibit*, 2005, Reno, NV, U.S.A., AIAA paper no. 2005–796.
47. Shen H and W Tam CK. Three-dimensional numerical simulation of the jet screech phenomenon. *AIAA J* 2002; 40: 33–41.
48. Tam CK, Parrish SA and Viswanathan K. Harmonics of jet screech tones. *AIAA J* 2014; 52: 2471–2479.
49. Powell A, Umeda Y and Ishii R. Observations of the oscillation modes of choked circular jets. *J Acoust Soc Am* 1992; 92: 2823–2836.
50. Panda J. Shock oscillation in underexpanded screeching jets. *J Fluid Mech* 1998; 363: 173–198.
51. André B, Castelain T and Bailly C. Shock-tracking procedure for studying screech-induced oscillations. *AIAA J* 2011; 49: 1563–1566.

Appendix

Notation

a	Speed of sound, m/s
d	Nozzle diameter, m
f_s	Screech frequency, Hz
g	Schlieren visualization gray level
G	Gain function
L_{sc}	Shock-cell length, m
M	Mach number
NPR	Nozzle pressure ratio
p	Pressure, Pa
q	Generic quantity
Q	Level of the Q-criterion
S_N	Shock tip number N
T	Temperature, K
u	Axial velocity, m/s

U Norm of the velocity, m/s
v Radial velocity, m/s
y Radial coordinate, m
z Axial coordinate, m
γ Heat capacity ratio
δ_θ Momentum thickness, m
Φ Phase with respect to a screech period, rad
ω Vorticity component, 1/s

Superscript

$\cdot^{pp}$ Peak-to-peak value of a fluctuating quantity
$\tilde{\cdot}$ Phase-averaged quantity
$\bar{\cdot}$ Time-averaged quantity
$\cdot^{sc}$ Coherent quantity, $q^{sc} = \tilde{q} - \bar{q}$
$\cdot'$ Fluctuating quantity, $q = \bar{q} + q'$
$< \cdot >$ Quantity averaged by the vortex tracking procedure
$^{i}\cdot$ Quantity referring to the inner region of the mixing layer
$^{o}\cdot$ Quantity referring to the outer region of the mixing layer

Lowerscript

$\cdot_i$ Quantity referring to the inner region of the mixing layer
$\cdot_j$ Quantity referring to the equivalent ideally expended jet
$\cdot_k$ Index related to the instant in the screech period
$\cdot_o$ Quantity referring to the outer region of the mixing layer
$\cdot_{rms}$ Rms value of a fluctuating quantity
$\cdot_{amb}$ Quantity referring to the ambient conditions

AIAA JOURNAL
Vol. 50, No. 9, September 2012

Technical Notes

Shock Oscillations in a Supersonic Jet Exhibiting Antisymmetrical Screech

Benoît André,* Thomas Castelain,† and Christophe Bailly‡
École Centrale de Lyon, 69134 Écully Cedex, France

DOI: 10.2514/1.J051802

I. Introduction

THIS contribution follows a Technical Note published by the authors in *AIAA Journal* [1], in which a shock-tracking algorithm was applied to a screeching underexpanded jet. It was shown that the shocks oscillate at the screech frequency, in a symmetrical or antisymmetrical manner, according to the screech mode. The temporal signals of two diametrically opposed near-field microphones were also considered. At a nozzle pressure ratio (NPR) of 2.54, corresponding to a flapping mode B, both microphones showed a simultaneous modulation of the screech amplitude at a frequency of the order of $1/1000$ of the screech frequency. A schlieren video was extracted from the complete recording for each one of the weak and strong screech spells. The tracking algorithm was applied on the resulting movies, and it was deduced that the shock oscillation amplitude increases with an increase in the screech level, which is in agreement with the analytical model proposed by Panda [2].

The picture of the flapping screech viewed by two diametrically opposed microphones appears, however, too simplistic, and a property of screech that remained unseen at that time is highlighted in the present work.

Screech is a tonal component of shock-associated noise arising in incorrectly expanded supersonic jets. It was first studied by Powell [3], who already mentioned the existence of modes. Of particular importance for the present study is the flapping mode B, whose pressure signal in the near field is antisymmetrical about a plane. The modal behavior of screech was later extensively studied, especially by Powell et al. [4] as well as Ponton and Seiner [5], who noted that the plane of antisymmetry can slowly rotate or oscillate. This feature, referred to in the following as plane rotation, was investigated in some detail by the authors [6] using a near-field azimuthal microphone antenna comprising 18 transducers located every 20 deg. It was shown that the plane rotation was related to the simultaneous presence of two counter-rotating helices of slightly different frequencies in the screech azimuthal-mode content. It was also explained that the screech level is minimum near the plane of antisymmetry and maximum perpendicular to that direction. In light of [6], it is believed that the strong amplitude modulation in time of the microphone signals in the original study [1] was caused by the rotation of the plane of antisymmetry. The plane rotation was then interpreted as a time modulation of screech strength due to the small number of microphones used.

The identification of the plane rotation in the acoustic field has suggested a possible rotation of the plane of antisymmetry of the shock motion. This question is considered in the present paper. The experimental facility is first presented. Then, results for two cases of flapping screech are discussed.

II. Experimental Setup

The supersonic jet is unheated and exhausts through a 38-mm-diam contoured convergent nozzle into an anechoic room. The wall static pressure is measured 15 nozzle diameters upstream of the exit. Stagnation pressure is then retrieved from the static pressure value through the estimate of the local Mach number in the measurement section.

Two schlieren systems are mounted, as sketched in Fig. 1a, on a frame downstream of the nozzle exit. One is a Z-type system, essentially consisting of two $f/8$, 203.2-mm-diam parabolic mirrors. The off-axis setting is limited to $2\alpha = 10$ deg. Because of a place constraint, the second schlieren apparatus is a double-pass system, including a beam splitter and a single spherical $f/12$, 203.2-mm-diam mirror. Both arrangements also use a light-emitting diode, a knife edge, and a high-speed Phantom V12 camera. The Z-type system is oriented so that the parallel light beams cross the jet horizontally. A vertical slice of the shock can thus be viewed, as shown in Fig. 1b (shock tips 1 and 2). The optical axis of the double-pass apparatus is set vertical. It thus gives a horizontal view of the jet (shock tips 3 and 4).

A circular near-field azimuthal microphone antenna, consisting of 18 6.35-mm-diam PCB Piezotronics condenser microphones located every 20 deg, is set in the nozzle exit plane approximately three nozzle exit diameters from the jet center. The antenna is also shown in Fig. 1a. The angle ϕ_m denotes the position of the microphones. The transducers located at $\phi_m = 0$ and 180 deg are directly above and under the shock tips visualized by the Z-type schlieren system. The transducers located around $\phi_m = 90$ and 270 deg are set to the left and right of the shock tips visualized by the double-pass schlieren system.

The frame rate of both cameras is 62,015 Hz, while the pressure signals are sampled at 102,400 Hz. One common trigger is used for both cameras and the sampling card so that all acquisitions are synchronized. Owing to the 4 GB RAM embedded in the cameras and the area of the sensors used, about 1.77 s can be recorded by the cameras at a time. According to the geometrical configuration and the objectives used on each camera, the Z-type and double-pass systems have spatial resolutions of 0.107 and 0.120 mm/pixel, respectively.

III. Shock Motion Features

In the following, a jet at a fully expanded Mach number of 1.50, corresponding to an NPR of 3.67, is visualized. The screech at this operating condition corresponds to a flapping mode, as documented in [6]. It was neither fully stable nor unstable so that a recording associated with a quiescent plane of antisymmetry and another one corresponding to a rotating plane have been performed. The present study focuses on the motion of the first shock.

A. Stable Screech

The stable case is considered here. The shock-tracking algorithm presented previously [1] has been applied to the movies recorded by

Received 16 December 2011; revision received 2 March 2012; accepted for publication 6 March 2012.

*Ph.D. Student, Laboratoire de Mécanique des Fluides et d'Acoustique, UMR CNRS 5509, 36 Avenue Guy de Collongue; benoit.andre@ec-lyon.fr.

†Assistant Professor, Laboratoire de Mécanique des Fluides et d'Acoustique, UMR CNRS 5509, 36 Avenue Guy de Collongue; also Université Lyon 1, 43 Boulevard du 11 Novembre 1918, 69622 Villeurbanne Cedex, France; thomas.castelain@ec-lyon.fr.

‡Professor, Laboratoire de Mécanique des Fluides et d'Acoustique, UMR CNRS 5509, 36 Avenue Guy de Collongue; also Institut Universitaire de France, 103 Boulevard Saint-Michel, 75005 Paris, France; christophe.bailly@ec-lyon.fr. Senior Member AIAA.

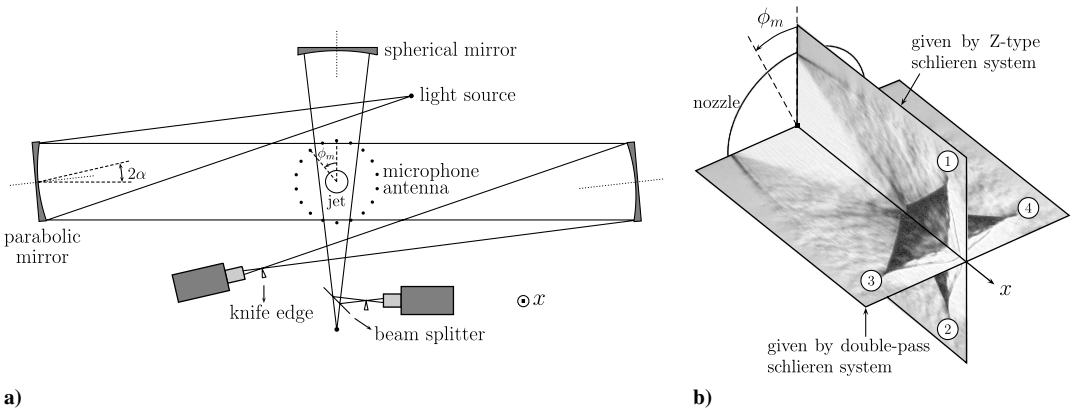

Fig. 1 a) Sketch of the schlieren apparatus with azimuthal microphone antenna (not to scale); b) representation of the two planes examined and definition of the shock tips.

each camera. This allows the position along the jet axis of each shock tip represented in Fig. 1 to be determined. Time traces of the results are displayed in Fig. 2 along with the temporal signal of the microphones located at $\phi_m = 0$ and 100 deg. It is apparent that the two microphones do not sense the same level of screech, which is typical of flapping screech modes, as recalled in Sec. I. Viewed along the direction of weak screech ($\phi_m = 0$–180 deg), the first shock motion has a weaker amplitude than when it is looked at along the direction of strong screech ($\phi_m = 90$–270 deg). The power spectral density of the shock motion signal shows that the shock oscillates exactly at the screech frequency. Phase averaging has been performed, and the shock-tracking algorithm has been applied to the averaged images (see [1]). The shock on the recording from the Z-type system has a magnitude of oscillation of 0.37 ± 0.05 mm, whereas the one of the shock on the double-pass recording is 1.2 ± 0.06 mm. Comparing these two figures gives a ratio of about 3. This is to be linked to the 3.7 ratio of root-mean-square pressure fluctuations between the corresponding microphones. It seems then that the near-field sound pressure level pattern associated with the flapping screech mode is imprinted in the jet and that the shocks are oscillating about the direction of the acoustical plane of antisymmetry, which would thus also be the plane of antisymmetry for the shock motion.

B. Unstable Screech

Another recording at a jet Mach number of 1.50 has been performed while the plane of antisymmetry of screech was rotating. The time trace of the acoustic signal at $\phi_m = 0$ deg is displayed in Fig. 3a. It features bursts similar to Powell et al.'s observation [4]. The spectra of the near-field microphone signals as well as that of the shock displacement data show a double peak, which can be associated to two counter-rotating helices of different frequencies (see [6]). The plane of antisymmetry therefore rotates, inducing the periodical vanishing of the screech signal measured at each azimuthal location.

A visualization of the rotation can be obtained as follows. To extract the time envelope of the bursts, the root-mean-square values of the pressure signals have been computed over 15 screech periods throughout the entire recording. The time period from 1.2 to 1.75 s is then selected from the plot in Fig. 3a because the bursts are there seen to be regular. For each azimuthal microphone, the mean phase angle

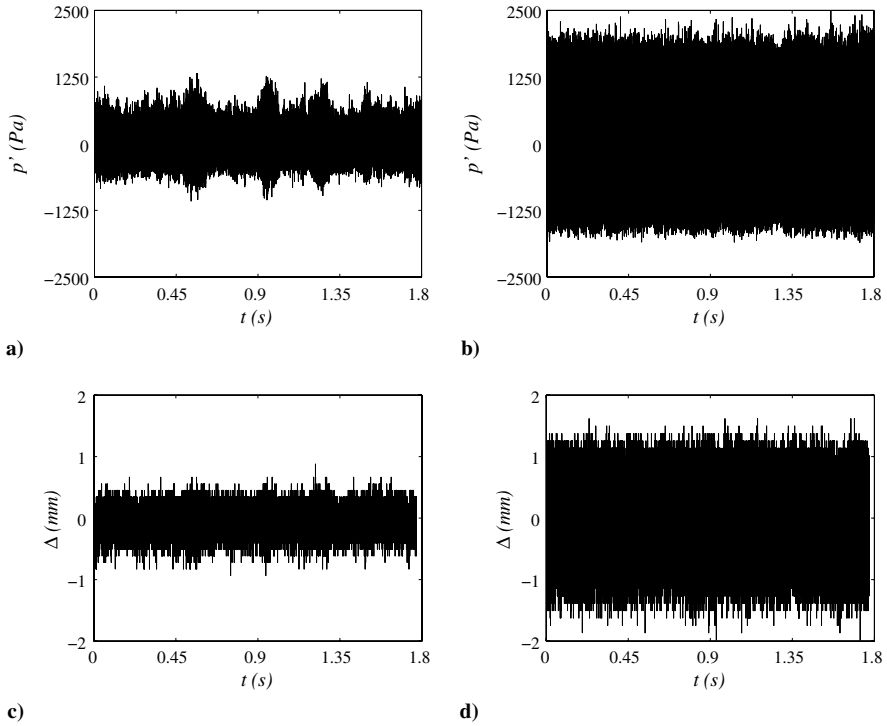

Fig. 2 Time trace of microphone signal at a) $\phi_m = 0$ deg, and b) $\phi_m = 100$ deg. Time trace of Δ, the shock axial displacement from its mean location, for c) tip 1, and d) tip 3.

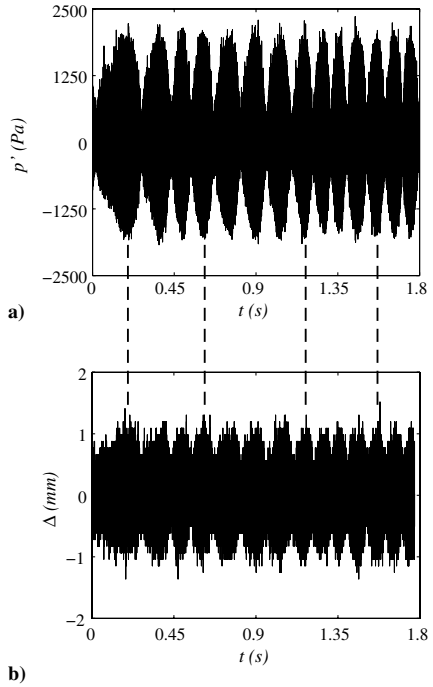

Fig. 3 Time traces of a) microphone signal at $\phi_m = 0$ deg, and b) location of the shock tip 1.

difference to the reference microphone located arbitrarily at $\phi_m = 0$ deg has been computed from the time delay yielding the maximum cross correlation between each pair of envelopes. The results are displayed in Fig. 4. The phase relations, written as $\Delta\psi$, are expressed as a fraction of the time period of the envelopes. Thus, $\Delta\psi = 0$ means that the bursts are in phase, whereas $\Delta\psi = \pm 0.5$ stands for an opposite phase relation. The evolution of the phase relations between envelopes is linear with the azimuthal angle, which reflects the stable rotation speed of the plane of antisymmetry.

The shock motion for shock tip 1 is presented in Fig. 3b. Here again, the oscillatory characteristics of the shock are closely linked to the pressure signal measured in the same plane because the bursts on both acoustic and shock motion signals are seen to be in phase.

This link is now investigated in greater detail by considering the motion of all shock tips. Envelopes for the shock motion signals have also been computed and are displayed for a time extract in Fig. 5, along with that of the microphones located at $\phi_m = 0$ and 100 deg. The envelopes of the shock displacement for the vertical view and of the microphone signal at $\phi_m = 0$ deg are in phase, as already noted in Fig. 3. The same statement holds true for the horizontal view of the shock with the microphone at $\phi_m = 100$ deg, although the phase matching is only approximate in this case because this microphone is not exactly in the plane of view of the double-pass schlieren system. Furthermore, the bursts for the two orthogonal schlieren views are in opposite phase relation, as are the associated pressure signals.

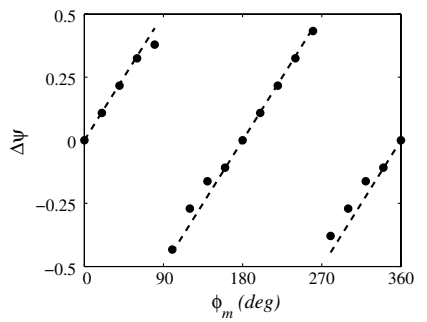

Fig. 4 Phase relation between each microphone of the azimuthal antenna and the microphone at $\phi_m = 0$ deg, represented by solid dots. Linear phase variation with 180 deg periodicity, represented by dashed lines.

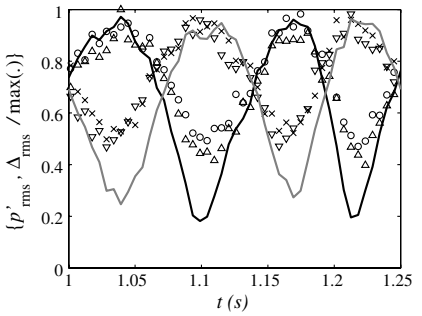

Fig. 5 Envelopes of pressure signal at $\phi_m = 0$ deg (black line), pressure signal at $\phi_m = 100$ deg (gray line), shock tip 1 (Δ), shock tip 2 (○), shock tip 3 (×), and shock tip 4 (∇).

The conclusion drawn in Sec. III.A is thus confirmed here; in the case of a flapping screech mode, the shocks inside the jet plume also flap about the same plane. When the acoustical plane rotates, so does the plane of antisymmetry inside the jet.

IV. Conclusions

The shock oscillations in an underexpanded supersonic jet at a fully expanded Mach number of 1.50 have been investigated by means of two schlieren systems set orthogonally to one another. At this operating condition, the screech is flapping. Two recordings of a stable as well as an unstable screech case have been performed. The instability is here the consequence of a rotating plane of antisymmetry arising from the coexistence of two counter-rotating helices of different frequencies. The shock motion has been tracked using the same algorithm as previously reported by the authors.

In the case of the stable flapping screech, the vertical and horizontal views of the first shock have shown very different oscillation amplitudes, which can be linked to the properties of the near acoustic pressure field. The similarity goes on when the plane of antisymmetry rotates; the modulation of screech strength in time at $\phi_m = 0$ deg exactly corresponds to a similar modulation of shock oscillation amplitude in the vertical view, whereas the bursts of the shock motion in the horizontal view are in opposite phase relation, as are the horizontal pressure signals. This emphasizes that the plane of antisymmetry of the shock motion rotates just like the acoustical plane of antisymmetry and that both planes are in fact only just one.

It is demonstrated here that the oscillation pattern inside the jet is an exact replica of that of the acoustic field, which should not be so surprising, owing to the causality relation linking the two. With a usual, two-dimensional view of the flow and of the acoustic pressure field, only a projection of the plane rotation on the viewing direction is observed, which does not permit all the dynamics of the shock oscillation and associated pressure fluctuation patterns to be unveiled.

Acknowledgments

This research has been funded by the Agence Nationale de la Recherche through the ANR-10-BLAN-937-01 project JESSICA. The authors wish to express their most sincere thanks to Jean-Michel Perrin, Edouard Salze, and Maria Karzova for their help in setting up the experiment and to Emmanuel Jondeau for the implementation of the synchronization procedure. Thanks are also due to Delphine Chareyron from the Laboratoire de Physique of École Normale Supérieure de Lyon and to Nathalie Grosjean for the lending of a high-speed camera.

References

[1] André, B., Castelain, T., and Bailly, C., "Shock-Tracking Procedure for Studying Screech-Induced Oscillations," *AIAA Journal*, Vol. 49, No. 7, 2011, pp. 1563–1566. doi:10.2514/1.J051057

[2] Panda, J., "Shock Oscillation in Underexpanded Screeching Jets," *Journal of Fluid Mechanics*, Vol. 363, 1998, pp. 173–198.

doi:10.1017/S0022112098008842
[3] Powell, A., "On the Mechanism of Choked Jet Noise," *Proceedings of the Physical Society, London, Section B*, Vol. 66, No. 12, 1953, pp. 1039–1056.
doi:10.1088/0370-1301/66/12/306
[4] Powell, A., Umeda, Y., and Ishii, R., "Observations of the Oscillation Modes of Choked Circular Jets," *Journal of the Acoustical Society of America*, Vol. 92, No. 5, 1992, pp. 2823–2836.
doi:10.1121/1.404398
[5] Ponton, M. K., and Seiner, J. M., "Acoustic Study of B Helical Mode for Choked Axisymmetric Nozzle," *AIAA Journal*, Vol. 33, No. 3, 1995, pp. 413–419.
doi:10.2514/3.12402
[6] André, B., Castelain, T., and Bailly, C., "Experimental Study of Flight Effects on Screech in Underexpanded Jets," *Physics of Fluids*, Vol. 23, No. 12, 2011, Paper 126102.
doi:10.1063/1.3671735

D. Papamoschou
Associate Editor

Review of Scientific Instruments ARTICLE scitation.org/journal/rsi

Dynamic analysis of a Rayleigh scattering setup using synthetic light signals from a modulated LED

Cite as: Rev. Sci. Instrum. 90, 063109 (2019); doi: 10.1063/1.5112802
Submitted: 15 January 2019 • Accepted: 2 June 2019 •
Published Online: 24 June 2019

Bertrand Mercier[1,a] and Thomas Castelain[2]

AFFILIATIONS

[1] Univ Lyon, École Centrale de Lyon, INSA Lyon, Université Claude Bernard Lyon I, CNRS, LMFA, UMR 5509, 36 Avenue Guy de Collongue, F-69134 Ecully, France

[2] Univ Lyon, Université Claude Bernard Lyon I, École Centrale de Lyon, INSA Lyon, CNRS, LMFA, UMR5509, 43 Boulevard du 11 Novembre 1918, F-69100 Villeurbanne, France

[a] b.h.mercier@tudelft.nl

ABSTRACT

Rayleigh scattering of a laser beam can be used for time-resolved local measurements of density in flows. A key-point of the approach lies in extracting flow density statistics from the measurement of the scattered-light power. Complex hardware equipment and software procedures are involved in this process. The present paper offers a method to assess the entire chain of acquisition of a typical setup in realistic conditions, and an analysis of its dynamic performances with respect to the theoretical expectations. This is achieved by simulating the light intensity fluctuations typically observed with a Rayleigh scattering setup, by use of a known light intensity fluctuation signal generated using a light-emitting diode modulated in output power. The tested Rayleigh scattering setup is shown to perfectly satisfy the theoretical predictions, meaning that it allows us to measure the spectrum of light intensity variations with an outstanding linearity within a dynamic range proportional to the square-root of the measurement time.

I. INTRODUCTION

In the context of experimental fluid mechanics, the local flow properties must be measured by keeping the smallest impact of the probing system on the flow. Optical methods are therefore well suited for such an objective. Methods based on the light scattered by the molecules constituting the flow itself are the least intrusive methods. Contrary to the methods requiring tracers like particles[2,13] that involve inertia lag, or fluorescing molecules[12] that slightly change the chemical flow composition, molecular scattering based methods maintain all flow properties unchanged. Light scattering processes can be inelastic, which means that the scattered light wavelength differs from that of the incoming light, or elastic when the scattered light wavelength is unmodified. Elastic processes generally refer to Rayleigh and Mie scattering. The former rests upon the hypothesis of small scattering particles in comparison with the light wavelength; the latter is generalized to model all kinds of particles. Visible light scattered by molecules is here considered; the scattering process can hence be modeled by the Rayleigh scattering. This mechanism was already exploited for local density measurements in high Mach numbers flows[4] in the early eighties with a 5 mW laser as light source, and a photomultiplier to examine the scattered light. Later in the nineties, planar density measurement systems were developed with the pulsed laser as light source, and the CCD camera as sensor.[1,3] Insightful results were obtained, but planar measurements were limited to snapshot of the density fields and could not offer time resolved results due to the limited repetition rate of the pulsed lasers. This limitation can be thought to be partially circumvented by use of pulse burst laser systems that generate burst of high intensity pulses at a high repetition frequency, but only for a short time.[11] In parallel with planar development, pointwise density measurement systems based on a continuous-wave laser were perfected by Panda and Seasholtz. Those systems demonstrated a good ability for measuring time-averaged density[9] and time-resolved density fluctuations.[7,8,10]

The principle of density measurements based on Rayleigh scattering is described as follows. When a molecule is illuminated by the laser light pointing towards a unique direction, it scatters a small fraction of this incident light toward all directions. The ability of a given molecule to scatter light of a given wavelength, and in a given direction relative to the polarization plane of the incident light, is represented by its differential scattering cross section $\partial\sigma/\partial\Omega$. Therefore, a part of this light can be detected by a device covering a solid angle $d\Omega$. For an incident laser light of power I and an observed air volume of size V_{sc}, the power of light detected by the device P is proportional to the number of scatterers in the volume, thus to the number of molecules, and to the density ρ such that

$$P = Q_E V_{sc} \frac{\partial\sigma}{\partial\Omega} d\Omega I \frac{N_A}{\mathcal{M}} \rho, \tag{1}$$

where Q_E is the quantum efficiency of the detector equal to the ratio of the detected light power to the incoming light power, $\mathcal{M}$ is the molar mass, and N_A is the Avogadro constant. For a given experimental setup and a given gas or gas mixture, this relation implies that P is proportional to ρ; the experiment specific proportionality constant can be determined by the calibration methods previously described.[6] A typical order of magnitude of the constant obtained by the authors[6] is 10^{-11} W/(kg m^{-3}) with $V_{sc} \simeq 1$ mm^3 and a 5 W laser. A convenient method to measure such a small power is to consider the detected light as a flux of photons Φ given by

$$\Phi = P/E \tag{2}$$

with $E = hc/\lambda$ the energy of a photon, h the Planck constant, and c the speed of light. For $P = 10^{-11}$ W, $\Phi \simeq 10^7$ photons/s. In order to estimate the power of the detected light, the photon arrival rate can be determined by counting their detections. Photons are commonly detected by a photomultiplier tube.

In practice, in addition to the light coming from the probed volume, a small amount of stray light is also detected. The stray light is for instance induced by the laser reflections on the rig and is constant in time. Consequently, a flux Φ_0 is added to the Rayleigh scattering contribution leading to

$$\Phi = k\rho + \Phi_0, \tag{3}$$

where k is a constant of proportionality set by the abovementioned physical parameters.

Photon counting is performed by a dedicated system which exhibits some limitations. One limitation is caused by the minimum time delay required by the counter to count two individual photon detections, resulting in a maximum achievable counting rate. Another limitation is the maximum length of continuous records that is mostly related to the size of the counter buffer memory. A well know commercial counter is the SRS SR-400 with only 5 ns of minimum time delay between two counts, but the maximum recording time is short. On the contrary, the Hamamatsu C9744 allows for much longer records but with a minimum time delay of 25 ns. As it will be further justified in Sec. II B, an intrinsic uncertainty arises in signals obtained by photon-counting and requires a large counting rate to be overcome. Besides, to analyze the dynamic of a multiscale phenomenon such as those often observed in fluid mechanics, the record must be as long as possible, but commercial systems do not fit these two constrains. The authors therefore decided to setup a customized system based on a high speed data acquisition card that digitizes a photomultiplier output signal and allows us to perform the counting *a posteriori* using a software procedure. A validation of this setup is proposed in Mercier *et al.*[6] on the basis of data recorded in high speed jets. One aim of the present contribution is to introduce a new procedure that helps in determining the dynamic performances of the optical setup and whose use could be generalized to the characterization of any photon-counting device. This procedure consists in simulating light intensity variations to be observed from Rayleigh scattering measurements in flows holding density fluctuations by use of a light-emitting diode (LED) driven by a prescribed fluctuating current signal. Setting the spectrum properties of this input signal close to those of real density fluctuations allows for assessing the entire chain of acquisitions by comparing the output signal based on photon counting to the input driving signal.

In Sec. II, the experimental setup, and the photon counting procedure are described. This is followed by the analysis of the static and the dynamic responses of the LED. Then, the spectral properties of the signal derived from a hot-wire measurement of the velocity in a turbulent flow to simulate density fluctuations are presented. Finally, the ability of the chain of acquisition and of the data processing procedure, to recover the reference signal from the light intensity measurement are assessed.

II. METHODOLOGY

A. Setup description

The setup is arranged to allow the conversion of known electric signals into light intensity and the light intensity into a photon count-rate. A block diagram of the system is provided in Fig. 1. The first process is handled by a specially designed voltage-controlled LED driving unit which supplies a conventional 3 mm in diameter low power green gallium phosphide (GaP) LED with a current i. This current is determined from the input voltage $V_{in} = \overline{V_{in}} + V'_{in}$, where V'_{in} is the fluctuating voltage, controlled externally, and $\overline{V_{in}}$ is the average voltage set inside the driving unit. The current flowing through the LED is continuously monitored by the output V_{out}. More details about the driving unit are provided in Sec. II C. The LED is held behind a 1 mm pinhole in the field of view of a Hamamatsu H7422p-40 photomultiplier within a distance of 10 cm. This is a current output photomultiplier suited for photon counting applications due to its low rise time of 1 ns. At the peak wavelength of the LED, which is close to 570 nm, the quantum efficiency of the photomultiplier is approximately 40%. To prevent the ambient stray light

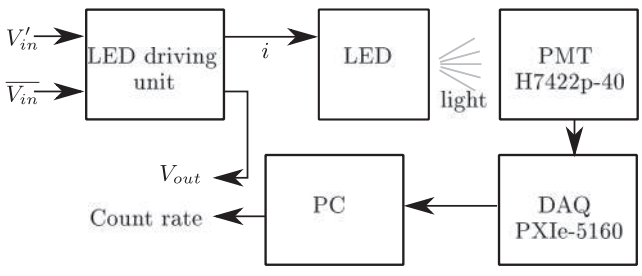

FIG. 1. Block diagram of the setup.

from biasing the measurements, the LED and the photomultiplier are placed in a dark box.

The output signal of the photomultiplier is digitized at a frequency of 1.25 GHz by a National Instrument PXIe-5160 and the photon counting operation is performed on the recorded digital signal.

B. Photon counting

Each photon detection by the H7422p-40 is converted into a burst of electrons at the photomultiplier output. It corresponds to a voltage pulse across the 50 Ω input impedance of the PXIe-5160 digitizer. The signal recorded during a run is therefore made of pulses corresponding to photon detections and of a low level background noise. An example of a signal obtained for a constant brightness of the LED is shown in Fig. 2. With such a signal, the background noise can be simply removed by considering only the peaks that are above a given threshold. The value of the threshold should be kept as low as possible to prevent missing photon detection signatures of low amplitude, but must be high enough to avoid counting any background noise as a detection. Once all peaks are identified, their times of arrivals are recorded in a table. A time history of the photon count rate $N_c(t)$ can then be obtained by counting all photons arrived during successive intervals of time. The width δt of these interval also define the sampling frequency $f_s = 1/\delta t$ of the photon count rate time history.

At this step, $N_c(t)/\delta t$ represents the number of counted photons per unit of time. However, as shown in Fig. 2, the delay between two photon detections is randomly distributed. Therefore, there is a probability for two photons to be detected within a very short delay. If the delay is shorter than a time constant τ called the pulse pair resolution, only one photon is counted. This time constant is related to the chain of acquisition, and its value is usually between 1 ns and 20 ns. Besides, the higher the count rate, the higher the probability for two detections to superimpose. This bias introduces a nonlinearity between $N_c(t)$ and $N(t)$, the unbiased value of the photons detection rate which is linearly related to the density.

It is, though, possible to recover the value of $N(t)$ from $N_c(t)$ by modeling the distribution of the delay between two detections using Poisson's statistics. The probability that n photons are detected during a time interval dt is

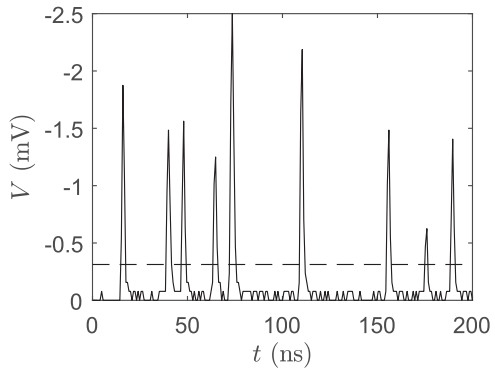

FIG. 2. Digitized photomultiplier output signal. The dashed line shows the threshold.

$$p(n, dt) = \frac{(\Phi dt)^n}{n!} e^{-dt\Phi}. \tag{4}$$

The probability that a photon is counted is equal to the probability that no photon is detected during the following time interval τ, that is, $p(0, \tau) = e^{-\tau\Phi}$. Consequently, the flux of counted photons is related to the flux of detected photon that is proportional to the density by

$$\Phi_c = \Phi e^{-\tau\Phi} \tag{5}$$

or, since $N_c = \Phi_c/f_s$ and $N = \Phi/f_s$,

$$N_c = N e^{-\tau N f_s}. \tag{6}$$

N is then obtained by inverting Eq. (6) using the Lambert-W function, or an approximated expression is[6]

$$N = \frac{N_c}{1 - \tau N_c f_s}. \tag{7}$$

The randomness of photon arrival leads to another difficulty. For a constant scattered power, a constant flux of photons is expected. However, when looking at Fig. 2, if a small interval of time is considered, say, 50 ns, it is clear that 3 photons are detected within $t = 0$ ns and $t = 50$ ns, while only one is detected between $t = 75$ ns and $t = 125$ ns. As a consequence, the measured flux of photons Φ_c can only be regarded if it is averaged during a long time. The values of N that are determined from N_c and Eq. (7) during much smaller time interval to allow high frequency analysis are therefore affected by the so-called *shot noise*. This noise follows Poisson's statistics, for which the variance of the noise $\mathrm{VAR}(N_{sn})$ is equal to the expected value $\overline{N}$. Thus, the standard deviation of $N_c(t)$ due to the shot noise N_{sn}^{rms} is

$$N_{sn}^{rms} = \sqrt{\overline{N(t)}}. \tag{8}$$

Moreover, the Poisson distribution can be well approximated by a white Gaussian distribution for $\overline{N}$ greater than 12.

C. LED driving unit

The role of the LED driving unit is to control the LED light intensity by applying an arbitrary electric signal at the input. Low current GaP LED light intensity is nearly linearly related to the current over a wide current range; see for instance the Vishay TLHG4605 LED datasheet. Consequently, the driving unit was designed as a voltage to current converter based on a low noise operational amplifier. The schematics of the driving unit are provided in Fig. 3. For a perfect operational amplifier, the voltage must be the same at the + and − pins of the circuit; therefore, the input voltage V_{in} is equal to the output voltage V_{out}. Since for a perfect amplifier, no current flows through pins + and −, the current flowing through the feedback branch is the same as that through the resistor R. Then, for the perfect operational amplifier,

$$i = \frac{V_{out}}{R} = \frac{V_{in}}{R}. \tag{9}$$

A capacitor C_c, chosen such that its impedance is much larger than the LED dynamic impedance $\mathrm{d}V/\mathrm{d}i$ below a few megahertz is installed to prevent high frequency oscillations. Consequently, the current flowing through the capacitor is negligible with respect to i in the range of frequency considered. The current i, also measured by

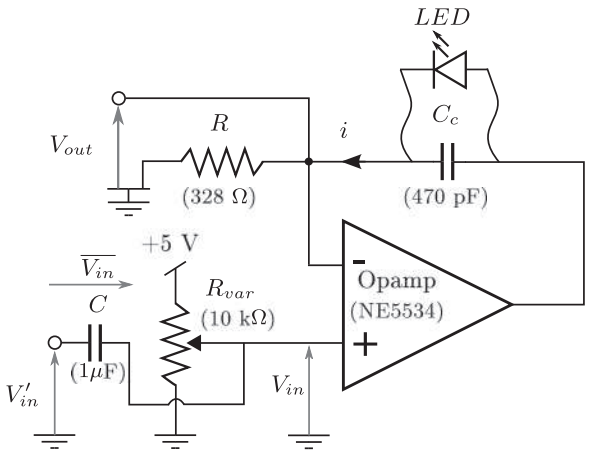

FIG. 3. Simplified schematic of the LED driving unit.

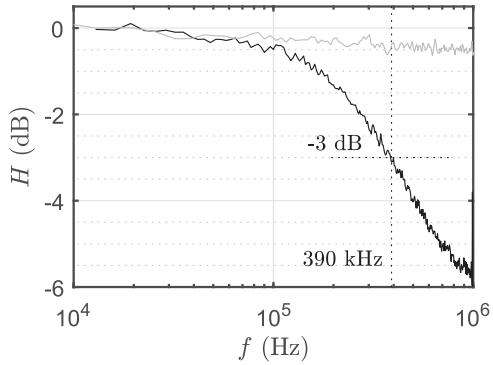

FIG. 5. Frequency response of the LED intensity in black and of the output current of the driving unit in gray.

the voltage drop across the resistor R, is thus also the current flowing across the LED.

D. Driving unit performances

The static performances of the system made of the driving unit and the LED are assessed by applying a series of constant input voltages V_{in} to the driving unit and by measuring simultaneously the time-averaged values of the output current i and the photon flux collected by the photomultiplier. The challenge resides in preventing the LED junction from heating-up when high currents are applied, which would reduce its efficiency and bias the results. This difficulty is worked around by reducing the measurement time at a given V_{in} and by repeating measurements to reduce the shot noise influence of the photon flux results. The evolution of $\overline{\Phi}_c$ and $\overline{\Phi}$ with $\overline{i}$ are provided in Fig. 4. The detected flux Φ is corrected from Φ_c by Eq. (7) with $\tau = 1.6$ ns as determined in a previous study.[6] The difference between these two quantities is caused by the pile-up effect briefly presented in Sec. II B and increases when the flux of photons rises, as expected. Although the light intensity of the LED rises very slowly with the current below $i = 4$ mA, a region where Φ increases linearly with i is observed between $i = 5$ mA and $i = 12$ mA. This linearity is comparable to that observed for density measurements, as stated in Eq. (3). As a consequence, from these measurements in static conditions, it can be concluded that as long as the current is kept within the linear region, variations of i, and thus, variations of the input V_{in}, can be used to simulate variations of flow density.

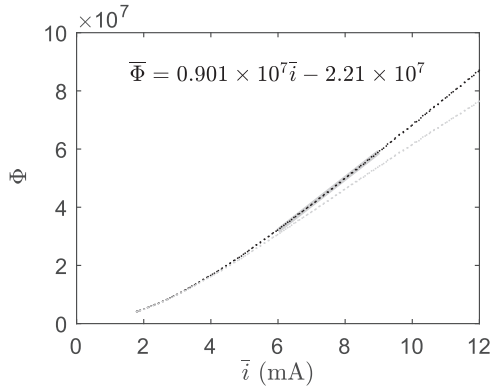

FIG. 4. Counted photon flux Φ_c (gray dotted curve) and detected photon flux Φ (black dotted curve) against the current i that flow through LED. The gray line shows the best fit in the linear region of the calibration curve.

Dynamic performances are evaluated by applying a sine sweep of frequency ranging from 10 kHz to 1 MHz to the driving unit input. The average current is set at 7.57 mA, and the sine amplitude is 2.00 mA. The frequency responses of the driving unit, and of the LED associated photon count rate are presented in Fig. 5. The response of the driving unit output current i is nearly flat with a loss of only −0.5 dB at 1 MHz. The response of the LED light intensity is measured by tracking the amplitude of the fluctuations of the collected flux of photons against the sweep frequency. The efficiency of the LED decreases with the frequency, with a −3 dB cut-off frequency of 390 kHz. However, the response of the LED is very close to that of the driving unit up to 100 kHz. Therefore, the bandwidth of the setup is [0 100 kHz].

These results show that the light intensity of the LED can be modulated by an input reference signal. It therefore allows for assessing the ability of the system to measure accurately any light intensity fluctuation in real applications. There are two constrains for the input signal with the present setup; the minimum driving voltage V_{in} is high enough for the current to be higher than 5 mA, and the frequency content of the signal is contained between DC and 100 kHz.

III. REFERENCE DENSITY-LIKE SIGNAL

On the basis of the abovementioned properties, the system is able to transpose arbitrary electric signals into light flux provided its maximum frequency does not exceed 100 kHz. For the validation of the chain of acquisition, and of the processing methods, this signal must be representative of a real local density time history. In particular, it must comply with the turbulence properties, as for instance an appropriate integral time scale. Ideally, the signal should

be related to the density in a compressible flow and obtained either numerically, experimentally, or analytically using synthetic turbulence models for instance. Nevertheless, the present study concerns the ability of the Rayleigh scattering setup to correctly resolve the input spectrum of light fluctuations. This aptitude is considered to be weakly dependent of the nature of the input as long as it correctly represents the physics of a turbulent process. Rather than a density signal, for this study, the chosen reference signal is a velocity signal extracted from a 120 s hot wire measurement in a turbulent boundary layer. In fact, both velocity and density signals are expected to feature similar characteristics of the turbulence. The normalized spectrum of this signal is presented in Fig. 6. It has a dynamic of approximately four decades between the frequencies normalized by the sampling frequency 10^{-3} and 0.5, which is convenient for assessing the dynamic of the Rayleigh scattering based measurement system.

This signal is uploaded into a Tektronix AFG3102 arbitrary signal generator from which it is possible to adjust the rms value and the frequency. The DC offset is set independently on the driving unit. According to the driving unit performances, and to the available memory of the AFG3102 which is only capable of storing 128 000 samples, the signal is generated with a sampling frequency of 102.4 kHz, leading to a Shannon frequency of 51.2 kHz and a duration of 1.25 s.

The DC current is set to produce the same flux of photons as the Rayleigh scattering produces for a constant density, in a classical experimental setup. For instance, previous calibrations performed by the authors[5,6] led to a typical photon flux $\Phi \simeq 4.0 \times 10^7 \rho$ photons/s. For $\overline{\rho} = 1.2$ kg/m^3, one obtains $\overline{\Phi} = 4.8 \times 10^7$ photons/s, corresponding to a current $\overline{i} = 7.80$ mA according to the calibration curve of Fig. 4. The rms value of the current fluctuations i'_{rms} is determined to match a realistic turbulent intensity here defined as $\mathcal{I} = \Phi'_{rms}/\overline{\Phi}$, giving

$$i'_{rms} = \frac{\mathcal{I}\overline{\Phi}}{0.90 \times 10^7}. \tag{10}$$

For a typical value of $\mathcal{I} = 5\%$, $i'_{rms} = 0.27$ mA.

These figures can of course be adapted to explore the response of any system in different experimental conditions, either for low photon fluxes involving a large shot noise contribution or large photon fluxes for which corrections of the pile-up effect are of primary importance.

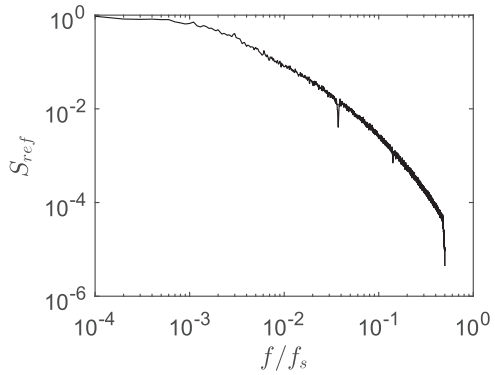

FIG. 6. Normalized spectrum of the reference signal for the LED intensity modulation.

IV. ESTIMATION OF THE FLUCTUATION SPECTRUM

A. Shot noise reduction method

In this section, we aim at estimating the spectrum of the current signal of features detailed in Sec. III. In any case, the signal of current is kept in the linear response region of the LED ensuring a similarity between the LED brightness and the light collected from a Rayleigh scattering process. Thus,

$$\Phi = ki + \Phi_0, \tag{11}$$

$$N = \frac{k}{f_s} i + \frac{\Phi_0}{f_s}. \tag{12}$$

The value of k is the slope of the linear region of the calibration curve in Fig. 4, and Φ_0 is the zero crossing flux of the fitting curve. Here, $k = 9.01 \times 10^6$ and $\Phi_0 = -2.21 \times 10^7$.

In most flows, the density fluctuations are small, and the shot noise is likely to be the strongest contribution to the photon count rate spectrum, and hence, to the LED current spectrum. Besides, the shot noise is a Poisson noise, thus a white noise. The level $P_{N_{sn}}$ of the shot noise contribution N_{sn}^{rms} in the count rate spectrum can therefore be determined easily from Parseval's identity since white noises have flat spectra. Indeed,

$$Var(N_{sn}) = \int_0^{f_s/2} P_{N_{sn}} df = P_{N_{sn}} \frac{f_s}{2} \tag{13}$$

and, from Poisson's law, $Var(N_{sn}) = \overline{N}$, and thus,

$$P_{N_{sn}} = \frac{2\overline{N}}{f_s}. \tag{14}$$

Furthermore, one has from Eq. (12),

$$\overline{N} = \frac{k\overline{i} + \Phi_0}{f_s} \tag{15}$$

and

$$N' = \frac{k}{f_s} i' \tag{16}$$

leading in terms of spectra to

$$P_{N_{sn}} = \frac{k^2}{f_s^2} P_{i_{sn}}. \tag{17}$$

By combining Eqs. (14), (15), and (17), the contribution of the shot noise in the LED current spectrum reads

$$P_{i_{sn}} = 2\frac{\overline{i} + \Phi_0/k}{k}. \tag{18}$$

The flow density $\overline{\rho}$, or the LED current $\overline{i}$ in this analogy, is in general imposed by the experiment. Therefore, the shot noise level in the density or current spectrum can only be reduced by increasing k. Yet, the value of k is upper bounded both by the pile-up effect and by the limits of the laser technologies.

Strategies to reduce the shot noise though exist. Panda and Seashlotz[10] proposed using two photomultipliers that probe

simultaneously the same volume. In Mercier *et al.*,[6] a method based on the same principle is provided, but instead of using two photomultipliers to obtain two signals, only one is used, and the count-rate time history is divided in two as follows: consider a signal $N_c(t)$ with $t = 0, dt, 2dt, 3dt, \ldots$, the first signal N_1 is made from the samples at $t = 2ndt$ with $n = 0, 1, 2, 3, \ldots$, and the second N_2 is made from the samples at $t = (2n + 1)dt$. Each signal is the sum of a coherent contribution, with the subscript s, representative of the physical signal to be characterized, and a noncoherent contribution associated with the shot noise, with the subscript sn. This gives

$$\begin{aligned} N_1 &= N_{1_s} + N_{1_{sn}}, \\ N_2 &= N_{2_s} + N_{2_{sn}}. \end{aligned} \tag{19}$$

These two signals are divided into m segments $N_1^i(t)$ and $N_2^i(t)$ with $i = 1, 2, 3, \ldots, m$ of time duration l_t determining the final frequency resolution Δf of the spectrum such that $\Delta f = 1/l_t$. Then, the cross-spectrum of the fluctuation $P_{N_1N_2}$ is obtained as follows:

$$P_{N_1N_2}(f) = \frac{2}{m}\sum_i^m F_{N_1^i}(f)F_{N_2^i}^*(f), \tag{20}$$

where F is the Fourier transform and * denotes the complex conjugate. Using the decomposition in Eq. (19),

$$\begin{aligned} P_{N_1N_2}(f) = \frac{2}{m}\sum_{i=1}^m & \underbrace{F_{N_{1_{sn}}^i} F_{N_{2_s}^i}^* + F_{N_{1_s}^i} F_{N_{2_{sn}}^i}^*}_{\text{(a)}} \\ & + \underbrace{F_{N_{1_{sn}}^i} F_{N_{2_{sn}}^i}^*}_{\text{(b)}} + \underbrace{F_{N_{1_s}^i} F_{N_{2_s}^i}^*}_{\text{(c)}}. \end{aligned} \tag{21}$$

Terms (a) and (b) involve the shot noise contributions $N_{1_{sn}}^i$ and $N_{2_{sn}}^i$ that are random and independent. Besides, their complex Fourier transform coefficients are also random and centered on zero. As a consequence, for large values of m, the contribution to the sum of terms (a) and (b) vanishes out. The term (c) only involves coherent contributions. Then,

$$\lim_{m\to\infty} |P_{N_1N_2}(f)| = |\frac{2}{m}\sum_{i=1}^m F_{N_{1_s}^i} F_{N_{2_s}^i}^*|. \tag{22}$$

Moreover, if the sampling frequency is high enough with respect to the frequency of the coherent fluctuations, N_{1_s} and N_{2_s} are expected to be strongly correlated, and only time shifted by a delay dt. Therefore, for large value of m, $P_{N_1N_2}(f)$ is a good approximation of the spectrum of the signal s

$$\lim_{m\to\infty} |P_{N_1N_2}(f)| \simeq |P_{N_{1_s}N_{1_s}}| \simeq |P_{N_{2_s}N_{2_s}}|. \tag{23}$$

Unfortunately, the number m of signal segments is limited and a residual contribution of the shot noise remains in the fluctuations. This corresponds to a noise floor in the spectra of value $P_{N_{res}}$. This noise floor is reached when the shot noise contribution is much larger than the coherent fluctuations. For that reason, terms (a) and (c) in Eq. (21) that involve coherent fluctuation are neglected compared to the term (b), and the residual noise floor $P_{N_{res}}$ is

$$P_{N_{res}} = \left|\frac{2}{m}\sum_{i=1}^m F_{N_{1_{sn}}^i} F_{N_{2_{sn}}^i}^*\right|. \tag{24}$$

The expected value of $P_{N_{res}}$ can be determined as a function of m by noting z_i the random complex number $z_i = e^{j\theta_i}$, where $j = \sqrt{-1}$, and θ_i is a random variable such that $F_{N_{1_{sn}}^i} F_{N_{2_{sn}}^i}^* = |F_{N_{1_{sn}}^i} F_{N_{2_{sn}}^i}^*| z_i$. Since N_1 and N_2 are both extracted from N by halving the sampling frequency, from Parseval's identity

$$|F_{N_{1_{sn}}^i} F_{N_{2_{sn}}^i}^*| = \frac{4\overline{N}}{f_s} = 2P_{N_{sn}}. \tag{25}$$

Equation (24) becomes

$$P_{N_{res}} = \frac{2P_{N_{sn}}}{m}\left|\sum_{i=1}^m z_i\right| = \frac{4\overline{N}}{mf_s}\left|\sum_{i=1}^m z_i\right|. \tag{26}$$

Noting that

$$\begin{aligned} |\sum_{i=1}^m z_i| &= \left(\sum_{i=1}^m z_i \sum_{j=1}^m z_j^*\right)^{1/2} \\ &= \left(\sum_{i=1}^m\sum_{j=1}^m \underbrace{z_i z_j^* \delta_{ij}}_{i=j} + \sum_{i=1}^m\sum_{j=1}^m \underbrace{z_i z_j^* (1-\delta_{ij})}_{i\neq j}\right)^{1/2} \end{aligned} \tag{27}$$

and that

$$\begin{aligned} \sum_{i=1}^m\sum_{j=1}^m z_i z_j^* \delta_{ij} &= m, \\ \lim_{m\to\infty}\sum_{i=1}^m\sum_{j=1}^m z_i z_j^* (1-\delta_{ij}) &= 0, \end{aligned} \tag{28}$$

we obtain

$$P_{N_{res}} = \frac{4}{\sqrt{m}}\frac{\overline{N}}{f_s} \tag{29}$$

similarly in this particular application,

$$P_{i_{res}} = \frac{4}{\sqrt{m}}\frac{\bar{i} + \Phi_0/k}{k}. \tag{30}$$

The residual noise floor emerging from the shot noise decreases with $\sqrt{m}$; large values of m are therefore required to reduce the noise floor by orders of magnitude. The number m of segments is set on one hand by the recording length, and on the other hand by the desired frequency resolution of the spectrum. Lower resolution (higher value of Δf) means more segments for the same recording time, and thus lower noise floor.

B. Validation

In this section, the decay of the level of the noise floor with the number of segments is verified and compared to the prediction in Eq. (30). Then, the effect on the spectra of the signal splitting needed for the shot noise reduction is analyzed.

The data set used in this section consists of 1170 independent records of 0.86 s each, this duration being the longest record achievable by the PXIe-5160 digitizer with the present configuration. The total length of the record is therefore a little longer than 1000 s. Each record is initially a photomultiplier output signal from which count rate time histories are extracted following the method provided in Sec. II B.

For the analysis of the noise floor decay, the sampling frequency f_s of the count rate time history $N(t)$ is chosen to be f_s = 409.6 kHz. With that f_s, the maximum frequency of the fluctuating current spectrum P_i is $f_s/4$ = 102.4 kHz. Besides, the signal generator used to generate V'_{in} at the LED driving unit input has a sampling frequency of 102.4 kHz. The maximum frequency of LED brightness fluctuation is therefore 51.2 kHz. Hence, the fluctuations measured on the spectrum P_i are only attributable to the residual noise floor within the range 51.2 kHz–102.4 kHz. As a consequence, the residual noise floor $P_{i_{res}}$ is estimated as the average value of P_i between 51.2 kHz and 102.4 kHz. The evolution of $P_{i_{res}}$ against m is displayed in Fig. 7. For the values of m between 2 and 1170 (which corresponds to the total number of independent recordings), the spectrum P_i is evaluated using m recordings; for the values of m greater than 1170, recordings are partitioned, and P_i is evaluated from the partitions. A maximum value of 344 partitions by recording is used, leading to the maximum value $m = 344 \times 1170 = 4 \times 10^5$. A very good agreement is found between the measured and the predicted values of $P_{i_{res}}$. For m below 5×10^4, the decay slope is −0.5 as expected. Above, $P_{i_{res}}$ slightly oscillates near the prediction. The model given in Eq. (30) to predict the shot noise level given the calibration parameters and the number of segment m is validated, and provides consistent predictions.

The analysis now focuses on the effect on spectra of splitting N into N_1 and N_2. To this purpose, spectra of the current fluctuations P_i are computed with N sampled at different frequencies. The sampling frequencies f_s = 409.6 kHz, f_s = 102.4 kHz, and f_s = 25.6 kHz are retained. The largest is well above the LED current fluctuations, while the smallest is similar with the high frequencies of i'.

The three spectra, each evaluated with a frequency resolution of 100 Hz, are shown in Fig. 8. The spectrum obtained from the direct current measurement through V_{out} is also plotted for the comparison. For the two lowest f_s cases, the spectrum points out a strong decay of the amplitude for frequencies approaching the highest spectrum frequency. This drop is expected and corresponds to the reducing point to point coherence for high frequencies. An error larger than 5% is observed at $0.08f_s$ for f_s = 25.6 kHz and $0.10f_s$ for f_s = 102.4 kHz. These frequencies depend upon the coherence of turbulence in the investigated flow, but the present signal was chosen to be representative for typical turbulent flow. To prevent spectra from being biased, it is therefore reasonable to choose a sampling frequency at least 10–12 times larger than the maximum frequency of interest for the study. The value of 12 might seem to be large, but it must be put together with the fact than even if there was no bias, the minimum sampling frequency would be 4 times the desired frequency. Hence, the sampling frequency should only be multiplied by 3 to suppress the bias.

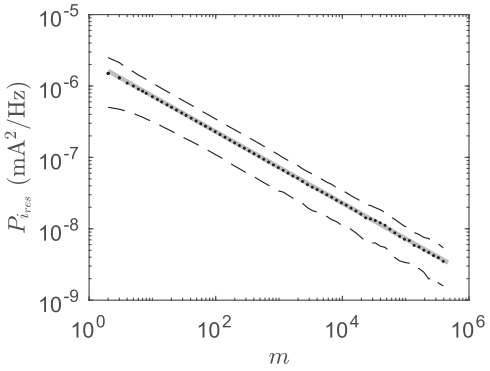

FIG. 7. Residual noise floor as a function of the number of segments used to compute the spectrum. Black dotted curve: measured value, gray solid curve: prediction from Eq. (30). Black dashed curve: ±1 standard deviation of the shot noise level.

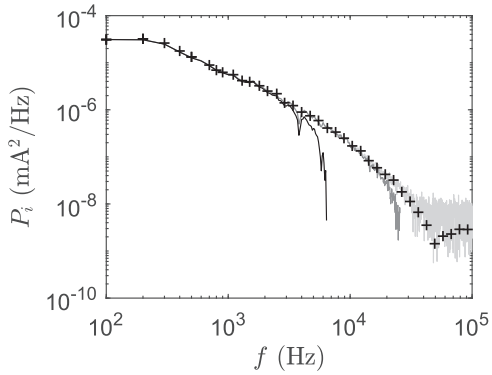

FIG. 8. Spectra for three different sampling frequencies. Light gray solid curve: f_s = 409.6 kHz, gray solid curve: f_s = 102.4 kHz, black solid curve: f_s = 25.6 kHz, and plus sign: reference measurement.

C. Practical spectra estimation with shot noise minimization

In practical estimations of density spectra from turbulent flows, the residual noise floor due to shot noise can prevent one from capturing the decay of turbulence level at a "high" frequency, typically above 1–10 kHz. On the other hand, flow field characterization often relies on a fine frequency resolution to capture possible resonances (e.g., cavity flows) or flow global instabilities (e.g., wake of bluff body flows), the signature of which are typically in the range of frequency 0.1–1 kHz at usual scales. These two constraints are not compatible as shown by Eq. (30): a low residual noise floor requires m to be large, and hence, a large frequency resolution also. A practical way to circumvent this feature is to estimate the spectrum of a given signal from the concatenation of portions of spectra computed with different frequency resolutions.

The result of such a procedure is illustrated in Fig. 9. This example is based on the same signal as that of Fig. 8, but analyzed using four different frequency resolutions: 20 Hz below 1 kHz, 100 Hz between 1 kHz and 10 kHz, 400 Hz between 10 kHz and 30 kHz, and 1600 Hz at frequencies above 30 kHz. The resulting spectrum indeed shows the main features of the original spectra while keeping the shot noise level below 10^{-8} A^2/Hz, allowing for a very good agreement between the measured spectrum from the fluctuations of LED light intensity and the reference current spectrum. In particular, low frequency features that were not visible in Fig. 8 with a frequency resolution of 100 Hz appear with the spectrum concatenation, whereas in the meantime, the shot noise level is lower in Fig. 9 than in Fig. 8.

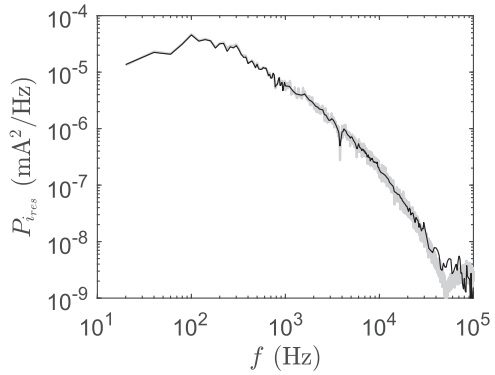

FIG. 9. Spectrum of the current fluctuations. Black solid curve: concatenated spectra, gray solid curve: reference spectrum.

V. CONCLUSION

A dynamic analysis of a Rayleigh scattering setup based on synthetic light signals is performed. Light signals are generated by a modulated LED fed by a dedicated driving unit, whose input corresponds to a sample of turbulent velocity signal. This system was found to allow for simulating the light fluctuations associated with a Rayleigh scattering process at frequencies up to 100 kHz.

The unit is designed to simultaneously measure the light intensity signal with the Rayleigh scattering setup and an electrical output signal that mimics the real light power emitted by the LED source. This allows for an effective comparison between the expected and the measured light signal characteristics, and, in particular, their spectral behaviors.

Spectra of the light signals measured by a photomultiplier, as used in classical Rayleigh scattering setups, are affected by the shot noise that imposes a residual noise floor, which limits the effective dynamic of the measurements. This noise floor can be reduced by applying a specific data processing to the signals. The procedure is however shown to introduce a bias that vanishes providing light signals are sampled at a frequency at least ten times larger than the maximum frequency of interest in the spectrum.

A model is derived to predict the performance of this data processing and is successfully compared to the experimental results. The model shows that the noise floor level is inversely proportional to the square root of the recording time, and to the square root of the frequency resolution. It therefore allows us to predict the minimum recording time needed to reach a desired noise floor level with a given frequency resolution. Conversely, for a given recording time, the proper frequency resolution for an appropriate shot noise level is provided by the model.

ACKNOWLEDGMENTS

This work was performed within the framework of the Labex CeLyA of Université de Lyon, within the program "Investissements d'Avenir" (Nos. ANR-10-LABX-0060/ANR-11-IDEX-0007) operated by the French National Research Agency (ANR), and is also partially supported by the industrial Chair ADOPSYS co-financed by SAFRAN-SNECMA and ANR (No. ANR-13-CHIN-0001-01).

REFERENCES

[1]N. J. Dam, M. Rodenburg, R. A. L. Tolboom, G. G. M. Stoffels, P. M. Huisman-Kleinherenbrink, and J. J. ter Meulen, "Imaging of an underexpanded nozzle flow by UV laser Rayleigh scattering," Exp. Fluids **24**(2), 93–101 (1998).

[2]N. Damaschke, V. Kühn, and H. Nobach, "A fair review of non-parametric bias-free autocorrelation and spectral methods for randomly sampled data in laser Doppler velocimetry," Digital Signal Process. **76**, 22–33 (2018).

[3]K. Fiedler, O. Sieber, and C. Jakiel, "Quantitative density measurements by Rayleigh scattering behind a plane turbine cascade," AIAA J. **35**(8), 1303–1308 (1997).

[4]P. Kreisler, W. Tietsch, and K. Bethge, "Measurement of the density of a gas jet by light scattering," Nucl. Instrum. Methods **177**(2-3), 521–527 (1980).

[5]B. Mercier, "Développement d'une méthode de mesure de la masse volumique par diffusion Rayleigh appliquée à l'étude du bruit de jets, et contribution à l'étude du screech dans les jets supersoniques sous détendus," Ph.D. thesis, 2017-LYSEC61, École Centrale de Lyon, 2017.

[6]B. Mercier, T. Castelain, E. Jondeau, and C. Bailly, "Density fluctuations measurement by Rayleigh scattering using a single photomultiplier," AIAA J. **56**(4), 1310–1316 (2017).

[7]J. Panda, "Two point space-time correlation of density fluctuations measured in high velocity free jets," AIAA Paper 2006-0006, 2006.

[8]J. Panda, "A molecular Rayleigh scattering setup to measure density fluctuations in thermal boundary layers," Exp. Fluids **57**(12), 183 (2016).

[9]J. Panda and R. Seasholtz, "Density measurement in underexpanded supersonic jets using Rayleigh scattering," AIAA Paper No. 98-281, 1998.

[10]J. Panda and R. G. Seasholtz, "Experimental investigation of density fluctuations in high-speed jets and correlation with generated noise," J. Fluid Mech. **450**, 97–130 (2002).

[11]M. J. Papageorge, C. Arndt, F. Fuest, W. Meier, and J. A. Sutton, "High-speed mixture fraction and temperature imaging of pulsed, turbulent fuel jets auto-igniting in high-temperature, vitiated co-flows," Exp. Fluids **55**(7), 1763 (2014).

[12]I. van Cruyningen, A. Lozano, and R. K. Hanson, "Quantitative imaging of concentration by planar laser-induced fluorescence," Exp. Fluids **10**(1), 41–49 (1990).

[13]J. Westerweel, G. E. Elsinga, and R. J. Adrian, "Particle image velocimetry for complex and turbulent flows," Annu. Rev. Fluid Mech. **45**(1), 409–436 (2013).